

Stationary Liquid Fuel Fast Reactor

Reactor Concepts

Won Sik Yang

Purdue University

In collaboration with:

Argonne National Laboratory

Thomas Sowinski, Federal POC

Patrick McClure, Technical POC

Final Report on Stationary Liquid Fuel Fast Reactor

W. S. Yang, T. Jing, Y. S. Jung, S. Shi, G. Yang

School of Nuclear Engineering
Purdue University

C. Grandy, A. Borowski, L. Krajtl

Nuclear Engineering Division
Argonne National Laboratory

T. Johnson

Chemical Science and Engineering Division
Argonne National Laboratory

September 30, 2015

Executive Summary

For effective burning of hazardous transuranic (TRU) elements of used nuclear fuel, a transformational advanced reactor concept named SLFFR (Stationary Liquid Fuel Fast Reactor) was proposed based on stationary molten metallic fuel. The fuel enters the reactor vessel in a solid form, and then it is heated to molten temperature in a small melting heater. The fuel is contained within a closed, thick container with penetrating coolant channels, and thus it is not mixed with coolant nor flow through the primary heat transfer circuit. The makeup fuel is semi-continuously added to the system, and thus a very small excess reactivity is required. Gaseous fission products are also removed continuously, and a fraction of the fuel is periodically drawn off from the fuel container to a processing facility where non-gaseous mixed fission products and other impurities are removed and then the cleaned fuel is recycled into the fuel container.

A reference core design and a preliminary plant system design of a 1000 MWt TRU-burning SLFFR concept were developed using TRU-Ce-Co fuel, Ta-10W fuel container, and sodium coolant. Conservative design approaches were adopted to stay within the current material performance database. Detailed neutronics and thermal-fluidic analyses were performed to develop a reference core design. Region-dependent 33-group cross sections were generated based on the ENDF/B-VII.0 data using the MC²-3 code. Core and fuel cycle analyses were performed in theta-r-z geometries using the DIF3D and REBUS-3 codes. Reactivity coefficients and kinetics parameters were calculated using the VARI3D perturbation theory code. Thermo-fluidic analyses were performed using the ANSYS FLUENT computational fluid dynamics (CFD) code.

Figure 0.1 shows a schematic radial layout of the reference 1000 MWt SLFFR core, and Table 0.1 summarizes the main design parameters of SLFFR-1000 loop plant. The fuel container is a 2.5 cm thick cylinder with an inner radius of 87.5 cm. The fuel container is penetrated by twelve hexagonal control assembly (CA) guide tubes, each of which has 3.0 mm thickness and 69.4 mm flat-to-flat outer distance. The distance between two neighboring CA guide tube is selected to be 26 cm to provide an adequate space for CA driving systems. The fuel container has 18181 penetrating coolant tubes of 6.0 mm inner diameter and 2.0 mm thickness. The coolant tubes are arranged in a triangular lattice with a lattice pitch of 1.21 cm. The fuel, structure, and coolant volume fractions inside the fuel container are 0.386, 0.383, and 0.231, respectively. Separate steel reflectors and B₄C shields are used outside of the fuel container. Six gas expansion modules (GEMs) of 5.0 cm thickness are introduced in the radial reflector region. Between the radial reflector and the fuel container is a 2.5 cm sodium gap.

The TRU inventory at the beginning of equilibrium cycle (BOEC) is 5081 kg, whereas the TRU inventory at the beginning of life (BOL) was 3541 kg. This is because the equilibrium cycle fuel contains a significantly smaller fissile fraction than the LWR TRU feed. The fuel inventory at BOEC is composed of 34.0 a/o TRU, 41.4 a/o Ce, 23.6 a/o Co, and 1.03 a/o solid fission products. Since uranium-free fuel is used, a theoretical maximum TRU consumption rate of 1.011 kg/day is achieved. The semi-continuous fuel cycle based on the 300-batch, 1-day cycle approximation yields a burnup reactivity loss of 26 pcm/day, and requires a daily reprocessing of 32.5 kg of SLFFR fuel. This yields a daily TRU charge rate of 17.45 kg, including a makeup TRU feed of 1.011 kg recovered from the LWR used fuel. The charged TRU-Ce-Co fuel is composed of 34.4 a/o TRU, 40.6 a/o Ce, and 25.0 a/o Co.

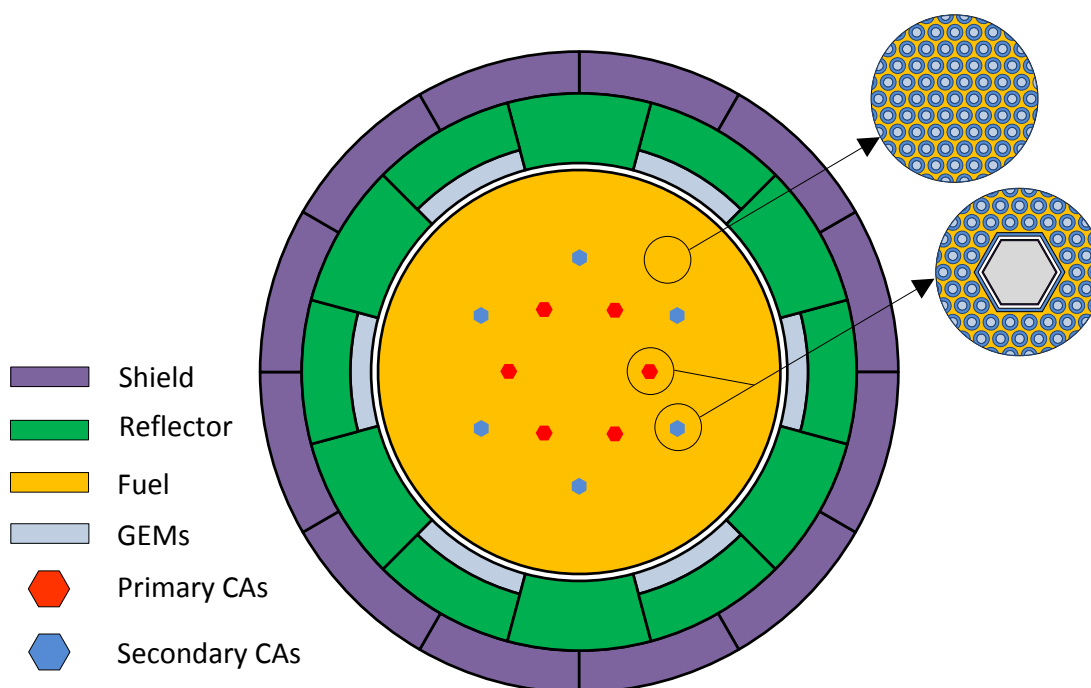


Figure 0.1. Schematic Radial Layout of 1000MWt SLFFR Core

Table 0.1. Main Design Parameters of SLFFR-1000 Loop Plant

Parameter	SLFFR-1000 Loop
Reactor Power	1000 MWth, 390 MWe
Coolant	Sodium
Coolant Temperature, Inlet/Outlet	450 °C / 550 °C
Total Coolant Flow Rate	7910 kg/sec
Charge Fuel Composition	34.4 a/o TRU, 40.6 a/o Ce, and 25.0 a/o Co alloy
TRU Inventory	3541 kg at BOL, 5081 kg at BOEC
Fuel Container Material	Refractory Ta-10W alloy
Fuel Container Size	1.8 m diameter, 1.5 m height
Cycle Length	Continuous batch-type refueling
Plant Life	60 years
Reactor Vessel Size	6.35 m diameter, 8.5 m height
Structural and Piping Material	Austenitic Stainless Steel
Primary Pump	Four (4) centrifugal primary pumps
Power Conversion Cycle	Reference: Rankine Steam Cycle
Cycle Efficiency/Plant Efficiency	~41.5% / 39%

Since uranium-free fuels are used for SLFFR, the delayed neutron fraction is about two thirds of conventional breeder reactors, and the Doppler coefficient that provides prompt reactivity feedback is practically zero. However, SLFFR has a large, negative axial expansion reactivity coefficient due to the thermal expansion of liquid fuel, which is also prompt. The axial expansion reactivity coefficient of SLFFR is 8.5 times more negative than that of a 1000 MWt Advanced Burner Reactor (ABR) concept of zero TRU conversion ratio with conventional solid fuel. The radial expansion of the fuel container of SLFFR due to an increased coolant inlet temperature yields a small positive radial expansion reactivity coefficient under the assumption that the fuel height is reduced to preserve the fuel volume without fuel density change. The sodium void worth of SLFFR is 4.5\$, which is significantly less positive than that of ABR (8.0\$).

The multi-channel CFD analyses showed that the peak temperatures at the interface between the liquid fuel and coolant tubes including CA guide tubes is lower than the imposed design limit of 700 °C with designed inlet flow allocation. The highest structural temperature appears at the inner surface of the Ta-10W fuel tank, which is also below the design limit. The analysis results indicate that the SLFFR of a zero TRU conversion ratio would be feasible while satisfying the conservatively imposed design constraints.

A reference plant concept of 1000 MWt SLFFR was developed as well. The loop-type arrangement of primary heat transport system was selected for this study due to the relative compactness of the reactor vessel, which supports the use of a rapid and frequent refueling system that does not require a large span across the reactor vessel head. The overall plant site arrangement is shown in Figure 0.2. The major systems – the reactor vessel containing the reactor core and the primary heat transport system, the intermediate heat transport system with the sodium to water stream generators, and the Rankine-cycle power conversion system – are shown in an elevation view in Figure 0.3. The reactor and the primary heat transport systems are located essentially below grade. Note that all of the nuclear components of the plant are located on a nuclear island, which is seismically isolated from its base mat foundation, which is also illustrated in Figure 0.3.

The primary system is configured in a loop-type arrangement with the reactor core and the direct reactor auxiliary cooling system (DRACS) heat exchangers contained in a reactor vessel, and the primary pumps and intermediate heat exchangers located in shielded cells outside the reactor vessel. The intermediate heat exchangers are established at the appropriate elevation to support natural circulation.

The power conversion system adopted for this loop concept is the Rankine steam cycle. Four 250 MWth once-through helical coil steam generators are used and sized for the 1000 MWth power level. These steam generators generate superheated steam in one pass of the steam generator. The system cycle efficiency is ~41.5% and the overall plant efficiency is 39%. A sodium-water reaction protection system is also included in the design as part of the primary plant auxiliary systems.

The intermediate sodium exits the IHX and flows to the helical coil steam generator located on the nuclear island. The intermediate sodium heats the feed water that turns to saturated steam and then to superheated steam before it exits the steam generator. The superheated steam then flows to the turbine-generator performing work and generating electricity. The steam exits

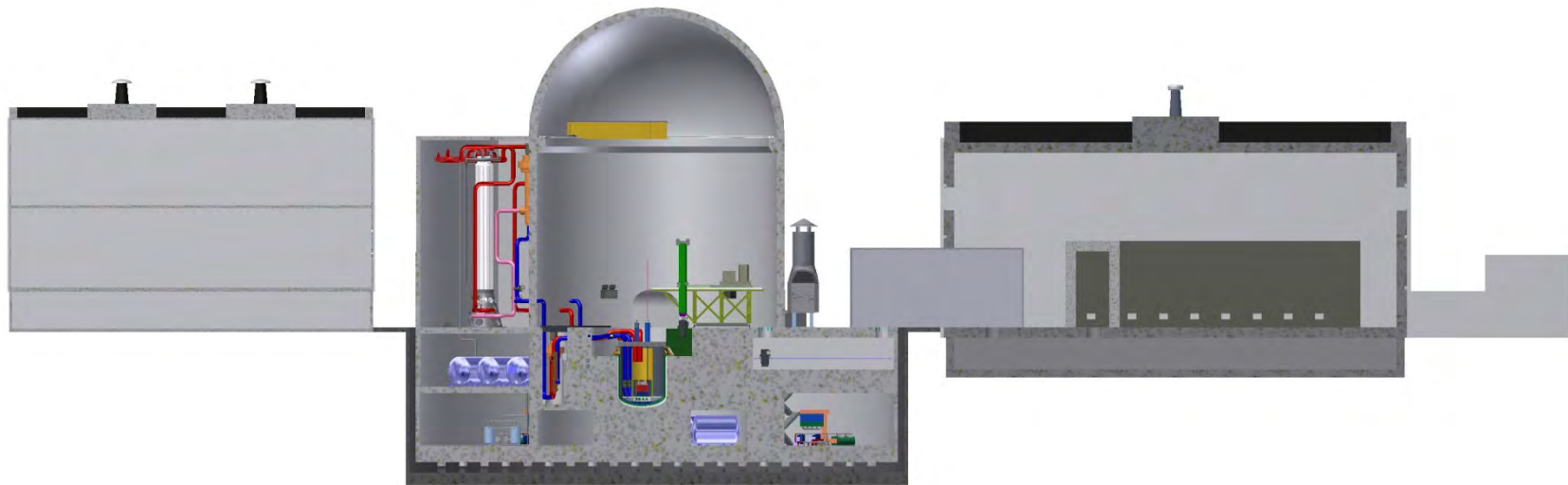


Figure 0.2. Elevation View of Primary System, Intermediate System, and Steam Generators

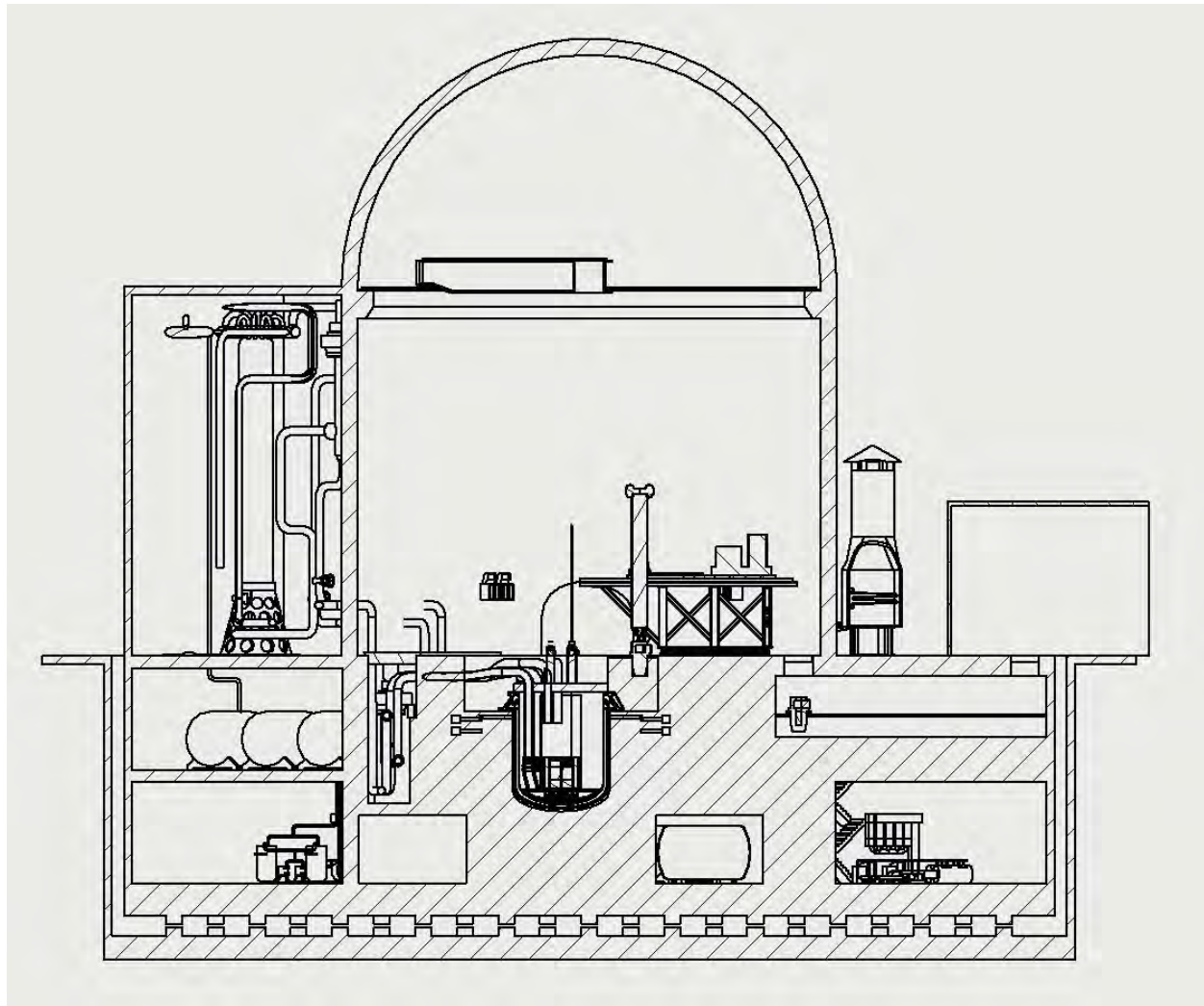


Figure 0.3. Elevation View of Nuclear Island

the turbine generator, and it is condensed in the main condenser as condensate. The condensate then goes through a series of heat exchangers and pumps to pressurize and preheat the condensate into feed water of the right temperature and pressure for introduction into the steam generator.

Removal of decay heat from the reactor core is a fundamental safety function. In the loop SLFFR design, normal decay heat removal is through the normal power conversion systems. However, a direct reactor auxiliary cooling system (DRACS) is provided, having both forced flow and natural convection capability. This system removes decay heat from the pool to the atmosphere using heat exchangers located in the cold part of the sodium pool and in the atmosphere above grade. If electrical power is available, forced flow can be used; in an emergency such as during the loss of all site power, natural convection flow will remove the decay heat.

The fuel handling, commissioning and startup are similar in concept to other fast reactor design concepts with the exception that for the SLFFR, fuel in a molten liquid state will need to be removed from the core. In order to maintain the criticality without excess reactivity control, the fuel handling system removes a small fraction of fuel from the reactor fuel tank thus removing fission products from the reactor. As illustrated in Figure. 0.4, the molten fuel is removed using the fuel-unloading machine that is designed to lower a gripper device that connects to a fuel sipper. After the fuel is removed from the reactor vessel through the “sipper”, it is processed in the fuel cycle facility and then blended with external TRU fuel feed. The sodium system and the balance of SLFFR plant can be commissioned and started up in the normal conventional manner for any sodium-cooled fast reactor system. The initial core load is comprised of solid fuel pellets and the loaded fuel will be melted by using a set of high temperature core-immersion heaters that will be inserted into the coolant tube. The recycling process for liquid TRU fuel was developed. It is capable of removing a sufficient fraction of fission products to maintain a low fuel melting point, and recover more than 99% of the actinides. The processing flowsheet is shown in Figure. 0.5.

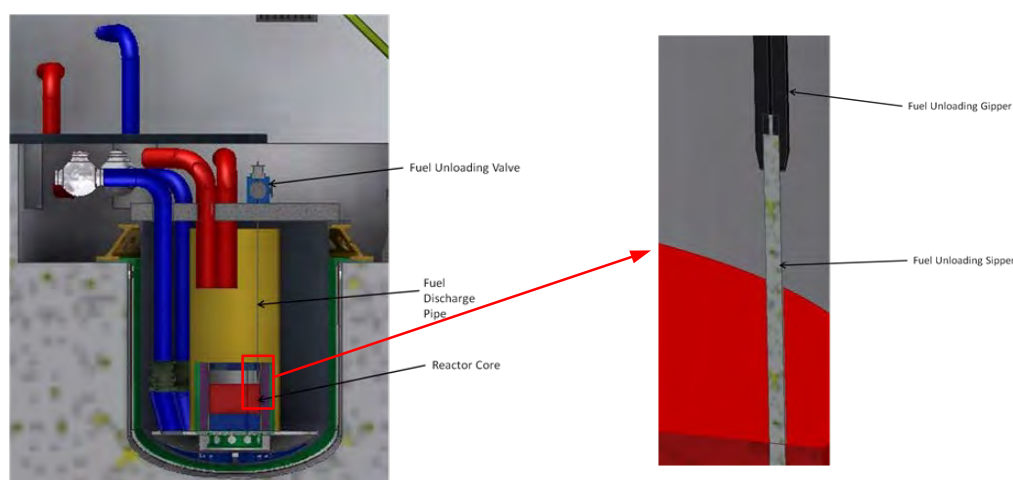


Figure 0.4. In-vessel Fuel Handling System

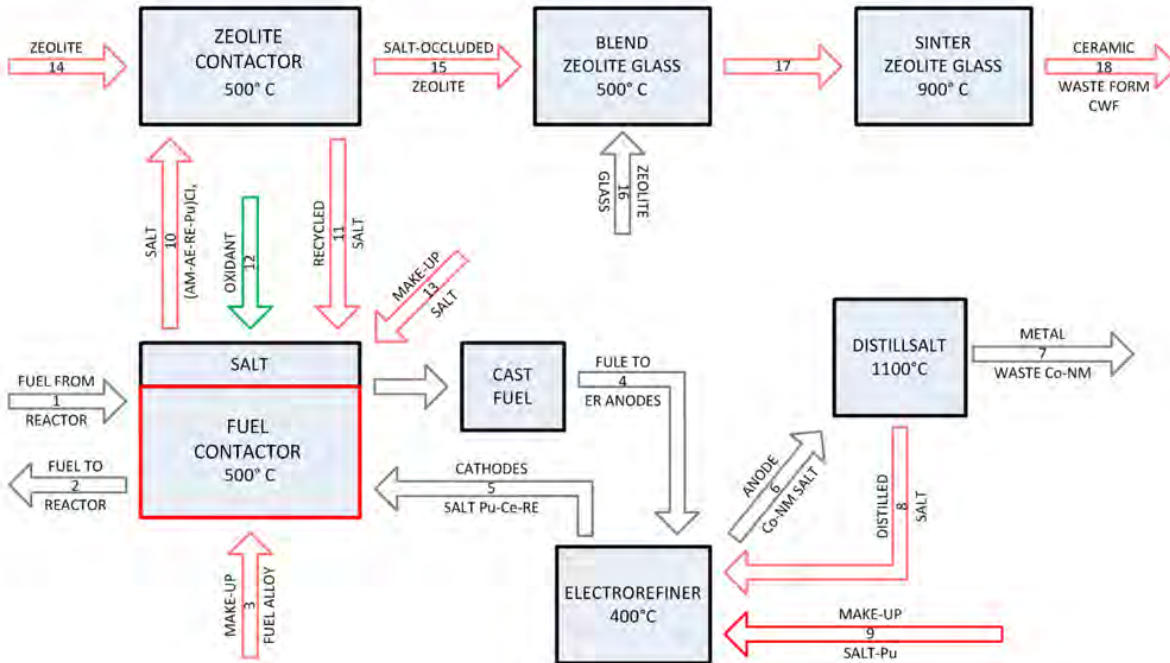


Figure 0.5. Concept for SLFFR Fuel Processing Flowsheet

The safety analyses of the SLFFR design for various hypothetical accident scenarios were performed using a multi-channel safety analysis code named MUSA, which was developed in this project to handle the unconventional geometry of the SLFFR core. The analysis results showed that the SLFFR design would provide inherent protection against damaging consequences in low probability accident sequences involving multiple equipment failures. Three beyond-design basis accidents (BDBA) was analyzed, including the unprotected transient overpower (UTOP), unprotected loss of heat sink (ULOHS), unprotected loss of flow (ULOF). The transients of power and peak coolant temperature for the three BDBAs are shown in Figure 0.6 and Figure 0.7. An UTOP accident with a step reactivity insertion of 0.5\$ was terminated with an elevated coolant outlet temperatures of 919K, 889K and 858K for the hot, average and periphery channels, respectively. A parametric study was also performed to find the maximum reactivity insertion that can be passively controlled without the reactor scram. The peak coolant temperature stays below the sodium boiling temperature for a step reactivity insertion up to 2.5\$. For an ULOHS accident, the power decreased to an asymptotic value of ~1% full power, which balances the heat ejection by the decay heat removal system, and the coolant inlet and peak outlet temperatures increased to 978K and 981K, respectively, which have a more than 200K margin to the sodium boiling temperature at the outlet pressure of 0.16 MPa. For a ULOF accident, the GEMs provided a sufficient negative reactivity. The maximum coolant outlet temperature for the hot channel was 912K, which has a significant margin to the sodium boiling temperature, and the new asymptotic fuel temperature was above the freezing point.

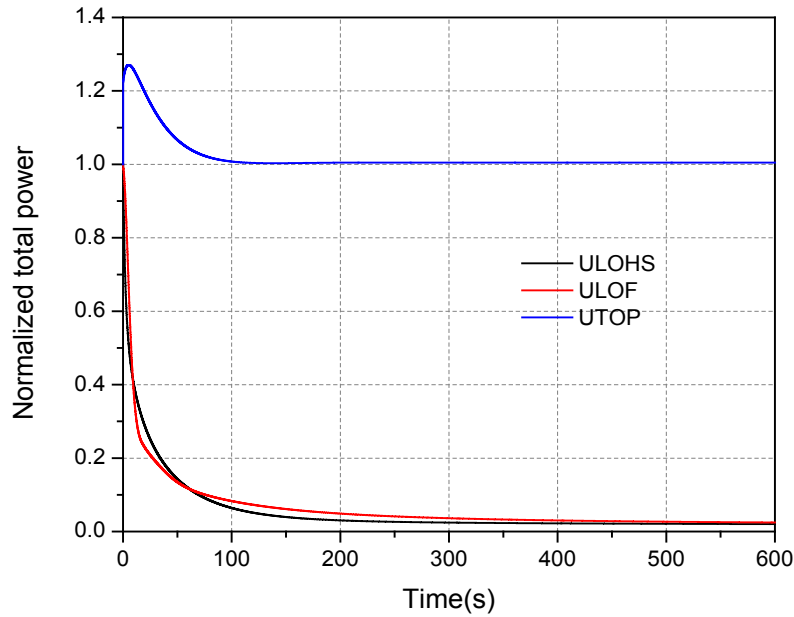


Figure 0.6. Power Transients for UTOP, ULOHS and ULOF Accidents

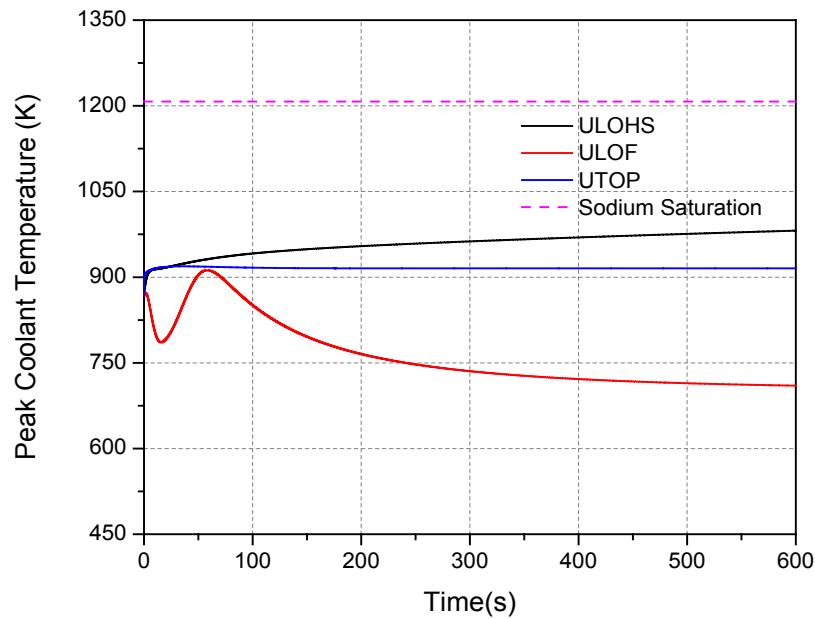


Figure 0.7. Peak Coolant Temperature Transients for UTOP, ULOHS and ULOF Accidents

A readiness assessment of the SLFFR technology was performed. The technology maturity levels of the plant components are provided in Table 0.2. In reviewing the technology readiness

of the system and components that comprise the SLFFR, it is apparent that the fuel-structure system of the reactor will be the greatest challenge with this reactor plant to understand whether this technology is feasible. It has the lowest technology readiness of all of the system and components thus should be the focus of future research and development efforts to continue the maturation of the SLFFR.

Table 0.2. SLFFR-1000 Loop Plant Technology Readiness Assessment

Reactor Component		Technology Maturity
Coolant		TRL 8
Coolant Purification Technology		TRL 8
Fuel Tank Structural Materials		TRL 3
Fuel Startup/Driver		TRL 2-3
Fuel Tank with Coolant Tubes		TRL 3
Primary System Configuration		TRL 7-8
Reactor Vessel and Structures		TRL 9-9
Intermediate Heat Exchanger		TRL 6-7
Primary and Secondary Pumps		TRL 6-7
Emergency Decay Heat Removal		TRL 6-7
Structural Material		TRL 8-9
Inert Gas System		TRL 8-9
Cover Gas Cleanup System		TRL 6-7
Reactivity Control System		TRL 6
Containment		TRL 8-9
Balance of Plant	Steam Generators	TRL 6-7
	Steam Plant minus Steam Generator	TRL 8-9
Seismic Isolation	Rubber and Steel Seismic Isolators	TRL 7
	Multiple Friction Pendulum System	TRL 5-6
Instrumentation and Control	Analog Control	TRL 9
	Digital Control Systems	TRL 8-9
Maintenance and Inspection Technology	Under Sodium Inspection System	TRL 5
	Compact Robotic Inspection Vehicle	TRL 5
Fuel Handling Systems		TRL 5-6
Fuel Reprocessing System		TRL 4-6

Table of Contents

Executive Summary	i
Table of Contents	xi
List of Figures	xv
List of Tables.....	xix
1. Introduction	1
2. Development of Reference Core Design	5
2.1. Core Concept.....	5
2.2. Selection of Fuel and Container Materials.....	6
2.3. Design Constraints	10
2.4. Computational Methods and Models	18
2.4.1. Multi-group Cross Section Generation.....	18
2.4.2. Fuel Cycle Analyses	19
2.4.3. Kinetics Parameters and Reactivity Coefficients	20
2.4.4. Computational Thermo-Fluidic Dynamics Analyses	22
2.5. Reference Core Design	25
2.5.1. Core Design Studies	25
2.5.2. Reference Core Design and Performances	27
2.5.2.1. Reference Core Design Description	27
2.5.2.2. Fuel Cycle Performance Characteristics	30
2.5.2.3. Kinetics Parameters and Reactivity Coefficients	34
2.5.2.4. Reactivity Control Requirements and Shutdown Margins.....	35
2.5.2.5. Orifice Zoning and Steady-state Thermal-Fluidic Analysis.....	38
2.5.3. Gas Expansion Modules	44
2.5.3.1. Design of Gas Expansion Modules	44
2.5.3.2. Reactivity Worth of Gas Expansion Modules	45
3. Overall Plant Design Description	49
3.1. Reactor Enclosure System	49
3.1.1. Reactor Vessel Assembly	49
3.1.2. Reactor Vessel	51
3.1.3. Reactor Vessel Top Enclosure Head (Deck)	51
3.1.4. Reactor Vessel and Deck Support Structure.....	53
3.1.5. Guard Vessels and Piping.....	55
3.1.6. Redan	55
3.1.7. Upper Internals Structure.....	56
3.1.8. Lower Internals Structure	57
3.1.9. Core Support Structure	57
3.1.10. Reactor Containment Boundary	57
3.2. Primary Heat Transport System	58
3.2.1. System Requirements and Description.....	58
3.2.2. Primary Sodium Mechanical Pump.....	59

3.2.3. Intermediate Heat Exchanger	59
3.2.4. Primary Heat Transport System (PHTS) Piping	62
3.3. Intermediate Heat Transport System	63
3.3.1. System Requirements and Description.....	63
3.3.2. Intermediate Sodium Pump	65
3.3.3. IHTS Piping.....	65
3.3.4. IHTS Sodium Storage Tank, Expansion Tank, and Cleanup System	66
3.4. Power Generating System.....	66
3.4.1. System Requirements and Description.....	66
3.4.2. Steam Generator System	67
3.4.2.1. Steam Generator.....	67
3.4.2.2. Steam Cycle.....	69
3.5. Fuel Handling System.....	70
3.6. SLFFR-1000 Site Plan	75
4. Development of Operation Strategies	77
4.1. Fuel Handling.....	77
4.2. Commissioning and Startup.....	78
4.3. Fuel Recycling	80
4.3.1. Process Description	80
4.3.2. Material Balance.....	82
5. Safety Analyses	87
5.1. Quasi-static Reactivity Balance Analysis	87
5.2. Transient Analyses.....	92
5.2.1. Unprotected Transient Overpower	95
5.2.2. Unprotected Loss of Heat Sink	99
5.2.3. Unprotected Loss of Flow	101
6. Evaluation of Technology Readiness	105
6.1. Technology Readiness Levels.....	105
6.2. Technology Readiness Evaluation for SLFFR Systems	113
7. Conclusions	123
References	125
Appendix A. Computational Models of Safety Analysis Code MUSA	131
A.1. Overall Solution Scheme	131
A.2. Core Neutronics Model.....	132
A.3. Reactivity Feedback Model	134
A.4. Multi-Channel Thermal-Fluidic Model	139
A.4.1. Single-Channel Thermal-Fluidic Model	140
A.4.1.1. Numerical Methods for Flow Equations	142
A.4.1.2. Numerical Methods for Heat Conduction Equations	146
A.4.2. Flow Split Calculation.....	149
A.5. Primary Loop Thermal-Fluidic Model.....	151
A.5.1. Energy Balance Equations.....	152

A.5.2. Compressible Equation for Liquid Segments	153
A.5.3. Momentum Equation for Liquid Segments	154
A.5.4. Compressible Volume Pressure Changes	157
A.5.4.1. Compressible Volume with No Cover Gas	158
A.5.4.2. Compressible Volume with Cover Gas	159
A.5.5. Primary Loop Solution Strategy	161
Appendix B. User's Guide of Safety Analysis Code MUSA	163
B.1. Input Data Description	163
B.2. Sample Input File	164

List of Figures

Figure 0.1. Schematic Radial Layout of 1000MWt SLFFR Core	ii
Figure 0.2. Elevation View of Primary System, Intermediate System, and Steam Generators.....	iv
Figure 0.3. Elevation View of Nuclear Island.....	v
Figure 0.4. In-vessel Fuel Handling System	vi
Figure 0.5. Concept for SLFFR Fuel Processing Flowsheet.....	vii
Figure 0.6. Power Transients for UTOP, ULOHS and ULOF Accidents.....	viii
Figure 0.7. Peak Coolant Temperature Transients for UTOP, ULOHS and ULOF Accidents	viii
Figure 2.1. Schematics of Fuel Container and Reactor Core of SLFFR.....	6
Figure 2.2. Ternary Composition Diagram for Pu-Ce-Co (Ref. 21).....	7
Figure 2.3. Temperature Dependence of Ta Capsule Lifetime (Capsule Wall Thickness of 0.71 to 0.76 mm, from Ref. 27)	9
Figure 2.4. A Thermodynamic Modeling of Co-Ce System (Su et al., calculation, Ref. 41).....	12
Figure 2.5. Phase Diagram of Pu-Co (Okamoto et al, experimental, Ref. 42)	12
Figure 2.6. Phase Diagrams of Pu-Ce (Okamoto, experimental, Ref. 42).....	13
Figure 2.7. 30 at. % Vertical Section of Pu-Ce-Co System (Ellinger et al, experimental, Ref. 43)	13
Figure 2.8. Liquid Projection and Isothermal Section at 415 °C of Pu-Ce-Co System (Ref. 43).....	14
Figure 2.9. Phase Diagram of Am-Np-Pu (Oagawa, calculated, Ref. 50)	15
Figure 2.10. Phase Diagram of Am-Pu (Ellinger et al, experimental, Ref. 43)	15
Figure 2.11. Phase Diagram of Am-Pu (Okamoto, experimental, Ref. 45).....	16
Figure 2.12. Phase Diagram of Cm-Pu (Okamoto, experimental, Ref. 46)	16
Figure 2.13. Phase Diagram of Cm-Pu (Shushakov, experimental, Ref. 48)	17
Figure 2.14. Phase Diagram of Np-Pu (Sheldon et al., experimental, Ref. 42).....	17
Figure 2.15. Phase Diagram of Np-Pu (Poole et al, experimental, Ref. 51)	18
Figure 2.16. RZ Neutronics Model of 1000 MWt SLFFR.....	19
Figure 2.17. Multi-channel Model of SLFFR Core for FLUENT Calculations	23
Figure 2.18. Mesh Configurations of Single Channel Model for FLUENT Calculations	23
Figure 2.19. Temperature Distributions of Three Single Channel CFD Models	24
Figure 2.20. Schematic Radial Layout of Preliminary 1000 MWt SLFFR Core.....	27
Figure 2.21. Schematic Radial Layout of Reference Core Design of 1000 MWt SLFFR	28
Figure 2.22. Radial Layout of CA Guide Tube without and with CA Insertion.....	29
Figure 2.23. Comparison of Isotopic Fractions of Different TRU Compositions	31
Figure 2.24. Reactivity Worth of Primary Control Systems at BOL and EOEC.....	37
Figure 2.25. Reactivity Worth of Secondary Control Systems at BOL and EOEC.....	37

Figure 2.26. SLFFR Core Power Distribution	39
Figure 2.27. Temperature Distributions from CFD Analysis with Optimal Coolant Velocities	41
Figure 2.28. Liquid Fuel Flow Pattern at the Core Center Region	42
Figure 2.29. Whole-core Coolant Temperature Distribution for Optimal Flow Distribution.....	42
Figure 2.30. Schematic View of the Elevation of Gas and Sodium Interface in GEMs....	45
Figure 2.31. Sodium Free Surface Height with Different Initial Gas Volume	46
Figure 2.32. GEM Worth versus Elevation of Sodium and Gas Interface	47
Figure 3.1. SLFFR-1000 Reactor Vessel Assembly	49
Figure 3.2. Plan View of Primary and Secondary Systems	50
Figure 3.3. Example of Reactor Vessel Deck Cross-Section and Box Structure	53
Figure 3.4. Reactor Vessel/Deck Support Structure	54
Figure 3.5. SLFFR Lower Internal Structure.....	57
Figure 3.6. Illustration of IHX in Shielded Cell	61
Figure 3.7. Plan View of Orifice Baffle Plate Design	61
Figure 3.8. Illustration of IHTS Layout	64
Figure 3.9. HCSG Design Characteristics (GE PRISM Mod B Basis)	68
Figure 3.10. Overall Cycle Efficiency	69
Figure 3.11. SLFFR Fuel Handling – Primary Vessel.....	70
Figure 3.12. In-vessel Fuel Handling System	71
Figure 3.13. Fuel Handling Gripper and Unloading Sipper.....	71
Figure 3.14. Fuel Unloading Machine – Over Reactor Vessel	72
Figure 3.15. Fuel Unloading Machine – Over Reactor Vessel	72
Figure 3.16. Fuel Unloading Machine – in Transfer Position	73
Figure 3.17. Fuel Unloading Machine – in Transfer Position	73
Figure 3.18. Spent Fuel Handling Cask	74
Figure 3.19. Spent Fuel Handling Cask – Inside View	74
Figure 3.20. Elevation View – Showing Fuel Transfer Tunnel	75
Figure 3.21. SLFFR-1000 Reactor Site (Plan View).....	75
Figure 3.22. SLFFR Reactor Site (Isometric View)	76
Figure 4.1. Concept for Processing SLFFR Fuel.....	81
Figure 5.1. Axial Distributions of Coolant Temperature Changes from Initial Steady-State Distribution.....	91
Figure 5.2. Axial Distributions of Fuel Temperature Changes from Initial Steady-State Distribution.....	91
Figure 5.3. Axial Distributions of Doppler Constant for Three-Channel Model of SLFFR Core	92

Figure 5.4. Axial Distributions of Fuel Worth for Three-Channel Model of SLFFR Core	93
Figure 5.5. Axial Distributions of Structure Material Worth for Three-Channel Model of SLFFR Core.....	93
Figure 5.6. Axial Distributions of Sodium Worth for Three-Channel Model of SLFFR Core	94
Figure 5.7. Transient of Coolant Inlet and Hot Channel Temperatures for UTOP Accident.....	96
Figure 5.8. Transient of Total Power for UTOP Accident (long term and short term)	97
Figure 5.9. Component-wise Reactivity Transients for UTOP Accident	97
Figure 5.10. Transient of Peak Coolant Temperatures for UTOP Accident with Different Reactivity Insertions	98
Figure 5.11. Transient of Total Power for UTOP Accident with Different Reactivity Insertions	98
Figure 5.12. Transient of Coolant Inlet and Hot Channel Temperatures for ULOHS Accident.....	100
Figure 5.13. Transients of Total Power, Decay Heat, and Flow Rate for ULOHS Accident.....	100
Figure 5.14. Component-wise Reactivity Transients for ULOHS Accident	101
Figure 5.15. Transients of Coolant Temperatures for ULOF Accident	102
Figure 5.16. Transients of Total Power, Decay Heat, Flow Rate and Power to Flow Ratio for ULOF Accident.....	102
Figure 5.17. Component-wise Reactivity Transients for ULOF Accident	103
Figure 6.1. NASA Technology Readiness Levels	105
Figure A.1. Three Channel Example of Axial Distributions of Doppler Constant.....	135
Figure A.2. Three Channel Example of Axial Distributions of Fuel Worth.....	136
Figure A.3. Axial Meshes of Original and Expanded Fuel.....	136
Figure A.4. Three Channel Example of Axial Distributions of Structure Material Worth	138
Figure A.5. Three Channel Example of Axial Distributions of Sodium Worth	139
Figure A.7. Schematic Planar View of Single Channel Thermal-Fluidic Model	140
Figure A.8. Axial Discretization and Main Volume of Thermal-Fluidic Channel	143
Figure A.9. Mesh Structure for Heat Conduction Calculations in Fuel and Coolant Tube	147
Figure A.10. Schematics of Primary Heat Transport System	152

List of Tables

Table 0.1. Main Design Parameters of SLFFR-1000 Loop Plant	ii
Table 0.2. SLFFR-1000 Loop Plant Technology Readiness Assessment.....	ix
Table 2.1. Properties of Pu-Ce-Co Eutectic Fuel, Ta-10W and Sodium	11
Table 2.2. Isotopic Composition (wt. %) of LWR TRU Feed	20
Table 2.3. Temperatures and Power Densities of Single Channel CFD Calculations	24
Table 2.4. Estimated Peak Temperature at the Interface between Fuel and Coolant Tube.....	26
Table 2.5. Multiplication Factors Obtained with TWOANT	26
Table 2.6. Main Design Parameters of Reference Core Design of 1000 MWt SLFFR....	28
Table 2.7. Main Design Parameters of Control Assembly and Guide Tube.....	29
Table 2.8. Core Performance Characteristics at BOL of Reference 1000 MWt SLFFR..	30
Table 2.9. Equilibrium Cycle Performance Characteristics of Reference SLFFR Design	31
Table 2.10. Isotopic TRU Fraction (w/o) of SLFFR Inventories and Charge Materials ..	32
Table 2.11. Heavy Metal Mass Flow Rates (kg/day) of SLFFR for Daily Reprocessing Rate of 1/300 of Fuel Inventory	33
Table 2.12. Kinetic Parameters and Reactivity Coefficients of Reference Core Design of 1000 MWt SLFFR at EOEC	34
Table 2.13. Comparison of Reactivity Coefficients and Kinetics Parameters of Reference Core Design at BOL and EOEC.....	35
Table 2.14. Reactivity Control Requirements of SLFFR.....	36
Table 2.15. Primary and Secondary Control System Worth at BOL and EOEC.....	37
Table 2.16. Properties of Four Flow Orifice Zones	38
Table 2.17. Temperatures (°C) Obtained from Multi-Channel CFD Analyses with Core- Averaged Coolant Inlet Velocity	39
Table 2.18. Minimum Coolant Inlet Velocities and Corresponding Peak Temperatures (°C) Obtained from Multi-Channel Analyses	40
Table 2.19. Temperatures (°C) Obtained from Multi-Channel CFD Analyses with Optimal Coolant Inlet Velocities	41
Table 2.20. Dimensionless Parameters Related to Buoyancy-driven Flow	41
Table 2.21. Pressure Loss Coefficients and Pressure Losses in Four Flow Zones	44
Table 2.22. GEM Worth for Different Elevations of Sodium and Gas Interface	46
Table 3.1. Mechanical Pump Design Parameters.....	59
Table 3.2. Intermediate Heat Exchanger Design Parameters (rough estimate)	60
Table 3.3. Scaled Once-Through HCSG Design Data for 1000 MWt Plant Design	68
Table 3.4. Site Buildings with Dimensions.....	76
Table 4.1. Material Balance of Processing SLFFR Fuel (1/2).....	83
Table 4.2. Material Balance of Processing SLFFR Fuel (2/2).....	84
Table 4.3. Assumed Parameter Values Used in Recycling Material Balance Estimation	85

Table 5.1. Comparison of Asymptotic Coolant Inlet and Outlet Temperatures (K) Obtained from Quasi-static and Transient Analyses for SLFFR Design without GEMs	90
Table 5.2 Point Kinetics Model Specifications	94
Table 5.3. Primary Loop Design Parameters and Specifications for SLFFR	95
Table 5.4. Design Parameters and Steady-State Solution of Thermal-Fluidic Channels ..	95
Table 6.1. Advanced Recycling Reactor Technology Readiness Level Definitions	107
Table 6.2. Advanced Recycling Reactor Technology Readiness Level Definitions (continued)	108
Table 6.3. Advanced Recycling Reactor Technology Readiness Level Definitions (continued)	109
Table 6.4. Example – Advanced Recycling Reactor – Transmutation Technologies from GNEP Program	110
Table 6.5. Example – Advanced Recycling Reactor – Transmutation Technologies from GNEP Program (continued)	111
Table 6.6. Example – Advanced Recycling Reactor – Transmutation Technologies from GNEP Program (continued)	112
Table B.1. MUSA Input Blocks and Specifications	163

1. Introduction

Advanced fuel cycle options have been explored worldwide to transmute the hazardous transuranics (TRU) of used nuclear fuels. The primary goal of the transmutation mission is to remove TRU elements from the waste stream and to fission those in advanced nuclear systems, producing about one MW-day of energy for every gram. The transmutation performance of different systems is determined mainly by transmutation physics characteristics. Fissile isotopes are likely to fission in both thermal and fast spectrum systems, with a higher fission fraction in fast systems. However, fertile isotopes have very small fission probabilities in thermal reactor systems, and thus they are converted into higher actinides instead of being consumed by fission. In fast reactor systems, the fission probabilities of actinides increase significantly due to higher fission to capture ratios, and more fission neutrons per fission are produced. As a result, transuranic isotopes are consumed efficiently in fast reactor systems with less generation of higher actinides. [1]

The net consumption rate of TRU can be maximized by reducing the TRU conversion ratio (i.e., production to destruction ratio) to zero by utilizing uranium-free fuel. However, the neutronics properties of uranium-free fuel make it very difficult, if not impossible, to develop a critical fast reactor with conventional solid fuels. In particular, reactivity feedback coefficients are significantly degraded; the Doppler coefficient of uranium-free fuel is almost zero or becomes slightly positive, depending on fuel composition, and the delayed neutron fraction is reduced noticeably. [2] In addition, the burnup reactivity loss is much faster at a low conversion ratio, and hence appropriate means for reactivity compensation must be employed (e.g., shorter length cycles with more frequent refueling or a large number of control assemblies). The difficulty in achieving very low or zero TRU conversion ratios in critical fast reactors gave a strong motivation for developing the accelerator-driven transmutation of waste (ATW) system concept in late 1990s and early 2000s, but ATW systems were found to be not cost-effective compared to critical fast reactor systems. [3]

As an alternative to conventional solid fuel fast reactor, a new type of metallic fuel reactor concept named the Stationary Liquid Fuel Fast Reactor (SLFFR) [4] is proposed in this study. SLFFR is based on stationary molten metallic fuel with a co-located reprocessing system for ease of used fuel cleanup and recycling. This new type of integrated reactor plant system would be able to consume essentially all the heavy metal within the reactor fuel. This transformational approach is simpler than conventional fast reactor technology and has the potential for large capital cost reductions for the overall fuel cycle.

A reference core design and a plant system design of a 1000 MWt TRU-burning SLFFR concept was developed using TRU-Ce-Co fuel, Ta-10W fuel container, and sodium coolant. Conservative design approaches were adopted to stay within the current material performance database. Detailed neutronics and thermal-fluidic analysis were performed to develop a reference core design. Neutronics analyses were performed using the fast reactor analysis codes of Argonne National Laboratory. Region-dependent 33-group cross sections were generated using the MC²-3 code [5] based on the ENDF/B-VII.0 library. Core and fuel cycle analyses were performed in theta-r-z geometries using the DIF3D [6] and REBUS-3 [7] codes. The reactivity coefficients and kinetic parameters were calculated using the VARI3D perturbation theory code [8]. Thermo-fluidic analyses for material temperatures were conducted using the ANSYS FLUENT computational fluid dynamics (CFD) code [9].

Because of chemical activity and opaqueness of sodium coolant, fuel handling is relatively difficult in sodium-cooled reactors than in commercial water reactors. The SLFFR has advantage over conventional SFRs in simple fuel handling and recycling and low fabrication costs because the fuel is operated in the stationary liquid phase. Utilizing the operating experiences of SFRs and the molten liquid state of fuel, preliminary operation strategies were developed for fuel handling, commissioning and startup, and fuel recycling.

The potential safety performance characteristics of the SLFFR design were assessed by developing a multi-channel safety analysis code (MUSA) tailored to handle the unconventional geometry of the SLFFR core design. MUSA was designed for coupled neutronics and thermal-fluidic calculations. The core was modeled by one-dimensional parallel channels. The primary heat transport system was modeled by connecting two compressible volumes (representing the inlet and outlet plenums) by two liquid segments (one representing the core and the other representing the hot leg, the intermediate heat exchanger and the cold leg). A point kinetics model with six delayed neutron groups was used to represent power transients, and the reactivity feedback was evaluated by combining the temperature and density variations of liquid fuel, structural material and sodium coolant with the corresponding axial distributions of reactivity worth for individual thermal-fluidic channels.

The scope of the safety analyses focused on the ability of SLFFR to provide inherent protection against damaging consequences in low probability accident sequences involving multiple equipment failures. Three beyond design basis accident (BDBA) scenarios of primary importance for passive safety were analyzed: unprotected transient over power (UTOP), unprotected loss of flow (ULOF) and unprotected loss of heat sink (ULOHS).

A reference plant concept of 1000 MWt SLFFR was also developed. The loop-type arrangement of the primary heat transport system was selected for this study due to the relative compactness of the reactor vessel that supports the use of a rapid and frequent refueling system that does not require a large span across the reactor vessel head. The reactor core, the direct reactor auxiliary cooling system (DRACS) heat exchangers are contained in a reactor vessel, and the primary pumps and intermediate heat exchangers located in shielded cells outside the reactor vessel. The intermediate heat exchangers are established at the appropriate elevation to support natural circulation. Preliminary core operation strategies were developed as well. Applying the accumulated experiences for sodium cooled fast reactors, the operational procedures for fuel handling, and plant commissioning and startup were established. The reprocessing flowsheet was also developed for the liquid TRU fuel of SLFFR based on the liquid metal-salt chemistry developed in the Chemical Technology Division at Argonne National Laboratory.

The technology maturity of the SLFFR plant was evaluated using the Technology Readiness Levels (TRLs) approach. TRLs are a systematic metric/measurement system that supports assessments of the maturity of a particular technology and the consistent comparison of maturity between different types of technology. [10] The Global Nuclear Energy Partnership (GNEP) program established technology readiness levels for evaluating the three technologies that comprised the program, namely, the Advanced Recycling Reactor, the fuel fabrication plant, and the reprocessing facility. These three facilities were to address the safe, secure expansion of nuclear power both internationally and domestically while reducing proliferation risks and effectively addressing the challenges of nuclear waste disposal. The technology readiness

criteria developed in the GNEP program developed were used in evaluating the SLFFR for commercial applications.

This report is organized as follows. In Chapter 2, the reference core design of SLFFR and its performance characteristics are discussed along with the computational methods and models used in the development of the design. The description of selected materials and associated design constraints are also provided. The Chapter 3 presents the description of the overall plant concept, including the reactor enclosure system, the primary heat transport system, the intermediate heat transport system, the power generation system, and the fuel handling system. The operation strategies are described in Chapter 4. In Chapter 5, the safety analysis results for hypothetical accidents are represented. Chapter 6 presents the evaluation of the technology readiness of the SLFFR. Conclusions are discussed in Chapter 7. Detailed description of MUSA code is given in Appendix A, including the physical models, numerical algorithms, and a user's guide is provided in Appendix B.

2. Development of Reference Core Design

2.1. Core Concept

In order to overcome the difficulty in achieving very low or zero TRU conversion ratios in critical fast reactors with conventional solid fuels, a new type of metallic fuel reactor concept named the Stationary Liquid Fuel Fast Reactor (SLFFR) is proposed in this study. SLFFR is based on stationary molten metallic fuel with a co-located reprocessing system for ease of used fuel cleanup and recycling. The degraded reactivity coefficients of solid uranium-free fuels can be overcome by utilizing the large prompt negative reactivity feedback due to the thermal expansion of molten fuels.

Although all the current power reactors use solid fuels, molten fuel reactors were recognized early in the nuclear era as having potential advantages over solid fuel reactors. Liquid metallic alloy fuels have several advantages over solid fuels such as the large negative reactivity feedback due to thermal expansion, continuous fission product cleanup due to the release of the bulk of gaseous fission products, simplified fuel handling, low fuel fabrication costs, increased resistance to irradiation damage and dimensional changes, and on-line refueling and fission product removal. [11]

Various fluid fuel reactors have been studied using metal alloys, molten salts, aqueous solutions and suspensions, and dispersion fuels of solid fuel particles entrained in carrier fluid. [12] In the flowing fuel systems, however, fuel materials and fission products are in intimate contact with a large array of components and systems, and hence some difficulties are encountered or anticipated, including structural material corrosion, inspection and maintenance of contaminated systems, fuel pumping, phase separation, and loss of delayed neutrons. Several non-flowing molten fuel fast reactors were also investigated or proposed. [11,13,14] For example, in the 1 MWt test reactor LAMPRE I (Los Alamos Molten Plutonium Reactor Experiment I), each fuel element consists of plutonium-iron eutectic alloy encased in a 0.66 mm thick tantalum capsule. [11]

The fundamental concept of SLFFR is to use non-flowing liquid metallic alloy fuel of TRU in a closed fuel container. In the initial operation, the fuel enters the reactor vessel in a solid form and then be heated to molten temperatures in a small melting heater. The fuel will be contained within a closed, thick container with penetrating coolant channels (see Figure 2.1), and thus will neither be mixed with coolant nor flow through the primary heat transfer circuit. The fuel container plays the role of conventional fuel cladding, and thus the defense-in-depth principle is retained as opposed to other flowing fluid fuel concepts. The makeup fuel is semi-continuously added to the system, and thus a very small excess reactivity is required. Gaseous fission products will be also removed continuously, and a fraction of the fuel will be periodically drawn off from the fuel container to a processing facility where non-gaseous mixed fission products and other impurities will be removed and then the cleaned fuel will be recycled into the fuel container.

The large negative reactivity feedback of molten fuel allows the use of a uranium-free fuel that yields a zero TRU conversion ratio, and results in inherent safety characteristics. The molten fuel, which is already in its most reactive state, would also eliminate the concern about the potential for a hypothetical core disruptive accident. The continuous addition of makeup

fuel and removal of gaseous fission products will compensate for the reactivity loss due to fuel depletion, making the reactivity control requirements minimal. The thick fuel container and continuous fission gas removal will eliminate the traditional concern of fuel cladding integrity due to irradiation and buildup of fission gas pressure, and thus will allow a very high burnup. Simple-geometry fuel container and minimal reactivity control requirements will result in a very simple reactor core system. This system can also be operated at a high power density and temperature; the high power density would lead to a compact core system, and the high operating temperature would yield a high thermal efficiency. Combination of these characteristics will provide a large potential to reduce the capital cost per unit energy produced drastically.

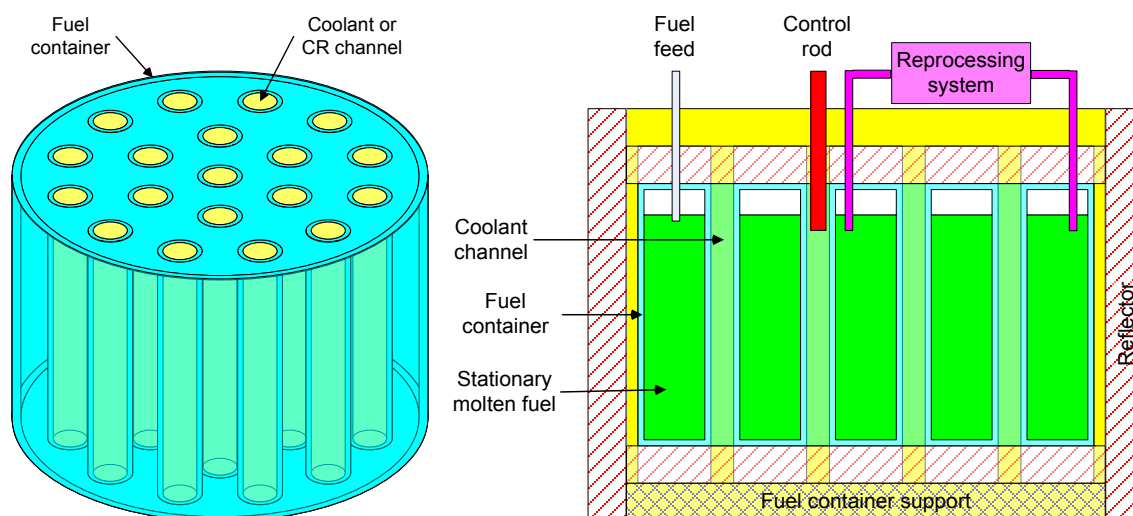


Figure 2.1. Schematics of Fuel Container and Reactor Core of SLFFR

2.2. Selection of Fuel and Container Materials

Literature surveys were performed to select the fuel alloy forms and fuel container materials and to compile their properties required for neutronics and computational fluid dynamics (CFD) calculations. The key concept of SLFFR is to use non-flowing liquid metallic alloy fuel of TRU in a closed fuel container. Thus, among various fluid fuel reactors using metal alloys, molten salts, aqueous solutions and suspensions, and dispersion fuels of solid fuel particles entrained in carrier fluid [12], non-flowing molten fuel fast reactors [13-15] were targeted. In particular, the literatures were surveyed for the materials used in the 1 MWt test reactor LAMPRE I (Los Alamos Molten Plutonium Reactor Experiment I) [15-18], where each fuel element consists of plutonium-iron eutectic alloy encased in a 0.66 mm thick tantalum capsule, and those tested or considered in the subsequent programs [11,19-22].

A large amount of information on the properties of liquid plutonium alloys was generated during the LAMPRE project [11,15-22] at Los Alamos Scientific Laboratory. Low melting alloys of plutonium occur in the binary systems with Fe, Co, Ni and Cu. The 1 MWt test reactor LAMPRE I used plutonium-iron eutectic alloy ($\text{Pu}_{0.9}\text{Fe}_{0.1}$) contained in tantalum capsules [11,18]. However, the low melting point of 410 °C exists only for the composition of 90 atom % Pu and balance Fe. Consequently, the high Pu density dictates a low allowable specific power

The potential for corrosion of the fuel container and loss of the fuel was one of the major concerns for liquid fuels. For the LAMPRE project, tantalum alloys were selected for the structural material that is in contact with the liquid fuels. In the temperature range of interest for molten-Pu-fueled power reactors, i.e., 450-750 °C, the Pu attack on Ta is by means of intergranular penetration (IGP). Pu penetration occurs by grain boundary diffusion in the Ta and eventually reaches the external surface of the containment causing a failure. Corrosion tests were performed for various combinations of Pu alloy fuels and Ta alloy capsules of 0.76 mm thick [11,22,27]. Tests encompassed fuel concentrations from 5 to 8 gPu/cm³ in contact with

Ta and Ta-W alloys up to 10 w/o W up to 1100 °C. The test results showed that the Pu-Ce-Co alloy was much less corrosive to Ta than liquid Pu or Pu-Fe alloys.

Considering all Pu-Co-Ce alloy penetration tests (all combinations of fuel composition, container material, and test temperature) showed that 203 tests resulted in 33 observations of surface Pu contamination of which 32 have been in welds. The one exception is the failure of Ta, 6.5 gPu/cm³, 3000 hours at 750 °C. This failure was in the gas phase midway between the fuel level and the top seal weld. The results of these tests indicate that container walls are not penetrated by Pu-Co-Ce (in dramatic contrast to Pu-Fe fuel), but that only welds are subject to penetration, at times up to 10500 hours at 850 °C. When welds are not considered, there is strong indication that significant corrosion of Ta or Ta-W alloys will not occur during a core lifetime below 850 °C. The lifetime of Pu-Co-Ce alloys contained in Ta or Ta-W alloys will be significantly better than for Pu-Fe alloy.

Spallation of the Ta-Co precipitated layer was observed in some tests; however, in many cases, i.e., Pu-Co-Ce fuels containing less than 5 gPu/cm³, the layer did not form in significant quantity below the liquid level within the times studied (up to 3000 hours). Fuels of 8 gPu/cm³ do form Ta-Co intermetallic layers below the fuel level, whereas 6.2 gPu/cm³ fuel appears to be a borderline. No pitting corrosion due to preferential Ta-Co layer spallation was observed in tests. However, tests at 1100 °C of Pu-Fe fuel (which forms a similar reaction layer, Ta-Fe) did definitely indicate pitting and subsequent IGP through the container wall near the pit. In addition to allowing IGP, pitting decreases wall thickness, due to concentrated Ta solution effects and may form a hole completely through the container wall.

Although the number of capsules tested to determine the effect of carburization was small, there was evidence to suggest an enhancement of corrosion resistance, probably by protection of seal welds below the fuel phase. (Results obtained with Pu-Fe fuel also support this contention.) Application of ~3 µm TaC on the surface of Ta-W alloy eliminated corrosion and penetration of Pu through grain boundaries in the weld structures of the fuel containment. Based on the experimental results shown in Figure 2.3, an expected average lifetime of 20 years at 700 °C was predicted for both Ta capsule containing Pu-Ce-Co and carburized Ta capsule containing liquid Pu. Since container strength was important for withstanding large thermal and pressure stresses, Ta-5W alloy was selected, which has satisfactory mechanical properties at the operating temperatures of LAMPRE (750-800 °C). Since no penetration of carburized Ta-5W capsules was observed, it was concluded carburized Ta-5W had at least as good corrosion resistance to Pu as carburized Ta.

A further area of concern was the expansion of the fuel on freezing. The Pu-Co-Ce alloys exhibit large volumetric expansions during freezing of from 1 to 3% for Pu concentrations from 0 to 8 gPu/cm³. If the fuel is maintained in the liquid phase, mechanical integrity of the capsules is assured. Three solutions were considered to this potential problem. First, an attempt was made to modify this expansion characteristic by means of additives to the fuel, i.e., making the fuel a quaternary or higher order alloy. However, the additives that were tried did not eliminate the problem. A second method was to employ a container of sufficient strength so that the fuel, rather than the container, will deform. Ta-5W alloys appeared quite promising in this respect. The third potential solution was to avoid freezing the fuel. LAMPRE I was operated for some three years without allowing the fuel temperature to drop below the melting point of the Pu-Fe

fuel (410°C), but this is an operational inconvenience. However, evidence from irradiation tests indicate that melt-freeze cycling of a core may be possible without mechanical damage.

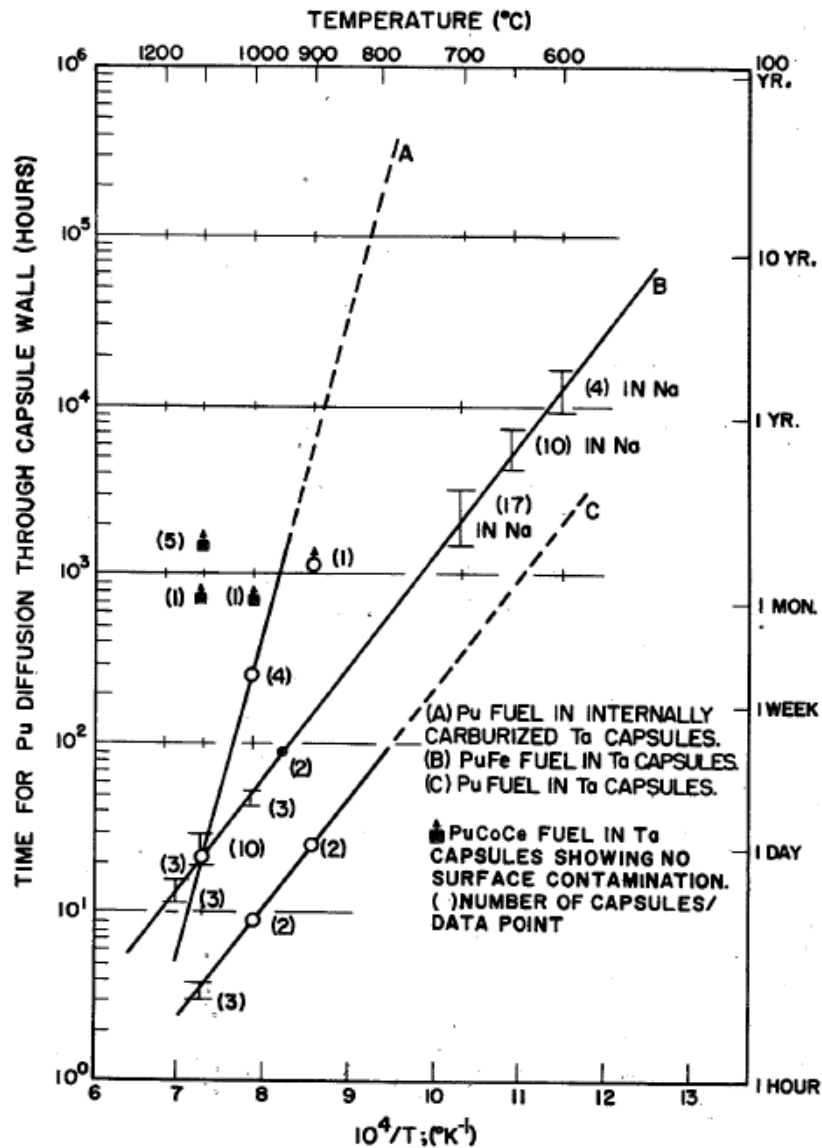


Figure 2.3. Temperature Dependence of Ta Capsule Lifetime (Capsule Wall Thickness of 0.71 to 0.76 mm, from Ref. 27)

The third concern is associated with mass transport or irradiation-damage of the carburized layer on the internal surface of the container. Preliminary evidence indicates neither of these effects will be of operational importance. Thermal gradient mass transport of Ta was demonstrated by tracer techniques. The maximum rate observed for a 100 °C ΔT (from 600 to 700 °C) with 5 g/cm³ Pu-Co-Ce, was less than 2.5 μm per year. With 8 gPu/cm³ fuel and a 100 °C ΔT (from 650 to 750 °C), the average rate of transfer of Ta was 4.8 μm per year. Mass transfer rates of these magnitudes should present little difficulty, providing that pitting be not initiated.

2.3. Design Constraints

Based on the experimental results of the LAMPRE project, TRU-Ce-Co ternary fuel was selected for SLFFR. Additional literature surveys were performed to determine the effect on the melting temperature of adding minor actinides (MA) to Pu-Ce-Co alloys, but it was found that the information available in the literature is not sufficient to determine the effects, even qualitatively. To evaluate properly the changes in the melting temperature intervals, it is needed to perform Density Functional Theory (DFT) and Molecular Dynamics (MD) calculations, followed by thermodynamic integration to retrieve the Gibbs free energy of the relevant phases.

It was therefore decided to perform the design studies under the assumption that the melting point of Pu-Ce-Co ternary fuel would not be increased significantly by the addition of a few percent of minor actinides (MA), while performing a preliminary evaluation of Pu-Ce-Co-MA systems. Since container strength is important for withstanding large thermal stresses and preventing tube distortion during fuel freezing (although it was reported that evidence from irradiation tests indicated that melt-freeze cycling might be possible without mechanical damage), Ta-10W was selected as the fuel container material. Since tantalum is compatible with sodium up to 1000 °C [28], sodium was selected as the coolant. While no definite temperature limit was established in the LAMPRE project, a conservative limit of 700 °C was selected for the fuel and container interface temperature.

Compilation of the properties of selected materials required for neutronics and computational fluid dynamics calculations was also performed. Table 2.1 summarized the correlations for these properties along with the references [29-40]. Some correlations were derived from the referenced data.

For a preliminary evaluation of Pu-Ce-Co-MA systems, binary and ternary phase diagrams were surveyed for Pu-Ce-Co systems together with Am, Cm, and Np. To produce quadruple phase diagrams, the thermodynamic database of all the relevant binary and ternary system should be available. Taking Pu-Ce-Co-Am as an example, additional thermodynamic information for binary Am-Pu, Am-Ce and Am-Co, and ternary Am-Pu-Ce, Am-Pu-Co, and Am-Ce-Co are needed in order to calculate the quadruple phase diagram based on the thermodynamic database of the ternary Pu-Ce-Co system.

So far, the binary Ce-Co system was studied by both experiments and thermodynamic modeling. [41] The phase diagram for binary Pu-Ce and Pu-Co, and ternary Pu-Ce-Co are also available. [42-44] Except for Ce-Co, there is no thermodynamic database available for all the systems in order to calculate their phase diagram. The phase diagrams of several binary actinides system have been studied by experiments and calculations. [45-50] Okamoto studied the binary phase diagram of Am-Pu, Cm-Pu by experiments. [45-47] Shushakov also studied the phase diagram of Pu-Cm system. [48] Turchi et al thermodynamically assessed the Am-Pu system with input from ab initio calculations. [49] Ogawa studied the ternary phase diagram of Pu, Np and Am with brewer valence bond model. [50] These phase diagrams are shown in Figure 2.4 to Figure 2.15. However, there is no thermodynamic information available for binary Am-Co, Am-Ce, Cm-Co, Cm-Ce, Np-Co, and Np-Ce systems.

Table 2.1. Properties of Pu-Ce-Co Eutectic Fuel, Ta-10W and Sodium

Property	Correlation	Reference
Pu-Ce-Co Fuel		
Density (g/cm ³)	19.6Pu-56.2Ce-24.2Co (a/o) $\rho = 9.38 - 6.17 \times 10^{-4} T$ (°C)	29, 30, 31
	31.5Pu-43.0Ce-25.5Co (a/o) $\rho = 10.48 - 6.52 \times 10^{-4} T$ (°C)	
	47.9Pu-28.4Ce-23.7Co (a/o) $\rho = 12.29 - 7.71 \times 10^{-4} T$ (°C)	
Specific Heat (J/g-K)	$C_p = 0.128 + 2.79 \times 10^{-4} T$ (°C)	32
Conductivity (W/m-K)	$k = 5.8 + 0.0153 T$ (K)	33
Viscosity (g/cm-s)	$\eta = T \times 10^{1654.5/T - 5.8515}$ (K)	29, 30, 31
Ta-10W		
Density (g/cm ³)	$\rho = 16.92 - 1.9 \times 10^{-4} T$ (°C)	34, 35, 36
Specific Heat (J/g-K)	$C_p = 0.1326 + 2.123 \times 10^{-5} T$ (K)	34, 37
Conductivity (W/m-K)	$k = 48.3 + 0.0222 T$ (K)	38
Sodium		
Density (kg/m ³)	$\rho = 1011.8 - 0.22054 T - 1.9226 \times 10^{-5} T^2 + 5.6371 \times 10^{-9} T^3$ (K)	39
Specific Heat (J/g-K)	$C_p = 1.6582 - 8.4790 \times 10^{-4} T + 4.4541 \times 10^{-7} T^2 - 2992.6 T^{-2}$ (K)	40
Conductivity (W/m-K)	$k = 124.67 - 0.11381 T + 5.5226 \times 10^{-5} T^2 - 1.1842 \times 10^{-8} T^3$ (K)	40
Viscosity (Pa-s)	$\eta = \exp(-6.4406 - 0.3958 \ln T + 556.835 / T)$ (K)	40

Therefore, a lot of work needs to be done to generate the thermodynamic databases for all the relevant quadruple systems in order to calculate the liquidus projections. In addition, to calculate the liquidus from thermodynamic database, the effect of alloying of Am, Cm or Np metal on the melting temperature of ternary Pu-Ce-Co might be also inferred from the elastic or bonding properties upon alloying. However, this approach cannot provide qualitative prediction of the melting temperature, and the applicability of this approach to Pu-Ce-Co system has not been tested.

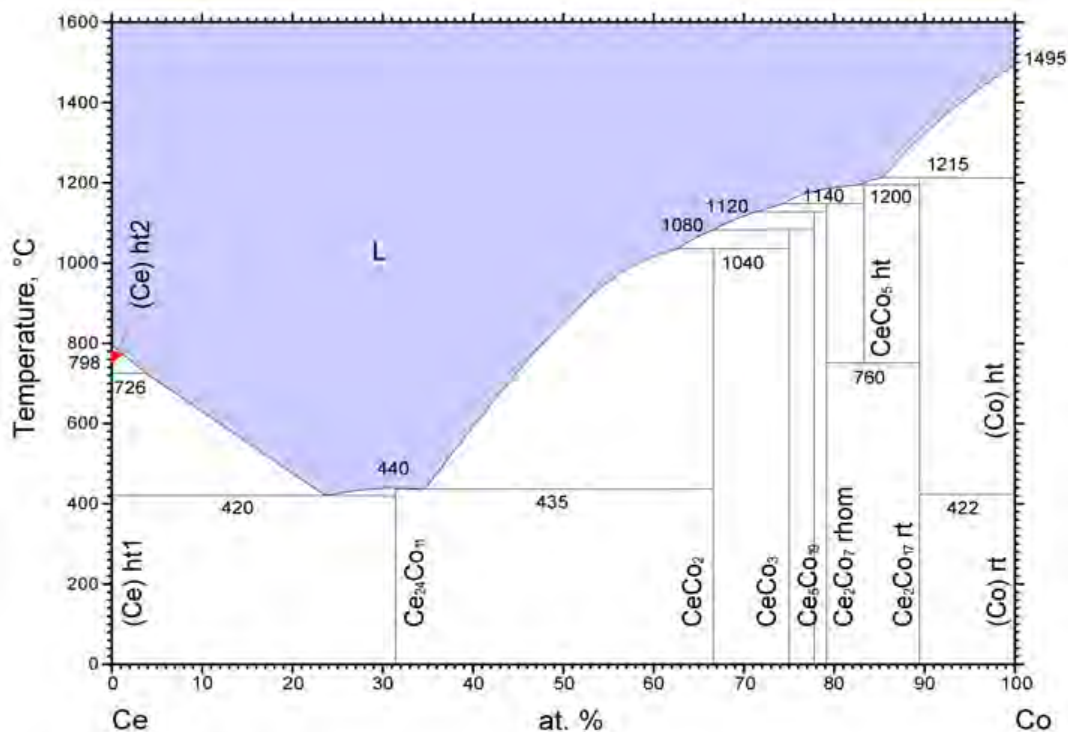


Figure 2.4. A Thermodynamic Modeling of Co-Ce System (Su et al., calculation, Ref. 41)

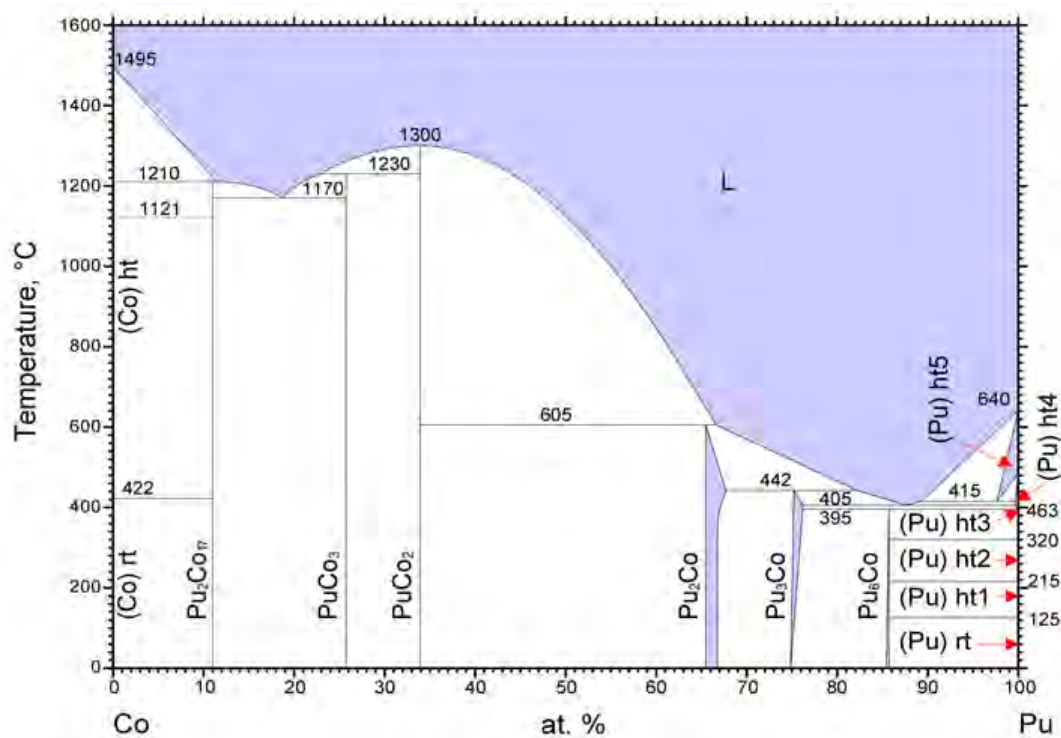


Figure 2.5. Phase Diagram of Pu-Co (Okamoto et al, experimental, Ref. 42)

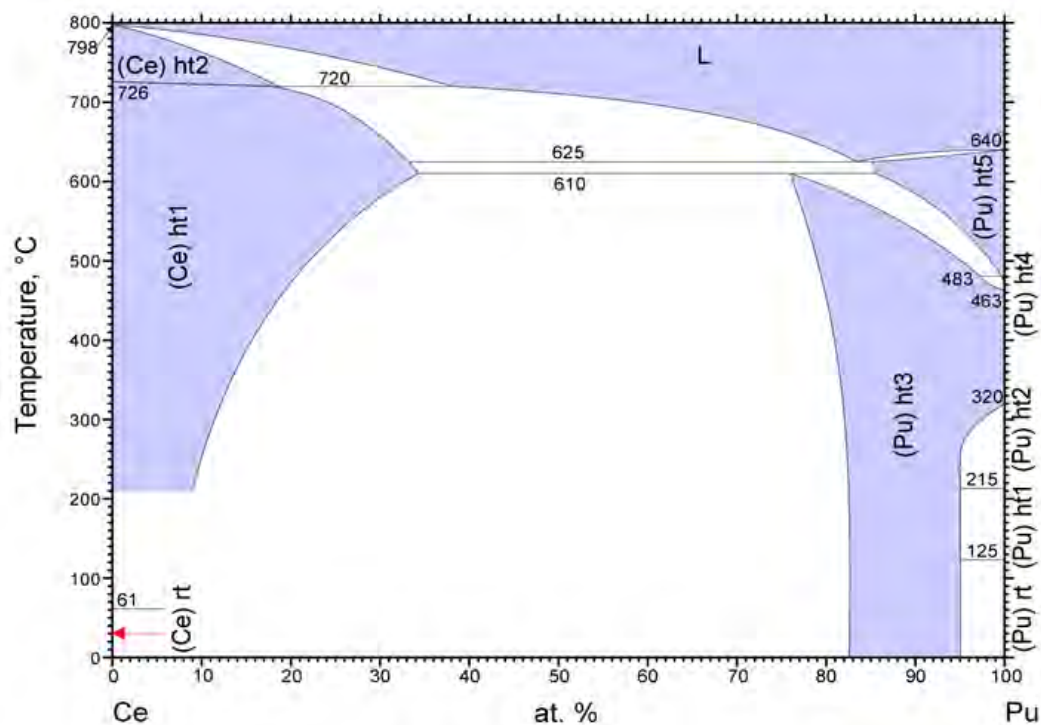


Figure 2.6. Phase Diagrams of Pu-Ce (Okamoto, experimental, Ref. 42)

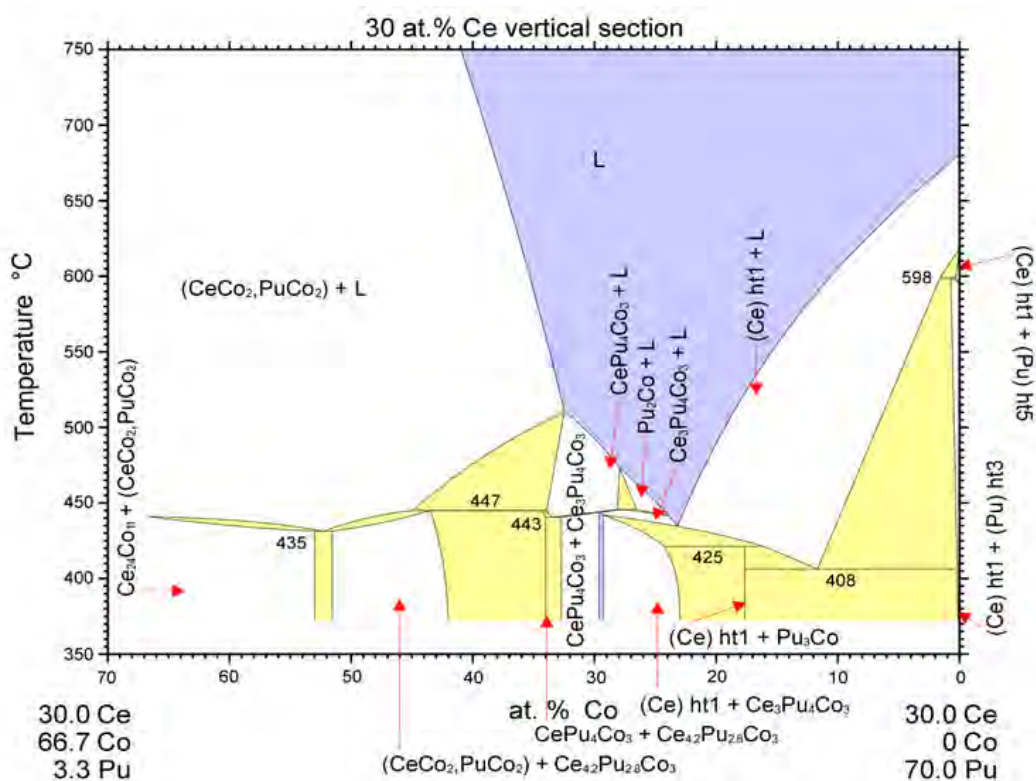
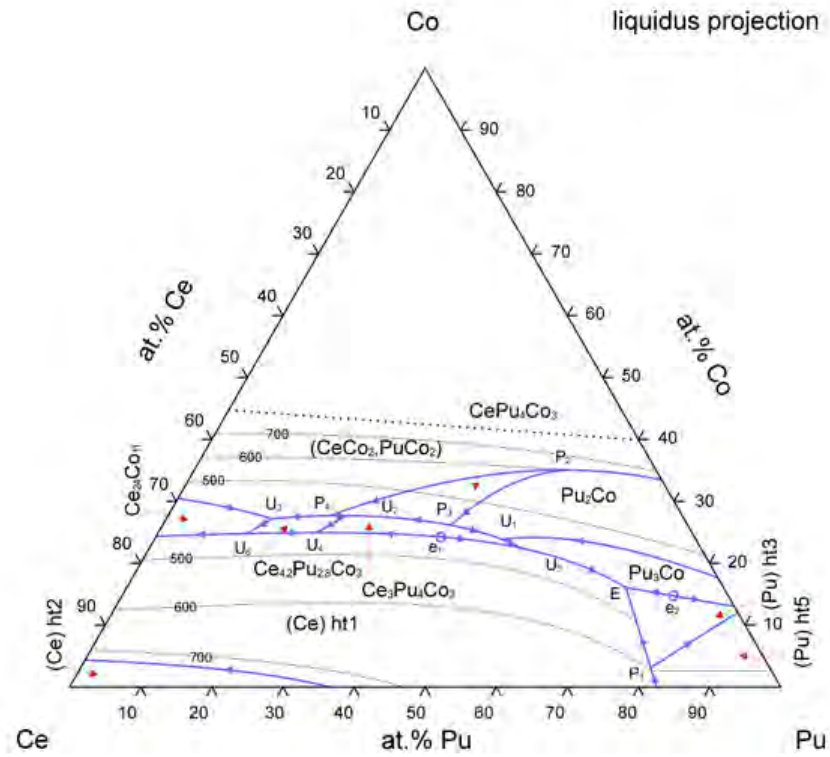


Figure 2.7. 30 at. % Vertical Section of Pu-Ce-Co System
(Ellinger et al, experimental, Ref. 43)



Isothermal sections
at 601, 580, 500,
447, 443, 435, 430,
425, 415, 408 °C

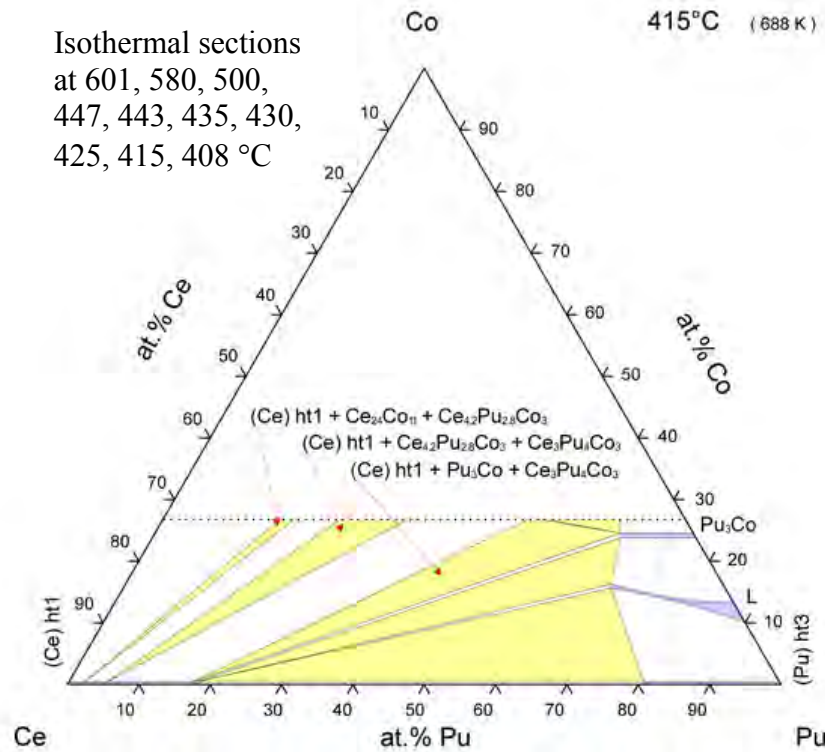


Figure 2.8. Liquid Projection and Isothermal Section at 415 °C of Pu-Ce-Co System (Ref. 43)

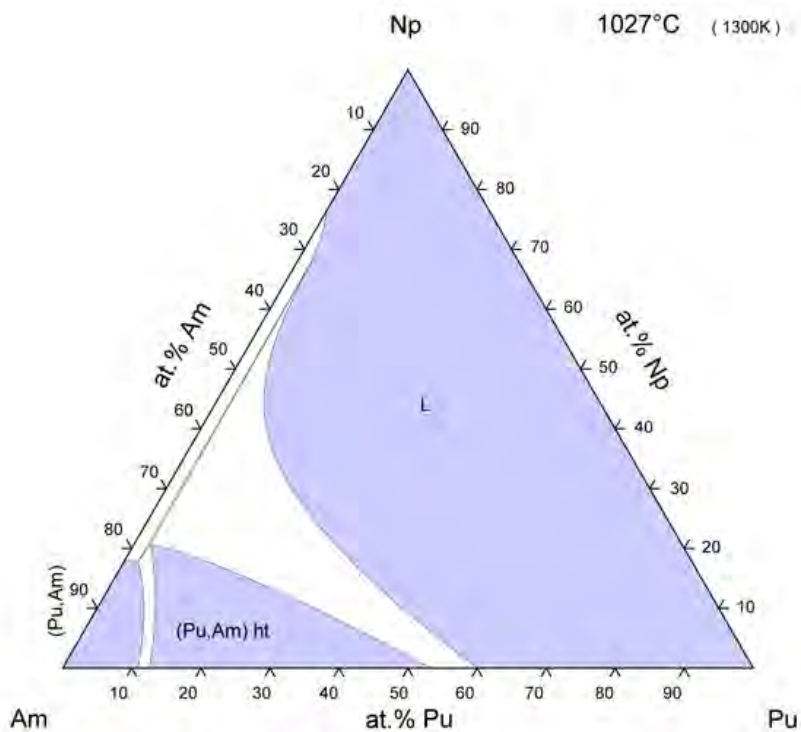


Figure 2.9. Phase Diagram of Am-Np-Pu (Oagawa, calculated, Ref. 50)

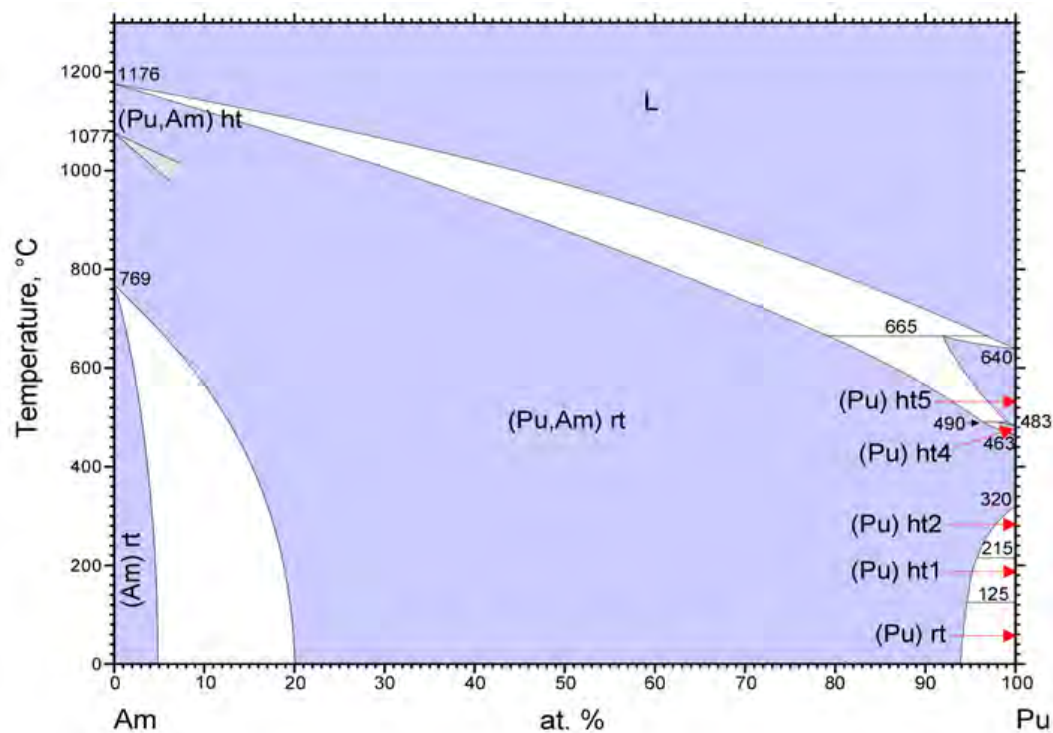


Figure 2.10. Phase Diagram of Am-Pu (Ellinger et al, experimental, Ref. 43)

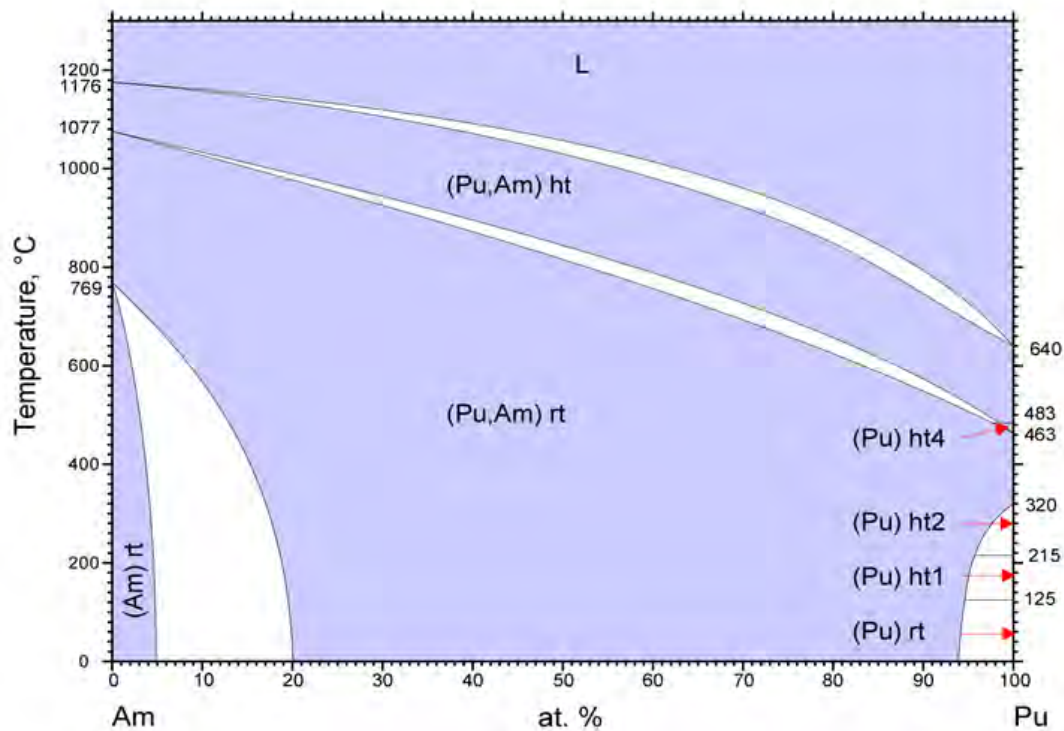


Figure 2.11. Phase Diagram of Am-Pu (Okamoto, experimental, Ref. 45)

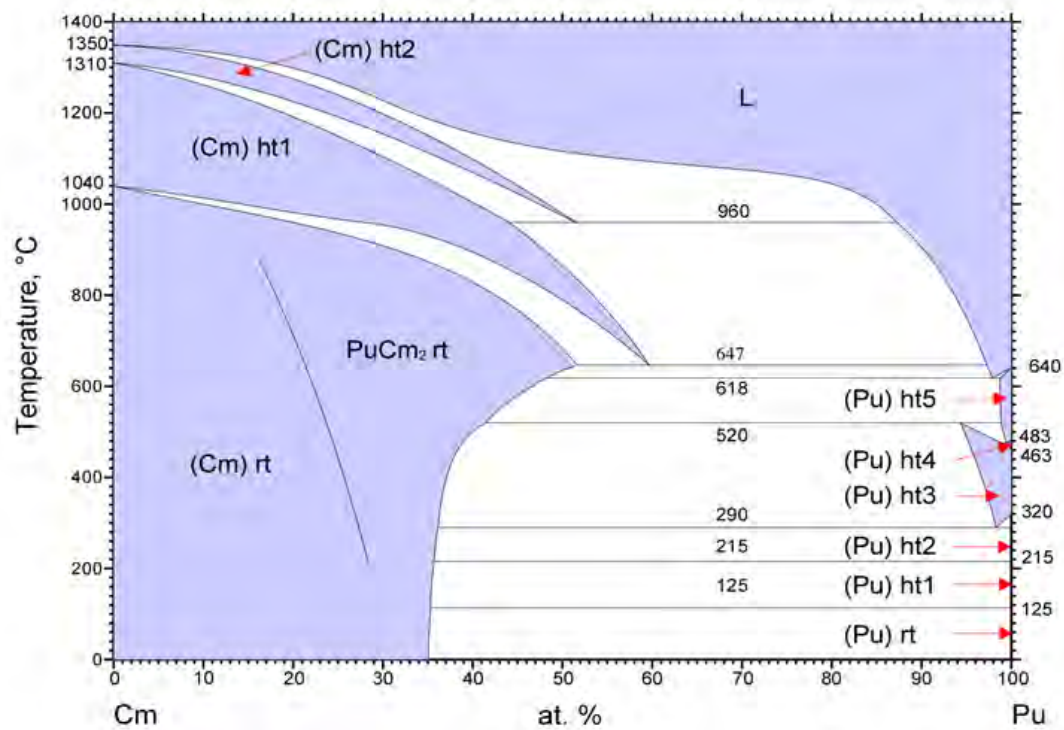


Figure 2.12. Phase Diagram of Cm-Pu (Okamoto, experimental, Ref. 46)

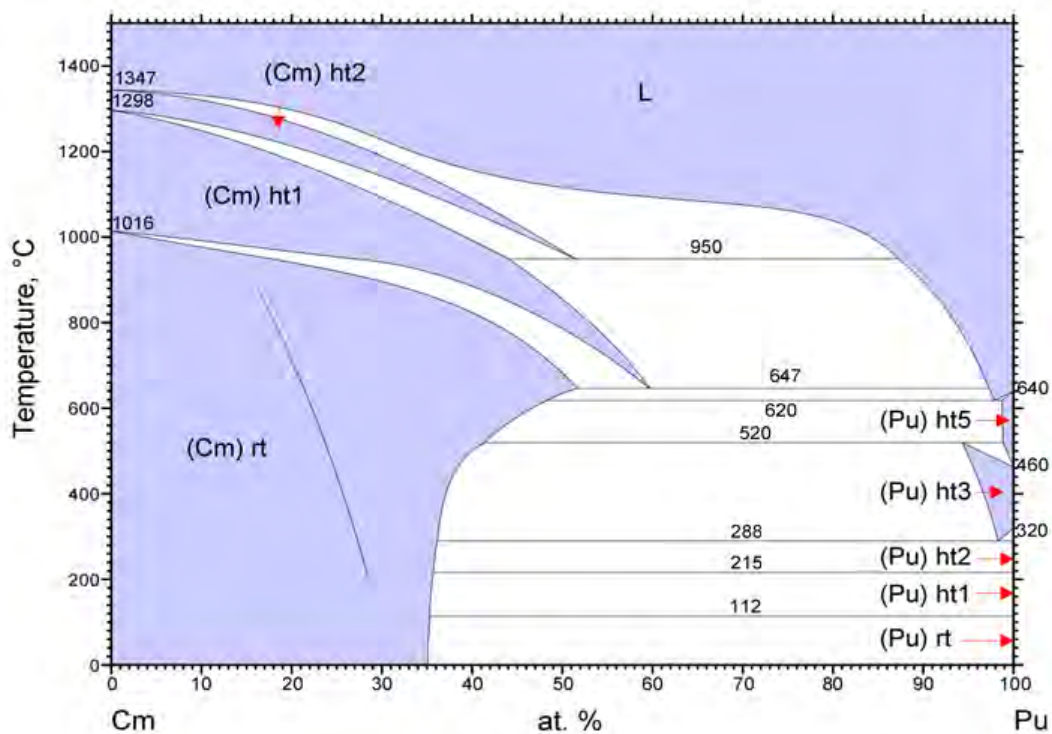


Figure 2.13. Phase Diagram of Cm-Pu (Shushakov, experimental, Ref. 48)

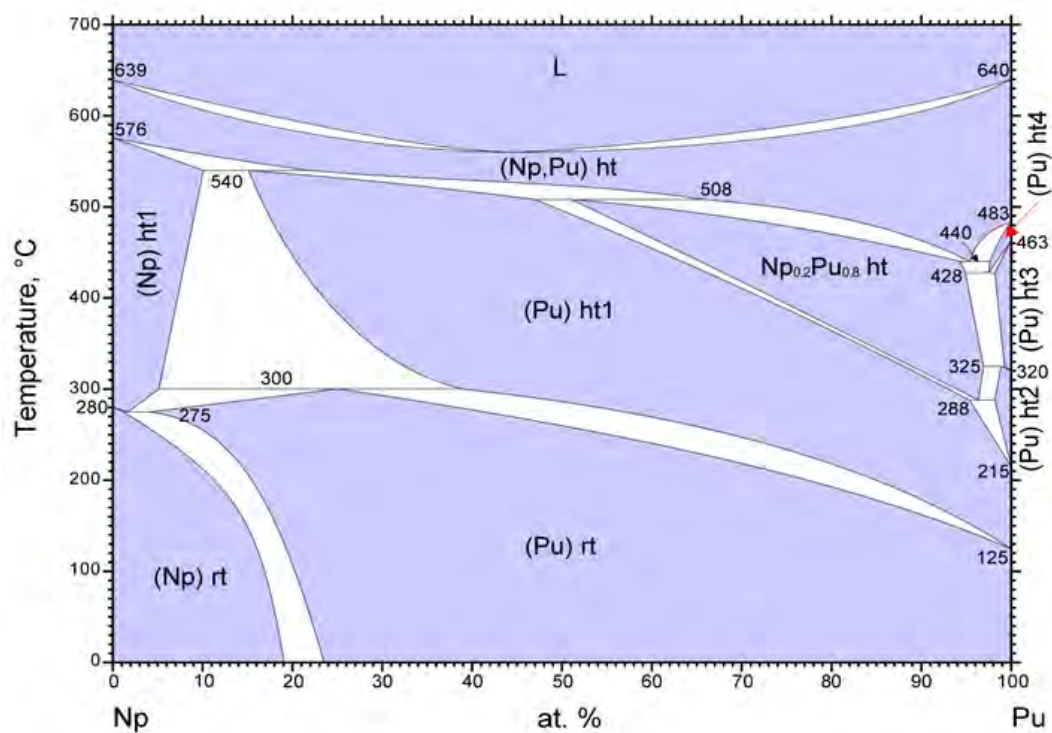


Figure 2.14. Phase Diagram of Np-Pu (Sheldon et al., experimental, Ref. 42)

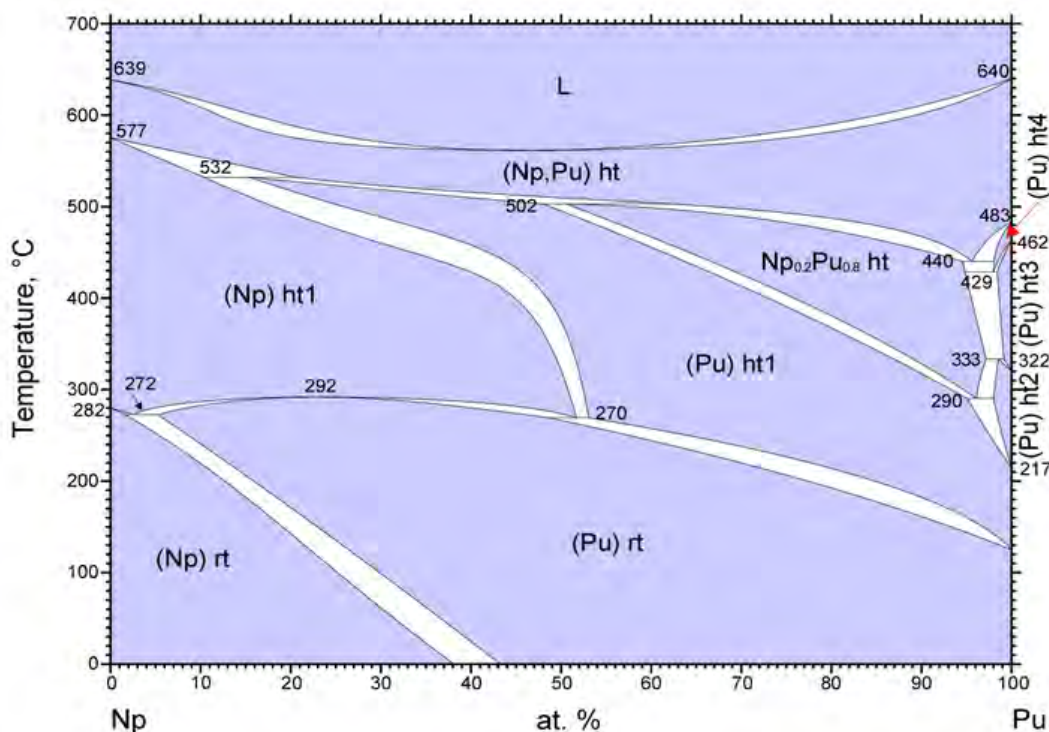


Figure 2.15. Phase Diagram of Np-Pu (Poole et al, experimental, Ref. 51)

2.4. Computational Methods and Models

Neutronics analyses were performed using the fast reactor analysis code of Argonne National Laboratory. Region-dependent 33-group cross sections were generated based on the ENDF/B-VII.0 data using the MC²-3 code [5]. Core and fuel cycle analyses were performed in cylindrical-z geometries using the DIF3D [6] and REBUS-3 [7] codes. Reactivity coefficients and kinetics parameters were calculated using the VARI3D perturbation theory code [8]. Thermo-fluidic analyses were performed using the ANSYS FLUENT computational fluid dynamics (CFD) code [9].

2.4.1. Multi-group Cross Section Generation

Using the MC²-3 code and the ENDF/B-VII.0 data, region-dependent 33-group cross sections were generated for a core configuration in cylindrical-z core geometry similar to one shown in Figure 2.16. Since the fuel composition to achieve criticality is not known a priori, MC²-3 calculations were repeated by varying the TRU concentration in TRU-Ce-Co alloy fuel until the core multiplication factor at the normal operating condition is close to unity when all the control rods are out of the core. The core-averaged fuel, container, and coolant temperatures at the normal operating condition were estimated using a single channel model. For reactivity coefficient calculations, cross sections were also generated for elevated temperature and sodium void conditions. Specifically, cross sections were generated for three additional conditions: 1) doubled fuel temperature, 2) voided flowing sodium in the core and above, and 3) voided flowing sodium and doubled fuel temperature.

In each MC²-3 calculation, self-shielded 2082-group isotopic cross sections were first prepared for each region by numerical integration of the pointwise cross sections based upon the narrow resonance approximation. Then, a 2082-group transport calculation was conducted for the whole-core RZ model in Figure 2.16 using the discrete ordinate transport code TWODANT [52]. Finally, region-dependent 33-group cross sections were determined by condensing the 2082-group cross sections of each region using the 2082-group TWODANT flux moment solution. Except for cerium, krypton, and xenon, the fission products were modeled using fissionable-isotope-dependent lumped fission products. Lumped fission product cross sections were generated for U-235, U-238, Np-237, Pu-238, Pu-239, Pu-240, Pu-241, Pu-242, Am-241, Am-243, and Cm-244 using the fission product yield data of ENDF/B-VII.0.

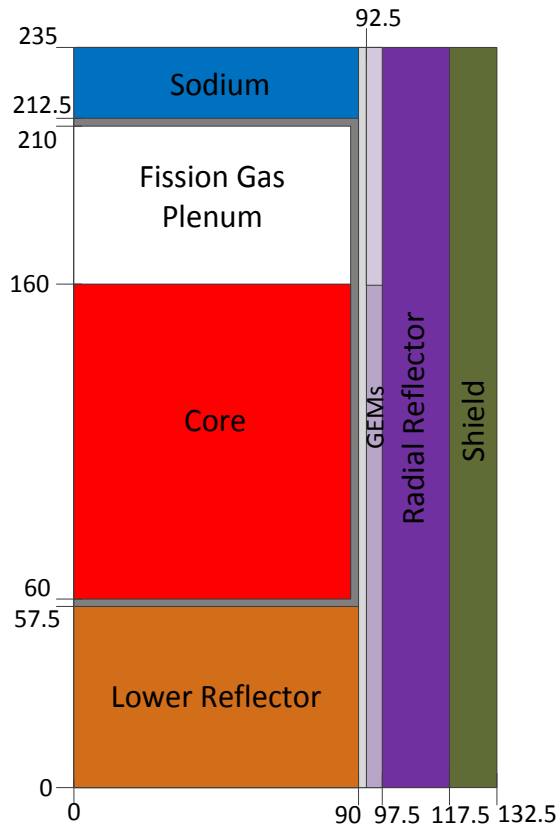


Figure 2.16. RZ Neutronics Model of 1000 MWt SLFFR

2.4.2. Fuel Cycle Analyses

Core and fuel cycle analyses were performed in cylindrical-z geometries using the REBUS-3 [7] and DIF3D [6] codes. Core performance characteristics were evaluated for the beginning of life (BOL) and a TRU recycled equilibrium cycle. The BOL core is assumed loaded with the TRU fuel recovered from LWR spent fuel, and the TRU fraction in the TRU-Ce-Co fuel was determined so that the multiplication factor is 1.003. The isotopic TRU composition of TRU was obtained from 10-year cooled LWR spent fuel with 50 GWd/MT burnup as shown in Table 2.2.

Table 2.2. Isotopic Composition (wt. %) of LWR TRU Feed

Isotope	Fraction (%)	Isotope	Fraction (%)	Isotope	Fraction (%)
Np-237	6.64	Pu-242	5.03	Cm-243	0.01
Pu-238	2.75	Am-241	4.65	Cm-244	0.50
Pu-239	48.65	Am-242m	0.02	Cm-245	0.04
Pu-240	22.98	Am-243	1.47	Cm-246	0.01
Pu-241	6.93	Cm-242	0.00	Cm-247	0.00

For the recycled equilibrium cycle calculation, the semi-continuous fuel cycle of SLFFR was approximated by a 300-batch, 1-day fuel cycle. The TRU recovered from reprocessed SLFFR fuel was used as the primary TRU feed and the TRU recovered from the spent LWR fuels was used as external makeup feed. It was assumed that the gaseous fission products xenon and krypton are removed continuously. The cerium nuclides were treated separately along with xenon and krypton while the other fission products were represented by fissionable isotope dependent lumped fission products.

2.4.3. Kinetics Parameters and Reactivity Coefficients

Reactivity coefficients and kinetics parameters were calculated using the VARI3D perturbation theory code [8]. The coolant, fuel, and structural material density coefficients and the coolant void worth were determined. The first-order perturbation theory option was used for density coefficients, while the exact perturbation theory option was employed for the coolant void worth. The effective delayed neutron fraction and prompt neutron lifetime were also calculated using the VARI3D code. The radial and axial expansion coefficients were determined by direct eigenvalue differences of the base and perturbed conditions using the DIF3D code. Two sets of Doppler coefficients were calculated at flooded and voided sodium conditions using the VARI3D code.

With the approximation that the Doppler coefficients are inversely proportional to the absolute fuel temperature, the Doppler constant was calculated by doubling the average fuel temperature. The reactivity change due to doubled fuel temperature can be written as

$$\Delta\rho = \int_{T_f}^{2T_f} \frac{d\rho}{dT}(T)dT = \int_{T_f}^{2T_f} \frac{C_D}{T} dT = C_D \ln 2 \quad (2.1)$$

where ρ is the reactivity and T_f is the core averaged fuel temperature. Thus, the Doppler coefficient at the average fuel temperature was determined as

$$\frac{d\rho}{dT}(T_f) = \frac{C_D}{T_f} = \frac{\Delta\rho}{T_f \ln 2} \quad (2.2)$$

The axial expansion coefficient is the reactivity effect due to the uniform axial expansion of fuel and the corresponding reduction of fuel density. Since the core radius is fixed, the core-averaged fuel density is reduced by the increased active core height as

$$\frac{d\bar{\rho}_f}{dH_c} = -\frac{\bar{\rho}_f}{H_c} \quad (2.3)$$

where $\bar{\rho}_f$ is the average fuel density in the core and H_c is the active core height. As a result, the reactivity change due to axial fuel expansion can be written as

$$\frac{d\rho}{dH_c} = \left. \frac{\partial\rho}{\partial H_c} \right|_{\bar{\rho}_f} + \left. \frac{\partial\rho}{\partial\bar{\rho}_f} \right|_{H_c} \frac{d\bar{\rho}_f}{dH_c} = \left. \frac{\partial\rho}{\partial H_c} \right|_{\bar{\rho}_f} - \frac{\bar{\rho}_f}{H_c} \left. \frac{\partial\rho}{\partial\bar{\rho}_f} \right|_{H_c} \quad (2.4)$$

Using the volumetric expansion coefficient α_v of fuel, this reactivity coefficient with respect to core height change can be converted into a temperature coefficient with respect to fuel temperature increase (excluding the Doppler effects) as

$$\frac{d\rho}{dT_f} = \left. \frac{\partial\rho}{\partial H_c} \right|_{\bar{\rho}_f} \frac{dH_c}{dT_f} + \left. \frac{\partial\rho}{\partial\bar{\rho}_f} \right|_{H_c} \frac{d\bar{\rho}_f}{dT_f} = \alpha_v H_c \left. \frac{\partial\rho}{\partial H_c} \right|_{\bar{\rho}_f} - \alpha_v \bar{\rho}_f \left. \frac{\partial\rho}{\partial\bar{\rho}_f} \right|_{H_c} = \alpha_v H_c \frac{d\rho}{dH_c} \quad (2.5)$$

This temperature coefficient due to axial fuel expansion was calculated by increasing the fuel height by 1% and correspondingly reducing the fuel density by 1%.

In a conventional solid fuel core, the radial expansion coefficient represents the reactivity effect due to the uniform expansion of the grid plate caused by increased coolant inlet temperature and the corresponding reduction of the effective densities of fuel and structure within the core. Since the active core height is fixed, the core-averaged fuel and structural material densities are reduced by increased core radius as

$$\frac{d\bar{\rho}}{dR_c} = -2 \frac{\bar{\rho}}{R_c} \quad (2.6)$$

where $\bar{\rho}$ is the average fuel or structural material density in the core and R_c is the active core radius. As a result, the reactivity change due to radial core expansion can be written as

$$\begin{aligned} \frac{d\rho}{dR_c} &= \left. \frac{\partial\rho}{\partial R_c} \right|_{\bar{\rho}_f, \bar{\rho}_s} + \left. \frac{\partial\rho}{\partial\bar{\rho}_f} \right|_{R_c, \bar{\rho}_s} \frac{d\bar{\rho}_f}{dR_c} + \left. \frac{\partial\rho}{\partial\bar{\rho}_s} \right|_{R_c, \bar{\rho}_f} \frac{d\bar{\rho}_s}{dR_c} \\ &= \left. \frac{\partial\rho}{\partial R_c} \right|_{\bar{\rho}_f, \bar{\rho}_s} - 2 \frac{\bar{\rho}_f}{R_c} \left. \frac{\partial\rho}{\partial\bar{\rho}_f} \right|_{R_c, \bar{\rho}_s} - 2 \frac{\bar{\rho}_s}{R_c} \left. \frac{\partial\rho}{\partial\bar{\rho}_s} \right|_{R_c, \bar{\rho}_f} \end{aligned} \quad (2.7)$$

where $\bar{\rho}_s$ the core-averaged structural material density. Using the linear expansion coefficient of the grid plate, this reactivity coefficient with respect to core radius change can be converted into a temperature coefficient with respect to the coolant inlet temperature as

$$\begin{aligned} \frac{d\rho}{dT_{in}} &= \left. \frac{\partial\rho}{\partial R_c} \right|_{\bar{\rho}_f, \bar{\rho}_s} \frac{dR_c}{dT_{in}} + \left. \frac{\partial\rho}{\partial\bar{\rho}_f} \right|_{R_c, \bar{\rho}_s} \frac{d\bar{\rho}_f}{dT_{in}} + \left. \frac{\partial\rho}{\partial\bar{\rho}_s} \right|_{R_c, \bar{\rho}_f} \frac{d\bar{\rho}_s}{dT_{in}} \\ &= \alpha_l R_c \left. \frac{\partial\rho}{\partial R_c} \right|_{\bar{\rho}_f, \bar{\rho}_s} - 2\alpha_l \bar{\rho}_f \left. \frac{\partial\rho}{\partial\bar{\rho}_f} \right|_{R_c, \bar{\rho}_s} - 2\alpha_l \bar{\rho}_s \left. \frac{\partial\rho}{\partial\bar{\rho}_s} \right|_{R_c, \bar{\rho}_f} = \alpha_l R_c \frac{d\rho}{dR_c} \end{aligned} \quad (2.8)$$

where T_{in} is the coolant inlet temperature. This temperature coefficient due to radial core expansion is typically calculated by increasing the core radius by 1% and correspondingly reducing the fuel and structural material densities by 2%.

On the other hand, for the SLFFR using liquid alloy fuel, the radial expansion of the fuel container caused by increased coolant inlet temperature would reduce the liquid fuel height without changing the fuel density. In this case, the active core height is reduced by increased core radius as

$$\frac{dH_c}{dR_c} = -2 \frac{H_c}{R_c} \quad (2.9)$$

As a result, the reactivity change due to radial core expansion can be written as

$$\begin{aligned} \frac{d\rho}{dR_c} &= \left. \frac{\partial \rho}{\partial R_c} \right|_{H_c, \bar{\rho}_s} + \left. \frac{\partial \rho}{\partial H_c} \right|_{R_c, \bar{\rho}_s} \frac{dH_c}{dR_c} + \left. \frac{\partial \rho}{\partial \bar{\rho}_s} \right|_{R_c, H_c} \frac{d\bar{\rho}_s}{dR_c} \\ &= \left. \frac{\partial \rho}{\partial R_c} \right|_{H_c, \bar{\rho}_s} - 2 \frac{H_c}{R_c} \left. \frac{\partial \rho}{\partial H_c} \right|_{R_c, \bar{\rho}_s} - 2 \frac{\bar{\rho}_s}{R_c} \left. \frac{\partial \rho}{\partial \bar{\rho}_s} \right|_{R_c, H_c} \end{aligned} \quad (2.10)$$

Using the linear expansion coefficient α_l of the fuel container, this reactivity coefficient with respect to core radius change can be converted into a temperature coefficient with respect to the increase of the coolant inlet temperature as

$$\begin{aligned} \frac{d\rho}{dT_{in}} &= \left. \frac{\partial \rho}{\partial R_c} \right|_{H_c, \bar{\rho}_s} \frac{dR_c}{dT_{in}} + \left. \frac{\partial \rho}{\partial H_c} \right|_{R_c, \bar{\rho}_s} \frac{dH_c}{dT_{in}} + \left. \frac{\partial \rho}{\partial \bar{\rho}_s} \right|_{R_c, H_c} \frac{d\bar{\rho}_s}{dT_{in}} \\ &= \alpha_l R_c \left. \frac{\partial \rho}{\partial R_c} \right|_{H_c, \bar{\rho}_s} - 2\alpha_l H_c \left. \frac{\partial \rho}{\partial H_c} \right|_{R_c, \bar{\rho}_s} - 2\alpha_l \bar{\rho}_s \left. \frac{\partial \rho}{\partial \bar{\rho}_s} \right|_{R_c, H_c} = \alpha_l R_c \frac{d\rho}{dR_c} \end{aligned} \quad (2.11)$$

Thus, the radial expansion coefficient of SLFFR was calculated by increasing the fuel container radius by 1%, reducing the structural material density by 2%, and reducing the active core height by 2%.

2.4.4. Computational Thermo-Fluidic Dynamics Analyses

Thermo-fluidic analyses were performed using the ANSYS FLUENT computational fluid dynamics (CFD) code [9]. Since it was unrealistic to perform detailed CFD calculations for the whole core containing more than ten thousand coolant tubes, a three-level CFD analysis scheme was used. First, an appropriate mesh size was determined by performing mesh sensitivity analyses using a single channel model. Then, in order to examine the peak temperatures and liquid fuel movement, multi-channel analyses were performed for three different representative regions of the core: central, middle, and periphery. The multi-channel models for these three regions are shown in Figure 2.17. Finally, the whole core CFD analysis was performed using a porous media model. In FLUENT calculations, the pressure-based flow solver was used along with the standard k - ϵ turbulence model. Both the sodium coolant and liquid fuel were modeled as liquid, and the fission gas above the fuel region was modeled as air.

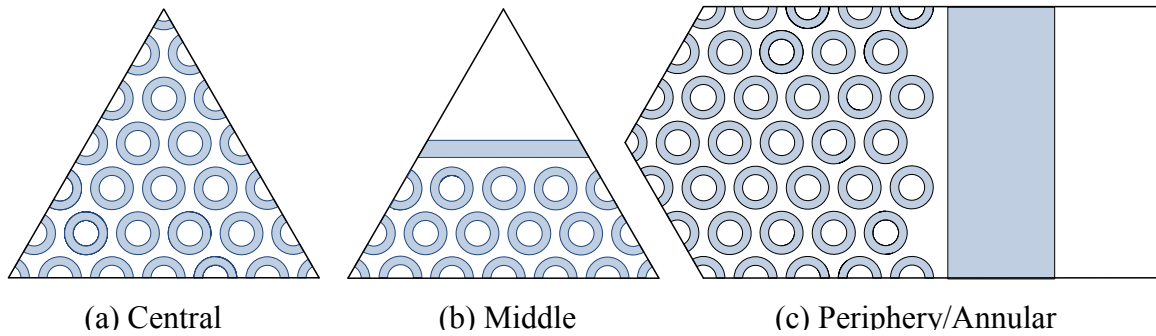


Figure 2.17. Multi-channel Model of SLFFR Core for FLUENT Calculations

Figure 2.18 shows the three mesh configurations of single channel model used for mesh sensitivity analyses. The single channel model is composed of four distinct regions: liquid fuel, sodium coolant, coolant tube, and fission gas regions. 10,520, 84,160 and 447,040 hexahedral elements were used for case 1, case 2, and case 3 in Figure 2.18, respectively. Figure 2.19 shows the resulting temperature distributions, and Table 2.3 summarizes the power densities and temperatures. It can be seen that the three meshes yields almost the same bulk coolant temperature. However, the peak fuel temperature predicted by the case 1 is $\sim 24^\circ\text{C}$ higher than those of the cases 2 and 3. Therefore, the case 2 mesh was used for subsequent multi-channel analyses as a trade-off between computational accuracy and efficiency.

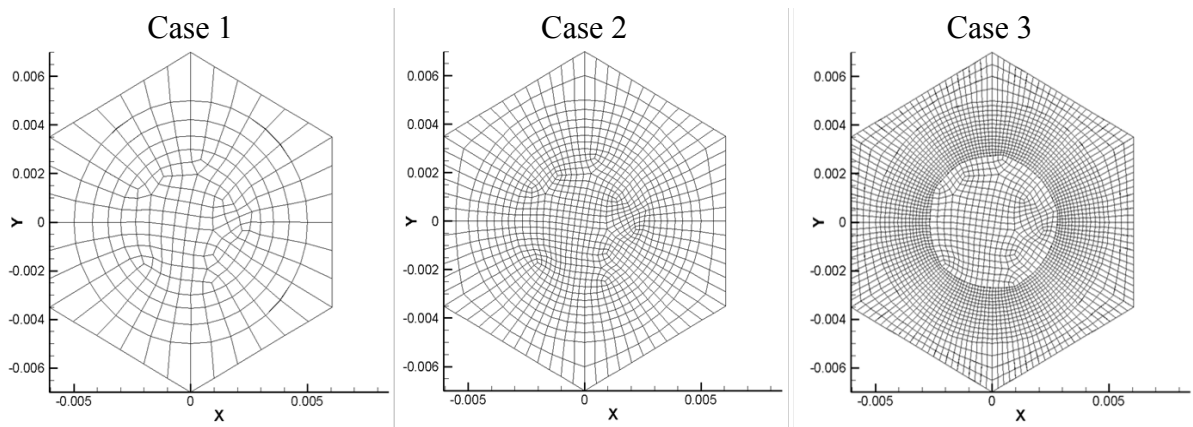


Figure 2.18. Mesh Configurations of Single Channel Model for FLUENT Calculations

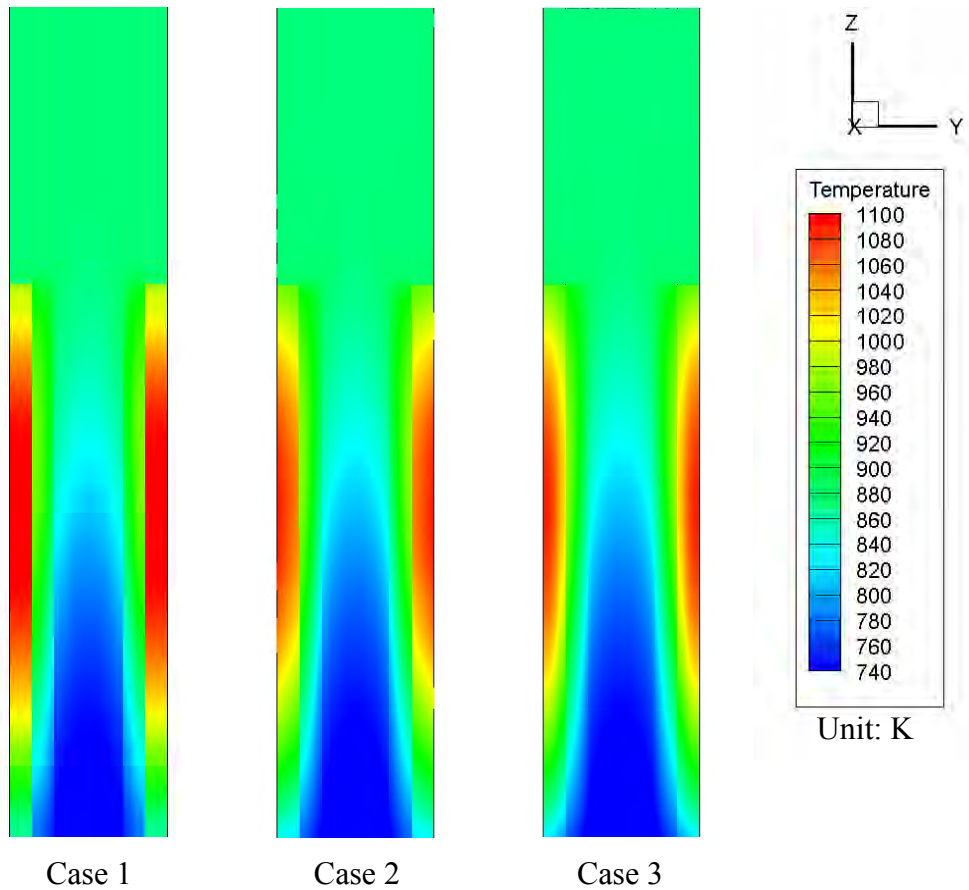


Figure 2.19. Temperature Distributions of Three Single Channel CFD Models

Table 2.3. Temperatures and Power Densities of Single Channel CFD Calculations

	Case 1	Case 2	Case 3
Peak Fuel Temperature (°C)	847.4	823.5	820.3
Peak Temperature at The Interface Between Fuel and Coolant Tube (°C)	698.1	699.1	703.4
Peak Coolant Temperature (°C)	612.0	612.8	614.1
Bulk Coolant Outlet Temperature (°C)	604.3	604.2	604.2
Coolant Inlet Temperature (°C)	450.0	450.0	450.0
Coolant Temperature Increase (°C)	154.3	154.2	154.2
Average Power Density (W/cm ³)	1620	1620	1620
Maximum Power Density (W/cm ³)	2110	2110	2110
Number of Mesh	10,520	84,160	447,040

2.5. Reference Core Design

2.5.1. Core Design Studies

A parametric study was performed to determine the feasibility of SLFFR for transmuting TRU from used light water reactor (LWR) nuclear fuel. Using TRU-Ce-Co ternary fuel with a fixed cobalt fraction of 25 a/o, Ta-10W fuel container, and sodium coolant, design calculations were performed to develop a core design of a 1000 MWt TRU-burning SLFFR. The core dimensions, the number of coolant tubes, and the TRU content in TRU-Ce-Co fuel were iteratively determined to minimize the TRU loading while providing a sufficient heat transfer area from fuel to coolant so that the peak temperature at the fuel and container interface is less than the imposed limit of 700 °C. Core performance characteristics were evaluated for a TRU recycled equilibrium cycle, which was approximated by a 300-batch, 1-day fuel cycle. The TRU recovered from the SLFFR was used as the primary TRU feed with the makeup TRU feed recovered from the LWR spent fuel. The isotopic TRU composition of makeup TRU was obtained from 10-year cooled LWR spent fuel with 50 GWd/MT burnup.

Since the melting point of Pu-Ce-Co fuel alloy is near 420 °C for a wide range of Pu content, the coolant inlet temperature was set to 450 °C. In order to reduce the peak temperature at the fuel and container interface without increasing the coolant flow area excessively, the average temperature rise across the coolant tube was set to 100 °C. Since the melting point of Ta-10W is 3030 °C, TRU-Ce-Co fuel can easily be maintained in a molten state using fission power without a significant concern of fuel container integrity.

In order to determine the number of coolant tubes and the active core height to provide a sufficient heat transfer area, the peak temperatures were estimated at the equilibrium cycle using a simple single channel thermal-fluidic model. Table 2.4 shows the estimated peak temperature at the interface between fuel and coolant tube for different coolant tube designs, fuel container size and active core heights. It can be seen that Case 3 and Case 4 satisfy the imposed limit of 700 °C for the peak temperature at the fuel and container interface with sufficiently high fuel height. Based on these results, Case 3 and Case 4 with an active core height of 100 cm were selected for further neutronics calculations.

Table 2.5 shows the calculated multiplication factors for Case 3 and Case 4 with two different fuel compositions. The multiplication factor of Case 3 for the start-up core was too low when it is loaded with 19.6TRU-56.2Ce-24.2Co fuel, and it became excessively high when loaded with 35TRU-40Ce-25Co fuel. The estimated fuel composition to make Case 3 critical was 25TRU-50Ce-25Co. Case 4 with 19.6TRU-56.2Ce-24.2Co fuel appears a reasonable one for assumed operating strategy, so it was selected for a more detailed design study.

With further design iterations, a preliminary core design was developed based on the Case 4. A schematic radial layout of the preliminary core design is shown in Figure 2.20. Separate steel reflectors and B₄C shields were used outside of the fuel container in order to reduce the fuel container mass for easier handling and to reduce the amount of refractory Ta-10W alloy which is more expensive than steel. The fuel container is a 2.5 cm thick cylinder with an inner radius of 85 cm. The ternary alloy fuel is composed of 20 a/o TRU, 56 a/o Ce and 24 a/o Co. The critical TRU mass at the beginning of life (BOL) was 3242 kg. The active core height for the initial criticality was calculated to be 100 cm. However, the container height was set at 150 cm to allow for an extended period of operation without removing solid fission products. The

fuel container has 14491 penetrating tubes of 6.0 mm inner diameter and 2.0 mm thickness. These coolant tubes are arranged in a triangular lattice with a lattice pitch of 1.21 cm. The fuel, structure, and coolant volume fractions in the core were 0.445, 0.339, and 0.216, respectively.

Table 2.4. Estimated Peak Temperature at the Interface between Fuel and Coolant Tube

Parameters			Case 1	Case 2	Case 3	Case 4
Total Power (MWt)			1000	1000	1000	1000
Fuel Container	Inner Radius (m)		0.75	0.75	0.75	0.85
	Outer Radius (m)		0.775	0.775	0.775	0.875
	Height (m)		1.5	1.5	1.5	1.5
Number of Coolant Channels			1261	5941	12481	14491
Coolant Tube	Thickness (m)		0.0035	0.0025	0.0020	0.0020
	Inner Diam. (m)		0.0254	0.0100	0.0060	0.0060
	Pitch (m)		0.0362	0.0166	0.0115	0.0121
Volume Fractions	Fuel		0.36182	0.35675	0.39137	0.44472
	Structure		0.25887	0.34966	0.37160	0.33948
	Coolant		0.37932	0.29359	0.23704	0.21580
Peak Interface Temperature Between Fuel and Coolant Tube (°C)	Fuel Height (m)	0.70	1982	980	798	764
		0.85	1729	904	754	726
		1.00	1553	851	724	700
		1.25	1352	791	689	670
		1.50	1218	751	666	650

Table 2.5. Multiplication Factors Obtained with TWOANT

Parameter		Case 3a	Case 3b	Case 4
Core Outer Radius	cm	77.5	77.5	87.5
Active Core Height	cm	100.0	100.0	100.0
Fuel Composition (at. %)	TRU/Ce/Co	19.6/56.2/24.2	35.0/40.0/25.0	19.6/56.2/24.2
Fuel Density	g/cm ³	8.762	10.191	8.926
Fuel Loading	kg	6470.5	7525.8	9547.5
TRU Loading	kg	2197.4	4116.6	3242.3
TRU Density in Fuel	g/cm ³	2.98	5.57	3.03
k-effective	TWODANT	0.87005	1.29148	1.00884

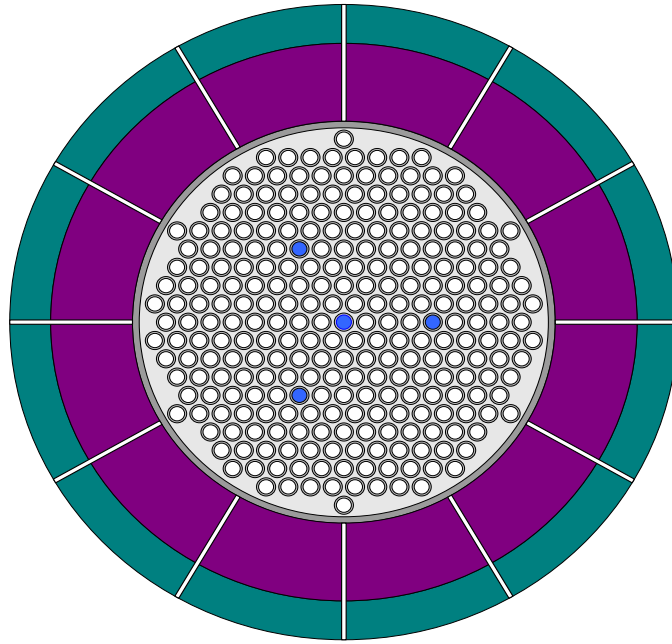


Figure 2.20. Schematic Radial Layout of Preliminary 1000 MWt SLFFR Core

2.5.2. Reference Core Design and Performances

2.5.2.1. Reference Core Design Description

A reference core design was developed by further modifying the preliminary core design through detailed neutronics and thermo-fluidic and transient analyses. Specifically, the core outer radius was increased from 87.5 cm to 90 cm to provide spaces for the control systems and the fuel feed and extraction lines. The coolant flow area was also increased with larger core radius. Two separate safety-grade reactivity control systems were introduced inside the fuel container. Six gas expansion modules (GEMs) of 5 cm thickness were introduced by replacing parts of the reflectors to provide a passive shutdown capability against the unprotected loss of flow (ULOF) accident. Figure 2.21 shows a schematic of the radial layout of the reference 1000 MWt SLFFR core, and Table 2.6 summarizes the main design parameters.

As in the preliminary design, separate steel reflectors and B₄C shields are used outside of the fuel container. The fuel container is a 2.5 cm thick cylinder with an inner radius of 87.5 cm. The fuel container has 18181 penetrating coolant tubes of 6.0 mm inner diameter and 2.0 mm thickness. The coolant tubes are arranged in a triangular lattice with a lattice pitch of 1.21 cm. The fuel, structure, and coolant volume fractions inside the fuel container are 0.386, 0.383, and 0.231, respectively.

Two separate safety-grade reactivity control systems are introduced to the internal region of the fuel container. Both the primary and secondary systems consist of six control assemblies (CAs). Each of the control systems is designed to shut down the reactor from any operating condition to the cold shutdown condition independently. The cold shutdown condition was defined at a sodium coolant temperature of 205 °C for the replacement of fuel tank, although

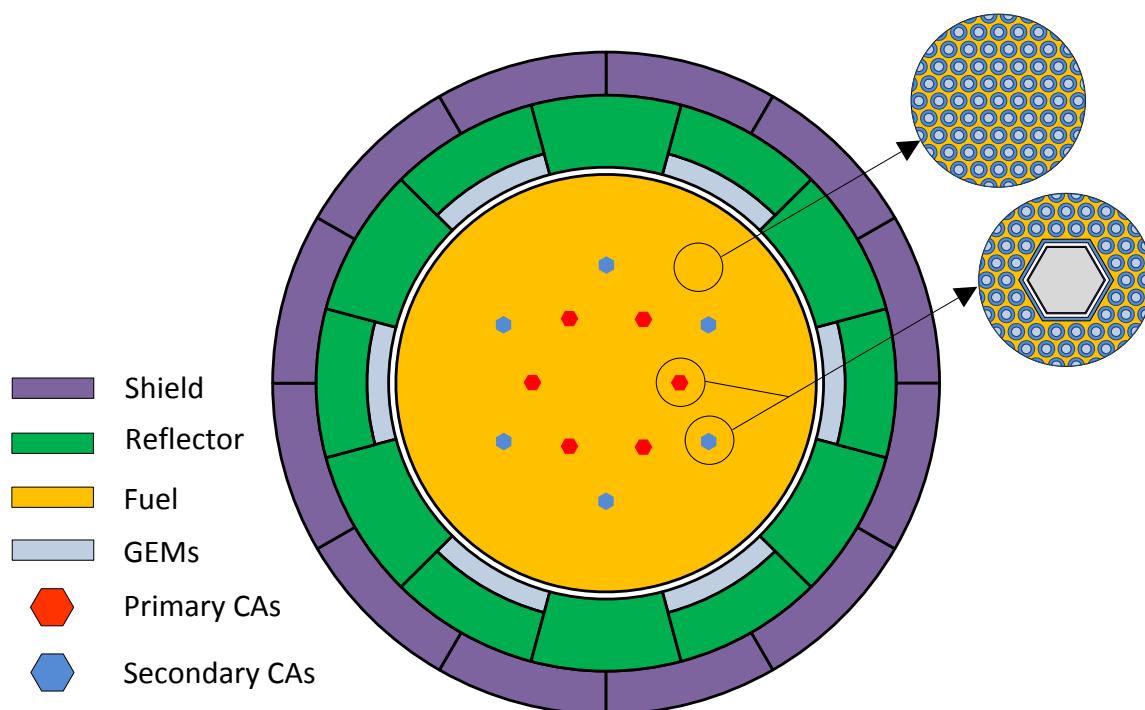


Figure 2.21. Schematic Radial Layout of Reference Core Design of 1000 MWt SLFFR

Table 2.6. Main Design Parameters of Reference Core Design of 1000 MWt SLFFR

Total Power (MWt)		1000
Fuel Container	Inner Diameter (cm)	170.0
	Thickness (cm)	2.5
	Height (cm)	150.0
	Active Core Height (cm)	100.0
Radial Reflector	Inner Diameter (cm)	185.0
	Thickness (cm)	27.5
B ₄ C Shield	Inner Diameter (cm)	240.0
	Thickness (cm)	15.0
Coolant Tube	Number of Tubes	18181
	Thickness (cm)	0.20
	Inner Diameter (cm)	0.60
	Lattice Pitch (cm)	1.21
Volume Fractions (inside of container)	Fuel	0.386
	Structure	0.383
	Coolant	0.231

the coolant temperature is maintained above the fuel freezing temperature of ~ 420 °C during a normal shutdown. The distances from the core center to the centers of primary and secondary control assemblies are ~ 25 cm and ~ 45 cm, respectively. The minimum distance between two neighboring CA guide tubes is selected to be 25 cm to provide a sufficient space for control rod driving systems. The CA guide tube is designed in a hexagonal shape, as shown in Figure 2.22, to lower the peak temperature at the CA guide tube and fuel interface by reducing the local liquid fuel area and thus the local heat source. A flow separation duct is installed inside the CA guide tube. The coolant flow in the gap between the CA guide tube and the separation duct will have higher velocity than the coolant flow inside the separation duct so that the peak temperature at the CA guide tube and fuel interface can be minimized and, meanwhile, the outlet temperature near the control assembly region can be flattened. The control assembly is composed of seven B₄C control rods with outer diameter of 1.81 cm and 90% B-10 enrichment. The main design parameters are summarized in Table 2.7.

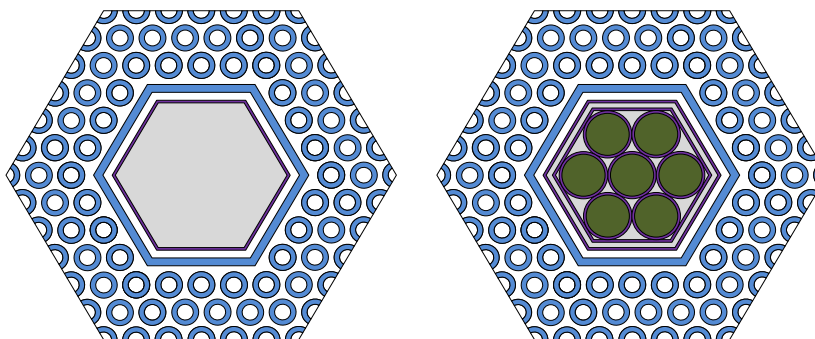


Figure 2.22. Radial Layout of CA Guide Tube without and with CA Insertion

Table 2.7. Main Design Parameters of Control Assembly and Guide Tube

Guide tube	Flat to Flat Distance between Outer Surfaces (cm)	6.94
	Tube Thickness (cm)	0.3
	Gap between Guide Tube and CR Duct (cm)	0.3
	Number of Coolant Tubes Removed	37
	Inner Tube Center to Core Center Distance (cm)	25.3
	Outer Tube Center to Core Center Distance (cm)	44.6
	Number of Inner Tubes	6
	Number of Outer Tubes	6
Control assembly	Control Assembly Duct Thickness (cm)	0.1
	Number of Control Rods	7
	Control Rod Outer Diameter (cm)	1.81
	Cladding Thickness (cm)	0.1

2.5.2.2. Fuel Cycle Performance Characteristics

Prior to the equilibrium cycle analysis, the core characteristics of beginning of life (BOL) were calculated to confirm an operation feasibility of the reference core design and to compare the performance characteristics with the equilibrium cycle. Table 2.8 summarizes the core performance characteristics of 1000 MWt SLFFR at the BOL. Because of uranium-free fuel, a theoretical maximum TRU consumption rate of 1.011 kg/day is achieved. The TRU inventory at BOL is 3,541 kg, and the daily burnup reactivity loss is 36.8 pcm. A daily TRU charge rate of 11.71 kg is required to overcome the burnup reactivity loss and maintain criticality. The charged TRU-Ce-Co fuel is composed of 24.14 a/o TRU, 51.82 a/o Ce, and 24.03 a/o Co. The power density is 413.1 W/cm³ and the power peaking factor is 2.25.

Table 2.8. Core Performance Characteristics at BOL of Reference 1000 MWt SLFFR

BOL Fuel Inventory (kg)	TRU	3541
	Ce	4445
	Co	867
	Fission Products	0
Multiplication Factor		1.00326
Burnup Reactivity Loss (pcm/day)		36.83
TRU Consumption Rate (kg/day)		1.010
Fuel Charge Rate (kg/day)	TRU (Makeup feed)	11.71
	Cerium	8.36
	Cobalt	2.09
Core-average Power Density (W/cm ³)		413.13
Power Peaking Factor		2.25

Table 2.9 summarizes the equilibrium cycle performance characteristics of 1000 MWt SLFFR. The TRU inventory at the beginning of equilibrium cycle (BOEC) is 5,081 kg, whereas the critical TRU mass at BOL was 3,541 kg. This is because the equilibrium cycle core contains a significantly smaller fissile fraction than the LWR TRU feed. The core average power density is 413.76 W/cm³, and the power peaking factor 2.10. As can be seen from the isotopic TRU fractions shown in Table 2.10, compared to the LWR spent fuel TRU, the Pu-239 fraction in the equilibrium cycle core is reduced by 50.2% whereas the Pu-240 fraction is increased by 50.1%. The fuel inventory at BOEC is composed of 34.0 a/o TRU, 41.4 a/o Ce, 23.6 a/o Co, and 1.0 a/o solid fission products. The fractions of individual isotopes in different TRU compositions are compared in Figure 2.23. Since uranium-free fuel is used, a theoretical maximum TRU consumption rate of 1.011 kg/day is achieved. The assumed 300-batch, 1-day fuel cycle requires a daily reprocessing of 32.5 kg of SLFFR fuel. This yields a daily TRU charge rate of 17.45 kg, including a makeup TRU feed of 1.011 kg recovered from the LWR used fuel. The charged TRU-Ce-Co fuel is composed of 34.43 a/o TRU, 40.57 a/o Ce, and 25.0 a/o Co. Table 2.11 shows the detailed isotopic mass flow rate of actinides.

Table 2.9. Equilibrium Cycle Performance Characteristics of Reference SLFFR Design

BOEC Fuel Inventory (kg)	TRU	5081
	Ce	3635
	Co	867
	Fission Products	116
Multiplication Factor	BOEC	1.00390
	EOEC	1.00364
Burnup Reactivity Loss (pcm/day)		26
TRU Consumption Rate (kg/day)		1.011
Fuel Charge Rate (kg/day)	TRU	17.45
	(Makeup TRU feed)	(1.011)
	Cerium	12.09
	Cobalt	3.11
Daily Reprocessing Rate of SLFFR Fuel (kg)		32.5
Core-average Power Density (W/cm ³)		413.76
Power Peaking Factor	BOEC	2.099
	EOEC	2.097

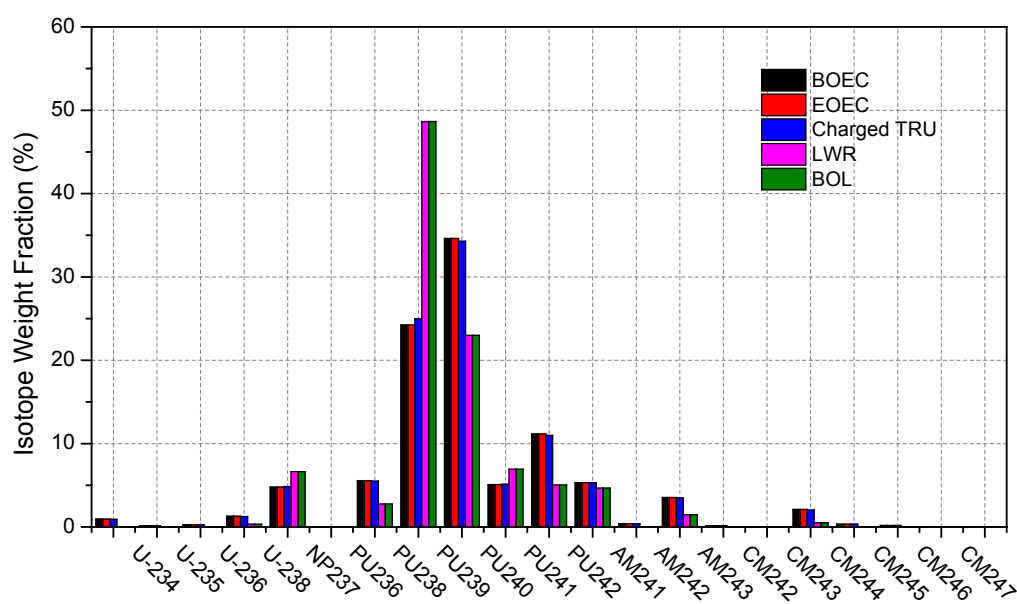


Figure 2.23. Comparison of Isotopic Fractions of Different TRU Compositions

Table 2.10. Isotopic TRU Fraction (w/o) of SLFFR Inventories and Charge Materials

Isotope	BOEC	EOEC	Charge	LWR TRU
U-234	0.934	0.934	0.910	0.000
U-235	0.130	0.130	0.126	0.002
U-236	0.250	0.250	0.243	0.002
U-238	1.271	1.271	1.243	0.325
NP-237	4.779	4.779	4.835	6.641
PU-236	0.000	0.000	0.000	0.000
PU-238	5.557	5.557	5.492	2.749
PU-239	24.235	24.230	24.964	48.653
PU-240	34.611	34.613	34.269	22.980
PU-241	5.079	5.078	5.115	6.926
PU-242	11.154	11.155	10.972	5.033
AM-241	5.298	5.298	5.297	4.654
AM-242	0.378	0.378	0.367	0.018
AM-243	3.537	3.538	3.476	1.472
CM-242	0.159	0.159	0.130	0.000
CM-243	0.007	0.007	0.007	0.005
CM-244	2.091	2.091	2.037	0.496
CM-245	0.331	0.331	0.322	0.038
CM-246	0.172	0.172	0.167	0.006
CM-247	0.018	0.018	0.017	0.000
CM-248	0.011	0.011	0.010	0.000

Table 2.11. Heavy Metal Mass Flow Rates (kg/day) of SLFFR for Daily Reprocessing Rate of 1/300 of Fuel Inventory

Isotope	Charge	Discharge	Destruction	SLFFR TRU Feed	LWR TRU Feed
U-234	0.159	0.158	0.001	0.159	0.000
U-235	0.022	0.022	0.000	0.022	0.000
U-236	0.042	0.042	0.000	0.042	0.000
U-238	0.217	0.214	0.003	0.214	0.003
NP237	0.844	0.776	0.067	0.776	0.067
PU236	0.000	0.000	0.000	0.000	0.000
PU238	0.958	0.925	0.033	0.930	0.028
PU239	4.356	3.864	0.492	3.864	0.492
PU240	5.979	5.745	0.234	5.747	0.232
PU241	0.893	0.829	0.064	0.823	0.070
PU242	1.914	1.864	0.051	1.864	0.051
AM241	0.924	0.871	0.053	0.877	0.047
AM242	0.064	0.064	0.000	0.064	0.000
AM243	0.607	0.592	0.015	0.592	0.015
CM242	0.023	0.029	-0.007	0.023	0.000
CM243	0.001	0.001	0.000	0.001	0.000
CM244	0.355	0.353	0.003	0.350	0.005
CM245	0.056	0.056	0.000	0.056	0.000
CM246	0.029	0.029	0.000	0.029	0.000
CM247	0.003	0.003	0.000	0.003	0.000
CM248	0.002	0.002	0.000	0.002	0.000
Total	17.45	16.44	1.011	16.44	1.01

2.5.2.3. Kinetics Parameters and Reactivity Coefficients

The kinetic parameters and reactivity feedback coefficients were calculated for the BOL and the end of equilibrium cycle (EOEC) configurations of SLFFR. Table 2.12 compares the reactivity feedback coefficients and kinetics parameters of SLFFR at EOEC with those of a 1000 MWt Advanced Burner Reactor (ABR) concept with a TRU conversion ratio of zero [2]. The ABR concept uses TRU-40Zr metallic fuel in conventional hexagonal solid fuel assemblies. To reduce the fuel volume fraction, small diameter pins were used with grid spacers and seven tie pins. To flatten the radial power distribution, fuel volume fraction zoning was used with different fuel pin diameters. The equivalent core radius is 2.22 m and the core height including the fission gas plenum is 2.92 m, and thus the ABR core volume is 3.3 times larger than that of SLFFR. The burnup reactivity loss of ABR is 17.8\$ over a relatively short cycle length of 132 effective full power days (EFPDs).

Table 2.12. Kinetic Parameters and Reactivity Coefficients of Reference Core Design of 1000 MWt SLFFR at EOEC

Parameter		SLFFR	ABR
Cycle Length	EFPD	n/a	132
Burnup Reactivity Loss	\$	n/a	17.8
Delayed Neutron Fraction		0.00200	0.00245
Prompt Neutron Lifetime	μ s	0.078	0.54
Axial Expansion Coefficient	cent/ $^{\circ}$ C	-1.72	-0.20
Radial Expansion Coefficient	cent/ $^{\circ}$ C	0.27	-0.61
Sodium Density Coefficient	cent/ $^{\circ}$ C	0.23	0.19
Sodium Void Worth	\$	4.50	7.95
Doppler Coefficient	cent/ $^{\circ}$ C	0.00	-0.01
Fuel Density Coefficient	cent/ $^{\circ}$ C	-2.07	-1.11
Maximum Gems Worth	\$	-2.27	n/a

Since uranium-free fuels are used for both SLFFR and ABR, the delayed neutron fraction is about two thirds of conventional breeder reactors. As expected, the Doppler coefficient that provides prompt reactivity feedback is practically zero for both SLFFR and ABR. However, the axial expansion coefficient of SLFFR is about 8.5 times more negative than that of the ABR because of a large thermal expansion coefficient of liquid metallic fuel. The sodium void worth of SLFFR is less positive than that of ABR due to the sodium gap and the GEMs at the SLFFR core periphery, which enhance the leakage in the sodium-voided situations. The radial expansion coefficient of ABR is negative because the average TRU density in the core is diluted when the grid plate expands with an increased inlet coolant temperature. On the other hand, the radial expansion of the fuel container of SLFFR results in a slightly positive radial expansion coefficient under the assumption that the fuel height is reduced to preserve the fuel volume without fuel density change. Since the core volume of ABR is 3.3 times larger than SLFFR core, the SLFFR has significantly larger leakage, resulting in a much smaller prompt neutron lifetime in SLFFR.

Table 2.13 compares the reactivity coefficients and kinetics parameters at BOL and EOEC. Since the core characteristics are almost identical with one-day cycle, the reactivity coefficients and kinetics parameters at the beginning of equilibrium cycle (BOEC) are the same with EOEC. Because of a smaller minor actinide fraction, the delayed neutron fraction at BOL is 7.5% larger than that at EOEC. The axial expansion, radial expansion, and fuel density coefficients at BOL are slightly smaller than those at EOEC are mainly because of the slightly larger delayed neutron fraction at BOL. It is noted that the sodium void worth at BOL is significantly smaller than that at EOEC because of the softer neutron spectrum due to the increased Ce fraction in fuel. The reactivity effect of sodium voiding (or density reduction) consists of two principal effects of opposite sign: 1) a negative reactivity due to increased neutron leakage, and 2) a positive reactivity due to hardening of neutron energy spectrum. The leakage effect is similar at BOL and EOEC, but the larger fraction of Ce in the fuel at BOL than at EOEC makes the BOL spectrum softer and consequently reduces the spectrum hardening effect.

Table 2.13. Comparison of Reactivity Coefficients and Kinetics Parameters of Reference Core Design at BOL and EOEC

Parameter		BOL	EOEC
Delayed Neutron Fraction		0.00215	0.00200
Prompt Neutron Lifetime	μs	0.090	0.078
Axial Expansion Coefficient	cent/ $^{\circ}\text{C}$	-1.64	-1.74
Radial Expansion Coefficient	cent/ $^{\circ}\text{C}$	0.25	0.27
Sodium Density Coefficient	cent/ $^{\circ}\text{C}$	0.16	0.23
Sodium Void Worth	\$	1.60	4.50
Doppler Coefficient	cent/ $^{\circ}\text{C}$	0.00	0.00
Sodium-Voided Doppler Coefficient	cent/ $^{\circ}\text{C}$	0.00	0.00
Fuel Density Coefficient	cent/ $^{\circ}\text{C}$	-2.01	-2.07
Structure Density Coefficient	cent/ $^{\circ}\text{C}$	0.45	0.49

2.5.2.4. Reactivity Control Requirements and Shutdown Margins

Reactivity control requirements were evaluated for the BOL and EOEC conditions by taking into account the temperature and power defects including a 15% overpower, the reactivity swing, and the associated uncertainties. The results are summarized in Table 2.14. The temperature defect was estimated by the reactivity change from the hot full power to the cold shutdown condition. The cold shutdown condition was defined for the replacement of fuel tank, although the coolant temperature is maintained above the fuel freezing temperature during a normal shutdown. The temperature defect includes the Doppler, sodium density change, axial expansion and radial expansion effect and it was calculated by multiplying the reactivity coefficients and the temperature change from the full power operating condition to the cold shutdown condition. The following core-averaged coolant and fuel temperatures of the reference core design were used in this evaluation: 450 $^{\circ}\text{C}$ for the coolant inlet temperature, 500 $^{\circ}\text{C}$ for the average coolant temperature and 735 $^{\circ}\text{C}$ for the average fuel temperature. As the cold shutdown condition, 205 $^{\circ}\text{C}$ is used for the coolant temperature. The liquid fuel has a volumetric expansion on freezing. To estimate the temperature defect conservatively, the fuel

freezing point of 420 °C is used for the fuel temperature at the cold shutdown condition. The estimated total control requirements are 6.21 \$ at BOL and 6.15 \$ at EOEC.

Table 2.14. Reactivity Control Requirements of SLFFR

Control Requirements (\$)		BOL	EOEC
Hot Full Power to Hot Zero Power	Doppler Effect	-0.004	-0.004
	Sodium Density Effect	-0.079	-0.113
	Axial Expansion	4.678	4.906
	Radial Expansion	-0.124	-0.137
Hot Zero Power to Cold Shutdown	Doppler Effect	-0.004	-0.003
	Sodium Density Effect	-0.388	-0.555
	Axial Expansion	0.657	0.689
	Radial Expansion	-0.607	-0.672
Sum		4.128	4.110
15% Overpower		0.619	0.616
Excess Reactivity		0.167	0.125
Uncertainties (RMS)	Temperature Defect (20%)	0.826	0.822
	Burnup Reactivity (50%)	0.083	0.062
	Criticality Prediction (\$)	1.000	1.000
	Sum	1.299	1.296
Total (\$)		6.213	6.147

The reactivity worth was calculated for various combinations of control assemblies inserted, as shown in Table 2.15. The control assembly worth was calculated using the theta-r-z geometry model of DIF3D. In this model, each hexagonal control assembly was modeled by a small annular segment of the same cross sectional area. Since the excess reactivity of SLFFR is very small, the primary and secondary control systems are designed to have a similar worth. The primary control system is composed of the inner six assemblies, and the secondary control system is composed of the outer six assemblies. Figure 2.24 and Figure 2.25 show the primary and secondary system reactivity worth at BOL and EOEC as a function of the tip position of control rod from the core bottom. The critical control position is around 80 cm for all cases. The primary and secondary control system worth at BOL and EOEC are shown in Table 2.15. Assuming one control assembly is stuck, the reactivity worth of the primary system is 14.94 \$ at BOL and 12.29 \$ at EOEC, and the reactivity worth of the secondary system is 10.71 \$ at BOL and 9.53 \$ at EOEC. The shutdown margin of the primary system is 8.72 \$ at BOL and 6.15 \$ at EOEC. The shutdown margin of the secondary system is 4.50 \$ at BOL and 3.38 \$ at EOEC. These results indicate that each of the primary and secondary control systems provides a sufficient shutdown margin.

Table 2.15. Primary and Secondary Control System Worth at BOL and EOEC

	BOL	EOEC
Primary Control System (\$)	16.30	12.78
Secondary Control System (\$)	11.74	9.96
Primary Control System with One Stuck Rod (\$)	14.94	12.29
Secondary Control System with One Stuck Rod (\$)	10.71	9.53

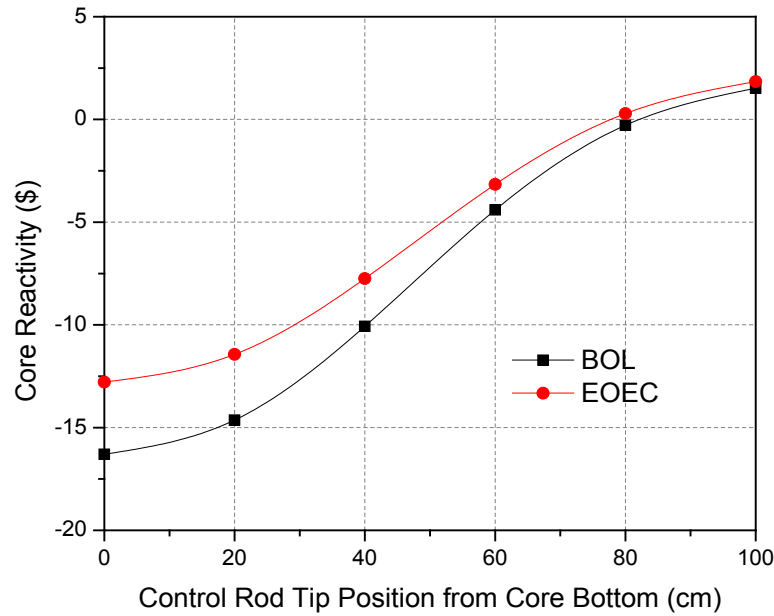


Figure 2.24. Reactivity Worth of Primary Control Systems at BOL and EOEC

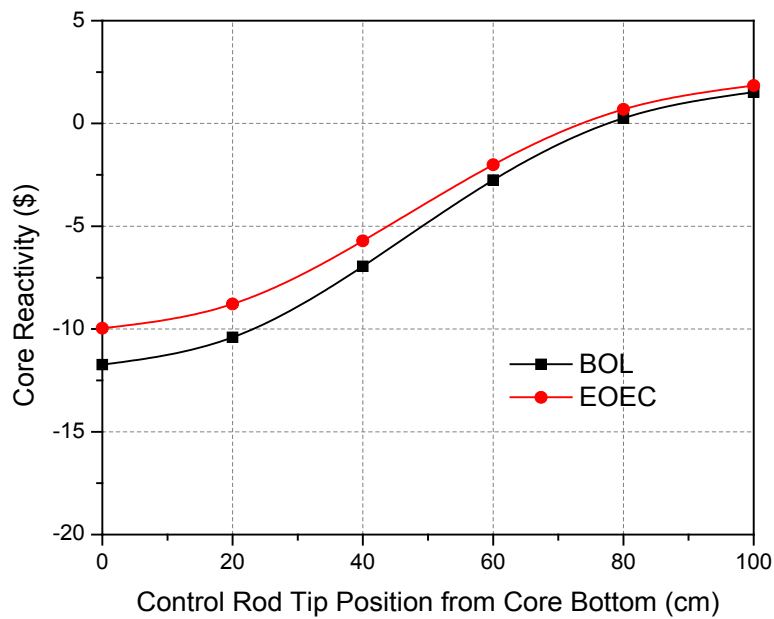


Figure 2.25. Reactivity Worth of Secondary Control Systems at BOL and EOEC

2.5.2.5. Orifice Zoning and Steady-state Thermal-Fluidic Analysis

To utilize the total coolant flow effectively, an optimal flow allocation was determined in such a way to minimize the peak temperature at the fuel and coolant tube (or CA guide tube) interface and to flatten the coolant outlet temperature. The core was divided into four flow orifice zones based on the radial power distribution: central, middle, periphery, and annular zones, as summarized in Table 2.16. The central zone includes 955 coolant tubes located within a radius of 20 cm. The middle zone is from the radius of 20 cm to 80 cm, which consists of the 12 control assemblies and 15036 coolant tubes. The periphery zone includes the four outermost rings of 2190 coolant tubes. The annular zone is the annular gap of 2.5 cm thickness between the fuel tank and the radial reflector. The annular zone includes no fuel, so a relatively low flow rate is allocated to this zone to cool the fuel tank in such a way that the peak temperature at the inner surface of the fuel tank does not exceed the imposed limit of 700 °C.

Table 2.16. Properties of Four Flow Orifice Zones

	Central	Middle	Periphery	Annular	Total
Inner/Outer Radii of Zone (cm)	0.0/20.0	20.0/82.0	82.0/87.5	90.0/92.5	N/A
Flow Area (cm ²)	270	4668	619	1433	6990
Number of Control Assemblies	0	12	0	0	12
Number of Coolant Tubes	955	15036	2190	0	18181

The coolant inlet velocities of these four orifice zones were determined to meet the design constraints on the peak temperature at the fuel and coolant tube interface as well as to flatten the distribution of the coolant outlet temperature to avoid the thermal striping on the upper internal structure.

The initial multi-channel CFD calculations were performed using the core-averaged inlet velocity of 13.4 m/s for all three regions, while the region-specific power distributions in fuel were obtained by unfolding the power distribution from the whole-core neutronics calculation with homogenized core compositions shown in Figure 2.26. The resulting peak and average core temperatures are summarized in Table 2.17. As expected, the highest power density at the core center yields the highest fuel and coolant temperatures. In the central region, the peak temperature at the fuel and coolant tube interface exceeds the imposed limit of 700 °C by 41 °C. The coolant outlet temperatures for different core regions vary in a large range from 646.3 °C at the core center to 502.2 °C at the core periphery. These results indicate that more coolant flow should be allocated to the central region by reducing the flow rates to the other regions.

In the next step, the minimum coolant inlet velocity to satisfy the peak temperature limit at the fuel and coolant tube interface was determined in each orifice zone, separately without preserving the total coolant flow rate. For the periphery region calculation, the coolant velocity in the annular zone was varied as well as the coolant velocity in the periphery zone. Table 2.18 presents the resulting minimum coolant velocity of each orifice zone and the corresponding peak temperatures. It can be seen that the inlet velocity of the central zone should be increased from 13.4 m/s to 17.8 m/s in order to meet the imposed peak temperature limit. The coolant velocities for the middle, periphery and annular zones can be reduced to 12.3 m/s, 10 m/s and 4 m/s, respectively. The total coolant mass flow rate corresponding to these minimum velocities

of individual flow zones is 6261.5 kg/s. This flow rate is about 21% smaller than the rated total flow rate of 7910 kg/s, which was obtained based on a coolant temperature rise of 100 °C across the core. Therefore, a proper allocation of the rated total flow rate to the four orifice zones can reduce the peak temperature at the fuel and coolant tube interface below the imposed limit with a sufficient margin.

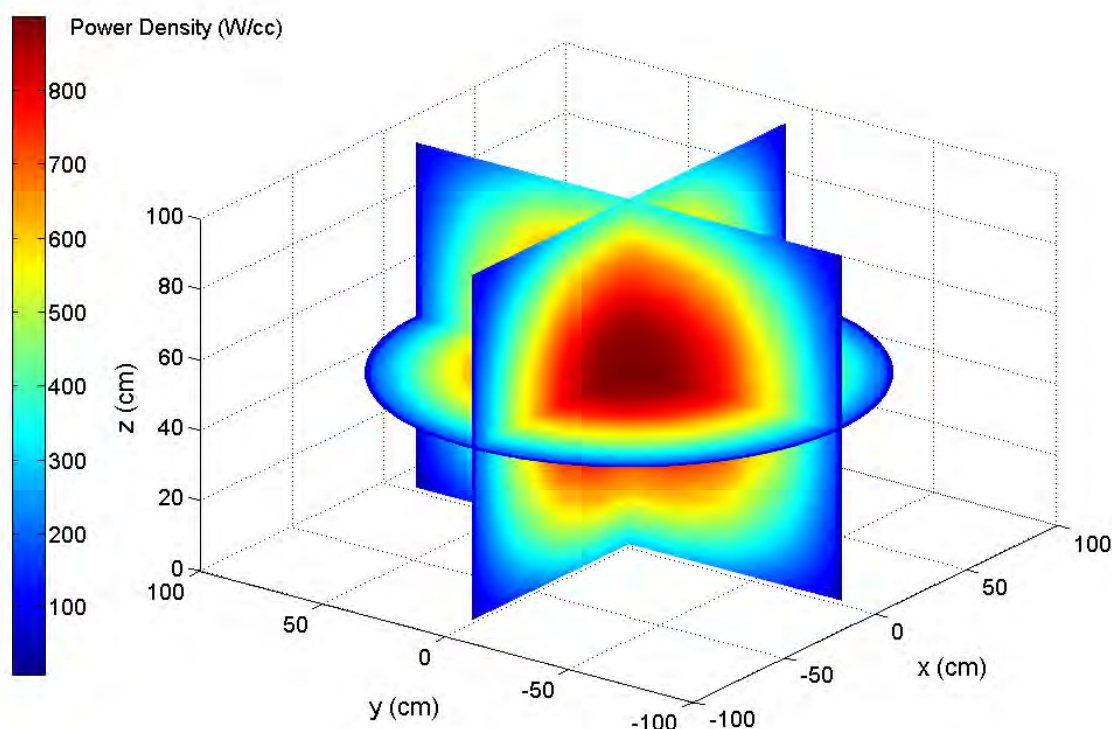


Figure 2.26. SLFFR Core Power Distribution

Table 2.17. Temperatures (°C) Obtained from Multi-Channel CFD Analyses with Core-Averaged Coolant Inlet Velocity

	Center	Middle	Periphery	Annular
Coolant Inlet Velocity (m/s)	13.4	13.4	13.4	13.4
Coolant Inlet Mass Flow Rate (kg/s)	305.5	5282.5	700.7	1621.1
Bulk Coolant Outlet Temperature	646.3	593.9	502.2	451.2
Peak Coolant Temperature	659.4	614.7	535.1	456.4
Peak Temperature at Fuel and Tube Interface	741.0	687.3	600.9	690
Peak Fuel Temperature	884.6	811.9	757.7	N/A

Table 2.18. Minimum Coolant Inlet Velocities and Corresponding Peak Temperatures (°C)
Obtained from Multi-Channel Analyses

	Center	Middle	Periphery	Annular
Minimum Coolant Velocity (m/s)	17.8	12.3	10	4.0
Minimum Mass Flow Rate (kg/s)	405.9	4959.5	522.9	483.9
Bulk Coolant Outlet Temperature	597.5	606.9	520.0	454.3
Peak Coolant Temperature	608.8	628.9	559.6	468.1
Peak Temperature at Fuel and Tube Interface	699.7	698.9	623.3	700.6*
Peak Fuel Temperature	852.0	820.9	765.1	N/A

*It is the peak temperature at the fuel tank inner surface.

Table 2.19 presents an optimal set of coolant velocities of the four orifice zones to meet the two design criteria simultaneously. Compared to the minimum velocities to meet the limit on the peak temperature at the fuel and tube interface in Table 2.18, the inlet velocity of the central region was increased from 17.8 m/s to 20.0 m/s to reduce the peak temperatures at the fuel and tube interface from 699.7 °C to 686.6 °C. The coolant velocity of the middle zone was increased from 12.3 m/s to 15.5 m/s to reduce the peak temperature at the fuel and tube interface from 698.9 °C to 677.1 °C. The inlet velocity of the periphery zone was increased slightly from 10 m/s to 11 m/s. The coolant velocity in the annular region was significantly increased from 4 m/s to 9.7 m/s to reduce the fuel tank inner surface temperature. The calculated peak temperatures with this optimum set of coolant velocities are shown in Table 2.19 and Figure 2.27. As shown in Figure 2.27, the temperature at the fuel and coolant tube interface is high at the central region because of the high power density. The peak structure temperature of the middle region appears at the outer surface of a control guide tube because of the relatively large local fuel volume fraction. The peak temperatures at the fuel and tube interfaces of the central, middle, and periphery regions are 686.6 °C, 677.1 °C and 614.2 °C, respectively, which are all have a sufficient margin to the design limit of 700 °C. The peak temperature of the fuel container is 694.7 °C, which is slightly higher and closer to the design limit than that of the coolant tubes. However, it would not be a concern since the container wall is 12.5 times thicker than coolant tubes. The bulk outlet temperatures of coolant are 581.1 °C, 575.3 °C and 514.2 °C for the central, middle and periphery regions. The maximum coolant outlet temperature occurs in the middle region. Relative to the uniform flow case, the difference between the bulk outlet temperatures of the middle and periphery regions is reduced from 87 °C to 61 °C.

The multi-channel calculations indicated the existence of natural convection or buoyancy driven flows in liquid fuel, although the speed is only ~1.2 mm per minute. This is consistent with the observations made in the LAMPRE I [11]. The flow pattern of the liquid fuel affects the interface temperature between the liquid fuel and coolant tube. Table 2.20 shows the dimensionless parameters related to buoyancy-driven flow. Figure 2.28 shows the liquid fuel flow pattern in the form of vectors and stream traces. The temperature is higher in a red region than in an adjacent yellow region, and hence the flow is upward in the red region and downward in the yellow region. The upward and downward flows form a natural circulation flow pattern driven by the buoyancy force.

Table 2.19. Temperatures (°C) Obtained from Multi-Channel CFD Analyses with Optimal Coolant Inlet Velocities

	Center	Middle (CR)	Periphery	Annular
Coolant Inlet Velocity (m/s)	20.0	15.5 (1.6)	11.0	9.7
Mass Flow Rate (kg/s)	456.0	5662.9 (43.0)	575.2	1173.5
Bulk Coolant Outlet Temperature	581.1	575.3	514.2	451.6
Peak Coolant Temperature	591.8	592.8	550.9	458.5
Peak Temperature at Fuel and Tube Interface	686.6	677.1	614.2	694.7
Peak Fuel Temperature	841.7	798.2	632.8	N/A

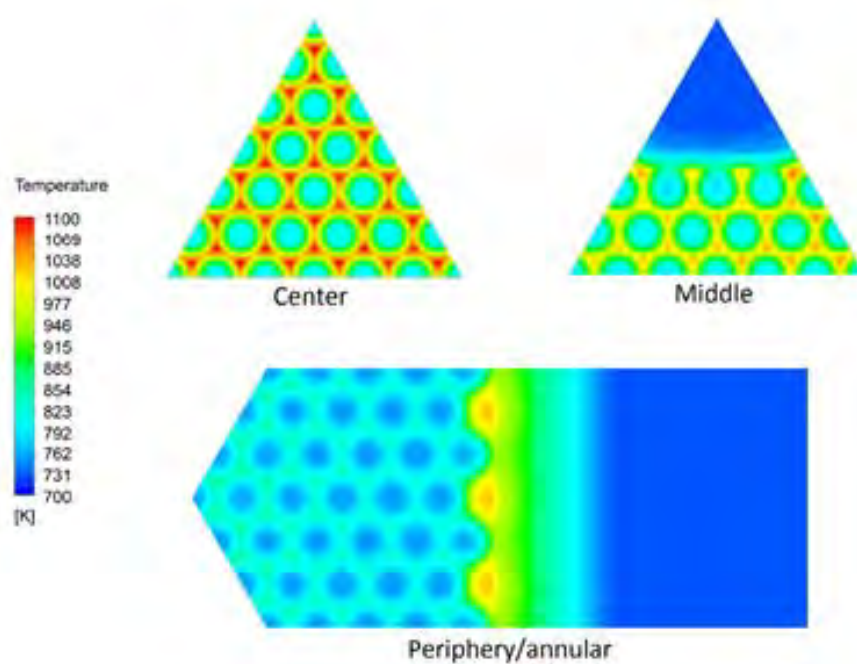


Figure 2.27. Temperature Distributions from CFD Analysis with Optimal Coolant Velocities

Table 2.20. Dimensionless Parameters Related to Buoyancy-driven Flow

Parameter	Value
Equivalent Hydraulic Diameter	5.89 mm
Thermal Expansion Coefficient	$65.2 \times 10^{-6} \text{ 1/K}$
Liquid Fuel Inlet Temperature	834 K
Liquid Fuel Outlet Temperature	966 K
Liquid Fuel Volume Averaged Z-Velocity	0.02 mm/s
Ratio of Grashof Number to Reynolds Number, Gr/Re^2	1.2×10^6
Rayleigh Number, Ra	4.4×10^3

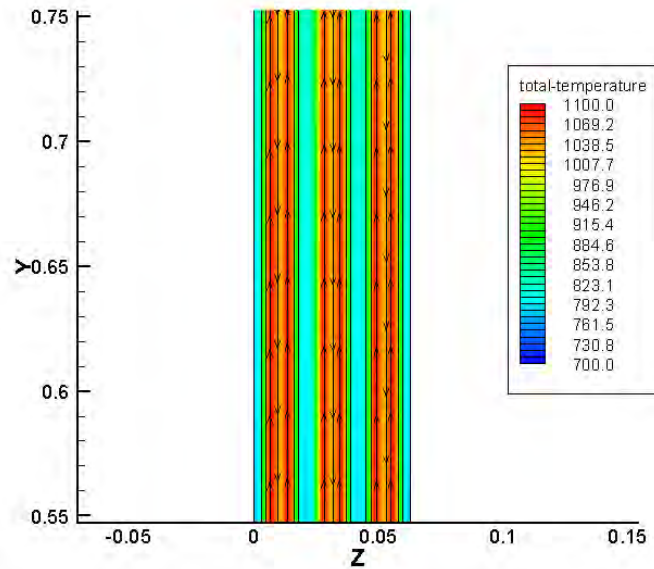


Figure 2.28. Liquid Fuel Flow Pattern at the Core Center Region

To investigate the coolant temperature distribution in the core, whole-core CFD analyses were performed with porous media models. The porosity of the core (i.e., coolant flow area over the whole core area) was about 0.2183. Other parameters such as the coolant velocity and inlet temperature were consistent with those in multi-channel analyses. The temperature increase of coolant was obtained with the core power distribution illustrated in Figure 2.26. Figure 2.29 presents a trimetric view of the coolant temperature of the SLFFR core at a height of 0.95 m above the bottom of fuel. The coolant temperature at the core center, middle, periphery and the annular regions are 826.9K, 811.1K, 791.5K and 723.4K, which agree well with the prediction of the multi-channel analyses.

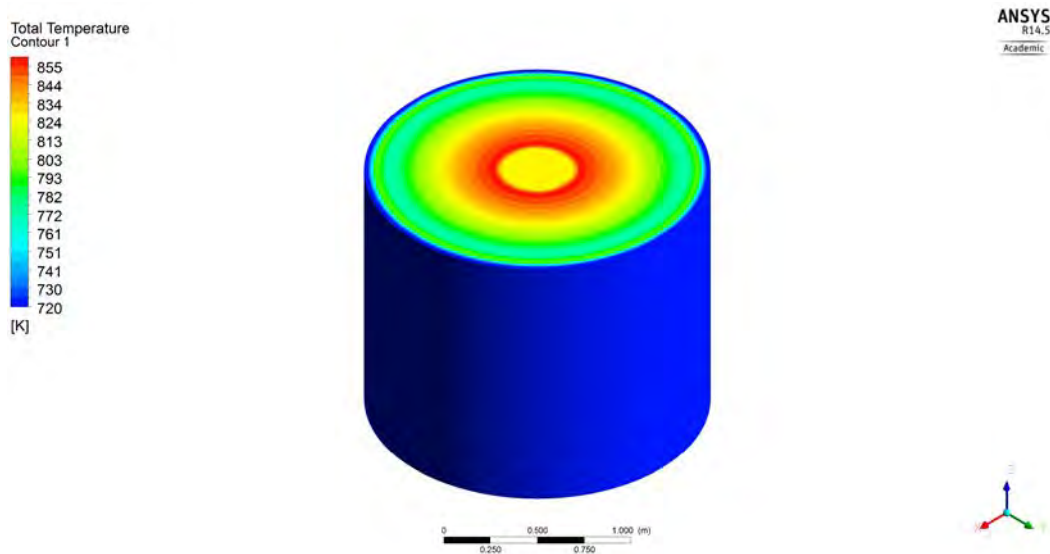


Figure 2.29. Whole-core Coolant Temperature Distribution for Optimal Flow Distribution

The optimal inlet flow velocities of the four flow orifice zones could be achieved by installing proper orifices to the coolant flow paths in such a way that the total pressure drop of each flow zone resulting from the corresponding optimum velocity is equal to that of other zones. In order to achieve the optimal coolant velocities while minimizing the total pressure drop across the fuel tank, the pressure loss coefficients of the orifices of the middle, periphery, and annular zones were determined without employing an orifice for the central zone, where the highest coolant velocity is needed.

By denoting the minor loss coefficient by K , the total pressure loss across the core (i.e., fuel tank) can be written as

$$\Delta P = \left[\frac{f(v)L}{D_h} + K \right] \frac{\rho v^2}{2} + \rho g L \quad (2.12)$$

where ΔP is the total pressure loss in the core, L is the length of the coolant tube, D_h is the equivalent hydraulic diameter of the coolant tube, ρ is the average coolant density and v is the coolant velocity. Depending on the Reynolds number Re defined as

$$Re = \frac{\rho v D_h}{\mu} \quad (2.13)$$

the turbulent friction factor f for a smooth tube may be obtained from the Blasius or McAdams relation as

$$f = \begin{cases} 0.316 Re^{-0.25}, & Re < 30,000 \text{ (Blasius relation)} \\ 0.184 Re^{-0.2}, & 30,000 < Re < 10^6 \text{ (McAdams relation)} \end{cases} \quad (2.14)$$

The minor pressure loss primarily results from flow separation that induces energy dissipation by violent mixing in the separated zones. Since a coolant or CR guide tube is a smooth, straight tube, only the pressure losses due to entrance, exit, and orifice are included in the current model. By representing the pressure loss due to entrance and exit and that due an inlet orifice separately, the pressure loss coefficient K can be written as

$$K = K_a + K_o \quad (2.15)$$

where K_a is the loss coefficient for entrance and exit pressure losses, and K_o is that for orifice pressure loss. The entrance and exit loss coefficients were obtained from Ref. 62; 0.23 for a slightly rounded entrance to a pipe from an inlet plenum and 1.0 for a tube exit to the outlet plenum. The outlet plenum was considered an infinite region compared to the small tube dimension and the outgoing coolant will lose all the kinetic energy at the exit. As a result, a loss coefficient K_a of 1.23 was used for each coolant tube. It was assumed that no orifice would be used for the coolant tubes in the central region, where the highest coolant velocity is needed, and thus the orifice loss coefficient was set to zero. The orifice loss coefficients for the other three flow zones were determined to yield the same pressure drop as the pressure drop in the central region. Table 2.21 presents the pressure loss coefficients and the resulting pressure drops in the four flow orifice zones. The core pressure drops without orifice are estimated from the steady-state single channel thermos-fluidic model with the corresponding inlet flow velocity. The orifice induced pressure drops were determined by the difference between the designed

pressure loss in the core and the core pressure loss without orifice in the steady state. The pressure loss coefficients were evaluated using Eq. (2.12) with the corresponding velocities.

Table 2.21. Pressure Loss Coefficients and Pressure Losses in Four Flow Zones

	Center	Middle	Periphery	Annular
Flow Velocity (m/s)	20.0	15.5	11.0	9.7
Designed Pressure Loss in Core (MPa)	0.609	0.609	0.609	0.609
Core ΔP Without Orifice (MPa)	0.609	0.381	0.205	0.081
Orifice Induced ΔP (MPa)	0	0.228	0.405	0.528
K_a	1.23	1.23	1.23	1.23
K_o	0	2.24	7.91	12.51
K	1.23	3.47	9.13	13.74

2.5.3. Gas Expansion Modules

2.5.3.1. Design of Gas Expansion Modules

The Gas Expansion Modules (GEMs) are employed in the SLFFR design to terminate the unprotected loss of flow (ULOF) accident passively without exceeding the sodium boiling temperature. GEMs were used originally in the Fast Flux Test Facility (FFTF) to enhance the negative reactivity feedback at elevated temperatures during a postulated ULOF accident. The gas region would expand with loss of core inlet pressure and increase neutron leakage. FFTF GEMs consist of a subassembly duct that has been capped at certain distance above the active core. They were placed at the core periphery and had a worth about 17 cents each when the pumps are off. Nine GEMs were loaded and provided a combined negative reactivity worth of about 1.5 \$ on ULOF. [64,65]

In SLFFR design, the reflector consists of twelve segments with a thickness of 27.5 cm. Six GEMs of 5 cm thickness were inserted at the periphery of the SLFFR core by replacing parts of the reflectors. The arrangement of GEMs is shown in Figure 2.21 and Figure 2.30. When the core is operated under a normal condition, the sodium and gas interface is located at the top of the active core where the initial inert gas pressure is balanced with the sodium coolant pressure (i.e., inlet pressure minus the gravitational pressure drop). When the pump is off, the coolant inlet pressure drops dramatically, causing the inert gas to expand until it reaches another pressure balance with the sodium coolant. The final elevation of the sodium and gas interface is determined by both the final coolant inlet pressure and the initial height of inert gas column. There is a possibility for the inert gas to get into the active core through the coolant tubes and introduce a positive reactivity. In order to maximize the negative reactivity insertion and prevent the possibility of the inert gas ingress into the core, the final elevation of the sodium and gas interface is designed to be located between the bottom of active core and the top of grid plate, which is 0.6 m lower than the active core bottom.

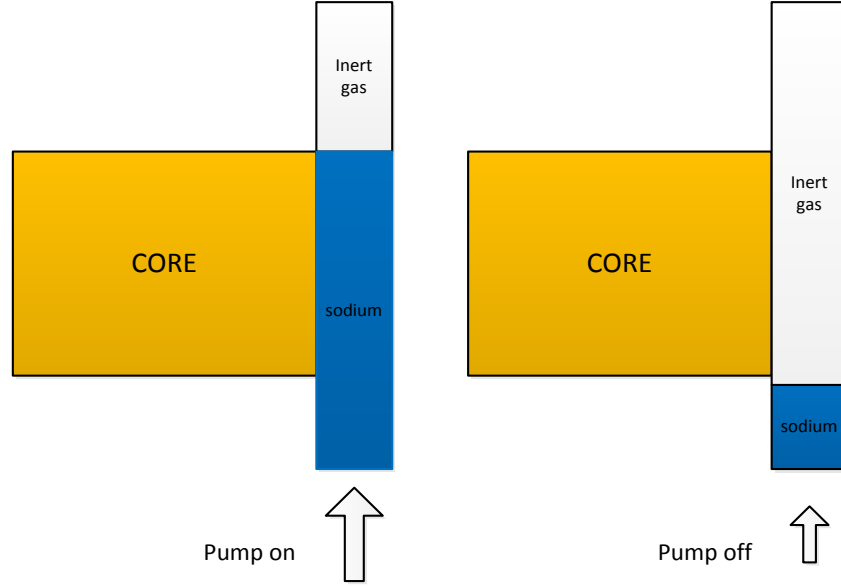


Figure 2.30. Schematic View of the Elevation of Gas and Sodium Interface in GEMs

2.5.3.2. Reactivity Worth of Gas Expansion Modules

The reactivity worth of GEMs was estimated as a function of the sodium column height in GEM. A quasi-static model was used assuming that the inert gas expand or compress adiabatically, an increase in the gas volume is equal to the decrease in liquid volume, and the sodium column height is instantaneously adjusted to the hydrostatic equilibrium with the inlet pressure change. At the entrance (i.e., bottom) of GEM, the sodium pressure is given by

$$P_g(t) + \rho gh(t) = P_{inlet}(t) \quad (2.16)$$

where P_g is the inert gas pressure, $h(t)$ is the height of sodium column from the bottom of GEM, and, is the coolant pressure at the bottom of GEM. Adiabatic expansion of the inert gas can be taken as

$$P_g(t) = P_{g0} \left[\frac{L}{H - h(t)} \right]^\gamma \quad (2.17)$$

where L is the initial height of inert gas column, and H is the total height of GEM and γ is the ratio of the specific heat at constant pressure to that at constant volume for the inert gas. For argon gas, was used. Inserting Eq. (2.17) into Eq. (2.16) yields

$$P_{g0} \left[\frac{L}{H - h(t)} \right]^\gamma + \rho gh(t) = P_{inlet}(t) \quad (2.18)$$

For a given coolant inlet pressure, Eq. (2.18) can be solved for $h(t)$.

Assuming a pump coast-down halving time of 8 seconds and an asymptotic natural circulation flow rate equal to 2% of nominal flow rate, the position of the sodium and inert gas interface was calculated as a function of time for different initial volumes of inert gas when pump is on. Figure 2.31 shows the elevation of the gas and sodium interface from the bottom

of the lower reflector for four different initial inert gas volumes. The elevation of the core bottom is 0.6 m from the bottom of the lower reflector. The final elevation of the sodium and inert gas interface is lower for a larger initial volume of inert gas. It is also found that the elevation of the sodium and inert gas interface is lowering faster as the initial inert gas volume increases. In order to increase the speed of the negative reactivity insertion during ULOF, a larger initial volume of inert gas is preferred. At the same time, to avoid the possibility for the inert gas to get into the core, a sufficient distance needs to be maintained from the bottom of the reflector. So m was selected as the initial height of the inert gas region.

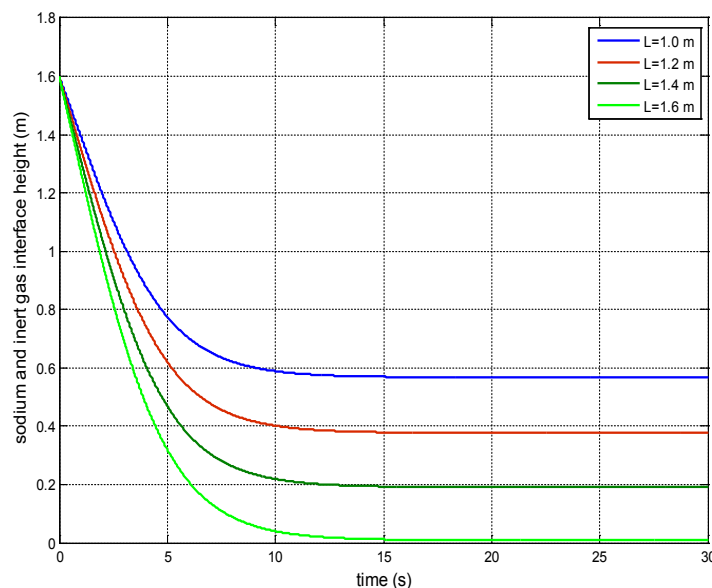


Figure 2.31. Sodium Free Surface Height with Different Initial Gas Volume

The GEM worth at each time point depends on the elevation of the sodium and gas interface at that time point. In order to determine the GEM worth as a function of the elevation of the sodium and gas interface, DIF3D calculations were performed using a theta-r-z geometry model. The GEM worth was determined by direct eigenvalue calculations. Since the k_{eff} changes smoothly with the elevation of the sodium and gas interface, the GEM worth curve was determined by calculating the eigenvalues for five different elevations of the interface. The results are shown in Table 2.22. The maximum GEM worth is -2.28 \$.

Table 2.22. GEM Worth for Different Elevations of Sodium and Gas Interface

Na Surface Height From The Core Bottom (m)	1	0.8	0.6	0.4	0.2	0
	1.00310	1.00310	1.00310	1.00310	1.00310	1.00310
	1.00310	1.00227	1.00079	0.99937	0.99863	0.99850
Worth (pcm)	0	-82	-230	-372	-446	-459
worth (\$)	0.00	-0.41	-1.14	-1.84	-2.21	-2.28

Figure 2.32 shows the GEM worth curve. The reactivity introduced by the GEMs as a function of the elevation of the sodium and gas interface was fitted into a fourth order polynomial as

$$\rho_{GEMs}(h) = -5.0215h^4 + 5.3606h^3 + 2.264h^2 - 0.3266h - 2.28 \quad (2.19)$$

Eq. (2.19) is used for the GEM reactivity calculation in the safety analysis code, which is discussed in detail in Appendix A. The performance of the GEMs for ULOF accident is discussed in Chapter 5.

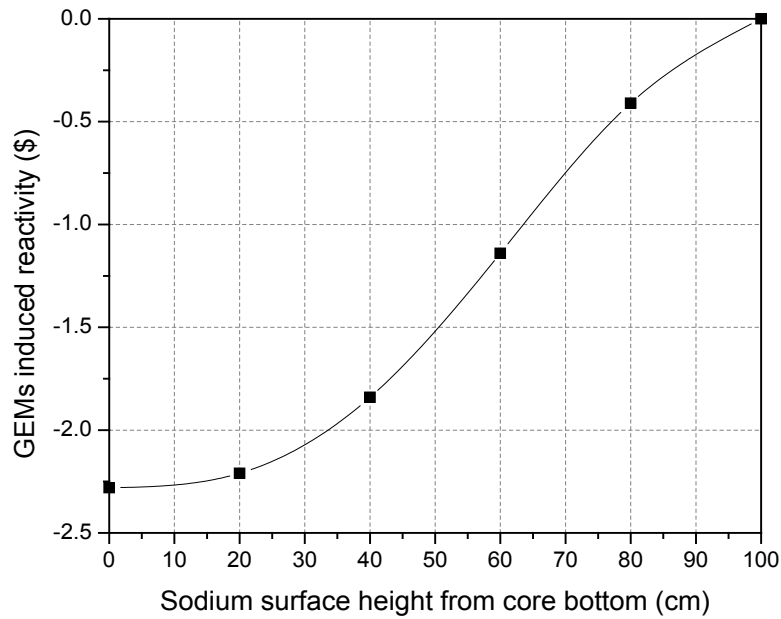


Figure 2.32. GEM Worth versus Elevation of Sodium and Gas Interface

3. Overall Plant Design Description

3.1. Reactor Enclosure System

3.1.1. Reactor Vessel Assembly

The reactor vessel assembly is comprised of the reactor vessel, the top closure head (or deck), the guard vessel, the vessel/deck support structure, the core support structure, the fuel container, the core barrel, thermal barriers, shielding, in-vessel sodium piping, and other permanent internal structures. The design is based on the experience with the reactor vessels used for the Fast Flux Test Facility (FFTF) and the Large Scale Prototype Breeder Reactor (LSPB) LMR reactor plants. A major difference, however, is that the design concept shown here separates the reactor and guard vessels and also employs a conical ring support structure that avoids the need for welding dissimilar metals. There are no penetrations in the reactor vessel; all equipment – piping, instrumentation, fuel handling equipment, and other components – penetrate the top closure head, or deck. The entire reactor vessel assembly is located in a steel-lined concrete cavity in the reactor containment building. The top of the reactor vessel deck is approximately at grade level. There is an inert gas (argon) blanket between the reactor vessel deck and the bulk sodium free surface. The design of the reactor vessel assembly incorporates appropriate measures and details that will facilitate fabrication, construction, and operational maintenance. Figure 3.1 shows the arrangement of the components of the reactor vessel assembly, and Figure 3.2 shows the planar view of the primary and secondary systems.

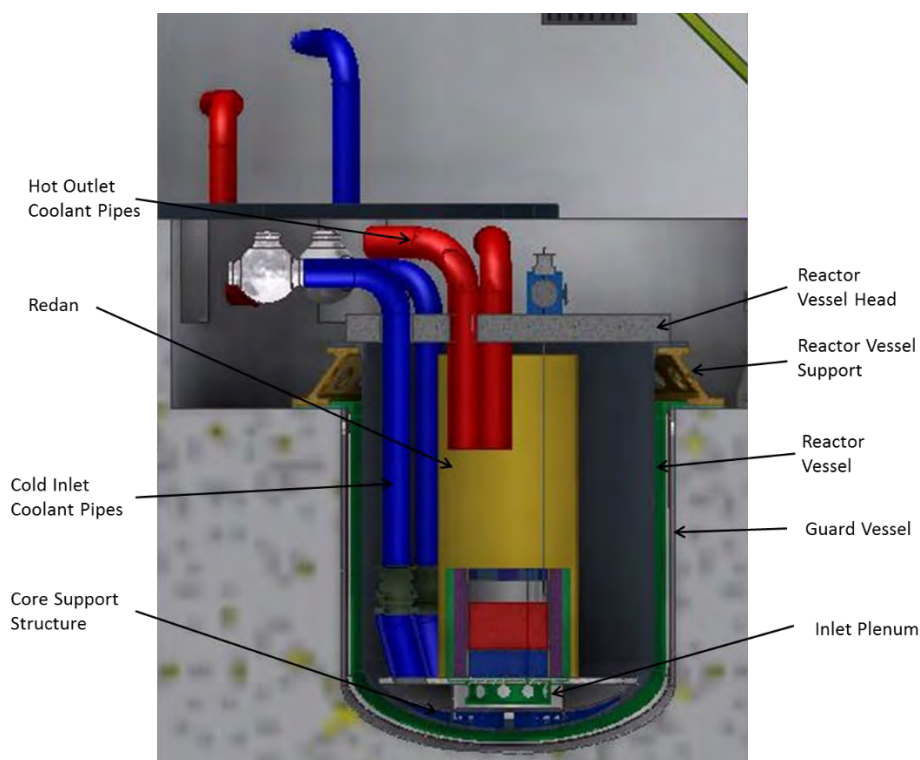


Figure 3.1. SLFFR-1000 Reactor Vessel Assembly

The reactor vessel assembly is designed to:

- Provide a very high level of reliability of primary sodium containment.
- Provide support for the reactor core, reactor vessel internals, and certain components of the fuel handling system.
- Accommodate high static loads at design temperatures.
- Accommodate loads from design basis natural hazards.
- Accommodate loads from design basis accidents, including dynamic loads and thermal transients.
- Ensure symmetrical radial thermal expansion of the reactor vessel assembly about its vertical center axis.
- Provide reliable positioning of supported components.

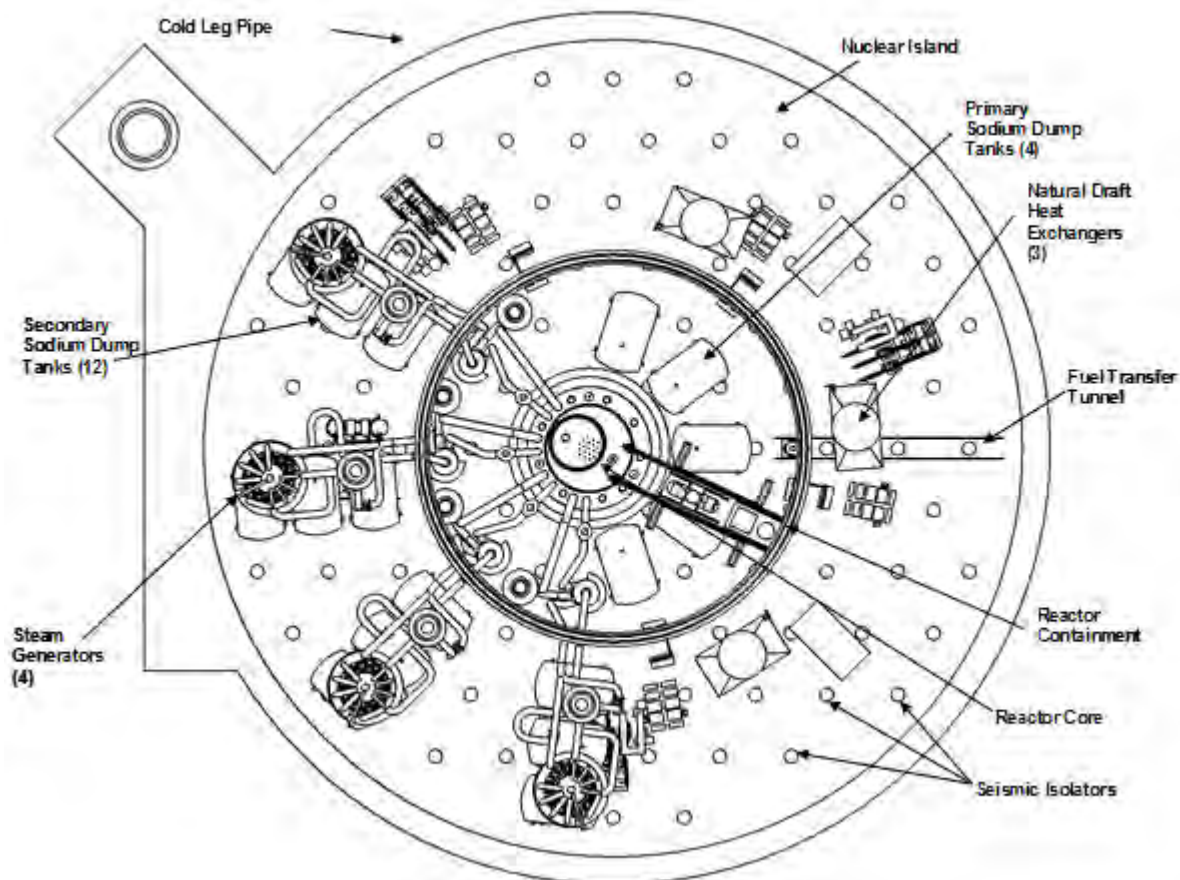


Figure 3.2. Plan View of Primary and Secondary Systems

3.1.2. Reactor Vessel

The reactor vessel is constructed of austenitic stainless steel, Type 304 or Type 316. The cylindrical shell and bottom head have an inside diameter of 6.35 m and a thickness of 2 inches (5.08 cm) for both the cylindrical shell and the toro-spherical bottom head¹. The overall height of the reactor vessel is 8.5 m. The reactor vessel is suspended at its top flange on the conical support ring (frustum) that also provides support for the reactor vessel (RV) deck. The use of bolting to attach the RV and the deck to the support frustum avoids the necessity of using bi-metallic welds to join the vessel and support.

The height of the reactor vessel is established from the core height to keep the core covered during refueling, and in the event of a leak in the reactor vessel that would drain the primary sodium into the guard vessel, resulting in a drop in the sodium level. This sodium level is called the “faulted” primary sodium level. The diameter of the reactor vessel is established from the core diameter, and the inlet and outlet piping.

The reactor vessel will be designed in accordance with the requirements of the ASME B&PV Code, Section III, Division 1, Subsection NB-Class 1, Seismic Category I.² In addition to the dead loads of the weight of the primary sodium, and all loads from the deck and core support structure, the design will meet the ASME Code requirements for normal and transient thermal loads, and for loads and displacements resulting from design basis earthquakes.

3.1.3. Reactor Vessel Top Enclosure Head (Deck)

The reactor vessel top enclosure (referred to as the deck), forms the top head of the reactor vessel. The major functions of the deck are: (1) to provide the upper boundary for the primary sodium coolant and cover gas and (2) to provide structural support for all of the equipment penetrating the top of the reactor vessel. In turn, the deck transfers the weight of the reactor vessel and deck and all of their contents to the vessel/deck support, and then to the reactor cavity concrete structure. It also provides thermal and radiation shielding. Thus, the structural integrity of the deck is an important element of the overall safety of the reactor design.

The design goals and functions for the deck are:

- To accommodate all dead loads, including the weight of the deck and all supported equipment.
- To provide a high degree of structural redundancy.
- To provide a high level of structural stiffness, such that vertical deflections of equipment are acceptably low.

¹ A toro-spherical head consists of a toroidal transition piece connected to a spherical bottom shell. This unit is then attached to the reactor vessel vertical walls. A toro-spherical head is shallower than a spherical bottom head and thus reduces the overall height depth of the reactor vessel.

² If it should happen that, under certain accident or upset conditions, the temperature of some regions of the reactor vessel exceeds 800 °F, the vessel will need to be designed to meet the requirements of Subsection NH of the ASME B&PV Code, Section III. This may also lead to a decision to change the vessel material to Type 316 SST.

- To provide a leak-tight barrier between the primary sodium cover gas in the reactor vessel and the operating floor of the Reactor Containment Building.
- To provide adequate biological shielding to allow personnel access to the area above the reactor vessel deck structure.
- To provide for the effects of the Design Basis Earthquakes, for both horizontally and vertically applied loads.
- To accommodate thermal stresses and displacements resulting from the very large temperature drop across the deck.
- To provide thermal shielding between the top of the sodium cover gas and the deck structure.
- To provide a structure that is feasible to fabricate onsite, and a design that allows reasonable access for in-service inspection (ISI) during the life of the plant.

The design concept selected for this loop plant design is a welded stressed-skin, box type structure although the details are not shown. It is a concept used on SuperPhenix and for some U.S. plant studies performed several years ago. The box-beam concept selected for this loop plant has several very desirable attributes:

- The box beam structure is highly redundant, i.e., failure of a local structural element does not lead to failure or collapse of the deck. In one study done by the General Electric Company (GE) [53], they used this concept and found that analysis showed that complete failure of the bottom plate (or “skin”) would not lead to collapse of the deck.
- Adequate stiffness is achieved with modest stress levels without resorting to massive structures that would be difficult to fabricate and erect.
- The design has considerable margin to accommodate accident conditions, such as abnormal cover gas pressures and loss of deck cooling.
- The concept is compatible with a simple conical support skirt that can accommodate both applied seismic loads and differences in temperature between the deck and the reactor building steel-lined walls.
- The design can accommodate the use of gas cooling in the interior of the deck structure.
- The design can accommodate access to important structural elements for in-service inspection (ISI) and maintenance.
- The design concept provides considerable flexibility in the arrangement of reactor components located on the deck.
- It appears that the concept has excellent potential for extrapolation to larger sizes required for large liquid metal reactor (LMR) plants.

The current reactor vessel deck has an outer diameter of 7.01 m and a depth of ~1 m. The material for the deck is SA-516 Grade 70 carbon steel. It is constructed of steel plates, rings, and penetration cylinders, all welded together to form a conservatively designed, highly

redundant structure, that supports all applied loads (including seismic loads) with very small deflections. With the exception of the central cylindrical ring, all of the steel plates and rings are 1.5 inches (3.81 cm) thick to avoid the need for onsite stress relieving. The central ring is 6 inches (15.2 cm) thick. The space inside the box structure is divided into many chambers by ribs (vertical plates) that connect the top and bottom plates and the inner, outer rings (see Figure 3.3). Under the imposed loadings, the ribs will take mainly the shear forces, whereas the top and bottom plates are designed to take the bending moments. Allowable stress levels will be those taken from the ASME B&PV Code, Section III, Division 1, Subsection NB (as applicable).

There are three major penetrations between the inner and outer rings. In addition, there are several other small penetrations (not shown) for instrumentation, sodium purification piping, and other uses. The three major penetrations provide support for the direct reactor auxiliary cooling system (DRACS) heat exchangers. The ribs are discontinued when they intersect with the penetrations. The chambers will be filled with 3/8 inch (0.95 cm) steel balls for radiation shielding. To provide thermal shielding, a stack consisting of twelve horizontal 1/4 inch (0.64 cm) steel plates, with a gap of 0.87 inch (2.21 cm) between adjacent plates, is hung from the deck bottom plate. In addition, on the top plate, there are several layers of thermal insulation to lower the temperature of the top area to allow for personnel access for maintenance and operations.

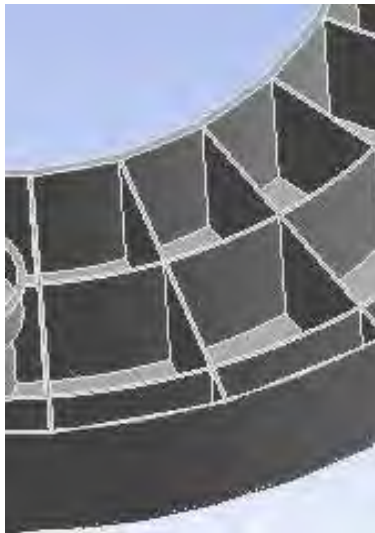


Figure 3.3. Example of Reactor Vessel Deck Cross-Section and Box Structure

3.1.4. Reactor Vessel and Deck Support Structure

The current design of the reactor vessel and deck support structure is a conical frustum made of carbon steel, SA-516 Grade 70 (see Figure 3.4). This structure provides support for the reactor vessel, its internals, and the reactor deck. The conical shell (frustum) has top and bottom flanges of 21 inches (533.4 mm) in width and 6 inches (152.4 mm) in thickness. The thickness of the conical shell is 4 inches (101.6 mm). The top flange provides the bearing surface for the reactor vessel and deck, and the bottom flange provides the bearing surface for transferring the loads to the reactor cavity concrete structure. If necessary, Lubrite® sliding plates will be inserted between the RV flange and deck support flange.

The use of a bolted joint and common conical support skirt for the reactor vessel and deck at the deck-vessel interface avoids the need for a bi-metallic structural weld between these components. It is recognized that this bolted joint and conical ring presents special alignment and erection problems. An almost identical design was employed in an ANL study for a 1000 MWe LMR plant conducted in 1982 [54]. In a detailed review of that design concept, the Chicago Bridge and Iron Company (CB&I), a highly qualified fabricator of nuclear vessels, concluded that not only was the design feasible, but that it represented an improvement over many of the alternative approaches for the vessel/deck support. CB&I stated that the fully machined support ring could be set into place with a single lift, aligned, leveled, and completed without the problems associated with in-containment welding, scaffolding, and temporary supports.

This conical ring concept has also been proposed in several LMR plant studies performed by GE and others [53]. The present concept for the SLFFR-1000 goes one-step further. Rather than placing the bolting inside of the deck structure as used in previous designs, the concept presented here incorporates reinforcing gusset assemblies welded to the outer ring surface of the deck and bolted to the top flange of the conical ring, thus allowing greatly improved access to all of the bolting. This not only facilitates construction but also benefits ISI and maintenance activities over the life of the plant. The gussets also provide positive structural resistance for seismic loads imposed on the support ring. An additional benefit obtains from the fact that by extending the outer diameter of the conical support ring, it is possible to support the ring, and all of its loads, directly on the reinforced concrete cavity wall without the need for the special heavy steel inserts used on some of the previous LMR design studies. There is an inert gas (argon) blanket between the reactor vessel cover and the bulk sodium free surface.

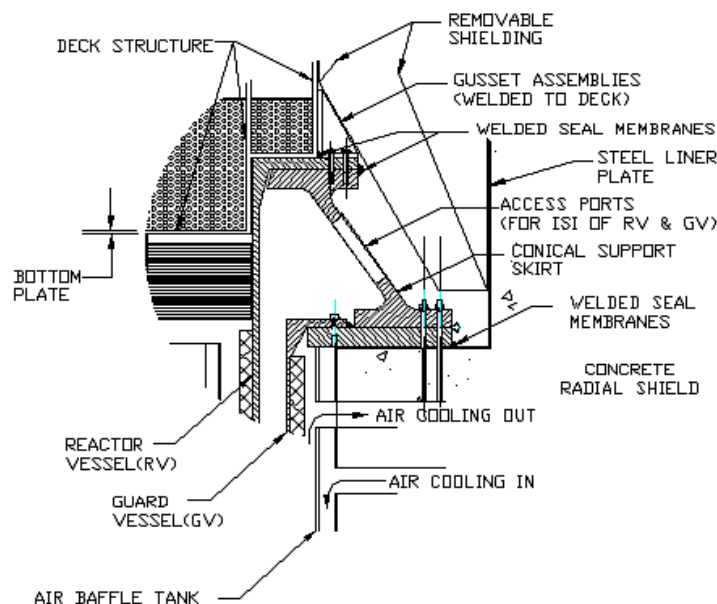


Figure 3.4. Reactor Vessel/Deck Support Structure

3.1.5. Guard Vessels and Piping

The guard vessel has one major function to contain the primary sodium coolant in the very unlikely event that it should leak from the reactor vessel. No ties, attachments, penetrations, or equipment are permitted on the guard vessel wall; except perhaps for tracks used for remote ISI of the reactor vessel. The diameter of the guard vessel is 6.9 m, and it has a height of 7.44 m. The entire guard vessel is 1 inch (2.54 cm) thick. The guard vessel is supported at its top by a flange bearing on a ledge in the reactor cavity wall. Suitable welded membranes will be used to seal the gas space between the guard and reactor vessels and to seal the joints between the reactor vessels and deck and conical support skirt. The guard vessel is completely independent of the reactor vessel and the deck. The annular gap between the guard vessel and the reactor vessel is 9 inches (22.9 cm) to allow for ISI of both vessels. This gap size results in a feasible size for access of remote viewing equipment, taking into account the need to assure that the faulted sodium level remains above the heat transfer path, and to allow for fabrication and erection tolerances needed in construction. Carbon steel will be used for the guard vessel to permit the use of a magnetic attachment of a remote device used during the ISI of the reactor and guard vessels, and to reduce plant capital cost.

The guard vessel provides the secondary containment for the primary sodium in the very unlikely event that the reactor vessel develop a leak. The guard vessel is sized such that the gap (9 inches) between it and the reactor vessel is:

- Wide enough to accommodate in-service inspection devices.
- Narrow enough to prevent the primary sodium from dropping to an unacceptable level within the reactor vessel if the reactor vessel should develop a leak. The sodium level must remain high enough to keep the integrity of the heat transport path to provide a path for natural convection cooling of the core during a leak in the reactor vessel.

Insulation is provided on the exterior of the guard vessel to reduce the heat lost to the guard vessel cooling system. A guard cooling shroud is provided on the outside of the insulation that forces air to flow around the supporting concrete structure and up over the guard vessel insulation to prevent overheating of the concrete support structure during normal and off-normal conditions.

There is also guard piping around the primary piping and a siphon break to prevent the primary sodium from draining and uncovering the core and heat transfer paths.

3.1.6. Redan

The core barrel and redan assembly is a single integrated unit that provides the internal structure for the reactor core assemblies and provides a barrier between the inlet and outlet sodium plenums. The core barrel is a right circular cylinder fabricated from stainless steel. It is attached to the inlet plenum and lower support structure. It also provides support for the core restraint system. The upper portion of the redan consists of a conical shell and cylindrical shell.

The redan consists of multiple formed plates welded together to form a shell that surrounds coolant outlet pipes and upper internal structure. The redan is supported vertically and seal welded to the core barrel. It is essentially a cylindrical/conical vessel, but without either a top

head or bottom head. The upper internal structure is located within the redan. The redan is one of the permanent structures within the primary reactor vessel (see Figure 3.1).

3.1.7. Upper Internals Structure

The upper internals structure (UIS) is a package of hardware suspended from the rotatable plug to about 3 inches above the core. The functions of the UIS are to:

- Support shroud tubes containing the single control rod driveline;
- Preserve critical alignments between this driveline and the core, under normal and off-normal (including seismic) conditions;
- Route and support instrumentation for monitoring the health of the core;
- Route and support other instrumentation such as loose-parts monitors and delayed-neutron sampling stations;
- Produce sufficient coolant mixing to mitigate thermal transients to downstream components;
- Provide support and alignment for the fuel charge piping and the fuel discharge line.

The outer boundary of the UIS is a shroud (essentially with an outside diameter of the core) with large-hole penetrations over part of its length. The penetrations release the core effluent horizontally to the hot upper plenum from which it travels upward, through the hot leg piping, and then to the inlets of the four IHXs. Within the shroud are twelve control-rod shroud tubes of 4-inch outer diameter. The shroud tubes are perforated for the release of coolant to the hot pool, at an elevation close to the free surface. The radial position of the shroud tubes are fixed by at least three horizontal guide plates, welded to the UIS shroud. The lower guide plate is close to the top of the fuel tank and is perforated to permit about 85% of the core effluent to reach the region between guide plates. The balance either goes up the shroud tubes or leaks through the 3-inch peripheral gap. In the region between guide plates, five loose-parts monitors are located (high-temperature submersible microphones attached to the outside of selected shroud tubes).

The upper guide plate is not perforated except for clearances at the 12 shroud penetrations to permit sliding due to differential thermal expansion. The upper guide plate is located high within the upper internal structure. Thus, almost all of the core effluent is forced to enter the hot upper plenum at least 4 feet below the upper plenum operating level. This should meet the objective of maintaining a quiet entrainment-free surface. If future flow tests reveal an undesirable degree of surface agitation, the upper guide plate can be dished, concave downward, to suppress further any upward flow vectors of sodium leaving the UIS.

The outlet sodium temperatures of core coolant channels are monitored by chromel-alumel, stainless steel sheathed, ungrounded thermocouples. These thermocouples are replaceable and installed in helium-filled wells. The thermocouple wells are positioned 3 inches above the centerline of core coolant channels.

3.1.8. Lower Internals Structure

The lower internals structure (LIS) consists of the fuel container, core barrel, core grid, and the inlet plenum structure (see Figure 3.5). The lower internals structure supports the core canister, the reflector, the radial shielding, the four sodium inlet pipes, and various shields, brackets and baffles. It is designed to withstand seismic events with acceptable stresses and deflections. The LIS contains the flow distribution system of inlet coolant that controls the rate of flow of the sodium coolant into the core canisters.

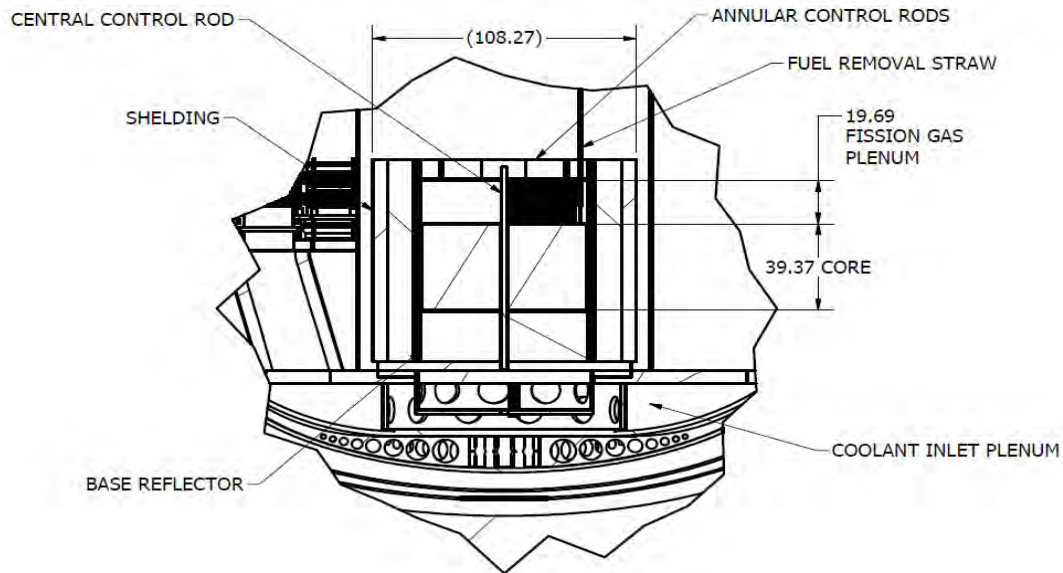


Figure 3.5. SLFFR Lower Internal Structure

3.1.9. Core Support Structure

The core support structure, shown in Figure 3.1 and Figure 3.5, provides support for the lower internals structure, the fuel container, the core barrel assembly, the primary sodium inlet pipes, brackets, and baffles. It is designed to the requirements of the ASME B&PV Code, Section III, Division 1, Subsection NG, Core Support Structures. The core support structure consists of a steel web structure supported on ribs formed to the contours of the bottom head of the reactor vessel, welded to the bottom head, and thus, becomes an integral part of the reactor vessel. Except for the bottom head of the reactor vessel, all the components of the core support structure are under compression. Therefore, there is no need for performing ISI on these components. The part of the core support structure that is in tension is that portion of the bottom head of the reactor vessel that is integral with the support structure. Welds in the bottom head of the reactor vessel near the core structure are subject to ISI during the life of the plant.

3.1.10. Reactor Containment Boundary

The loop SLFFR primary containment boundary is comprised of the reactor vessel, primary hot and cold leg piping, primary pump tank, reactor vessel enclosure, the tubes in the intermediate heat exchanger and in the direct reactor auxiliary cooling system (DRACS) heat

exchanger, and the sodium purification piping and components. These components maintain the containment for the primary radioactive sodium and form the first containment boundary. This initial boundary also includes the instrument thimbles and the cover gas piping system. If this first boundary is breached, then the next secondary confinement is composed of the following components: the reactor guard vessel, the primary sodium guard piping, the reactor containment, the intermediate sodium piping and steam generators, the direct reactor auxiliary cooling system intermediate piping and systems, the stainless steel-lined compartments around the reactor vessel support, the pump tank guard vessel, the IHX cell, the purification system cell confinement, and the reactor building that is maintained at a negative pressure with high efficiency particulate air (HEPA) filtered ventilation. If there is a breach in a thimble or cover gas system, the gas operates at a slightly higher pressure than the sodium, and therefore there will be no release of sodium to the environment. The reactor building always operates at a negative pressure compared to the outside environment. All effluents are filtered via HEPA filters before they are released into the environment. All of the primary radioactive sodium is located within the reactor building.

3.2. Primary Heat Transport System

3.2.1. System Requirements and Description

The basic function of the Primary Heat Transport System (PHTS) is to transport heat from the reactor to the intermediate heat transport system (IHTS) under normal and off-normal operating conditions. The arrangement of the PHTS is shown in Figure 3.2.

The PHTS consists of four primary pumps, four intermediate heat exchangers (IHXs), associated hot-leg and cold-leg piping, and expansion joints between the inlet piping and the inlet plenum header of the reactor. The four pumps and four IHXs are located outside the reactor vessel in separate, inerted shielding cells. The four pumps are located in the cold leg of the primary circuit in pump tanks and lined cells. Each of the four IHXs is located between the hot leg and cold leg piping in lined, inerted, and shielded cells. The PHTS piping runs are contained in shielded steel-lined concrete tunnels or conduits and have separate guard pipes surrounding the main sodium pipe to mitigate the effects of any sodium leakage. The hot primary sodium enters the IHX inlet through a nozzle at the top of the IHX shell, and the cooled sodium is discharged to the cold piping at the bottom of the IHX. The sodium enters the IHX approximately 12 inches below the upper tube sheet to reduce the amount of thermal stress on the tube sheet. A baffle plate is located just above the inlet of the IHX to maintain this static layer of sodium. The tube sheet is the thickest part of the IHX and thus minimizing the temperature transients on this part increases the longevity of the IHX.

A total sodium flow of ~7910 kg/sec removes the heat from the core and passes into the upper plenum at an average temperature of 550 °C. The core effluent mixes with the hot sodium in the outlet plenum and flows up and over into four IHXs. Approximately 250 MWt of heat is transferred from the primary to the secondary coolant in each IHX. The primary sodium leaves the IHX at 450°C and enters the cold loop piping to the inlets of the four primary pumps. Four pumps take the sodium from the cold loop and discharge it through discharge cold leg piping to the inlet plenum below the reactor core.

The PHTS must satisfy all normal and off-normal conditions specified in the duty cycle for the plant. In addition to full power 4-loop operation, the PHTS must provide heat removal for 50% power operation when only one IHTS loop is available or 75% when one primary pump is out-of-service. The system, along with the core and the IHX, is arranged to remove decay heat under natural circulation conditions. Maintainability and inspectability are important considerations in the design of the PHTS.

3.2.2. Primary Sodium Mechanical Pump

Mechanical centrifugal pumps can be adopted for the SLFFR. In the SLFFR design, the location of the suction of the primary pump is critical to ensure sodium circulation under a variety of operating conditions. Although there are many different types of mechanical pumps, only centrifugal pumps have been used in sodium cooled fast reactors and therefore are considered as the primary candidate. Only mechanical pumps are discussed in this section.

The mechanical pump was designed using a series of nomographs developed by Byron Jackson [55]. In the first nomograph, the specific speed and rotation speed are determined. In the second nomograph, the required power is determined. Then, in the third nomograph, the shaft diameter is determined. In the fourth nomograph, the pump case diameter, which is related to the impeller diameter, is determined. In the fifth nomograph, the size of the pump outer barrel is determined for the loop type configuration. Finally, in the sixth nomograph, the suction and discharge nozzle diameters are determined. This procedure estimates only the diameter of the pump. The length of the pump can be estimated from other considerations, namely the submergence depth should be greater than 0.9-1.2 m to prevent vortexing [56]. The resulting design parameters are summarized in Table 3.1.

Table 3.1. Mechanical Pump Design Parameters

Flow Rate, m ³ /min	140
Pump Head, m	84
Power, kW	2908
NPSH, m	14
Pump Length, m	6.3
Pump Case Diameter, m	1.78
Suction Nozzle Diameter, m	1.17
Impeller Diameter, m	1.35

3.2.3. Intermediate Heat Exchanger

The Intermediate Heat Exchangers (IHXs) transfer heat from the radioactive sodium coolant in the primary heat transport system to the nonradioactive sodium coolant in the intermediate heat transport system. Four sodium-to-sodium heat exchangers rated at 250 MWt each are used to transfer the 1000 MWt core power at full-power conditions corresponding to core inlet and outlet temperatures of 450 °C and 550 °C, respectively. The IHXs are located in shielded and inerted cells.

The heat exchanger arrangement selected is a shell-and-tube counter-current flow arrangement with the primary flow on the shell-side, and secondary sodium flow on the tube side. Major features of these heat exchangers are discussed in this section while key design information is provided in Table 3.2. The tube-side secondary flow was selected to simplify cleaning of the heat exchanger tubes in the event of a tube leak in a steam generator. Moreover, this configuration maximizes the ability of the IHX to accommodate any pressure transients that may arise if a steam generator tube rupture event were to occur since for a given tube wall thickness, the tubing is much stronger in tension (internal pressure source) versus compression (external pressure source).

Table 3.2. Intermediate Heat Exchanger Design Parameters (rough estimate)

Parameter	Value
Heat Transfer Capacity	250 MWt
Design	Straight tube, counter-flow
Heat Transfer Area	1067 m ²
Primary Sodium Temperature Inlet	550 °C
Primary Sodium Temperature Outlet	450 °C
Primary Sodium Mass Flow Rate	~1977.5 kg/s
Secondary Sodium Temperature Outlet	428 °C
Secondary Sodium Temperature Inlet	373 °C
Secondary Side Sodium Mass Flow Rate	~1977.5 kg/s
Tube Outer Diameter	1.59 cm
Tube Wall Thickness	0.889 mm
Tube Pitch	2.23 cm
Active Tube Length	3.72 m
Number of Tubes	6085
Shell Height	6.48 m
Shell Outside Diameter	1.86 m
Shell Thickness	1.9 cm
Shell Cross-sectional Area	2.6 m ²
Tube Material	9Cr-1Mo

The installation of the IHXs is illustrated in Figure 3.6. Each unit is vertically suspended within a lined cell. Primary sodium enters the shell side of each IHX approximately 20 cm below the upper tube sheet. The introduction of the sodium below the upper tube sheet minimizes the thermal shock to this relatively thick component during transients. The sodium then flows downward through the shell and vents through a 10 cm wide gap around the lower tube sheet that leads to the single 61 cm diameter exit nozzle that discharges directly into the cold leg piping.

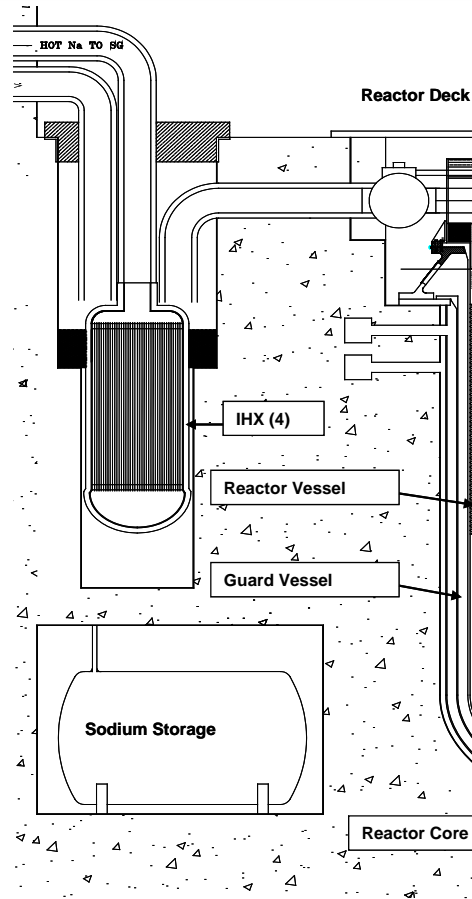


Figure 3.6. Illustration of IHX in Shielded Cell

The shell side of the IHX includes a series of horizontally mounted, disk and donut-type baffle plates uniformly spaced at 91 cm intervals along the length of the tube bank. Aside from providing lateral support for the tubes, these plates promote cross-flow and mixing that enhance thermal performance on the shell (primary) side. The plates are made from 6.4 mm steel plate, and they occlude 50% of the vertical flow path at each plate location. The plates are orificed (45% equivalent porosity) to reduce flow pressure drop; a schematic showing the orifice design is provided in Figure 3.7.

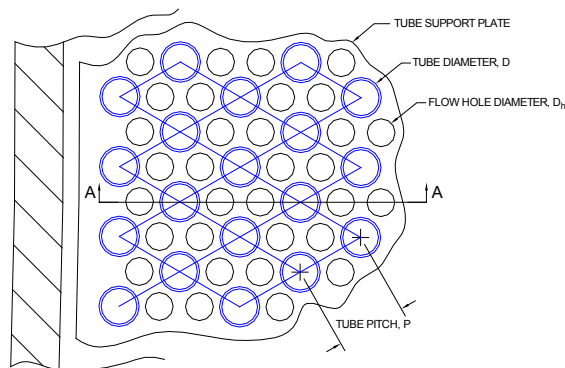


Figure 3.7. Plan View of Orifice Baffle Plate Design

Cold intermediate sodium enters the IHX through a central 61 cm diameter downcomer. The downcomer delivers the cold sodium through the lower tube sheet into a header manifold, where it then turns 180° and rises through the tube bank in counter current flow to the shell side primary sodium. The hot intermediate sodium exits the tubes into an upper header manifold, and then flows through an annular riser that is concentric to the downcomer. The downcomer is double walled with an annular gap for thermal insulation between the hot and cold streams. Both the downcomer and the 87 cm OD annular riser pipes are equipped with bellows just above the shroud to accommodate any differences in thermal expansion between the piping and the body of the IHX itself (each unit is rigidly attached to the removable plug in the reactor vessel head). The upper tube sheet is welded to the shroud, while the lower tube sheet floats. Thus, the design accommodates differential thermal expansion within the tube bank also.

Modified 9Cr-1Mo steel was chosen as the material of construction primarily because the thermal conductivity is higher than that of the austenitic steels such as Type 304 stainless steel. Since the heat transfer in sodium-to-sodium heat exchangers can be dominated by the tube wall thermal resistance, using modified 9Cr-1Mo steel results in considerable reduction in the required heat transfer area. The use of Type 304 stainless steel tubes would result in the need for as much as 20% more heat transfer area as compared to modified 9Cr-1Mo tubes with the same design characteristics. In addition, modified 9Cr-1Mo has a lower thermal expansion coefficient compared to Type 304 stainless steel. The higher thermal conductivity material results in lower temperature differences in component sections and, coupled with the reduced thermal expansion, results in lower thermal stresses in structural members. This is advantageous during thermal transients.

Straight tubes are selected to simplify fabrication and reduce flow-induced vibration problems. The design of the IHX has been selected such that the primary flow of sodium on the shell side provides a low pressure drop. The low pressure drop on the primary side is important from two viewpoints: 1) minimizing the pressure-related structural requirements for the IHX shell, and 2) promoting the ability to establish natural circulation of the primary sodium in the case of a loss-of-flow event. Adequate natural convection flow for shutdown heat removal is essential. One key element of the DRACS shutdown heat removal system relies on natural circulation of the primary sodium through the core and IHX to the sodium pool surrounding the core barrel.

3.2.4. Primary Heat Transport System (PHTS) Piping

The PHTS piping consists primarily of the main system hot and cold legs that make the necessary connections between the reactor, primary pumps, and the IHXs. The PHTS hot leg piping connects the primary sodium outlet from the reactor to the primary sodium inlet near the top of the IHX. The PHTS cold leg piping consists of two segments. The first segment connects the discharge side of the IHX to the inlet of the primary pump tank. The second segment connects the discharge from the primary pump tank to the reactor inlet nozzle and on down to the doughnut-shaped manifold, or torus, and associated piping, that encircles the inlet coolant plenum (header) which then directs the sodium flow into the reactor core. Each primary piping assembly (segment) is supported to take the appropriate mechanical, thermal and hydraulic loads.

The PHTS piping is constructed from 71 cm OD, 1.59 cm thick-walled (28 inch schedule 30) and 61 cm OD, 1.74 cm thick-walled (24 inch schedule 40) 316 stainless steel piping, primarily because its proven compatibility with sodium, lack of any issues with corrosion, and the ease of fabrication with this material. The use of this piping diameter and schedule maintains the sodium flow velocity through the primary piping system below ~ 7 m/sec, which is a rule-of-thumb design criterion for these types of systems. The use of 316 stainless steel requires dissimilar metal welds connecting the austenitic Type 316 stainless steel to the ferritic steels used in the IHX. The welding technology for joining these dissimilar metals is well established.

The PHTS piping is enclosed in secondary (guard) piping so that in the unlikely event of failure of the main system piping, the sodium is contained, which greatly reduces the possibility of a major sodium leak. All of the primary sodium system piping is located within shielded concrete steel-lined tunnels or conduits. Suitable access to these tunnels is provided to facilitate ISI operations.

3.3. Intermediate Heat Transport System

The intermediate heat transport system provides an isolation coolant circuit between the primary reactor coolant and the steam generator system. This intermediate circuit prevents leaks in the steam generator from directly influencing the reactor. The intermediate heat transport system consists of the intermediate sodium pump, the intermediate piping, the steam generator, and the auxiliary sodium systems.

3.3.1. System Requirements and Description

The Intermediate Heat Transport System (IHTS) circulates secondary (non-radioactive) sodium coolant, transporting heat from the radioactive sodium in the Primary Heat Transport System (PHTS) to the power generation system. Currently, the Rankine steam cycle is the reference power conversion system for the SLFFR. The IHTS is composed of four completely independent loops, as shown in Figure 3.8. This figure provides an isometric view of the piping runs to the steam generators. The flow rate through all four loops is controlled to maintain the primary sodium coolant temperature at design operation conditions. With the exception of the short pipe runs of the hot and cold sodium piping connected to the IHX and running from the IHX to the steam generators, the entire IHTS is contained within the steam generator facility that is part of the reactor building.

The secondary sodium exits the upper portion of the IHX after being heated to 528°C. The sodium then exits the reactor containment and traverses the short distance to the adjacent steam generator compartment that is on the nuclear island. Here, the hot sodium enters the top of the steam generator and transfers heat to the steam before exiting at the bottom of these units. After exiting, the secondary sodium circulates to the intermediate pump where it is pumped back to the reactor containment and tube side of the IHX.

The tube walls of the IHX constitute the principal barrier for isolation of the activated primary sodium from the sodium in the secondary system. In the unlikely event of an IHX tube leak, sodium leakage will occur from the IHTS to the PHTS because the secondary system is maintained at a pressure of at least 0.6 bar (8.5 psig) in excess of the primary system. The excess pressure is due to sodium hydrostatic head that is provided by the higher elevation of the secondary loop relative to the primary loop (see Figure 3.8). Radiation detectors on the outlet

(hot leg) piping from the IHX monitor for indications of contamination of the secondary loop sodium.

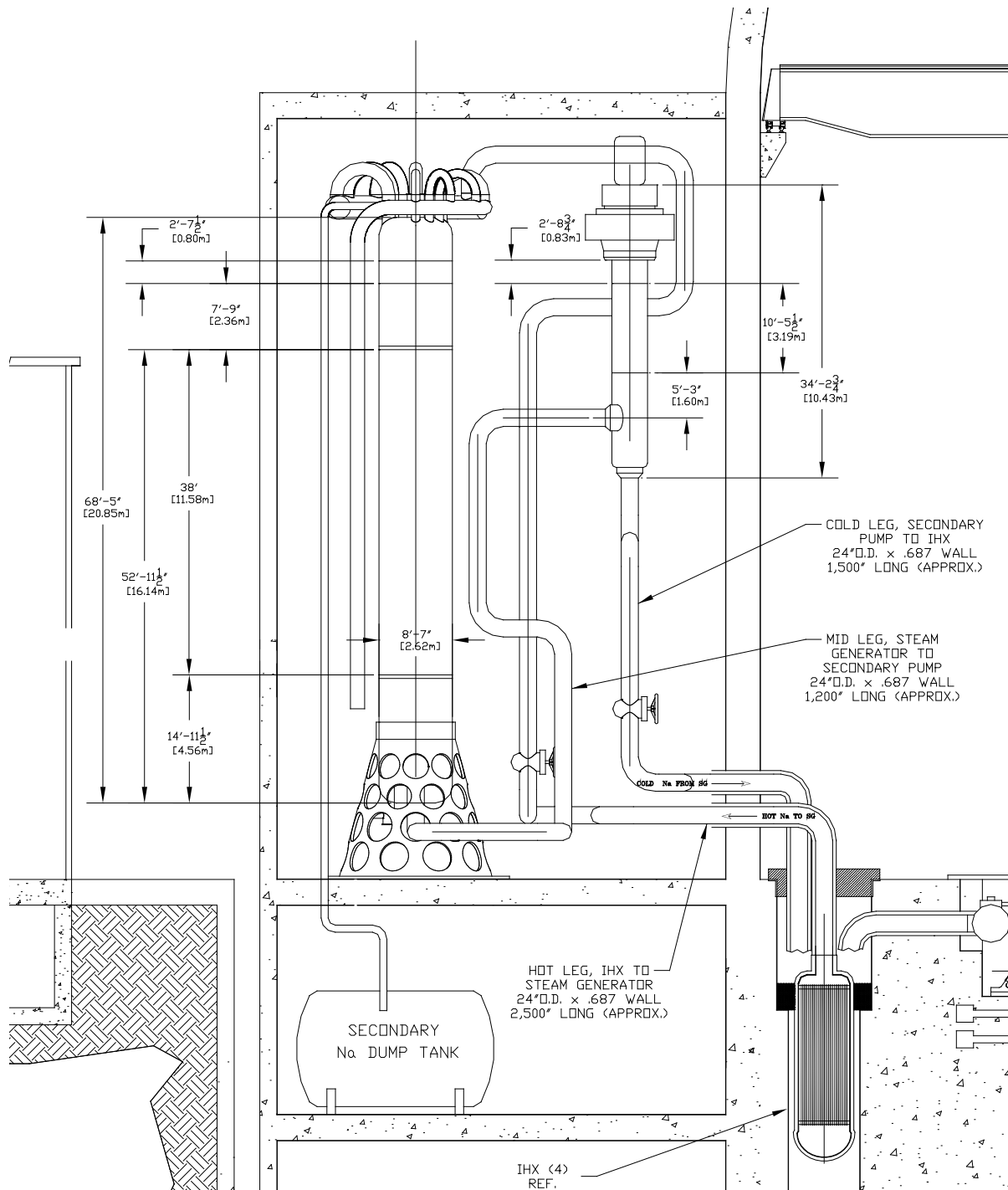


Figure 3.8. Illustration of IHTS Layout

Major components in each of the four loops include the mechanical pump, steam generator, sodium storage tank, and the piping connecting these components to each as well as the IHX and steam generator. Auxiliary systems that connect to the IHTS main loop, which are

necessary to achieve operational requirements, include a circulating sodium purification system, trace heating, thermal insulation, and instrumentation that monitors key system parameters including flow rate (with a permanently installed magnetic flowmeter in each cold leg) and temperature differential across the IHTS (with thermocouples installed at the steam generator inlet and outlet legs).

3.3.2. Intermediate Sodium Pump

One sodium pump is used in each IHTS loop. Each unit is a vertically mounted, single stage, single suction, free surface, centrifugal mechanical pump with a lower radial hydrostatic bearing operating in sodium that is fed from the delivery side of the impeller. The pump shaft rotates in two bearings; the lower being a radial hydrostatic bearing and the upper usually a radial-axial roller bearing or a liquid or grease lubricated sliding bearing. The impeller is usually positioned below the hydrostatic bearing. There is an axial or radial guiding duct. A gas shaft seal is placed below the upper bearing, and a flexible coupling connects the shaft of the pump and its variable speed electric drive. The stationary part of the intermediate sodium pump, consists mainly of a stationary tank, tank cover, internal structural assembly, and casing. The tank cover and all internals are removable. A thermal shield is located just below the tank cover. A pressurized argon cover gas is used between the sodium level in the pump tank and the thermal insulation. The cover gas is controlled at a reasonable pressure to maintain the pump net positive suction head (NPSH) available and to prevent air in-leakage into the system.

As in previous designs, each pump is installed in a tank with the piping inlet and exits at the top and bottom of the tank, respectively. The pumps are completely separate so that the IHTS loops can be operated independently to produce the desired operational characteristics. As noted earlier, the overall pump design is quite similar to the primary mechanical pump (see Section 3.2.2).

3.3.3. IHTS Piping

The IHTS piping consists primarily of the main system hot and cold legs that make the necessary connections between the IHX and the steam generator. The hot leg piping connects to the secondary sodium outlet of the IHX directly to the sodium inlet of the steam generator. The IHTS cold leg piping connects the sodium outlet from the steam generator to the intermediate pump tank inlet and then from the pump tank discharge to the secondary cold sodium inlet to the IHX.

The IHTS piping is constructed from 61 cm OD, 1.74 cm thick-walled (24 inch schedule 40) 316 stainless steel piping; this choice is driven by the same considerations as discussed for the PHTS piping. As with the PHTS piping, the use of 316 stainless steel requires dissimilar metal welds for which the welding technology is well established.

Inside the reactor building, the IHTS piping is enclosed in secondary (guard) piping so that in the unlikely event of failure of the main system piping, the sodium is contained, which greatly reduces the possibility of a major sodium leak. In addition, the steam generator building, containing the IHTS, is seismically isolated on the same platform as the reactor itself, which eliminates differential motions between these two structures during seismic events. This simplifies the design for piping hangers and supports that would otherwise need to be equipped

with snubbers or other motion-dampening devices if the reactor building were not integral to the nuclear island.

3.3.4. IHTS Sodium Storage Tank, Expansion Tank, and Cleanup System

A small secondary loop is included in the IHTS to maintain sodium volume and to provide a purification pathway for the secondary sodium. The loop supplies sodium from a cold trap to the mechanical pump tank to maintain a constant level of sodium in the IHTS loop. The recirculation system uses a fill and overflow approach to maintain the sodium level constant. Spillover into the overflow line of the mechanical pump tank flows through the secondary piping to the storage tank. Sodium is then pumped from the storage tank by a small recirculation pump through interconnecting piping to the cold trap. After circulating through the trap, the sodium circulates back to the pump tank.

The circulating sodium to the storage tank keeps the tank at the system temperature during normal operations. When flow is not available, trace heating is used to keep system components above the sodium freezing point.

Pressurized argon cover gas is maintained in the pump tank upper plenum. Subsystems must also be provided to control the pressure and supply of the argon cover gas.

3.4. Power Generating System

3.4.1. System Requirements and Description

A Rankine steam cycle is the reference power conversion system for SLFFR. This system utilizes heat from the intermediate heat transport system (IHTS) to produce steam. The steam is delivered to the turbine, which drives the electrical generator. This is the same power conversion technology that has been used for all sodium-cooled fast reactors built to date. This technology is well developed and, with the exception of the steam generators and the sodium water reaction pressure relief system (SWRPRS), the system components are largely off-the-shelf items available from commercial vendors. At this point, in the pre-conceptual design process, attention has been focused on the power production side of the system.

Steam generator concepts that have been developed over the years include the double-walled straight tube design that operated successfully for over 30 years for EBR-II, the hockey-stick design that was developed by Rockwell for the SAFR concept, and the helical coil steam generator (HCSG) that was developed by GE for the PRISM Mod-B concept. For the purposes of this pre-conceptual design, a modified version of the HCSG design is adopted, as it is readily scaled to different reactor power levels.

The main components of the steam generation system include four sodium heated steam generators (one for each IHTS loop), a feedwater system, and a steam distribution system. The sodium side of each steam generator is connected to the hot and cold legs of the main sodium piping on the secondary (tube) side of each IHTS loop.

The steam cycle selected for application to the SLFFR is a superheated cycle with dual reheats. The steam plant has not yet been sized for the SLFFR.

3.4.2. Steam Generator System

3.4.2.1. Steam Generator

The function of the steam generator is to produce steam for the turbine-generator set from the heat transported to it via the primary heat transport system and the intermediate heat transport system. Steam is generated under normal power conditions (40-100% power), and under decay heat conditions, using the Benson cycle. That is, water is preheated, evaporated, and superheated in the single pass through the steam generator with no recirculation. Each intermediate heat transport system feeds high temperature sodium to one steam generator. The steam generator building is located adjacent to the reactor containment building and on the base isolation system. Each steam generator unit operating at full power provides the turbine with steam at $\sim 500^{\circ}\text{C}$ and 2250 psig from approximately 250 MWt transferred from the IHTS. The steam generator produces superheated steam between 40 and 100% of the power.

As noted earlier, a steam generator design similar to that utilized in the GE Prism Mod B plant concept is proposed for the SLFFR. The steam generator is a helical coil, vertically oriented, sodium-to-water, countercurrent flow, shell-and-tube type unit featuring once-through operation. Four 250 MWt steam generator units are utilized for SLFFR, one for each IHTS loop.

The steam generator design utilizes the identical tube diameter, thickness, and pitch-to-diameter ratio as for the PRISM Mod B helical-coil design. Moreover, the tube length and helical pitch are the same. Thus, if the water and sodium mass flowrates per tube are conserved, then 184 tubes per unit are selected to achieve the required 250 MWt heat exchange rate based on a linear scaling of the Prism design (viz., 630 tubes for 845 MWt rating). A diagram that illustrates key elements of the scaled steam generator design is provided in Figure 3.9, while key design data are summarized in Table 3.3. Aside from the thermal power rating, the thickness of structural elements (i.e., upper and lower tube sheets, as well as shell and elliptical head thicknesses) have been scaled to approximately preserve peak mechanical stresses for a given pressure loading. Moreover, the diameters of inlet and exit piping on both the sodium and steam sides of the HCSG have been scaled to approximately preserve flow velocities, which then approximately preserves pressure drops at the various points within the steam generator.

During full power operation, feedwater flow to the steam generator is regulated by a 20 cm (8 inch) main control valve. The main feedwater line breaks into four 15 cm (6 inch) feedwater nozzles located on the bottom head of each unit. These nozzles supply water to the inlet of the steam generator at 256°C temperature and 167 bar pressure. The GE design incorporates flow restrictors with a pressure drop of 6.5 bars at the tube inlets to increase static and dynamic flow stability over a wide load range. After entering the steam generator, the water flows up through the tube side of the 3.18 cm OD, 98.5 m long tube bank while absorbing energy from the sodium on the shell side of the unit in a counter-current flow configuration. The water then exits the steam generator as superheated steam at a temperature of 500°C and pressure of 155 bars through four 20 cm diameter (8 inch) steam nozzles located in the top head of the unit. These four nozzles are then merged into the 30 cm diameter (12 inch) main steam line leading to the turbine generator building. To aid in plant control and monitoring, flowrate and temperature measurements are made both at the feedwater inlet and steam exits to the steam generator.

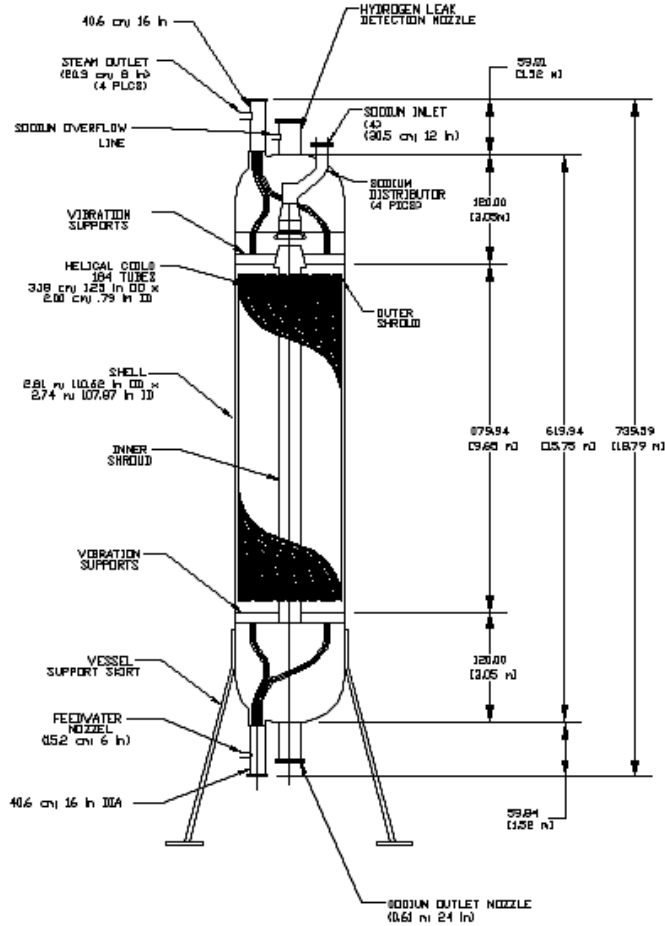


Figure 3.9. HCSG Design Characteristics (GE PRISM Mod B Basis)

Table 3.3. Scaled Once-Through HCSG Design Data for 1000 MWt Plant Design

Parameter	Value
Capacity	250 MWt
Operational Mode	Single Pass
Configuration	Cross-Flow; Shell and Helical Coil; Tube Side Water/Steam Flow
Number of Tubes	184
Tube OD	3.18 cm
Tube ID	2.00 cm
Overall Tube Length	98.5 m
Tube Material of Construction	2-1/4 Cr-1 Mo
Overall Tube Heat Transfer Surface Area	1806 m ²

On the shell side of the unit, sodium is split from the 61 cm diameter (24 inch) IHTS hot leg supply line from the IHX into four 30 cm diameter (12 inch) nozzles that provide the pathway for the sodium to enter through the upper elliptical head of the unit. The sodium then

flows in a counter-current flow configuration on the shell side of the heat exchanger while delivering heat to the steam/water mixture on the interior of the tubes. The sodium then exits the steam generator through a single 61 cm diameter (24 inch) pipe that constitutes the cold leg of the IHTS.

The total system can be operated on either 3 or 4 loops, so steam generator maintenance can be conducted during operation at 75% power. There are sodium isolation valves that allow for isolating the steam generators for maintenance and during steam generator casualties, if needed. The units are designed to accommodate the transients specified in the duty cycle.

Particular attention is devoted to the prevention and quick detection of leakages between water and sodium in the steam generator. The overall configuration and the design details are both evaluated in terms of prevention of leaks. Very high quality is demanded of the tube-to-tube and tube-to-tube sheet welds. A fast-response, leakage detection system is included in the IHTS and the steam generator systems. In case of a large sodium-water interaction, the steam generator includes a means of isolating and dumping the water side of the steam generator and discharging the reaction products into a separate vessel. Maintainability and repairability have a high importance in the design of the steam generator. In case of a leak, the location must be readily identified and methods of plugging the leaking tube easily implemented.

3.4.2.2. Steam Cycle

A Rankine superheated-steam cycle, power conversion system concept will be used for the SLFFR. The estimated system cycle efficiency is ~41.5% (see Figure 3.10) and the overall plant efficiency is 39%. Detailed information for this concept is not available at this time.

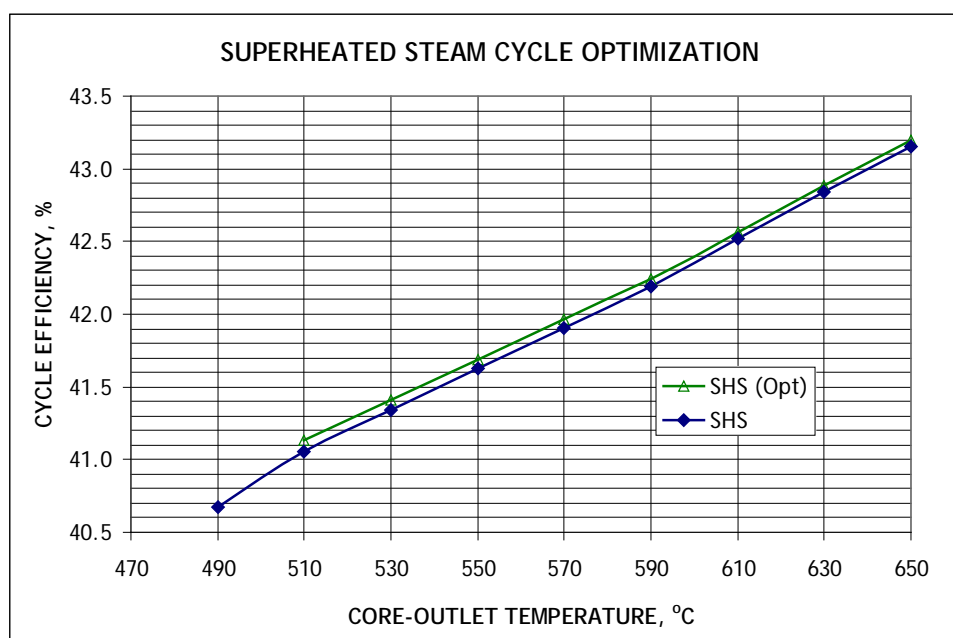


Figure 3.10. Overall Cycle Efficiency

3.5. Fuel Handling System

The fuel handling system is similar in concept to other fast reactor design concepts with the exception that for the SLFFR, molten fuel will need to be removed from the core while fresh recycled fuel in solid form is loaded into the core. The fuel is removed using the fuel-unloading machine that is designed to lower a gripper device that connects to a fuel sipper. This fuel sipper is made of stainless steel and is inserted into the periphery of the molten fuel through the fuel transfer pipe. A combination of inert gas pressurization and suction are used to fill the fuel sipper with spent fuel. The fuel-unloading machine then retracts the fuel sipper from the molten core. The spent fuel within the sipper then freezes during the removal process. The fuel sipper is then removed from the reactor vessel and inserted within the spent fuel transfer cask. Multiple sipper pipes fill with spent fuel can be contained within the spent fuel cask based upon criticality and shielding requirements. The spent fuel cask is then transferred to the fuel cycle building via reactor containment doors and a transfer tunnel between the two buildings. Reactor containment is continuously maintained in this configuration. Recycled fuel from the Fuel Cycle Building is made into metallic rods that are introduced during the refueling process to ensure that the reactor maintains criticality. The metallic recycled fuel rods are melted upon entry into the reactor fuel canister. Figure 3.11 through Figure 3.20 illustrate the SLFFR refueling process.

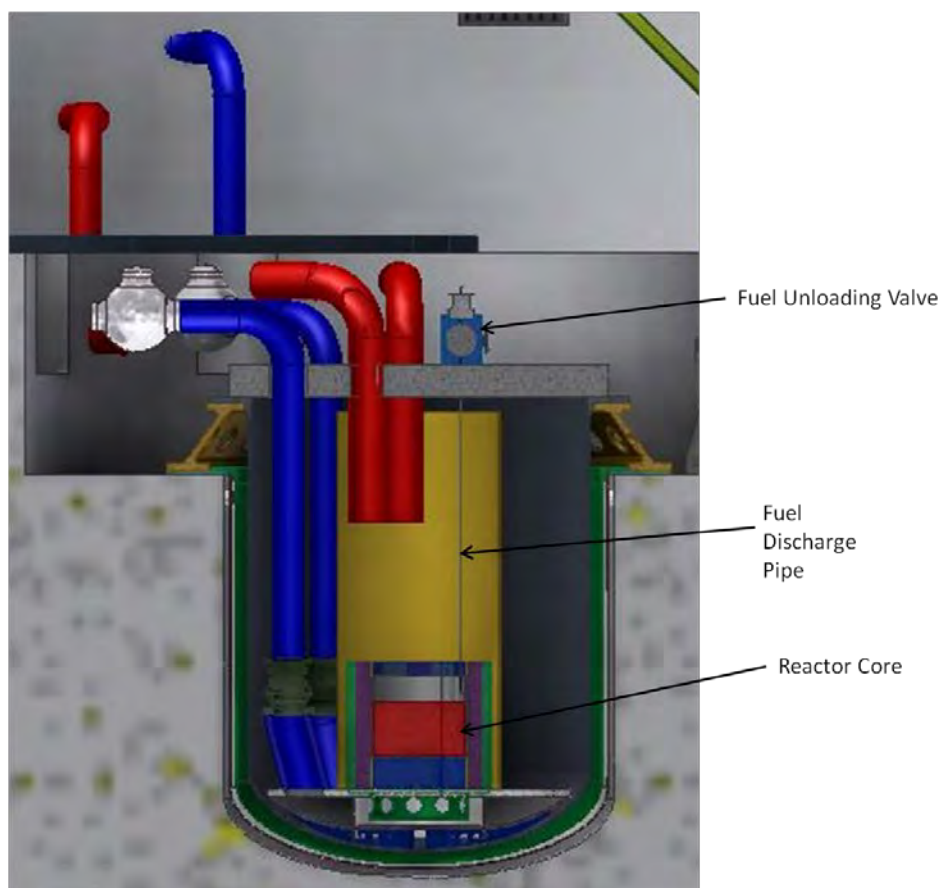


Figure 3.11. SLFFR Fuel Handling – Primary Vessel

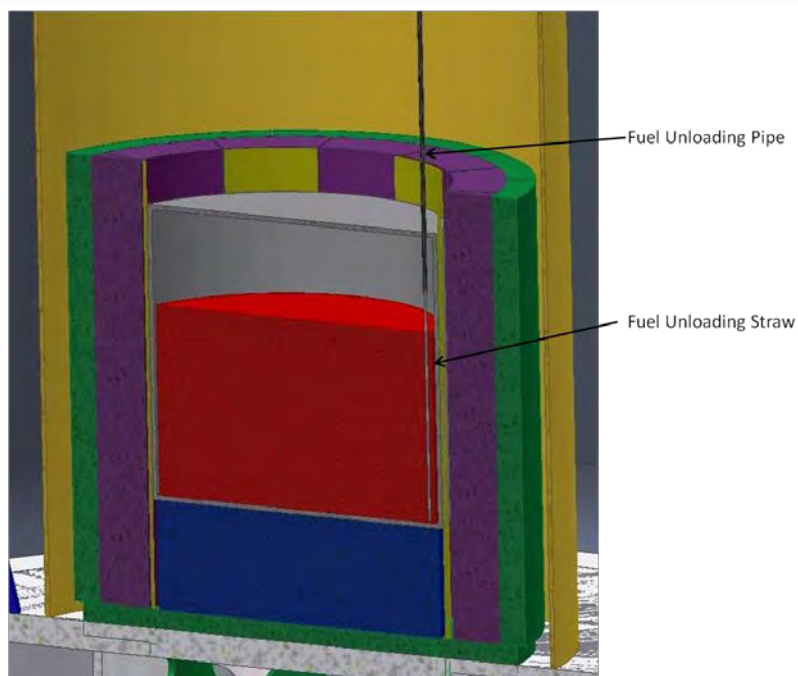


Figure 3.12. In-vessel Fuel Handling System

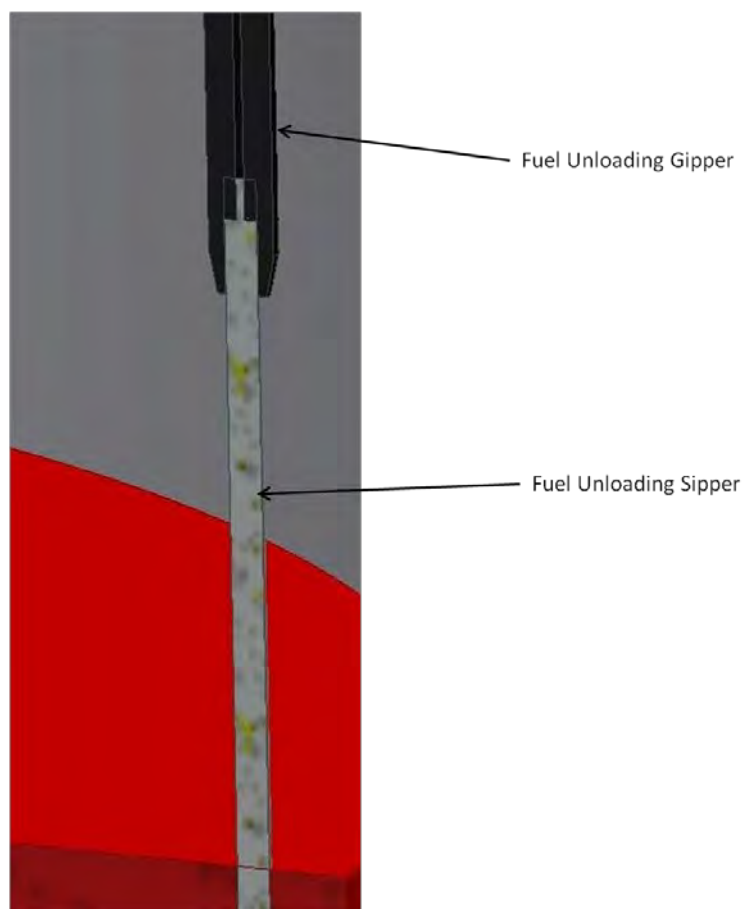


Figure 3.13. Fuel Handling Gripper and Unloading Sipper

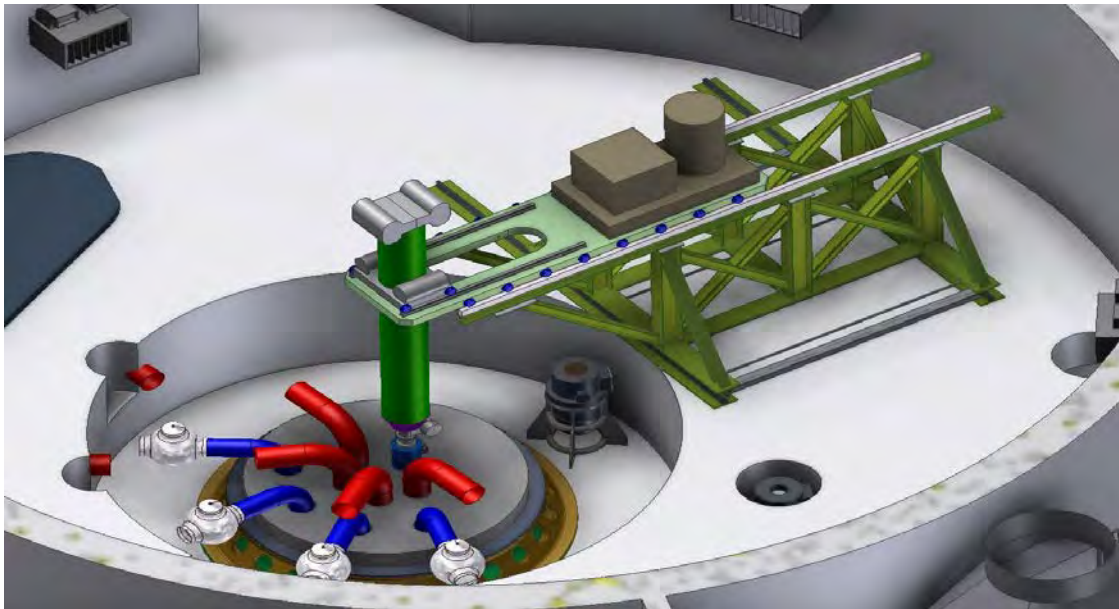


Figure 3.14. Fuel Unloading Machine – Over Reactor Vessel

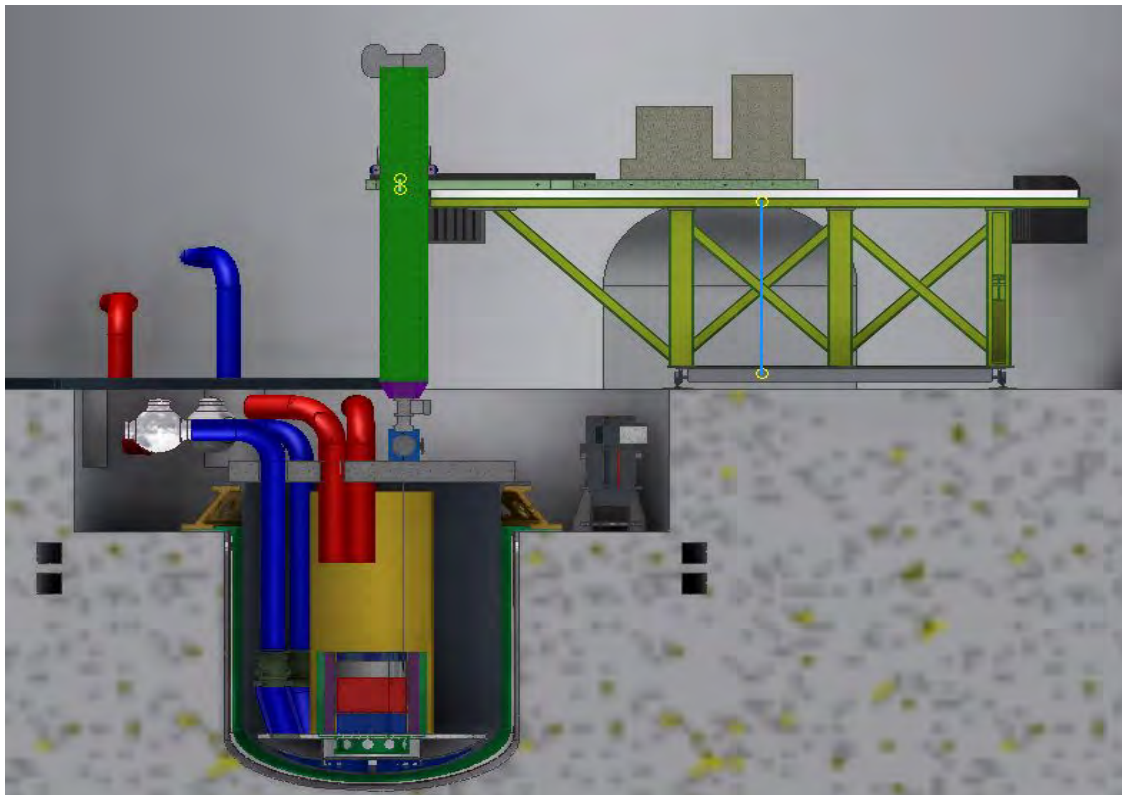


Figure 3.15. Fuel Unloading Machine – Over Reactor Vessel

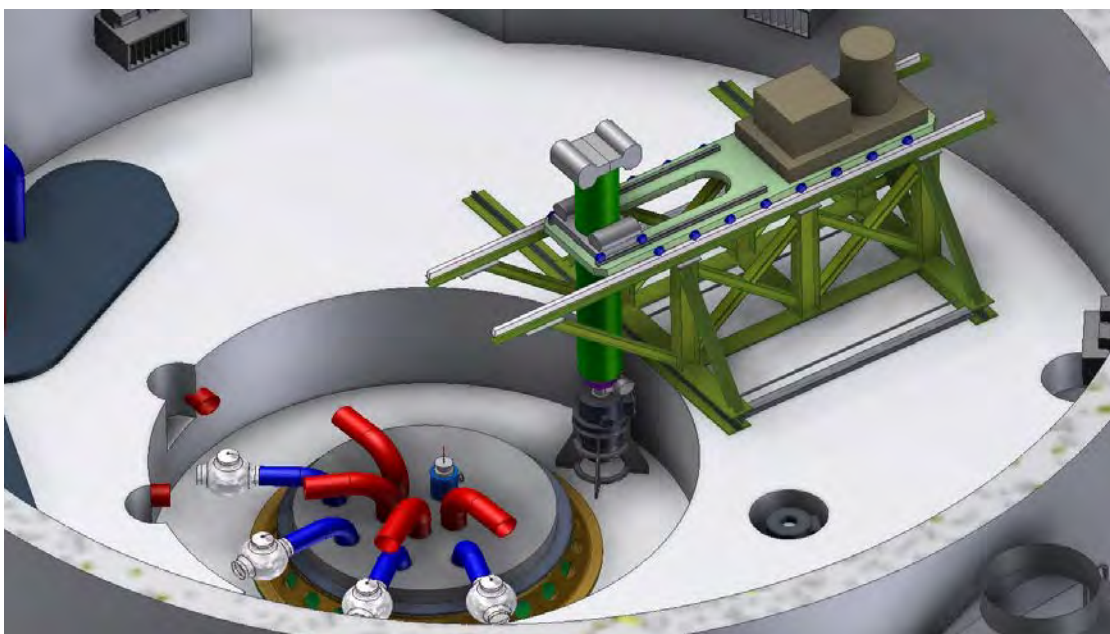


Figure 3.16. Fuel Unloading Machine – in Transfer Position

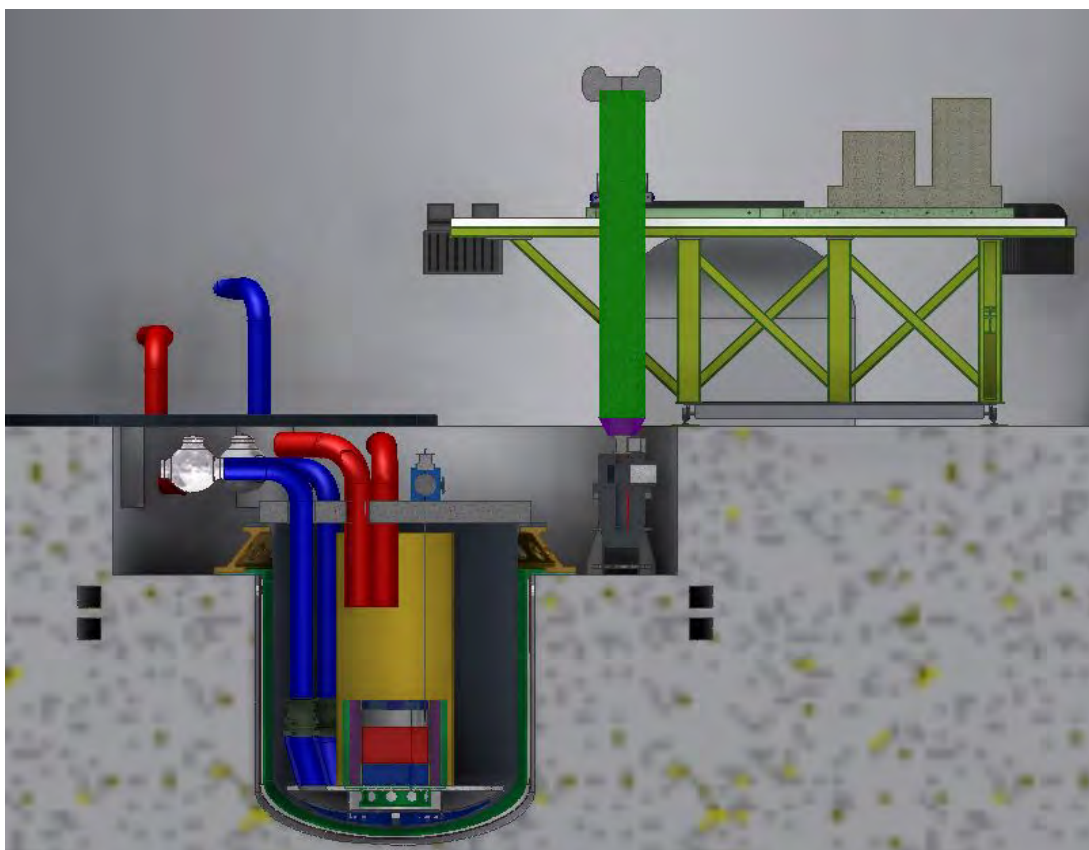


Figure 3.17. Fuel Unloading Machine – in Transfer Position

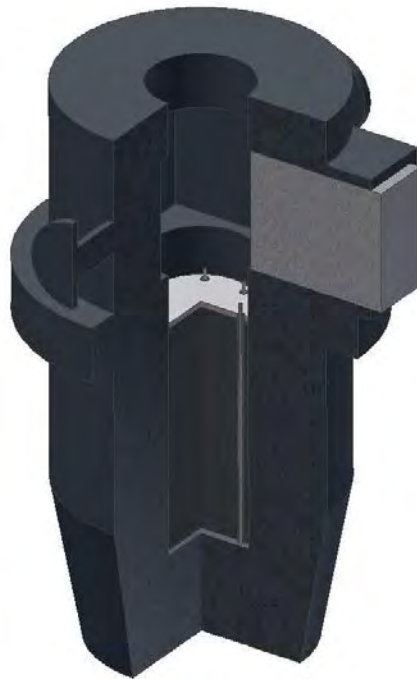


Figure 3.18. Spent Fuel Handling Cask

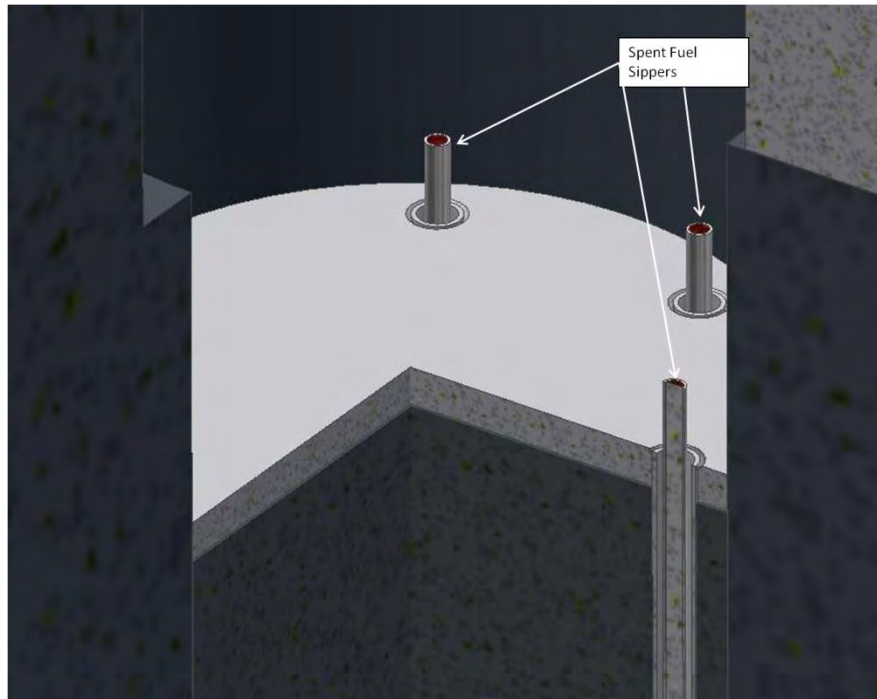


Figure 3.19. Spent Fuel Handling Cask – Inside View

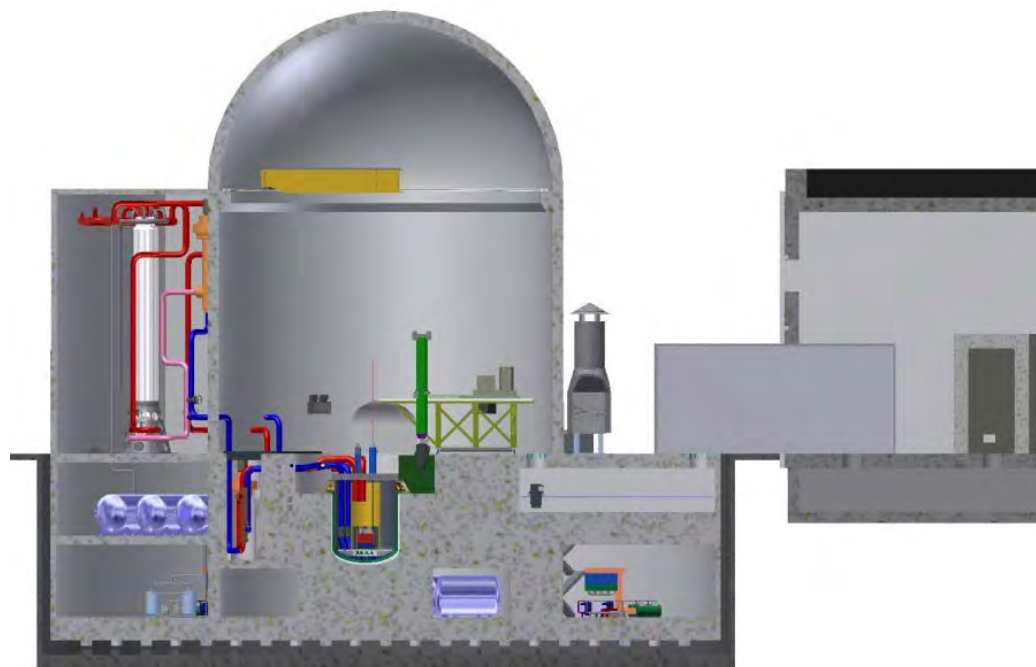


Figure 3.20. Elevation View – Showing Fuel Transfer Tunnel

3.6. SLFFR-1000 Site Plan

The building and structures for the SLFFR-1000 loop plant are very similar in size and type as the ABR-1000 pool plant with the exception of some dimensions for the reactor building and nuclear island. Figure 3.21 and Figure 3.22 provide an artist rendition of the SLFFR-1000 reactor side layout. Table 3.4 shows the listing of the loop-plant site buildings with their dimensions.

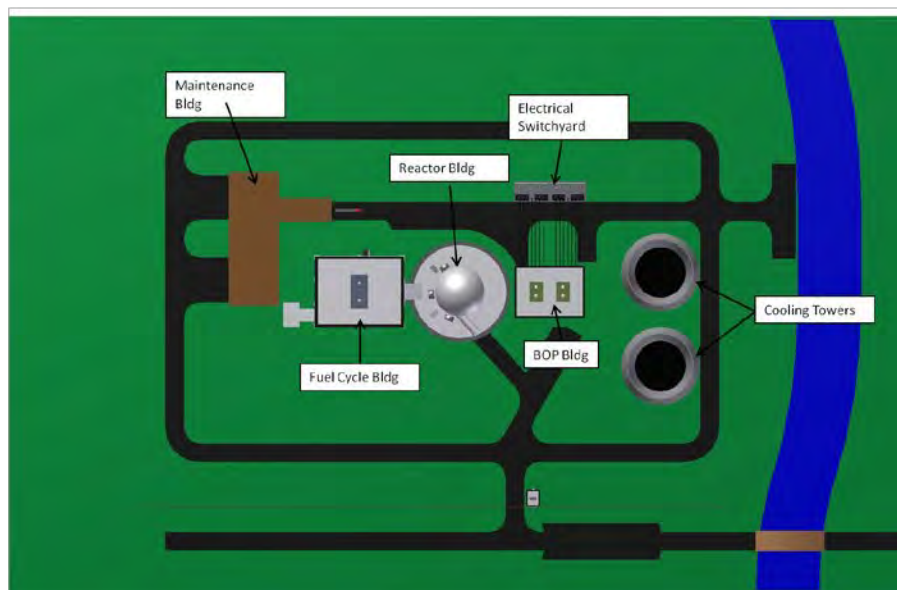


Figure 3.21. SLFFR-1000 Reactor Site (Plan View)

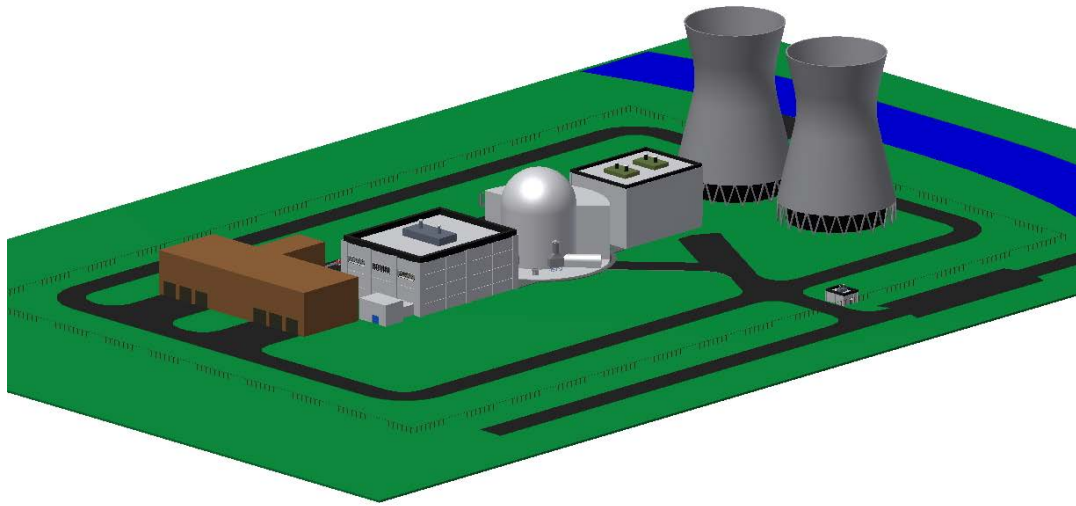


Figure 3.22. SLFFR Reactor Site (Isometric View)

Table 3.4. Site Buildings with Dimensions

Building Name	Footprint (ft ²)	Length (ft)	Width (ft)	Height (ft)
Security Gate House	900	30	30	16
Control/Personnel Building	12,576	131	96	30
Nuclear Island	41,909	231	231	154
BOP Building	22,575	175	129	175
Emergency Generator Building	3000	100	30	12
Balance of Plant Service Building	9,000	100	90	20
Cooling Towers (each)	19,113	156	156	60
Radwaste/ Maintenance Facility	24,000	120	200	40/80
Lift Station	1,200	40	30	16
Fuel Cycle Building	40,906	226	181	100

4. Development of Operation Strategies

Comparing to commercial water reactors, sodium cooled fast reactors have difficulties on operations due to reactive and opaque coolants. In the development of the SLFFR, it is essential to establish feasible operation procedures. The SLFFR has advantage over conventional SFRs with solid fuels in simple fuel handling and recycling because the fuel is operated in the stationary liquid phase. Based those advantages and the experience of SFRs, preliminary operation strategies were developed for fuel handling, commissioning and startup, and fuel recycling. In this section, the developed operational strategies for the 1000 MWt SLFFR core with a co-located reprocessing system are described.

4.1. Fuel Handling

The fuel handling system is a key element of any fast reactor design and is predominantly one of the more complex systems that are required to work in a comparatively harsh environment. Major requirements are that the system must be very reliable and relatively easy to maintain. In addition, the system should be designed so that it does not adversely affect plant economics from the perspective of capital investment or plant operations.

The fuel handling system is similar in concept to other fast reactor design concepts with the exception that for the SLFFR, fuel in a molten liquid state will need to be removed from the core while fresh recycled fuel in solid pelletized form is loaded into the core. The assumption that is made here is that the fuel once removed from the reactor will be solidified and handled in a solid form until it is returned to the reactor tank and melted.

The primary overall functions of a typical conventional fast reactor refueling system are as follows:

1. Receive, inspect, store, and prepare new core assemblies for insertion in the reactor vessel and core
2. Transfer assemblies between facilities (e.g., ex-vessel storage tank, reactor vessel and core, and fuel handling cell as appropriate)
3. Transfer core assemblies between the core and in-vessel storage or transfer positions or between core positions
4. Provide storage for irradiated core assemblies
5. Examine and prepare irradiated core assemblies for shipment
6. Provide inventory control of all core assemblies.

These functions will need to be modified for the SLFFR as follows:

1. Receive, inspect, storage, and prepare fuel pellets for insertion into the reactor vessel tank core
2. Transfer fuel pellets between facilities
3. Control insertion of fuel pellets into the reactor vessel tank core
4. Control the removal of the molten fuel from the reactor vessel tank core
5. Provide inventory control of all new or recycled fuel pellets and used fuel slugs.

In some ways, the refueling scheme is simpler for the SLFFR because only a single transfer machine will be used. Typical fast reactors have two refueling machines, one in-vessel and one ex-vessel. For the SLFFR, the molten fuel is removed using the fuel-unloading machine that is

designed to lower a gripper device that connects to a fuel sipper. This fuel sipper is made of TBD³ material and is inserted into the periphery of the molten fuel through the fuel transfer pipe. A combination of inert gas pressurization and suction are used to fill the fuel sipper with spent fuel. The fuel-unloading machine then retracts the fuel sipper from the molten core. The spent fuel within the sipper then freezes during the removal process. The fuel sipper is then removed from the reactor vessel and inserted within the spent fuel transfer cask. Multiple sipper pipes filled with spent fuel can be contained within the spent fuel cask based upon criticality and shielding requirements. The spent fuel cask is then transferred to the fuel cycle building via reactor containment doors and a transfer tunnel between the two buildings. Reactor containment is continuously maintained in this configuration. Recycled fuel from the Fuel Cycle Building is made into metallic rods that are introduced during the refueling process to ensure that the reactor maintains criticality. The metallic recycled fuel rods are melted upon entry into the reactor core canister.

After the fuel is removed from the reactor vessel through the “sipper”, it is processed in the fuel cycle facility and then blended with new fuel. This new recycled fuel, in a metallic solid form, is then inserted into the fuel insertion device to ensure that required core excess reactivity is ensured. The makeup feed rate of 1.01 kg/day is the amount of TRU taken from LWR spent fuel TRU. In order to maintain the criticality with a minimal excess reactivity control, the refueling system removes used fuel from the reactor fuel tank, thus removing fission products from the reactor. So, at equilibrium, the system is required to discharge and reprocess 32.5 kg of fuel per day, from which 16.4 kg TRU is recovered. The recovered TRU is mixed with the external TRU feed of 1.01 kg from LWR spent fuel to compensate for the burned TRU in the reactor, and subsequently 32.7 kg of TRU-Ce-Co (17.5 kg of TRU, 12.1 kg of Ce and 3.1 kg of Co) is charged per day.

4.2. Commissioning and Startup

The sodium system and balance of plant will be commissioned and started up in the normal conventional manner for any sodium-cooled fast reactor system. Before sodium fill of the SLFFR’s system and components, the completed and constructed sodium loops and vessels comprising the reactor plant will be heated and “baked out” under a partial vacuum to remove residual volatile compounds that can be removed before initial sodium fill. After the initial bake out, the system heaters will remain on and the facility will be filled with sodium. The heaters will consist of resistance and induction heating systems that can heat all of the sodium containing components, mainly piping and vessels, to a minimum of 121 °C (250 °F).

The initial reactor grade sodium will arrive to the SLFFR site in either rail or truck shipped tanker cars. A heating oil system will be used for heating the frozen sodium until it is in a molten state. Molten sodium from the tanker car will be pushed by inert gas (nitrogen is suitable for

³ This material will need to be developed. Ideally, the sipper tube will be made such that it can be reused in the reactor. A suitable material would allow the used fuel mixture to be pulled into the sipper in a molten state, followed by freezing (transition from molten to solid state), and then mold release from the sipper. The used fuel located in the sipper tube would freeze upon retraction from the core or during the process of removal from the reactor vessel.

this purpose) from the tanker car through a set of temporary filters to the intermediate heat transport system storage vessels. Once these storage vessels are filled, the sodium will be recirculated using the secondary purification system until the purity of the sodium is within specification. A plugging meter and/or sodium samples will be used to measure the sodium purity. A similar process will be used to fill the primary reactor vessel with sodium.

A standard conventional sodium-cooled fast reactor contains immersion heaters within the reactor vessel that allow the sodium to be heated above the sodium melting point. This allows the sodium to be maintained in a molten state during filling when decay heat levels in the core are insufficient to maintain sodium in liquid form. After initial sodium fill, the sodium will be circulated using a combination of the main coolant pumps (both primary and secondary) and the purification system as appropriate. The sodium will be purified using both the primary and secondary purification systems until the sodium is within specification. The SLFFR is now ready for the new fuel loading.

The SLFFR initial core load will be comprised of solid fuel pellets with a small void fraction. Initial core load will be 8853 kg of TRU fuel pellets with a composition of 40 wt% TRU, 50.2 wt% Ce, and 9.8 wt% Co. These solid fuel pellets will be inserted into a small melting heater connected to the fuel tank or directly into the fuel tank via the fuel insertion pipe. This fuel insertion pipe will be connected to the reactor fill cask located above the reactor vessel cover and sealed to the reactor vessel cover nozzle.

The anticipated melting point is ~ 420 °C (788 °F) under the assumption that the melting point of Pu-Ce-Co ternary fuel would not be increased significantly by the addition of a few percent of minor actinides (MA). This temperature is substantially higher than the melting temperature of the bulk sodium and thus will need to have separate heating elements to heat the fuel. It is also expected that the fuel will need to be re-melted if the control rods are inserted into the reactor tank during the early stages of the reactor core life and there is insufficient decay heat to maintain the SLFFR core fuel in a molten state.

Thus, it is expected that the SLFFR will need to have a set of high-temperature core immersion heaters that are fitted to an upper internal structure that will allow for the insertion and removal of the heaters into and out of the coolant tubes while allowing some coolant to circulate through the coolant channels. When the core requires melting, the heaters will be immersed partly into the coolant channels and the heaters will be turned on. The temperature of the reactor fuel will be raised slowly and from the top of the core (from a free surface) to ensure that the expansion of the fuel does not overstress the fuel tank and challenge the structural integrity of the fuel tank. As the upper surface of the fuel is melted, the reactor core immersion heaters are lowered into the coolant channels slowly and in steps to ensure that the solid fuel melts accordingly all the way to the bottom of the reactor fuel tank. Once the fuel has melted, the reactor can be “started up” using the control rod. The control rod will be withdrawn until the reactor is critical at a very low power, but sufficient power to maintain the core in a molten state or at least most of the core in a molten state. The core immersion heaters are still inserted into the reactor vessel tank at this low power level. As the control rod is further withdrawn and the reactor core heats up further, then the core immersion heaters are withdrawn until they are fully withdrawn from the coolant channels and the reactor core is at a self-sustaining power where the core can be maintained in a molten state.

It is expected that the core immersion heaters will be required because of the following operational states:

1. Transitioning the initial core from solid fuel to a molten fuel state.
2. Heating up and melting a frozen core but in such a way that the fuel melts from a free surface while adequate cooling is maintained.

Re-melting the core should be a straightforward process since Pu-Ce-Co fuel expands upon freezing and contracts upon melting.

4.3. Fuel Recycling

SLFFR fuel is a liquid metal alloy of TRU elements, cerium and cobalt with a nominal composition of 52.4 wt% TRU, 37.5 wt% Ce, and 8.9 wt% Co (34.0, 41.4, and 23.6 at%, respectively). Fuel with a burnup of 5.79% is discharged at a rate of 32.46 kg/day. A pyrochemical process for treating discharged SLFFR fuel is proposed based on liquid metal-salt chemistry developed in the Chemical Science and Engineering Division at Argonne National Laboratory. The proposed process is capable of removing a sufficient fraction of fission products to maintain a low fuel melting point, and recover more than 99% of the actinides. The cerium and cobalt that must be replaced each cycle depends inversely on the fractions of rare earth and noble metal fission products remaining in the processed fuel. However, rare earths, other than cerium, and noble metals raise the fuel melting temperature.

4.3.1. Process Description

Figure 4.1 is a diagram of the process. Molten fuel from the reactor (Stream 1) is contacted with a chloride salt (basically LiCl-KCl) in the Salt/Fuel Contactor. The reduction-oxidation conditions are controlled such that the “active” metal fission products (Rb, Cs, Sr, Ba, Sm, and Eu⁴) are oxidized and dissolved in the salt as mono- or divalent chlorides. These elements are easily separated from actinides and other rare earths that form trivalent chlorides. The redox conditions are controlled to oxidize enough rare earths to limit their concentration in the recycled fuel. A proportional amount of alloy cerium is also extracted into the salt and must be replaced in the recycled fuel. Because actinide chlorides are thermodynamically less stable than rare earth chlorides, actinide content of the salt will be about 1 – 2% of the rare earths. Noble metal fission products are not oxidized and they remain in the metal phase.

To remove noble metal fission products, a portion of the liquid fuel is withdrawn from the Contactor, solidified, chopped, and loaded into wire baskets (Stream 4). The loaded baskets become the anodes of the Electrefiner, which contains an electrolyte of LiCl-KCl-(TRU)Cl₃-(Ce-RE)Cl₃ and operates below the fuel melting point. Passing a current between the electrodes oxidizes the actinides and rare earths at the anode and deposits them as metals at the cathode leaving cobalt and noble metals in the anode basket. The metals on the cathodes with adhering electrolyte (Stream 5) are returned to the Fuel Contactor. Salt with plutonium (Stream 9) must be added to the Electrefiner to make up for the salt on the cathodes and maintain the actinide

⁴ In this process, it is likely that Sm and Eu form divalent chlorides and behave similar to alkaline earths.

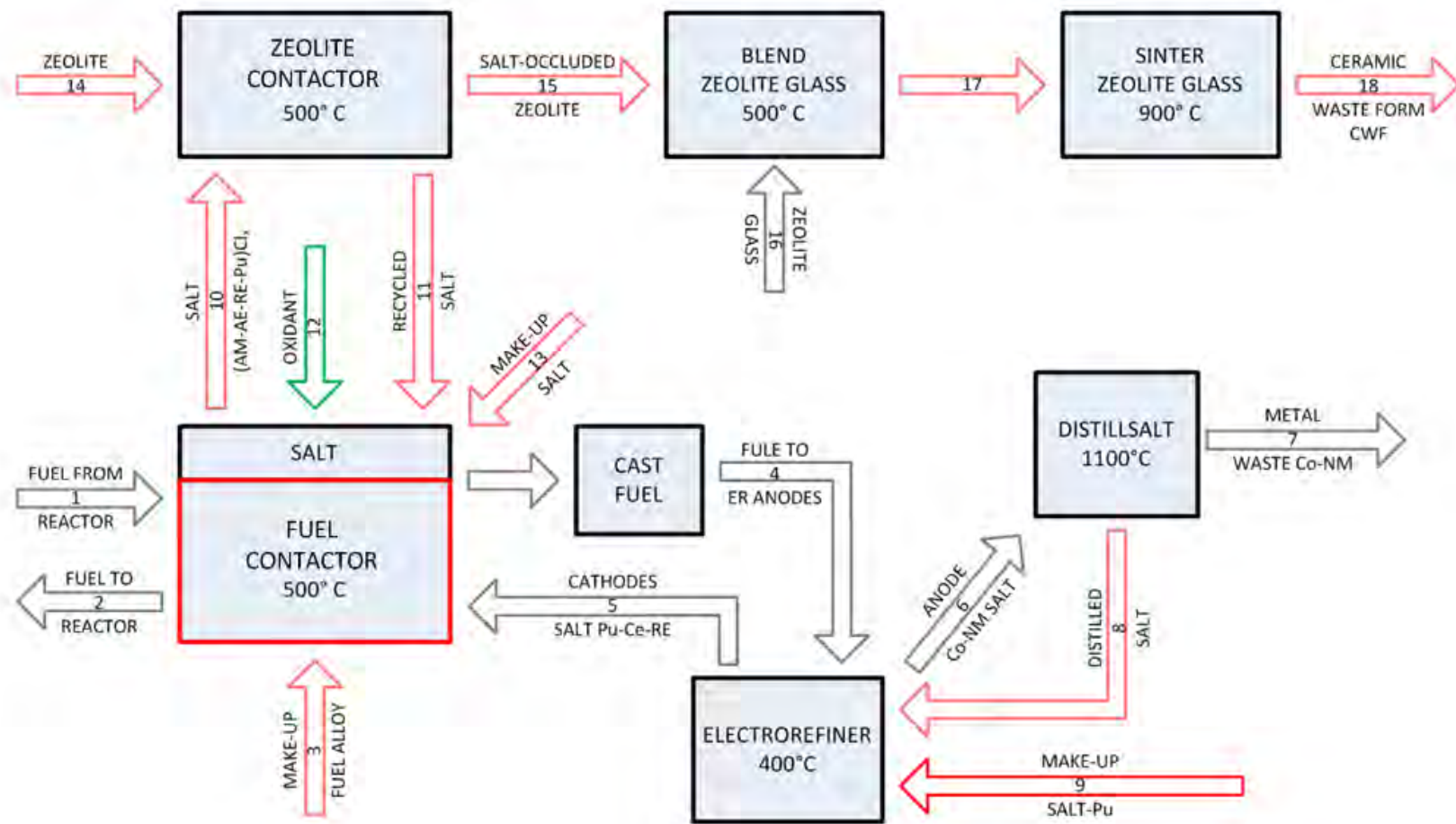


Figure 4.1. Concept for Processing SLFFR Fuel

concentration in the electrorefiner salt. Salt adhering to the cobalt and noble metals in the anode baskets is removed by vaporization and returned to the Electrorefiner. The noble metal-cobalt alloy remaining after salt removal is a waste.

A portion of the salt in the contactor (Stream 10) is removed and mixed with zeolite-A. Contact with zeolite can remove essentially all of the di- and trivalent chlorides, and a large fraction of Rb and Cs chlorides. The remaining salt is returned to the salt/fuel contactor. “Salt-occluded zeolite” (Stream 15), the reaction product between zeolite and chloride salts, is blended with additional zeolite and glass frit, and then sintered at a high temperature to convert the zeolite to sodalite and make a waste form that consists of a glass matrix with dispersed sodalite particles. Sodalite encapsulates the chloride ions along with some of the fission product cations. The balance of the fission product ions are dissolved in the glass as oxides.

In Stream 3, plutonium is added to replace that burned, cerium is added to replace that lost with the salt (Stream 10), and cobalt is added to replace that lost in the metal waste (Stream 7). A portion of the make-up plutonium is supplied in Stream 9.

4.3.2. Material Balance

The Table 4.1 and Table 4.2 are a material balance for one possible set of conditions that demonstrates the major process features. In those tables, Pu represents all actinides; AM is the alkali metal fission products Rb and Cs; AE is the fission products forming divalent chlorides Sr, Ba, Sm, and Eu; RE is the rare earths forming trivalent chlorides, Ce is the alloy cerium⁵, NM is the noble metal fission products Zr through Sb. Halides, selenium and tellurium are not considered. Fission product gases, Kr and Xe, are assumed removed in the reactor.

The material balance shown in Table 4.1 and Table 4.2 are evaluated based on the several assumed parameter values in Table 4.3. The top two parameters are most important. The first parameter is the weight fraction of rare earth fission products in the cerium alloy. Replacing cerium with any other rare earth raises the fuel melting point. Although other pertinent ternary phase diagrams are scarce, there are binary diagrams of cobalt with several other rare earths. Most of them display a eutectic corresponding to the 421 or 441 °C Co-Ce eutectic but with higher eutectic temperatures, e.g. 566 °C for Co- 35 at% Nd. It is estimated that a cerium alloy containing 20% rare earths raises the melting point of the fuel to about 450 °C. Decreasing this fraction increases both the make-up cerium and actinide losses. Actinides in Stream 10 are estimated to be 1 – 2% of the rare earth content, but are not calculated here. If necessary, the actinide loss can be reduced with a few additional process steps as described below.

The second important parameter is the weight fraction of noble metal fission products in the cobalt alloy. It is assumed that cobalt behavior is similar to noble metals. The effects of noble metals on fuel properties were not estimated, but they will most likely increase its melting point. Decreasing the noble metal fraction increases the make-up cobalt required and electrorefiner size. The molecular weight of the salt is relatively unimportant. The salt is basically the LiCl-KCl eutectic, but it contains NaCl from the zeolite.

⁵ Cerium behaves like the fission product rare earths, but it is treated separately here.

Table 4.1. Material Balance of Processing SLFFR Fuel (1/2)

Stream		1 Fuel from Reactor	2 Fuel to Reactor	3 Make-up fuel	4 Fuel to ER Anodes	5 ER Cathodes	6 ¹ Anodes to Distillation	7 Waste Metal	8 ¹ Distilled Salt	9 Make-up ER Salt
Metal, kg/day	Pu	16.090	17.073	0.724	9.023	9.023	-	-	-	-
	AM	0.082	-	-	-	-	-	-	-	-
	AE	0.110	-	-	-	-	-	-	-	-
	RE	2.023	1.888	-	1.135	1.098	-	-	-	-
	Ce	10.699	10.699	0.714	5.999	5.806	-	-	-	-
	NM	0.699	0.307	-	0.392	-	0.392	0.392	-	-
	Ce	2.760	2.760	1.548	1.548	-	1.548	1.548	-	-
Total Metals, kg/day		32.46	32.72	2.98	18.10	15.92	2	2	-	-
Salts, kg/day	Eutectic Salt	-	-	-	-	7.28	-	-	-	7.28
	PuCl ₃	-	-	-	-	0.41	-	-	-	0.41
	(AM)Cl	-	-	-	-	0	-	-	-	-
	(AE)Cl ₂	-	-	-	-	0	-	-	-	-
	(RE)Cl ₃	-	-	-	-	0.07	-	-	-	-
	CeCl ₃	-	-	-	-	0.34	-	-	-	-
Total Salts, kg/day		-	-	-	-	8.08	-	-	-	7.68

¹ All Salt with ER anodes separated and returned in Stream 8

Table 4.2. Material Balance of Processing SLFFR Fuel (2/2)

Stream		10 Fuel from Reactor	11 Fuel to Reactor	12 Make-up fuel	13 Fuel to ER Anodes	14 ER Cathodes	15 Anodes to Distillation	16 Waste Metal	17 Distilled Salt	18 Make-up ER Salt
Salts, kg/day	Eutectic Salt	7.28	24	19	-	5	-	5	-	5
	PuCl ₃	0.41	0.03	-	-	-	-	0.03	-	0.03
	(AM)Cl	-	0.20	0.11	-	-	-	0.11	-	0.11
	(AE)Cl ₂	-	0.17	-	-	-	-	0.17	-	0.17
	(RE)Cl ₃	-	0.23	-	-	-	-	0.23	-	0.23
	CeCl ₃	-	1.25	-	-	-	-	1.25	-	1.25
Total Salts, kg/day		7.68	26.18	19.54	-	5	-	6.66	-	6.66
Others, kg/day	Reductant, Li,	-	-	-	-	-	-	-	-	-
	Oxidant, Cl	-	-	0.44	-	-	-	-	-	-
	Zeolite	-	-	-	-	15.76	15.76	27.58	43.34	43.34
	Glass	-	-	-	-	-	-	14.30	14.30	14.30
Total Others, kg/day		-	-	0.44	-	15.76	15.76	41.88	57.64	57.64

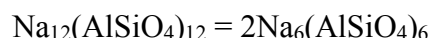
Table 4.3. Assumed Parameter Values Used in Recycling Material Balance Estimation

Parameter	Value
Weight fraction of rare earth fission products in cerium alloy	0.15
Weight fraction of noble metal fission products in cobalt alloy	0.1
Molecular weight of eutectic salt	60
Salt to metal weight ratio on electro-refining cathodes (stream5), kg/kg	0.5
Salt on electro-refining cathodes(stream 5), kg/day	8.197

The amount of reductant (lithium metal) or oxidant (Cl_2)⁶ needed to transfer rare earths from the fuel into the salt were calculated from the material balance. Alkali metals (Rb and Cs), alkaline earths (Sr and Ba), and two rare earths (Sm and Eu), which form divalent chlorides, must be oxidized into the salt along with the specified fraction of rare earths. The salt fed to the electrorefiner in Stream 5 is essentially a reductant. The redox balance calculated from the material balance returns values for gm-equivalents of either lithium or chlorine.

The performance of the Zeolite Contactor was evaluated from previous calculations based experimental data. Those calculations show that zeolite contactors are capable of removing essentially all of the di- and trivalent cations and more than 50% of the monovalent fission products. Stream 10 quantities are calculated from the assumed eutectic salt removed from the Fuel Contactor and the amounts of fission products and cerium chlorides calculated elsewhere.

Zeolite-A is $\text{Na}_{12}(\text{AlSiO}_4)_{12}$. The “unit cell,” $(\text{AlSiO}_4)_{12}$ anion, is a hollow molecular cage capable of enclosing 10 to 12 chloride ions with associated cations; 11 is assumed here. When heated above 850 °C, zeolite forms sodalite



Because each sodalite cage encapsulates only 2 chloride ions, additional zeolite (Stream 16) must be added to immobilize the chloride ions. Borosilicate glass is added to form a matrix for sodalite particles. Fission product cations are either contained in sodalite or dissolved in glass as silicates and aluminates. The product, Ceramic Waste Form, has been found to be an excellent high-level waste form comparable to Defense High-Level Waste Glass.

As mentioned above, the actinide content of the salt in the Fuel Contactor will be 1 to 2% of the rare earth and cerium content. Thus, if the required removal fraction of rare earth fission products is high, the actinide loss will be high, as well as the loss of alloy cerium. It is feasible to reduce the actinide loss (but not the cerium loss) by treating the salt from the electrorefiner (Stream 10) before it is sent to the zeolite contactor. In one method, the salt is contacted with a liquid metal solution of cerium in lead. Cerium in the metal phase extracts actinides in the salt. After the salt and metal have equilibrated, the metal is separated and contacted with fresh LiCl-KCl salt. The cerium and actinides in the metal are oxidized and transfer into the salt that is then sent to the Fuel Contactor. New cerium is dissolved in the lead and the solution recycled.

⁶ An oxidant is required under most conditions.

The equilibrium between the fuel alloy and salt in the Contactor is based on known thermodynamic free energies of the components. The metal and salt phases were assumed ideal solutions because activity coefficients are largely unknown. The equilibrium distribution of a large number of mono-, di-, and trivalent cations between the salt and zeolite-A has been measured [57, 58]. The separation of salt from noble metal wastes by distillation is based on the measured vapor pressure of the salts, which are available in various thermodynamic databases. Extractions between salt and lead are based on ideal solutions; a few distribution coefficients between lead and chloride salts have been measured [59], plutonium activity in lead has been reported [61] as well as solubility of several elements in lead [62]. The required process equipment has, for the most part, been demonstrated and reported primarily by Argonne's Chemical Engineering Division and Oak Ridge's Molten Salt Reactor program.

5. Safety Analyses

Safety analyses were performed to assess the safety performance characteristics of the SLFFR design. The analyses were performed using a multi-channel safety analysis code (MUSA), which was developed in this project to handle the unconventional core geometry of the SLFFR. A detailed description of the physical models of the MUSA code is provided in Appendix A, and a user's guide is provided in Appendix B. As an initial verification effort, the safety analyses for hypothesis accidents were performed using the MUSA code and the resulting asymptotic states were compared with the solution of quasi-static reactivity analysis [72]

The scope of the analyses focused on the ability of SLFFR to provide inherent protection against damaging consequences in low probability accident sequences involving multiple equipment failures. Specifically, the following three beyond design basis accidents (BDBA) of primary importance for passive safety were examined: unprotected transient overpower (UTOP), unprotected loss of heat sink (ULOHS), and unprotected loss of flow (ULOF).

5.1. Quasi-static Reactivity Balance Analysis

Preliminary tests of the MUSA code were performed by comparing the predicted asymptotic states with the corresponding values estimated from the analysis of quasi-static reactivity balance. If the reactor is stable against an external perturbation, a new asymptotic state will be reached after natural adjustment of the core power and temperature due to thermal feedbacks. By simulating the UTOP, ULOHS, ULOF, chilled inlet and pump over-speed accidents for a sufficiently long period using the SLFFR transient code, the asymptotic states were calculated and compared with the corresponding values estimated by solving the quasi-static reactivity balance equation.

The quasi-static reactivity for the new asymptotic state can be written as the sum of the reactivity changes due to the variations in power ($\Delta\rho_P$), flow rate ($\Delta\rho_F$), coolant inlet temperature ($\Delta\rho_{T_{in}}$) and the externally induced reactivity change ($\Delta\rho_{ext}$) as

$$\Delta\rho = \Delta\rho_P + \Delta\rho_F + \Delta\rho_{T_{in}} + \Delta\rho_{ext} = 0 \quad (5.1)$$

For transients that are slow compared to the time constants of heat-flow changes, temperature-induced geometry changes, and delayed neutrons, which are in the range of a fraction of second to several minutes, Eq. (5.1) can be represented as

$$\Delta\rho = A(P-1) + B(P/F-1) + C\delta T_{in} + \Delta\rho_{ext} = 0 \quad (5.2)$$

where P is the power normalized to the full power, F is the flow normalized to the full flow, δT_{in} is the change from the normal coolant inlet temperature, and $\Delta\rho_{ext}$ is the reactivity change caused by externally imposed changes in control rod position. In Eq. (5.2), $(A+B)$ is the power defect, which is the reactivity decrement experienced in going to the full power and flow condition from the zero-power isothermal condition at the coolant temperature, B is the power/flow coefficient of reactivity, and C is the inlet temperature coefficient of reactivity. The reactivity coefficients A , B , and C can be measured in terms of controllable external

perturbations $\Delta\rho_{ext}$, F , and δT_{in} , and Eq. (5.2) can be solved for the new asymptotic power level after passive self-adjustment.

The coefficients A , B , and C represent different combinations of the reactivity feedback coefficients, and they can be calculated as

$$A = (\alpha_D + \alpha_l)\Delta T_f \quad (5.3)$$

$$B = (\alpha_D + \alpha_{Na} + \alpha_l + 2\alpha_r)\frac{\Delta T_c}{2} \quad (5.4)$$

$$C = \alpha_D + \alpha_{Na} + \alpha_l + \alpha_r \quad (5.5)$$

where ΔT_f is the average fuel temperature increment relative to the average coolant temperature, and ΔT_c is the coolant temperature rise across the core. In these equations, α_D is the Doppler coefficient, α_{Na} is the sodium density coefficient, α_l is the axial expansion coefficient, and α_r is the radial expansion coefficient. In the current core design of SLFFR, $\Delta T_f = 127^\circ\text{C}$ and $\Delta T_c = 100^\circ\text{C}$. Using the reactivity feedback coefficients at the end of equilibrium cycle (EOEC) shown in, the integral coefficients can be estimated as $A = -231.94$ cents, $B = -47.25$ cents and $C = -1.22$ cents/ $^\circ\text{C}$.

For a UTOP accident, it is assumed that a rod runs out and introduces a positive reactivity $\Delta\rho_{TOP}$ while the flow and inlet temperature remain fixed. The positive reactivity is compensated by the negative reactivity of a power increase, and the increased power to flow ratio causes the outlet temperature to increase. With $F = 1$ and $\delta T_{in} = 0$, Eq. (5.2) yields the following power increase:

$$P = 1 + \frac{-\Delta\rho_{TOP}}{A + B} \quad (5.6)$$

The corresponding increase in the coolant outlet temperature is determined as

$$\delta T_{out} = \frac{-\Delta\rho_{TOP}}{A + B} \Delta T_c \quad (5.7)$$

For a ULOHS accident, the heat ejection by the balance of plant terminates, and the inlet temperature increases while the flow remains constant. Subsequently the negative reactivity induced by inlet temperature rise is compensated by a positive reactivity due to power decrease. As power decreases, the power to flow ratio decreases and the coolant outlet temperature T_{out} collapses onto the inlet temperature T_{in} . At the asymptote where $P \approx 0$ and $F = 1$, the reactivity balance in Eq. (5.2) yields the following inlet temperature change:

$$\delta T_{in} = \frac{(A + B)}{C}(1 - P) \quad (5.8)$$

Since the coolant outlet temperature is equal to the inlet temperature at the asymptote, the outlet temperature change can be determined as

$$\delta T_{out} = \frac{A+B}{C}(1-P) - \Delta T_c \quad (5.9)$$

For a ULOF accident, it is assumed that the primary pump runs down while the inlet temperature remains fixed. Consequently, the power to flow ratio increases, raising the core average coolant temperature and inducing a negative reactivity. The negative reactivity is compensated by the positive reactivity induced by a power reduction. If the coolant outlet temperature remains below the boiling point, a natural circulation flow will be established asymptotically and the power will settle at a low value such that the positive reactivity of power reduction balances the negative reactivity of core heat-up due to an increased power to flow ratio. Ideally with $P \approx 0$ and $\delta T_{in} = 0$, Eq. (5.2) yields the following power to flow ratio.

$$P/F = 1 + A/B \quad (5.10)$$

The corresponding increase in the coolant outlet temperature is determined as

$$\delta T_{out} = (A/B)\Delta T_c \quad (5.11)$$

If the ratio A/B is larger than $(T_{boil} - T_{out})/\Delta T_c$, where T_{boil} is the coolant boiling temperature, then the power decreasing rate is slower than the flow coast-down. This leads to coolant boiling and thus the reactor cannot be shutdown passively.

For a chilled inlet accident, it is assumed that the inlet temperature decreases while the flow remains fixed. The positive reactivity induced by inlet temperature decrease is compensated by a negative reactivity due to power increase. At the asymptote where $F = 1$, the reactivity balance in Eq. (5.2) yields the following power change:

$$P = 1 + \frac{C(-\delta T_{in})}{A+B} \quad (5.12)$$

The corresponding increase in the coolant outlet temperature is determined as

$$\delta T_{out} = \left[\left(\frac{C\Delta T_c}{A+B} \right) - 1 \right] (-\delta T_{in}) \quad (5.13)$$

For a pump over-speed accident, it is assumed that the primary pump speed increases within its cavitation limit while the inlet temperature remains fixed. Consequently, the power to flow ratio decreases, reducing the core average temperature and inducing a positive reactivity. The positive reactivity is compensated by the negative reactivity induced by a power increase. With $F > 1$ and $\delta T_{in} = 0$, Eq. (5.2) yields the following initial power to flow ratio:

$$P = \frac{A+B}{A+B/F} \quad (5.14)$$

The corresponding increase in the coolant outlet temperature is determined as

$$\delta T_{out} = \left[\frac{1}{1 + \frac{A}{A+B}(F-1)} - 1 \right] \Delta T_c \quad (5.15)$$

Table 5.1 compares the asymptotic coolant inlet and outlet temperatures of five beyond design basis accidents of a preliminary SLFFR design without GEMs estimated by the quasi-static reactivity balance with those determined by transient analyses using the MUSA code with a single channel thermal-fluidic model. In the ULOF accident, the maximum coolant temperature reaches the boiling point around 25 seconds after accident initiation. At this moment, the transient was terminated artificially because MUSA does not have a computational model for sodium boiling. Since the sodium void worth is positive (\$4.69), however, it is expected that the onset of sodium boiling would increase the power rapidly and lead to a severe accident. The quasi-static reactivity balance analysis yielded a consistent result; the estimated coolant outlet temperature was 1319K, which is $\sim 120^\circ\text{C}$ above the sodium boiling point ($\sim 1200\text{ K}$). Thus, the ULOF transient could not be terminated inherently, converging to a new asymptotic state. (Based on this observation, GEMs were implemented in the final core design of SLFFR.)

Table 5.1. Comparison of Asymptotic Coolant Inlet and Outlet Temperatures (K) Obtained from Quasi-static and Transient Analyses for SLFFR Design without GEMs

Postulated Accident	Quasi-static		Transient	
	inlet	outlet	Inlet	outlet
UTOP	723	841	723	840
ULOHS	954	955	1101	1103
ULOF	723	1319	-	-
Chilled inlet	673	795	673	789
Pump over-speed	723	815	723	815

For the UTOP, chilled inlet and pump over-speed accidents, the asymptotic coolant temperatures obtained from the MUSA transient calculations agree within 10°C with the values estimated from the quasi-static reactivity balance. On the other hand, for the ULOHS accident, the asymptotic coolant temperature predicted by the transient analysis is about 150°C higher than the value estimated from quasi-static reactivity balance. This temperature difference is due to the difference in reactivity feedback calculation between the two methods. In the MUSA model, the reactivity feedbacks are calculated by integrating the product of the axial distributions of temperature and density changes and the associated reactivity worth distributions along each channel, whereas the reactivity feedback coefficients used for the quasi-static reactivity analysis were obtained for uniform perturbations.

Figure 5.1 and Figure 5.2 show the axial distributions of the coolant and fuel temperature changes from the initial steady-state distributions obtained from the MUSA transient calculations. It can be seen that the temperature changes are relatively flat for the UTOP, chilled inlet and pump over-speed accidents. Thus, for these cases, the reactivity feedback coefficients based on uniform perturbations are similar to those of the transient analysis, and the quasi-static reactivity balance analysis yield similar results as the transient analysis. For the ULOHS accident, however, the temperature perturbations from the initial steady-state distributions show significant axial variations. As a result, the asymptotic coolant temperatures predicted from the quasi-static reactivity balance show relatively large deviations from those determined by

transient analysis. These results indicate that the MUSA code produces consistent asymptotic temperatures with the quasi-static reactivity balance analysis.

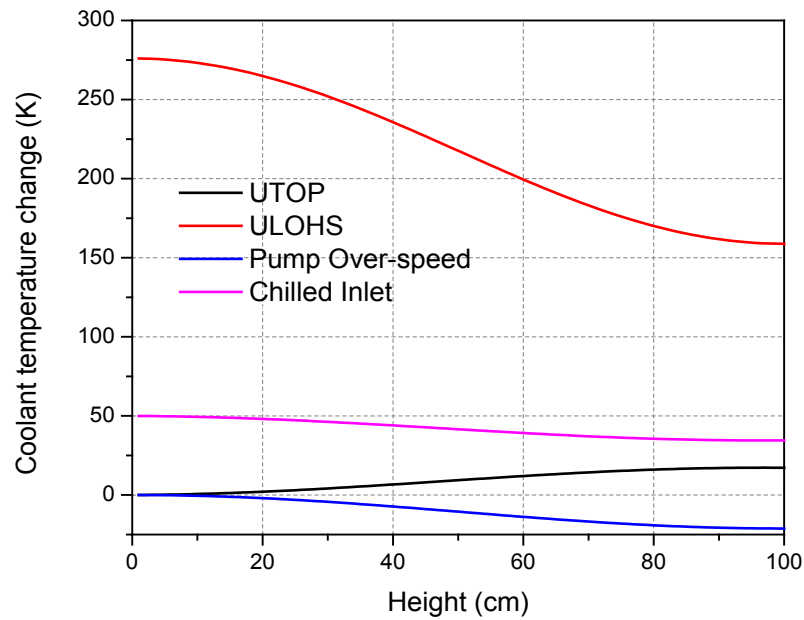


Figure 5.1. Axial Distributions of Coolant Temperature Changes from Initial Steady-State Distribution

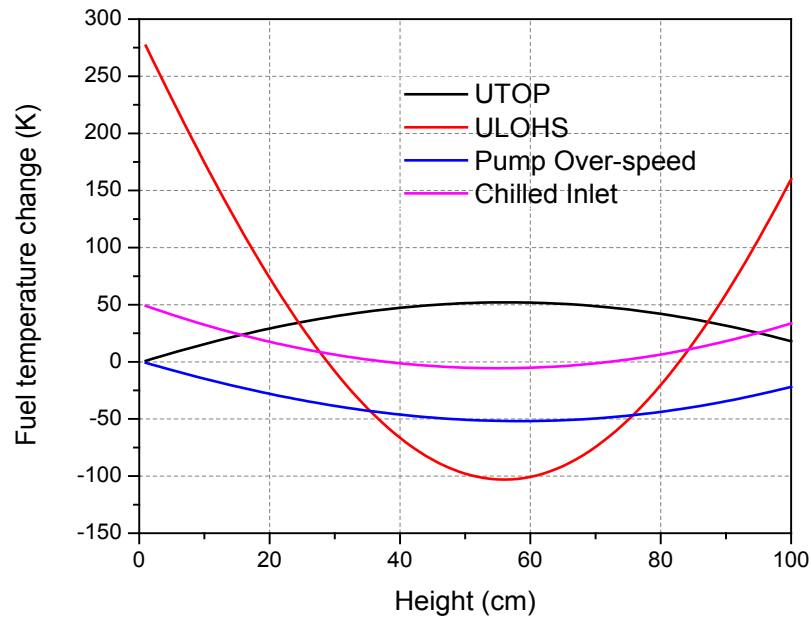


Figure 5.2. Axial Distributions of Fuel Temperature Changes from Initial Steady-State Distribution

5.2. Transient Analyses

Using the multi-channel safety analysis code MUSA, transient analyses were performed for three beyond-design basis accidents to investigate the passive safety characteristics of the core design of SLFFR with the equilibrium cycle condition. The core was modeled by three one-dimensional parallel channels. The primary heat transport system was modeled by connecting two compressible volumes (representing the inlet and outlet plenums) by two liquid segments (one representing the core and the other representing the hot leg, the intermediate heat exchanger and the cold leg). A point kinetics model with six delayed neutron groups was used to represent power transients. For the reactivity feedback calculation, the axial distributions of reactivity feedback coefficients were evaluated for each thermal-fluidic channel. The density coefficients of fuel, coolant and structure material as well as Doppler coefficient were considered.

Figure 5.3 to Figure 5.6 show the axial distributions of the feedback coefficients, which were calculated by integrating the reactivity worth distributions over the corresponding radial regions at each axial mesh. The channel 1, channel 2 and channel 3 represent the hot, average and periphery channels, respectively. The spatial distributions of the reactivity worth were obtained using the VARI3D perturbation theory code [8]. The distribution of Doppler constant was determined by doubling the fuel temperature. The reactivity worth distributions of coolant, structural material and fuel density variations were calculated by reducing the coolant density by 1% and increasing the structural material and fuel densities by 25% and 10%, respectively.

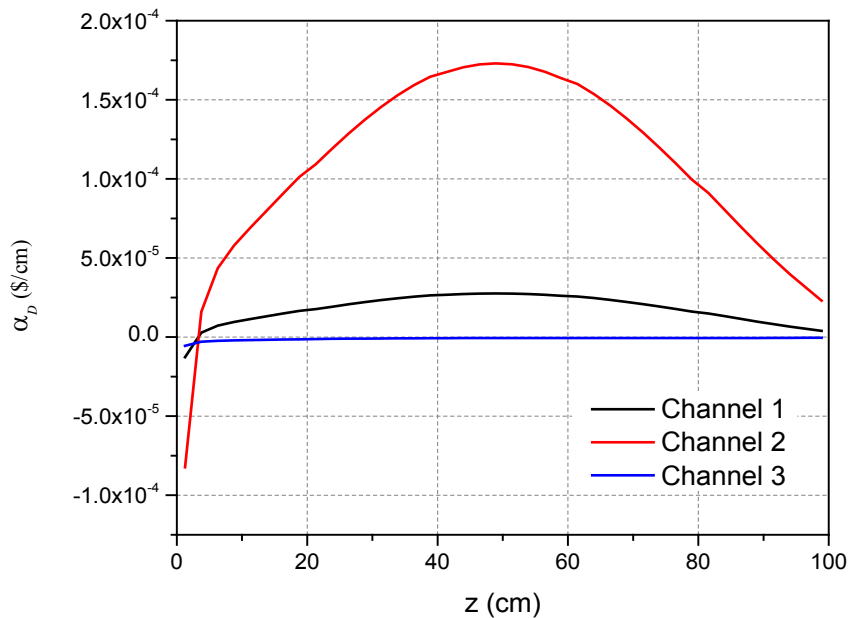


Figure 5.3. Axial Distributions of Doppler Constant for Three-Channel Model of SLFFR Core

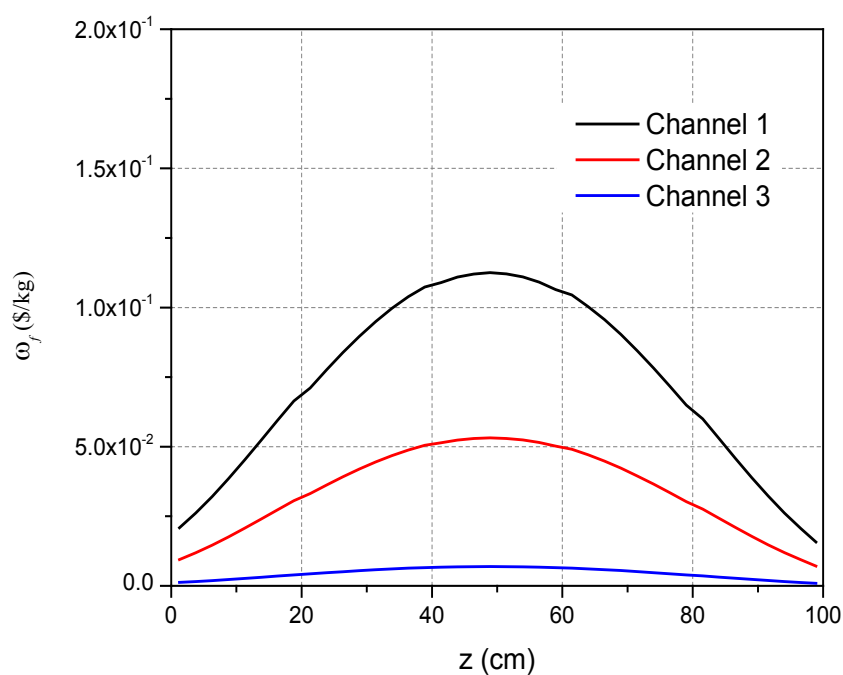


Figure 5.4. Axial Distributions of Fuel Worth for Three-Channel Model of SLFFR Core

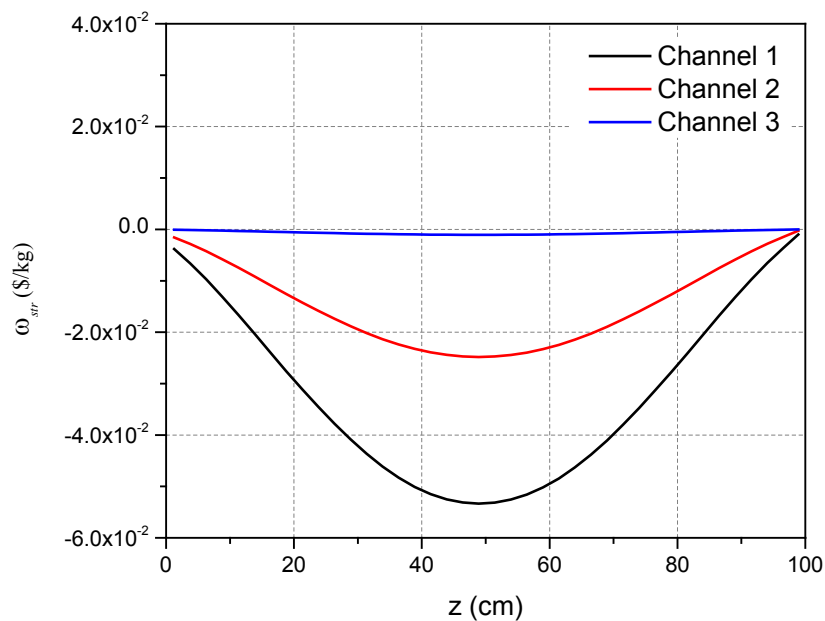


Figure 5.5. Axial Distributions of Structure Material Worth for Three-Channel Model of SLFFR Core

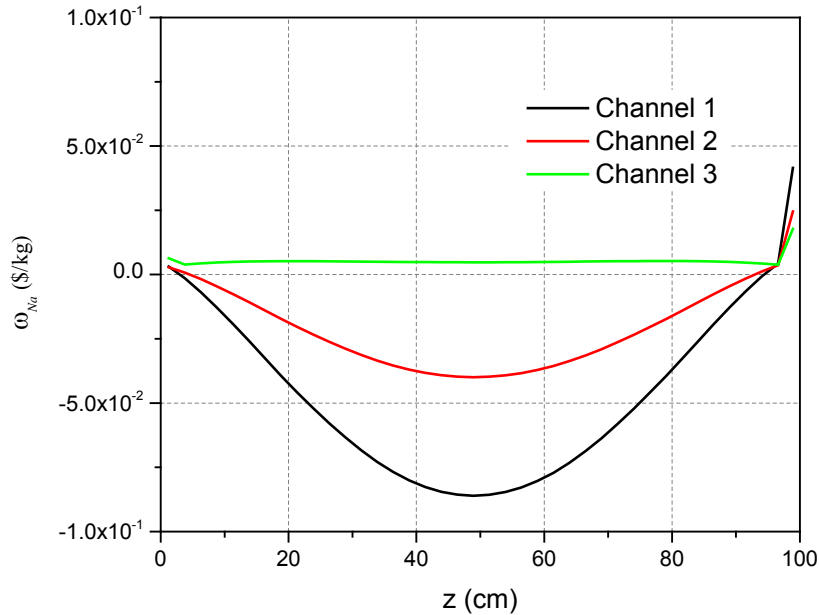


Figure 5.6. Axial Distributions of Sodium Worth for Three-Channel Model of SLFFR Core

Table 5.2 shows the prompt neutron lifetime, delayed neutron fractions and decay constants of delayed neutron precursors used in the analysis. The initial condition of the temperatures, pressures and coolant flow of the primary loop components were obtained from the steady-state solution. The steady-state solution was determined using the primary loop design parameters and specifications summarized in Table 5.3. The channel power, coolant outlet pressure, coolant inlet temperature, and flow rates are provide as shown in Table 5.4.

Table 5.2 Point Kinetics Model Specifications

Delayed Neutron Group	Effective Delayed Neutron Fraction	Decay Constant (s^{-1})
1	5.78E-05	1.34E-02
2	4.95E-04	3.06E-02
3	3.04E-04	1.15E-01
4	6.82E-04	2.98E-01
5	3.46E-04	8.56E-01
6	1.16E-04	2.88E+00
Prompt Neutron Life Time (s)		7.94E-08

Table 5.3. Primary Loop Design Parameters and Specifications for SLFFR

Pumping Head (MPa)	0.695	Total Length of Pipes (m)	20
Vessel Inside Diameter (m)	6.35	Pipe Diameter (m)	0.66
Height of Upper Plenum (m)	6	Height of Hot Leg (m)	6
Height of Cover Gas (m)	0.5	Height of Cold Leg (m)	8
Height of Lower Plenum (m)	1	Nominal IHX Pressure Drop (MPa)	0.119
Decay Heat Removal Power (kW)	10000	IHX Sink Temperature (K)	623
Pressure Expansion Coefficient	1.00E-07	Temp. Expansion Coefficient	1.74E-05

Table 5.4. Design Parameters and Steady-State Solution of Thermal-Fluidic Channels

Thermal-fluidic channel	Hot channel	Average channel	Periphery channel
Number of Coolant Tubes	955	15036	2190
Minor Pressure Loss Coefficient	1.23	3.47	9.13
Coolant Inlet Temperature (K)	723	723	723
Coolant Outlet Plenum Pressure (MPa)	0.154	0.154	0.154
Channel Power (kW)	86.7	56.5	29.3

5.2.1. Unprotected Transient Overpower

For the UTOP accident, an extremely unlikely initiator was considered by assuming that all the control assemblies holding down the maximum excess reactivity were ejected instantaneously. Although the maximum excess reactivity to be held down by the control system is 0.167 \$ at the BOL, a step reactivity insertion of 0.5 \$ was assumed conservatively. Figure 5.7 shows the transients of the coolant outlet, channel averaged structure, and channel averaged fuel temperatures in the hot channel as well as the coolant inlet temperature. Figure 5.8 shows the transients of the total power and decay heat. The feedback reactivity components are shown in Figure 5.9. It can be seen that the reactor reaches a new asymptotic state of the nominal power at elevated temperatures after 100 seconds into the transient. The positive reactivity inserted by the control rod run-out increases the power rapidly, which increases the fuel temperature almost adiabatically. The increased fuel temperature introduces a large negative reactivity due to thermal expansion of liquid fuel and thus reduces the rate of power increase. As a result, the power increases initially and then decreases back to the nominal power. The inserted figure in Figure 5.8 shows the transient behavior of the total power in a much smaller time scale. As can be seen, the inserted positive reactivity increases the power rapidly to a local maximum of ~163% nominal power at 0.0001 seconds. Subsequently, the competition of the negative prompt feedback due to the thermal expansion of liquid fuel and the delayed neutron source makes the power decrease to a local minimum of ~122% nominal power at

0.0008 seconds and then increase gradually until ~5 seconds. At ~5 seconds into the transient, the power level reaches a maximum of ~127% power and gradually decreases to the nominal power.

Because of the increased power level for a fixed coolant flow rate, the coolant outlet temperature increases monotonically to an asymptotic value as shown in Figure 5.7. The coolant inlet temperature also increases gradually to an asymptotic value because the heat removal by the secondary heat transport system is limited to the nominal rated power. As shown in Figure 5.9, the increased fuel temperature introduces a large negative feedback, but the increased coolant and structure temperatures introduce positive reactivity feedbacks. The resulting net reactivity decreases gradually to zero at ~26 seconds into the transient. The fuel temperature keeps increasing due the elevated power level. Thus, the net reactivity become negative until the power decreases to the nominal power and the reactor core reaches a new asymptotic state. The sum of the external reactivity of 0.5 β and the positive reactivity insertion due to the increased coolant and structure temperatures is compensated for by the negative reactivity inserted by the increased fuel temperature. The asymptotic coolant inlet temperature is 768K. The asymptotic coolant outlet temperatures are 915K, 878K and 857K for the hot, average and periphery channels, respectively. It is noted that the coolant outlet temperature of the hot channel has a margin of more than 280 °C to the sodium boiling point.

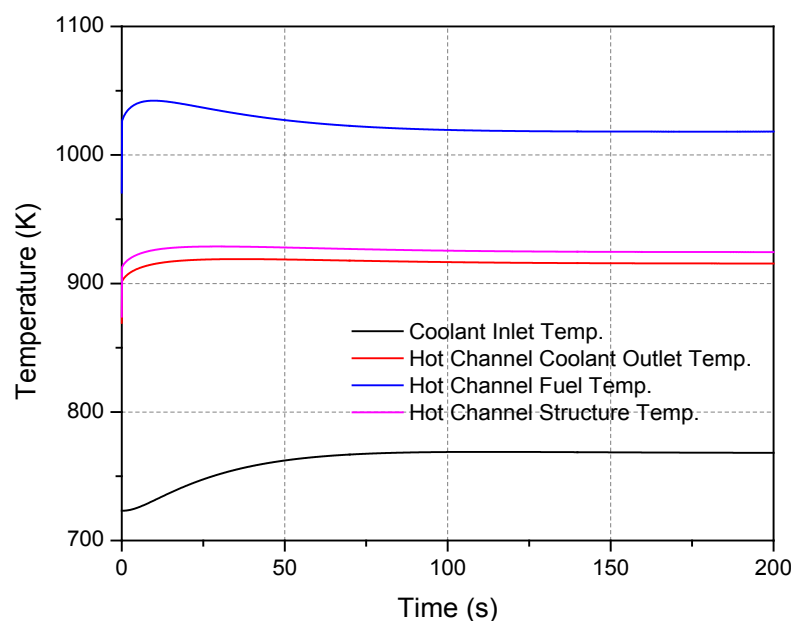


Figure 5.7. Transient of Coolant Inlet and Hot Channel Temperatures for UTOP Accident

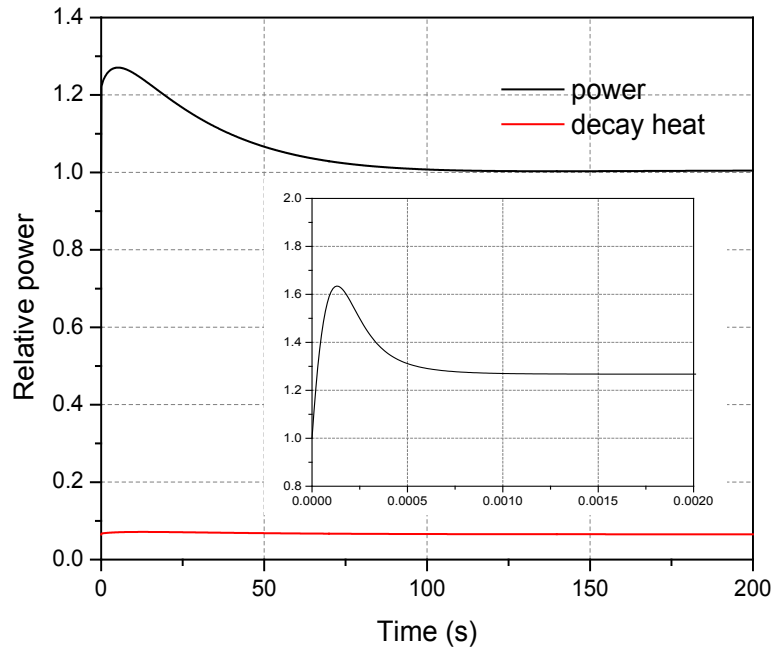


Figure 5.8. Transient of Total Power for UTOP Accident (long term and short term)

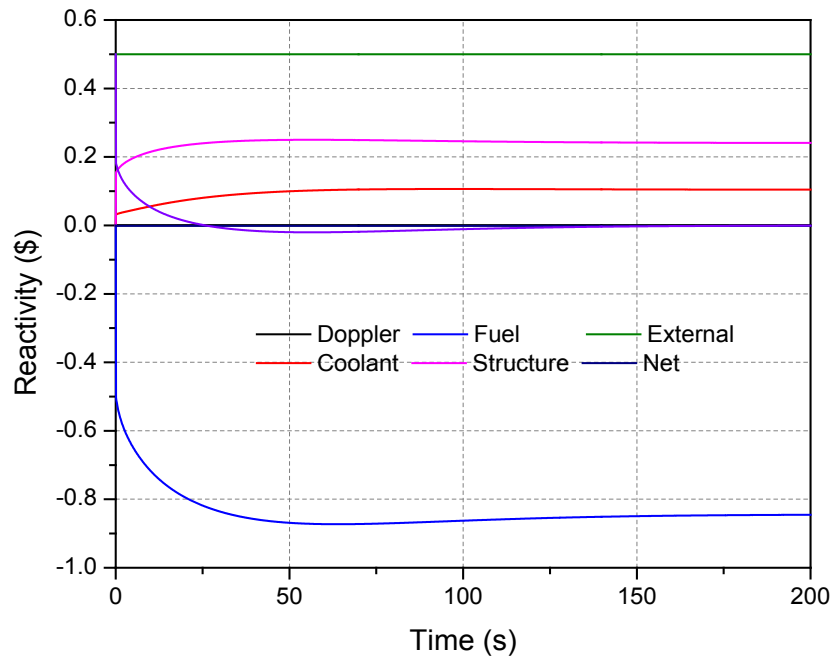


Figure 5.9. Component-wise Reactivity Transients for UTOP Accident

A parametric study was also performed to find the maximum reactivity insertion that can be passively controlled without reactor scram. Figure 5.10 and Figure 5.11 show the transients of the peak coolant temperature and the normalized power for a step reactivity insertion from 0.5 \$ to 2.5 \$. As expected, the peak coolant temperature and the peak power become higher with increasing reactivity insertion. However, it can be seen that the peak coolant temperature

stays below the sodium boiling temperature for a step reactivity insertion up to 2.5 \$. In this case, the peak power increases up to 2.7 times of the nominal power within a short period and eventually decreases to the nominal power.

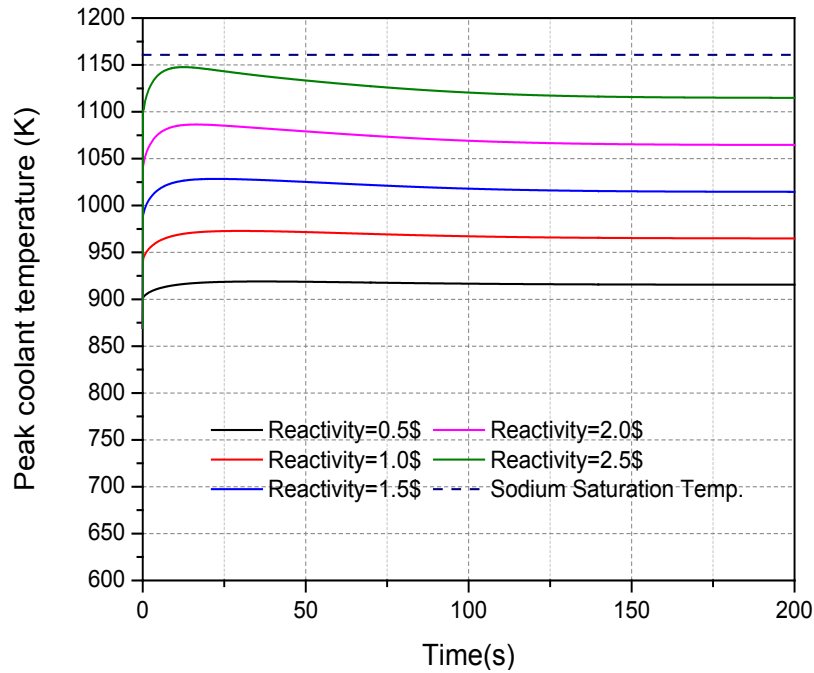


Figure 5.10. Transient of Peak Coolant Temperatures for UTOP Accident with Different Reactivity Insertions

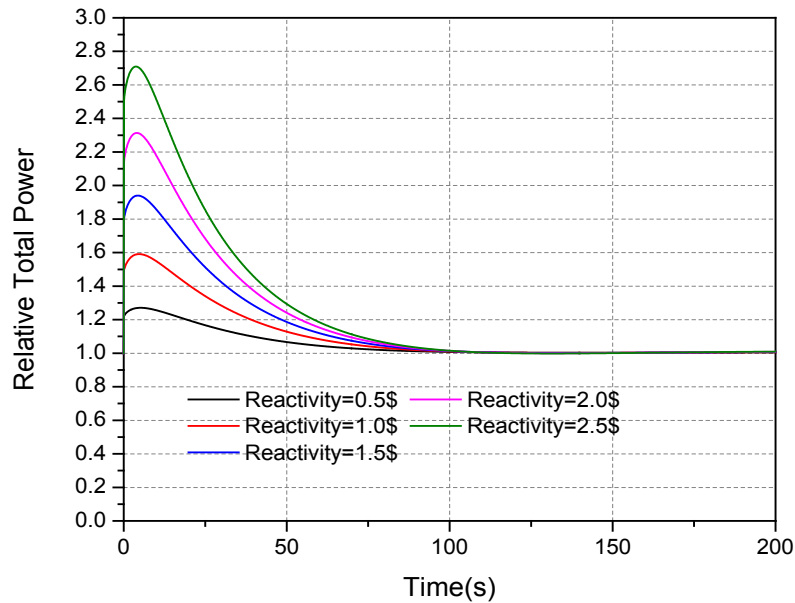


Figure 5.11. Transient of Total Power for UTOP Accident with Different Reactivity Insertions

5.2.2. Unprotected Loss of Heat Sink

For the ULOHS accident, it is assumed that the steam turbine is tripped and thus the heat ejection by the balance of plant terminates. This increases the coolant inlet temperature monotonically while the flow rate and power remain constant. The raised coolant inlet temperature increases the structure and fuel temperatures. The fuel density reduction due to thermal expansion introduces a negative reactivity feedback while the coolant and structure density reductions introduce positive ones. The fuel, structure, and coolant temperature coefficients are -2.07 cents/°C, 0.23 cents/°C, and 0.49 cents/°C, respectively. As a result, the negative reactivity introduced by the fuel temperature increase overwhelms the positive reactivity from the increased coolant and structure temperatures. The resulting negative net reactivity makes the power decrease. Figure 5.12 shows the time-dependent behaviors of coolant, fuel and structure temperatures in the hot channel. The power transient and the component-wise reactivity transients are shown in Figure 5.13 and Figure 5.14, respectively. It can be seen that the total power of the ULOHS transient converges to the same level as the decay heat level, i.e., the SLFFR design has an inherent shutdown capability against a ULOHS accident. At 600 seconds into the transient, the decay heat reduces to ~2.0% of full power although the fission power is almost zero. Since the heat removal capacity of DRACS is 1 % of the rated power, the coolant temperature keeps increasing until the decay heat balances the heat ejection by the DRACS. The inlet and outlet pressure also gradually increase due to the thermal expansion of the sodium within the upper and lower plenum, which are considered as compressible volumes. This results in an increase of sodium saturation temperature from 1203 K to 1227K. Thus, the coolant outlet temperature would have a margin of ~240 °C to the sodium boiling point. Once the decay heat becomes smaller than the DRACS heat removal capacity, the coolant temperature will start to decrease slowly. The structure and fuel temperatures will subsequently decrease but to a slightly larger degree because of reduced decay heat. The decreasing fuel temperature would increase the net reactivity and bring the system back to a critical state. At a new steady state, the positive reactivity introduced by increased coolant and structure temperatures is compensated for by the negative reactivity due to increased fuel temperature, and the net reactivity becomes zero.

At the early stage of the transient, the average fuel temperature in the hot channel decreases while the hot-channel coolant outlet temperature increases. Initially, the power to flow ratio of the hot channel is 1.2 times larger than that of the average and periphery channel. Thus, the increment in the average fuel temperature relative to the average coolant temperature in the hot channel is also about 1.2 times larger than that in the average and periphery channel. Because of the negative feedback due to the increased coolant inlet temperature, the reactor power rapidly decreases to the decay heat level with time, and hence the coolant temperature rise across the core decreases in all three channels. The coolant temperature rise decreases more rapidly in the hot channel than in the average and periphery channels since the channel power reduction is proportional to the initial power. As a result, in the hot channel, the enhanced heat transfer rate from fuel to coolant exceeds the heat generation rate at the reduced power level, making the averaged fuel temperature decrease. At ~40 seconds, the hot channel averaged fuel temperature reaches the minimum of 944K and start to increase due to the increased coolant inlet temperature. At 600 seconds into the transient, the core temperatures are converged to ~980K.

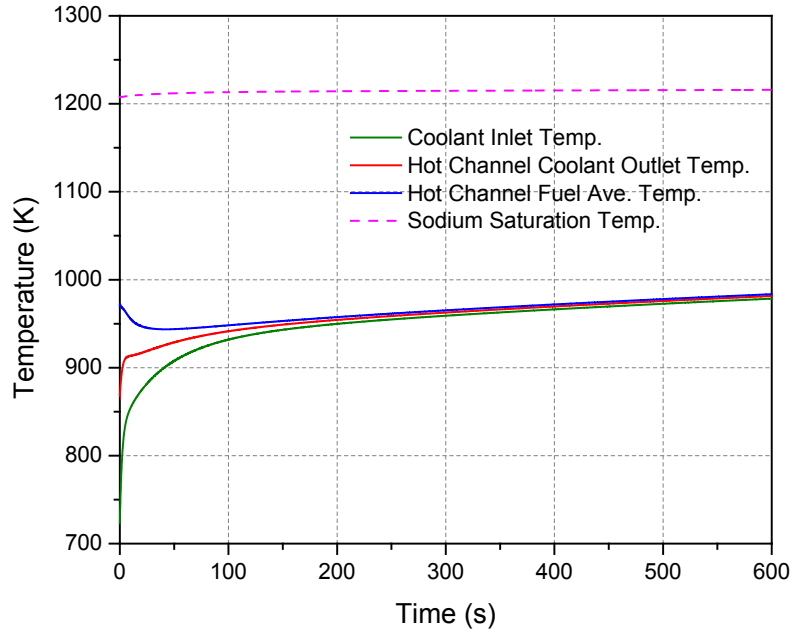


Figure 5.12. Transient of Coolant Inlet and Hot Channel Temperatures for ULOHS Accident

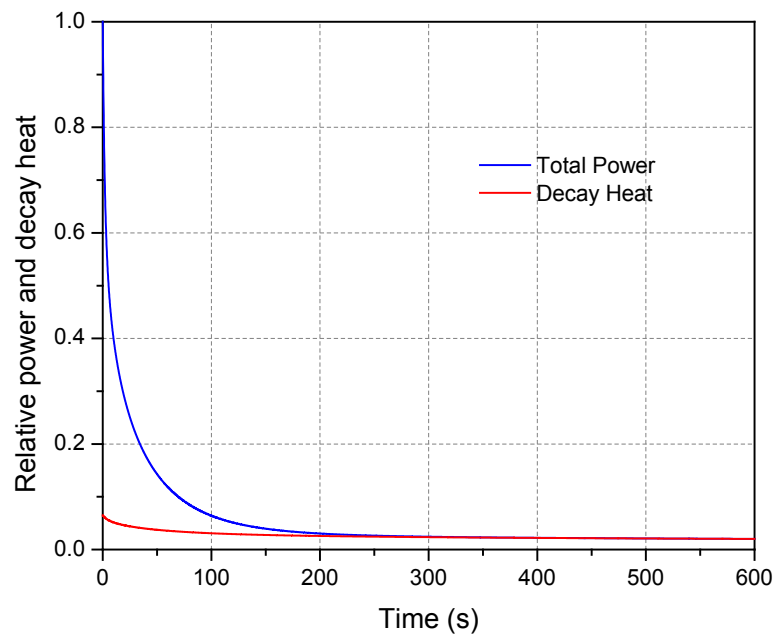


Figure 5.13. Transients of Total Power, Decay Heat, and Flow Rate for ULOHS Accident

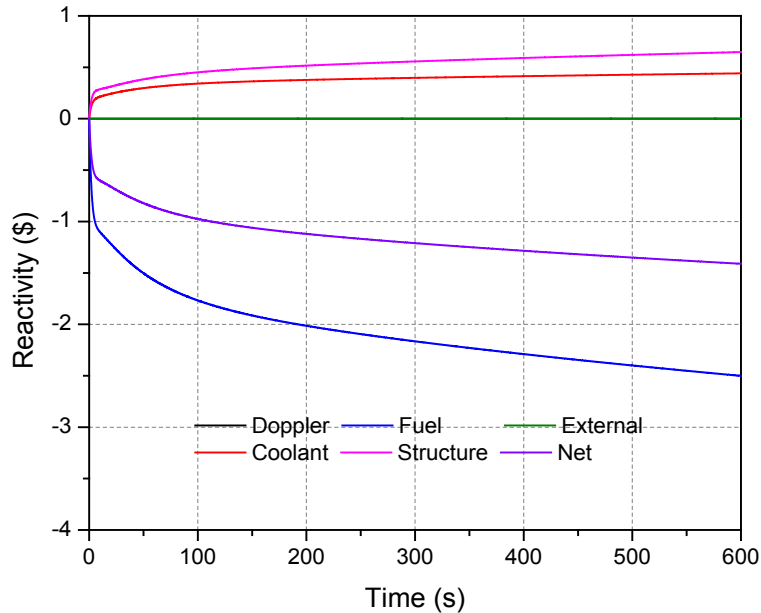


Figure 5.14. Component-wise Reactivity Transients for ULOHS Accident

5.2.3. Unprotected Loss of Flow

In the ULOF accident, it is assumed that all the power to the primary pumps is lost and the reactor fails to scram. The loss of power to the primary pumps leads to a flow coast-down, governed by the mechanical inertia of the pumps. In this analysis, a pump-halving time of 8 seconds is assumed. Figure 5.15 shows the coolant temperature transients for the ULOF accident. With the gas expansion modules (GEMs), the coolant outlet temperatures in the hot, average and periphery channels can be maintained below the sodium boiling temperature during the entire ULOF accident. At around ~58 seconds into the transient, the coolant outlet temperatures in the hot, average and periphery channels reach the maximum values of 912K, 851K and 789K, respectively. The peak coolant temperature in the hot channel has a margin of 288K to the sodium boiling point.

As shown in Figure 5.17, GEMs introduce a large negative reactivity rapidly through enhanced leakage. Due to the rapid negative reactivity insertion, within around 18 seconds of the transient, the total power decreases slightly faster than the decrease of the flow rate as shown in Figure 5.16. The power to flow ratio is less than one, causing the fuel temperature to decrease. The decreased fuel temperature introduces a large positive reactivity, which compensates for part of the negative reactivity induced by the GEMs and structural material density feedback. At around 20 seconds, the GEM worth reaches the maximum value in magnitude of -2.28\$. At the asymptotic state, the negative reactivity induced by GEMs, structure density change and coolant density change is fully compensated by the positivity reactivity due to the decreased fuel temperature, and the net reactivity approaches to zero. The pump head decreases almost to zero after around 50 seconds, and from this moment, the flow is driven mainly by the natural circulation. The fully established natural circulation flow rate is 4.6 % of the nominal flow rate.

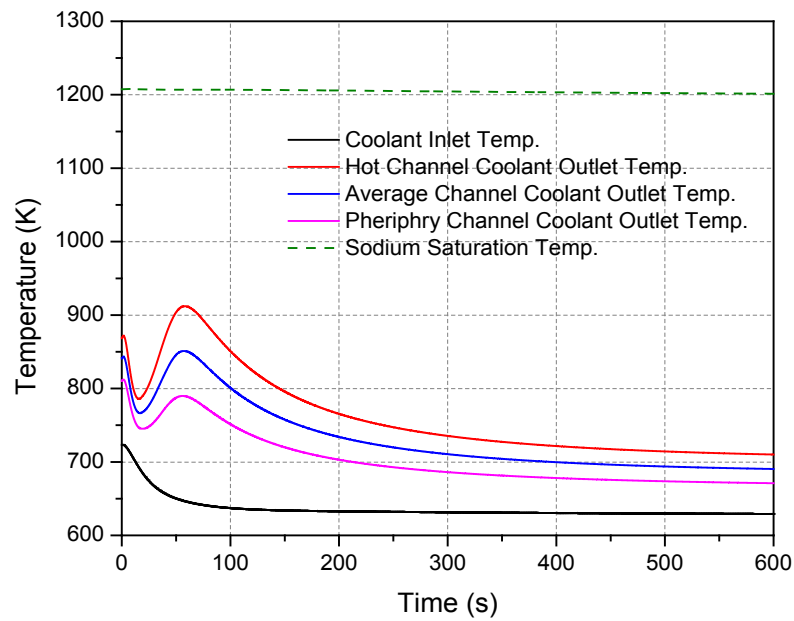


Figure 5.15. Transients of Coolant Temperatures for ULOF Accident

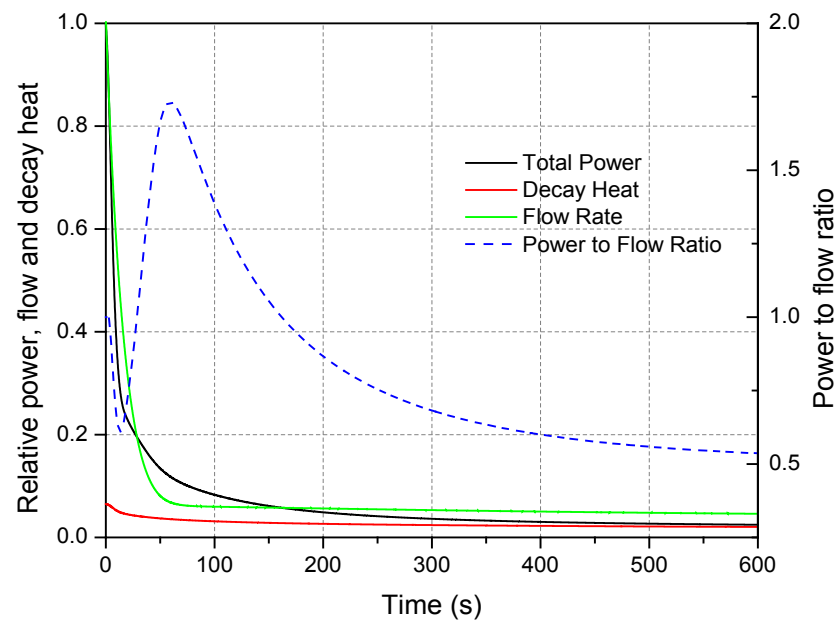


Figure 5.16. Transients of Total Power, Decay Heat, Flow Rate and Power to Flow Ratio for ULOF Accident

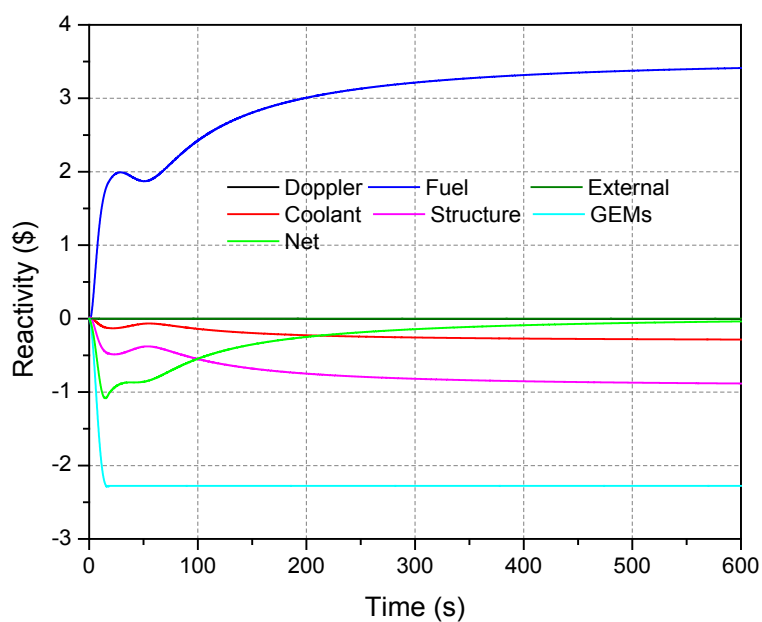


Figure 5.17. Component-wise Reactivity Transients for ULOF Accident

6. Evaluation of Technology Readiness

6.1. Technology Readiness Levels

The Global Nuclear Energy Partnership (GNEP) program established technology readiness levels for evaluating the three technologies that comprised the program, namely, the Advanced Recycling Reactor, the fuel fabrication plant, and the reprocessing facility. These three facilities were to address the safe, secure expansion of nuclear power both internationally and domestically while reducing proliferation risks and effectively addressing the challenges of nuclear waste disposal. The technology readiness criteria developed in the GNEP program were used in evaluating the SLFFR for commercial applications.

Technology Readiness Levels are a systematic metric/measurement system that supports assessments of the maturity of a particular technology and the consistent comparison of maturity between different types of technology. The TRL approach has been used by the National Aeronautics and Space Administration (NASA) space technology planning and by Department of Defense for many years. Figure 6.1 provides a summary view of the technology maturation process model for NASA space activities for which the TRLs were originally conceived; other process models may be used. However, to be most useful, the general model must include: (a) ‘basic’ research in new technologies and concepts (targeting identified goals, but not necessary specific systems); (b) focused technology development addressing specific technologies for one or more potential, identified applications; (c) technology development and demonstration for each specific application before the beginning of full system development of that application; (d) system development (through first unit fabrication); and (e) system deployment and operations.

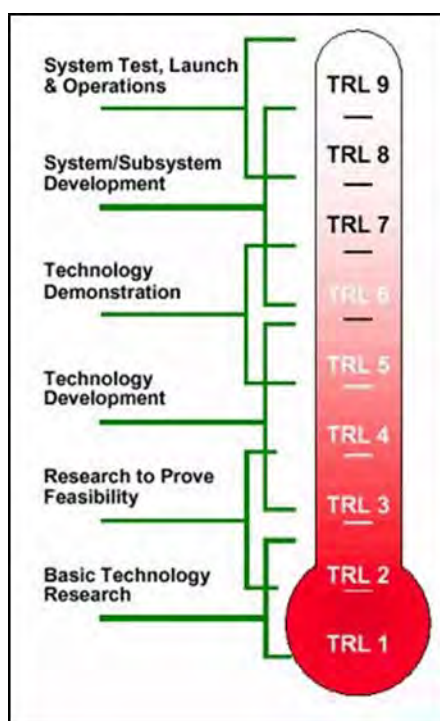


Figure 6.1. NASA Technology Readiness Levels

A TRL assessment can be used to inform technology development plans because the identification of technology readiness levels provides critical information to determine the research needed to advance each technology. It also provides a framework for coordinating work among the Department of Energy, national laboratories, universities, industry, and the international community.

As discussed in a Government Accountability Office Report [73], the experiences of government and commercial technology development programs indicate that demonstrating a high level of maturity before new technologies are incorporated into product development programs puts those programs in a better position to succeed. For technologies that are successfully developed, the gap between a technology's maturity as measured by its current TRL and the intended final target was recognized and closed before product development began, improving the chances for successful cost and schedule outcomes.

Two conditions are critical to closing the maturity gap. First, the right environment for maturing the technology must exist. Key to this environment is making the science and technology organization, rather than the program or product development manager, responsible for maturing the technology to a high TRL. When a maturity gap persists, managers are given the flexibility to take the time to mature the technology or decrease product requirements so that they can use another, already mature technology. Second, both technology and project managers are supported by disciplined processes, readily available information, readiness standards, and authority to ensure technology was ready for products. This support enables these managers to safeguard product development from undue technology risks.

Definitions and summary descriptions of TRLs for each technology area examined are provided in the following tables. The TRLs and illustrative examples related to an advanced recycling reactor ⁷ and its major sub-systems and components are given in Table 6.1 to Table 6.6. A summary level indication of the readiness of these technologies is also shown in these tables. The federal role in improving technical maturity diminishes as the technology approaches a level that is suitable for commercial deployment.

As shown in Table 6.4 to Table 6.6, the technical maturity of a conventional fast reactor component technology is high, and the technical risk is limited so long as program managers stay within the current fast reactor technology knowledge base. Components with technology readiness levels 7 or above should be ready for introduction into a sodium-cooled fast reactor prototype. A critical item for the GNEP transmutation mission was the development of transmutation fuels. Several of the fast reactor technology components show a range of technology readiness levels. Some fast reactor component technologies have already been successfully demonstrated to the degree that could be deployed with little technical risk. However, a number of the advanced fast reactor technologies, which are needed to achieve the long-term goal of a commercially viable fast reactor system, are not mature enough today for inclusion in an advanced sodium-cooled fast reactor prototype project and therefore require further development.

⁷ The advanced recycling reactor (ARR) is the term for the general concept of using a fast reactor to transmute actinides. The advanced burner reactor (ABR) is a specific facility project within AFCI.

Table 6.1. Advanced Recycling Reactor Technology Readiness Level Definitions

TRL	Category	Description	Advanced Recycling Reactor Definition and Examples
1	Concept Development	Lowest level of technology readiness. Scientific research begins to be translated into applied research and development	<p>New discoveries (i.e., in materials for cladding and ducts) may lead to performance improvement or cost reductions.</p> <p>At this technology readiness level, the basic properties of advanced materials might be studied (e.g., tensile strength as a function of temperature, irradiation effects, and compatibility with fast reactor coolants or fuels) and once shown that the program understands these fundamental properties, the advanced material would mature to the next TRL level.</p>
2		<p>Invention begins. Once basic principles are observed, practical applications can be invented. Applications are speculative and there may be no proof or detailed analysis to support the assumptions.</p>	<p>Although sodium-cooled fast reactor technology is relatively mature, new discoveries may result in performance improvements or cost reductions in future plants.</p> <p>For example, following the observation of advanced materials properties at TRL 1, the potential applications of the new material for structural materials applications, fast reactor fuel cladding, etc. can be defined. At this level, the application is still speculative; there is no experimental proof or detailed analysis to support the conjecture.</p>
3		Active research and development is initiated. This includes analytical studies and laboratory studies to validate physically analytical predictions of separate elements of the technology.	<p>Analysis of the performance of SSCs (System, Structure or Component) produces favorable results, but testing is needed to validate the prediction and provide data supporting key features. Examples would include testing of printed circuit heat exchangers to confirm performance with sodium and testing of new concepts for under-sodium in-service inspection of components and structures. In addition, a compact fast reactor loop concept might depend on the irradiation and thermo-physical properties of an advanced material: in this example, TRL 3 might be attained when these materials have undergone irradiation with subsequent post-irradiation examination and their post-irradiation thermo-physical properties are defined and known if everything else is deemed satisfactory.</p>

Table 6.2. Advanced Recycling Reactor Technology Readiness Level Definitions (continued)

TRL	Category	Description	Advanced Recycling Reactor Definition and Examples
4	Proof-of-Principle	Integration of basic technological components for testing in laboratory environment. Includes integration of “ad hoc” hardware in the laboratory.	Laboratory testing of individual components or portions of systems has been completed successfully. Examples would include separate effects testing of component performance, such as heat exchanger plugging tests or metallurgical compatibility testing or successful operation of gas-turbine components that might be used in a supercritical carbon dioxide (CO ₂) system.
5		Integration of basic technological components with realistic supporting elements for testing in relevant environment.	Individual components or portions of systems have been successfully tested at less-than-full scale in a test reactor, out-of-pile test facility or in another application. Examples would include successful testing of a section of a fuel element in a test reactor or successful testing of individual components of a sodium system in a sodium loop. For example, a full-size electromagnetic pump promising a simpler primary plant system design will be built and tested with a fully-immersed sodium environment (in a sodium component testing facility) and tested with its power supply and control system.
6		Model or prototype system testing in relevant environment	Systems, subsystems or components have been demonstrated at less-than-full scale in a test reactor, in an out-of-pile test facility or in another application. Examples would include successful demonstration of individual fuel elements in a test reactor, successful operation of a section of a steam generator in a sodium loop or successful operation of a supercritical CO ₂ energy conversion system under prototypic but non-nuclear conditions.

Table 6.3. Advanced Recycling Reactor Technology Readiness Level Definitions (continued)

TRL	Category	Description	Advanced Recycling Reactor Definition and Examples
7	Proof-of-Performance	Demonstration of prototype system in an operational environment at the engineering scale.	The SSC or system behavior has been successfully demonstrated under prototypic conditions in a test reactor or in an out-of-pile test facility if the SSC or system will never see a radiation environment during anticipated deployment operations. Examples would include successful testing of a fuel assembly or multiple fuel elements in a test reactor or successful operation of a sodium-water steam generator in a large test loop.
8		End of system development. Technology proven to work in operational environment at the engineering to full scale.	The SSC has been successfully deployed in operations of a sodium-cooled test reactor or a prototype of the SSC has been successfully deployed in power reactor operations, or a system characteristic has been demonstrated in an experiment (i.e., the Experimental Breeder Reactor-II (EBR-II) passive safety demonstration).
9		Full-scale application of technology in its final form at mission conditions.	<p>The system, structure or component has been successfully deployed in operations of a commercial sodium-cooled power reactor (or another commercial power reactor if the SSC is not sodium-related, such as containment structures), or a relevant system behavior has been demonstrated in such a reactor.</p> <p>This TRL does not include technologies for planned product improvement of ongoing or reusable systems. For example, an advanced fuel handling system concept for the commercial Advanced Recycling Reactor (ARR) plant would not start at TRL 9: such ‘technology’ upgrades would start over at the appropriate level in the TRL system.</p>

Table 6.4. Example – Advanced Recycling Reactor – Transmutation Technologies from GNEP Program

Fast Reactor Component	Technology Maturity	Technology Risk Description
Transmutation Fuel	TBD	TBD
Coolant Control Technology	TRL 8	Conventional technology demonstrated at full scale. There is very little technology risk associated with sodium coolant control technologies.
Core Materials	TRL 8	Demonstrated at full scale. Proven steel materials, but no vendor.
Startup Fuel	Mixed Oxide (MOX) – TRL 8-9 Metal U-Pu-Zr – TRL 7-8 Metal U-Zr – TRL 8-9	Both MOX and metal startup fuel technologies have been matured to the degree that they could be handed off to program managers with very little technology risk so long as compositions and performance requirements are within the range of test results.
Primary System	Conventional Primary Plant Systems – TRL 8 Compact Primary Plant Components – TRL 4-6 Advanced Primary Pumps– TRL 4-6	There is very little technology risk associated with using conventional demonstrated primary plant system and components. Compact and advanced primary pumps, which may be needed to reduce costs, are not mature technologies and therefore require further technology development and maturation before inclusion in fast reactor designs.
Reactor Vessel and Structures	TRL 8-9	There is very little technology risk associated with reactor vessels and structures using conventional demonstrated plant configurations and materials of construction.

Table 6.5. Example – Advanced Recycling Reactor – Transmutation Technologies from GNEP Program (continued)

Fast Reactor Component	Technology Maturity	Technology Risk Description
Structural Materials	Conventional stainless steels – TRL 8-9 Advanced stainless steels – TRL 3-5	Related to the reactor vessel and structures above, there is very little technology risk associated with using known and demonstrated conventional stainless steels for structural materials. However, there are advanced materials that are expected to contribute to reducing the costs of primary plant systems and structures. These advanced materials are not ready for program or product development and need to go through an appropriate technology maturation process.
Balance of Plant	Steam Generators – TRL 7 Steam Plant – minus steam generators – TRL 9 Advanced Energy Conversion Systems – TRL 4-6	Although there were some problems with early sodium steam generators, there is now substantial satisfactory experience from EBR-II, France, Japan, and Russia. Advanced energy conversion system (CO ₂ Brayton) is being considered for cost reduction. This technology must go through a maturation process before applications in the ABR program.
Containment	Light Water Reactor Containment technology – TRL 9 Advanced Containment technology– TRL 4-6	Demonstrated at full scale. Some features of advanced containment designs will require technology maturation.

Table 6.6. Example – Advanced Recycling Reactor – Transmutation Technologies from GNEP Program (continued)

Fast Reactor Component	Technology Maturity	Technology Risk Description
Seismic Isolation	Rubber and steel seismic isolators – TRL 7 Multiple friction pendulum system – TRL 5-6	There is limited experience (2 plants) in French Light Water Reactor designs and there are many applications in large buildings using rubber/steel isolators. There is less experience with multiple friction pendulum systems and some testing and technology maturation would be needed for widespread applications.
Instrumentation and Control	Analog Control – TRL 9 Digital Control Systems – TRL 7-8 Advanced passively-cooled nuclear instrumentation – TRL 5	Analog instrumentation and control technology have been demonstrated at full scale in both light water and fast reactors and are a mature technology. Digital control systems and advanced nuclear instrumentation systems are examples of advanced Instrumentation and Control components and systems that still require maturation.
Maintenance and Inspection Technology	Under sodium inspection system – TRL 5 Compact robotic inspection vehicle – TRL 5	New techniques for in-service inspection, especially under sodium inspection technology, needs to be demonstrated.
Fuel Handling Systems	Conventional dual rotatable plug with straight pull – TRL 8 Advanced compact pantograph with single rotatable plug – TRL 5	A conventional dual rotatable plug with straight pull fuel handling system could be deployed with very little technology risk. For cost reduction mission, a simplified fuel handling design needs to be developed.

6.2. Technology Readiness Evaluation for SLFFR Systems

Using the above criteria in Table 6.1 and the design documents (quarterly and annual reports from the project teams at Purdue and Argonne) for the SLFFR; a technology readiness assessment for the SLFFR was performed. The readiness of the following systems and components was estimated:

- Coolant
- Coolant Purification Technology
- Core Structural Materials
- Startup/Driver Fuel
- Primary System Configuration
- Reactor Vessel and Structures
- Intermediate Heat Exchanger
- Primary and Secondary Pumps
- Structural Materials
- Inert Gas System
- Cover Gas Cleanup System
- Reactivity Control System
- Balance of Plant
- Containment
- Seismic Isolation
- Instrumentation and Control
- Maintenance and Inspection Technology
- Fuel Handling Systems

The technology readiness of the above systems and components was compared with the criteria from Table 6.4 to Table 6.6. The technology readiness assessment is provided as followed:

Coolant - TRL 8

The technology maturity of coolant of SLFFR is in level eight. Sodium technology is considered conventional technology that had been demonstrated at full scale. There are at least two manufacturers of reactor grade sodium, DuPont (U.S.) and MSSA Métaux Spéciaux (France). There is another company in Mongolia, which also produces reactor grade sodium. However, it is currently produced for domestic applications in China. Reactor grade sodium can be delivered in tanker cars via rail, in ISO containers via truck, or in smaller containers like drums and “milking” pots. Grades of sodium that are more pure than reactor grade sodium are also available if needed.

Coolant purification technology - TRL 8

Once the sodium arrives, it is heated, filtered, and purified to remove oxides in the sodium during the primary and secondary system filling process. Crystallizer tanks are used to remove the oxides, hydrides, and other impurities associated with sodium systems. This crystallizer technology has been used since the 1940's. Carbon filter traps are used for the removal of nuclide contaminants in the sodium such as cesium. There is very little technology risk associated with sodium coolant control technologies.

Fuel Tank Structural Materials - TRL 3

Since the fuel tank strength is important for withstanding large thermal stresses and preventing tube distortion during fuel freezing, Ta-10W was selected as the fuel container material. Since tantalum is compatible with sodium, sodium was selected as the coolant. The material properties of Pu-Ce-Co fuel, Ta-10W, and sodium coolant were compiled for the subsequent neutronics and computational fluid dynamics calculations. A conservative limit of 700 °C was also selected for the fuel and container interface temperature. The core structural materials will have to withstand the effects of molten fuel corrosion and irradiation for the full life of the reactor plant or at least half the life with the design capability to remove the reactor fuel tank. The fuel, fuel tank, and sodium system will need to be tested under prototypic conditions to understand its performance for the life of the SLFFR plant. This technology system (although it appears to work on paper) will need to be tested in stages and is evaluated as an immature technology readiness especially under irradiation.

Fuel - Startup/Driver - TRL 2~3

The Pu-Ce-Co ternary fuel has a low melting temperature of 420 °C for a wide range of Pu content. In the current design, the selected TRU-Ce-Co fuel contains 16.8% minor actinides of the total TRU at the beginning of equilibrium cycle. It is assumed that the fuel melting temperature would not be changed significantly by adding this amount of minor actinide into the fuel. Experimental and simulation studies would be necessary to investigate the effect of the minor actinide concentration on the melting temperature of the assumed fuel alloy. A reduced melting temperature would not affect the design significantly. On the other hand, an increased melting temperature makes it necessary to increase the coolant inlet temperature. The current margin to sodium boiling higher than 100 °C for both ULOF and ULOHS accident scenarios indicates that there exists a room for a modest increase in the melting temperature. If the melting temperature is significantly increased, it might be necessary to reduce the coolant temperature rise across the core. This would necessitate an increased coolant flow rate and pump power.

Unlike conventional fast reactors which would be able to startup on a known fuel form that has a very high TRL level such as mixed oxide fuel (TRL 8-9), metallic fuel U-Pu-Zr (TRL 7-8), or metallic fuel U-Zr (TRL 8-9), the SLFFR cannot use a conventional startup fuel. It will be essential that it starts up on its Pu-Ce-Co fuel form and then transitions to the TRU based fuel form. This fuel form will need to undergo development to ensure that it performs adequately under irradiation. This will mean that this molten fuel will need to be irradiated under prototypic conditions in a special reactor to ensure that it will perform correctly for the SLFFR. The technology readiness is evaluated as relatively immature.

Fuel Tank with Flow Tubes - TRL 3

The expansion of the fuel on freezing is an area of concern. The Pu-Co-Ce alloys exhibit large volumetric expansions from 1% to 3% during freezing. Although it was reported that evidence from irradiation tests with Pu-Fe fuel encased in tantalum capsules indicated that the melt freeze cycling is possible without mechanical damage, it is desirable to avoid the fuel from freezing during both normal operational conditions and transient accidents. At the same time, to investigate the consequences of potential freezing, it is necessary to study the freezing characteristics of TRU-Pu-Co fuel. It would also be necessary to investigate higher alloys that provide better strength to withstand large thermal stresses and prevent tube distortion during fuel freezing.

To remove the heat generated in the fuel effectively, the coolant tubes are designed with a small diameter of 1 cm and are arranged in a narrow triangular lattice with a pitch of 1.21 cm. There are 18,181 coolant tubes penetrating the fuel tank, making the fuel tank topologically similar to a once-through steam generator. Thus, the potential risk of tube leak would be an issue, especially the leak along the welds between the coolant tubes and the fuel tank at the ends. The potential causes and mechanisms for coolant tube breach or break need to be studied in detail, including the tube corrosion with the contact on the TRU-Ce-Co fuel under a high temperature, the restraint tube thermal expansion, and the flow induced vibration with a relatively high coolant velocity. A study on the manufacturing technology to increase the reliability of coolant tubes is also required. In addition, it would be worthwhile to study different geometrical arrangements of fuel and coolant to minimize the potential for a fuel leak to the coolant system. Research on the failed tube detection system would be required.

Conventional failed fuel detection systems are based on monitoring increased cover gas activity or detecting delayed neutrons. A cover gas monitoring system mainly detects the xenon and krypton isotopes escaping from breached fuel cladding, and the delayed neutron monitoring system detects delayed neutrons emanating from fission products circulating in the coolant system. However, in the current conceptual design of the SLFFR, gaseous fission products are continuously removed, and a fraction of the fuel is periodically drawn off from the fuel container to a processing facility where nongaseous mixed fission products and other impurities are removed and then the cleaned fuel is recycled into the fuel container. As a result, the applicability of the conventional failed fuel detection systems to SLFFR would be limited. Other methods to detect failed coolant tube need to be developed. One potential method is adding “tagging” isotopes to the recycled fuel, which can be released easily to the coolant system through the tube breach and easy to detect. The fuel tank with flow tubes is considered a relatively immature technology.

Primary System Configuration - TRL7~8

The primary plant system is a conventional sodium loop technology that is close to the conventional plant design used in the Fast Flux Test Reactor and the Large-Scale Prototype Breeder Reactor (LSPB) reactor plants. The reactor vessel assembly is comprised of the reactor vessel, top closure head (or deck), the guard vessel, the vessel/deck support structure, the core support structure, fuel container, core barrel, thermal barriers, shielding, in-vessel sodium piping, and other permanent internal structures. The design is based on the experience with the reactor vessels used for the Fast Flux Test Facility (FFTF) and the Large Scale Prototype Breeder Reactor (LSPB) LMR reactor plants. A major difference, however, is that the design

concept for the SLFFR separates the reactor and guard vessels and also employs a conical ring support structure that avoids the need for welding dissimilar metals. There are no penetrations in the reactor vessel; all equipment – piping, instrumentation, fuel handling equipment, and other components – penetrate the top closure head, or deck. The entire reactor vessel assembly is located in a steel-lined concrete cavity in the reactor containment building. The top of the reactor vessel deck is approximately at grade level. There is an inert gas (argon) blanket between the reactor vessel deck and the bulk sodium free surface. The design of the reactor vessel assembly incorporates appropriate measures and details that will facilitate fabrication, construction, and operational maintenance. The primary coolant pumps and intermediate heat exchangers are located in inert cells around the reactor vessel system. The technology readiness level of this configuration is relatively high.

Reactor Vessel and Structures - TRL 8~9

There is very little technology risk associated with reactor vessels and structures using conventional demonstrated plant configurations and materials of construction.

Intermediate Heat Exchanger - TRL 6~7

The Intermediate Heat Exchangers (IHXs) transfer heat from the radioactive sodium coolant in the primary heat transport system to the nonradioactive sodium coolant in the intermediate heat transport system. Four sodium-to-sodium heat exchangers rated at 250 MWth each are used to transfer the 1000 MWth core power at full-power conditions corresponding to core inlet and outlet temperatures of 450 and 550 °C, respectively. The IHXs are located in shielded and inerted cells.

The heat exchanger arrangement selected is a shell-and-tube counter-current flow arrangement with the primary flow on the shell-side, and secondary sodium flow on the tube side. This configuration maximizes the ability of the IHX to accommodate any pressure transients that may arise if a steam generator tube rupture event were to occur, since for a given tube wall thickness the tubing is much stronger in tension (internal pressure source) versus compression (external pressure source).

The installation of the IHXs is vertically oriented in a shielded cell. Primary sodium enters the shell side of each IHX approximately 20 cm below the upper tube sheet. The introduction of the sodium below the upper tube sheet minimizes the thermal shock to this relatively thick component during transients. The sodium then flows downward through the shell and vents through a 10 cm wide gap around the lower tube sheet that leads to the single 61 cm diameter exit nozzle that discharges directly into the cold leg piping.

The IHX is conventional technology although the choice of materials has not been used in sodium fast reactor applications in the U.S. The tube material is modified 9Cr-1Mo, which has been developed, and code qualified. The steam generators developed in U.S. had 2.25Cr-1Mo steel. It is expected that there will be some fabrication development related to this tube material. In addition, modified 9Cr-1Mo may be the used in the future. The technology readiness of the intermediate heat exchangers is high.

Primary and Secondary Pumps - TRL 6~7

Mechanical centrifugal pumps were adopted for the SLFFR. In the SLFFR design, the location of the suction of the primary pump is critical to ensure sodium circulation under a

variety of operating conditions. Although there are many different types of mechanical pumps, only centrifugal pumps have been used in sodium cooled fast reactors and therefore are considered as the primary candidate.

One sodium pump is used in each IHTS loop. Each unit is a vertically mounted, single stage, single suction, free surface, centrifugal mechanical pump with a lower radial hydrostatic bearing operating in sodium that is fed from the delivery side of the impeller. The pump shaft rotates in two bearings; the lower being a radial hydrostatic bearing and the upper usually a radial-axial roller bearing or a liquid or grease lubricated sliding bearing. The impeller is usually positioned below the hydrostatic bearing. There is an axial or radial guiding duct. A gas shaft seal is placed below the upper bearing, and a flexible coupling connects the shaft of the pump and its variable speed electric drive. The stationary part of the intermediate sodium pump, consists mainly of a stationary tank, tank cover, internal structural assembly, and casing. The tank cover and all internals are removable. A thermal shield is located just below the tank cover. A pressurized argon cover gas is used between the sodium level in the pump tank and the thermal insulation. The cover gas is controlled at a reasonable pressure to maintain the pump net positive suction head (NPSH) available and to prevent air in-leakage into the system.

As in previous designs, each pump is installed in a tank with the piping inlet and exit at the top and bottom of the tank, respectively. The pumps are completely separate so that the IHTS loops can be operated independently to produce the desired operational characteristics.

The technical maturity of mechanical centrifugal pumps is very high. Mechanical pumps are used through the various extant and past sodium-cooled fast reactors.

Emergency Decay Heat Removal (Direct Reactor Auxiliary Cooling System) - TRL 6~7

The direct reactor auxiliary cooling system (DRACS) is a means for removing emergency decay heat from the reactor core. The DRACS system consists of multiple tube and shell heat exchangers made from modified 9Cr-1Mo steel that are submerged in the reactor vessel and that provide for removal of decay heat from the core under planned and emergency conditions. The DRACS system has been used in EBR-II and other reactor plants around the world. The use of modified 9Cr-1Mo steel will necessitate some development effort for this material for sodium applications but the technology development risk is low.

Structural Materials (Conventional Stainless Steels) - TRL 8~9

Related to the reactor vessel and structures above, there is very little technology risk associated with using known and demonstrated conventional stainless steels for structural materials. Known structural materials consist of 304 and 316 series stainless steels.

However, DOE NE-7 is in the process of developing advanced structural steels. There are advanced materials that are expected to contribute to reducing the costs of primary plant systems and structures. These advanced materials are not ready for program or product development and need to go through an appropriate technology maturation process. NE-7 is currently working on an austenitic stainless steel that will improve the performance of structural materials for sodium applications.

Inert Gas System (Argon Inert Gas System) - TRL 8~9

Argon gas will be used as the inert gas system. A pressure on demand system will be used to prevent air ingress into the primary and other liquid sodium systems. Argon inert gas has

been used since the beginning of sodium-cooled fast reactor technology. Argon is heavier than air and is very suitable for sodium applications. Argon gas is used in all conventional sodium-cooled fast reactors and the technology readiness for this inert gas system is very high.

Cover Gas Cleanup System - TRL 6~7

The argon cover gas will require cleaning periodically to remove contaminants. A typical system consists of a vapor trap, filters, compressors, tanks, cryogenic distillation columns, charcoal filters, piping and valves. This technology is very well known and there is very little technology risk associated with adopting this type of cover gas cleanup system.

Reactivity Control System - TRL 6

The fuel container has twelve hexagonal holes for the primary and secondary control systems. The drive and linkage mechanisms for the control rods will be a conventional system that was used in FFTF or CRBRP.

Balance of Plant (Steam Generators) - TRL 6~7

The SLFFR adopted a conventional steam plant technology with sodium-heat steam generators. Although there were some problems with early sodium steam generators, there is now substantial satisfactory experience from EBR-II, France, Japan, and Russia. The technology readiness for conventional steam generators is high, but there may be a learning curve for the fabrication and response of the selected steam generators for the SLFFR.

Balance of Plant (Steam Plant minus Steam Generators) - TRL 8~9

Conventional steam plant technology for a sodium-cooled fast reactor is a relatively mature technology with little technical risk. The main risk comes in the integration of the steam plant with the intermediate heat transport system and the control system put in place for the plant.

Containment - TRL 8~9

The SLFFR uses a conventional LWR-type containment of reinforced concrete that has been demonstrated at full scale. The containment is steel lined in areas where sodium may be in contact with concrete.

Seismic Isolation (Rubber and Steel Seismic Isolators) - TRL 7

There is limited experience (2 plants) in French Light Water Reactor designs and there are many applications in large buildings using rubber/steel isolators. The largest risk associated with seismic isolation technology for reactors in the U.S. will be regulatory risk, as the NRC has never seen an application for licensing that includes base isolation technology applied to the reactor. The GE-PRISM plant was submitted for pre-application licensing to the NRC. The SLFFR may or may not have base isolation technology included in the reactor plant. The issues associated with aircraft impact on base isolated structures will have to be addressed. Seismic isolators are used specifically to dampen the impact of earthquakes on structures. An aircraft impact on a structure varies depending upon whether the structure is fixed or on base isolation. Issues may arise with base isolated structures.

Seismic Isolation (Multiple Friction Pendulum System) - TRL 5~6

There is less experience with multiple friction pendulum systems and some testing and technology maturation would be needed for widespread applications for conventional and advanced reactor plants.

Instrumentation and Control (Analog Control) - TRL 9

Analog instrumentation and control technology have been demonstrated at full scale in both light water and fast reactors and are a mature technology.

Instrumentation and Control (Digital Control) - TRL 7~8

Digital control systems and advanced nuclear instrumentation systems are examples of advanced Instrumentation and Control components and systems that still require maturation.

Maintenance and Inspection Technology (Under Sodium Inspection System and Compact Robotic Inspection Vehicle) - TRL 5

New techniques for in-service inspection, especially under sodium inspection technology, needs to be demonstrated. Both technologies are relatively immature and will need to be developed.

Fuel Handling Systems (Conventional Dual Rotatable Plug with Straight Pull) - TRL 5~6

In some ways, the refueling scheme is simpler for the SLFFR because only a single transfer machine will be used. Typical fast reactors have two refueling machines, one in-vessel and one ex-vessel. For the SLFFR, the molten fuel is removed using the fuel-unloading machine that is designed to lower a gripper device that connects to a fuel sipper. This fuel sipper is made of TBD⁸ material and is inserted into the periphery of the molten fuel through the fuel transfer pipe. A combination of inert gas pressurization and suction are used to fill the fuel sipper with spent fuel. The fuel-unloading machine then retracts the fuel sipper from the molten core. The spent fuel within the sipper then freezes during the removal process. The fuel sipper is then removed from the reactor vessel and inserted within the spent fuel transfer cask. Multiple sipper pipes with spent fuel can be contained within the spent fuel cask based upon criticality and shielding requirements. The spent fuel cask is then transferred to the fuel cycle building via reactor containment doors and a transfer tunnel between the two buildings. Reactor containment is continuously maintained in this configuration. Recycled fuel from the Fuel Cycle Building is made into metallic rods, which are introduced during the refueling process to ensure that the reactor maintains criticality. The metallic recycled fuel rods are melted upon entry into the reactor core canister.

After the fuel is removed from the reactor vessel through the “sipper”, it is processed in the fuel cycle facility and then blended with new fuel. This new recycled fuel, in a metallic solid

⁸ This material will need to be developed. Ideally, the sipper tube will be made such that it can be reused in the reactor. A suitable material would allow the used fuel mixture to be pulled into the sipper in a molten state, followed by freezing (transition from molten to solid state), and then mold release from the sipper. The used fuel located in the sipper tube would freeze upon retraction from the core or during the process of removal from the reactor vessel.

form, is then inserted into the fuel insertion device to ensure that required core excess reactivity is ensured.

The development of the refueling system is relatively immature and it will require some technology development effort.

Fuel Reprocessing System - TRL 4~6

SLFFR fuel is a liquid metal alloy of TRU elements, cerium and cobalt with a nominal composition of 52.4 wt% TRU, 37.5 wt% Ce, and 8.9 wt% Co (34.0, 41.4, and 23.6 at%). Fuel with a burnup of 5.79% is discharged at a rate of 32.46 kg/day. The proposed fuel recycle process is capable of removing a sufficient fraction of fission products to maintain a low fuel melting point, and recover more than 99% of the actinides. The cerium and cobalt that must be replaced each cycle depends inversely on the fractions of rare earth and noble metal fission products remaining in the processed fuel. However, rare earths, other than cerium, and noble metals raise the fuel melting temperature.

Molten fuel from the reactor is contacted with a chloride salt (basically LiCl-KCl) in the Salt/Fuel Contactor. The reduction-oxidation conditions are controlled such that the “active” metal fission products (Rb, Cs, Sr, Ba, Sm, and Eu⁹) are oxidized and dissolved in the salt as mono- or divalent chlorides. These elements are easily separated from actinides and other rare earths that form trivalent chlorides. The redox conditions are controlled to oxidize enough rare earths to limit their concentration in the recycled fuel. A proportional amount of alloy cerium is also extracted into the salt and must be replaced in the recycled fuel. Because actinide chlorides are thermodynamically less stable than rare earth chlorides, actinide content of the salt will be about 1 – 2% of the rare earths. Noble metal fission products are not oxidized and they remain in the metal phase.

To remove noble metal fission products, a portion of the liquid fuel is withdrawn from the Contactor, solidified, chopped, and loaded into wire baskets. The loaded baskets become the anodes of the electrorefiner, which contains an electrolyte of LiCl-KCl-(TRU)Cl₃-(Ce-RE)Cl₃ and operates below the fuel melting point. Passing a current between the electrodes oxidizes the actinides and rare earths at the anode and deposits them as metals at the cathode leaving cobalt and noble metals in the anode basket. The metals on the cathodes with adhering electrolyte are returned to the Fuel Contactor. Salt with plutonium must be added to the electrorefiner to make up for the salt on the cathodes and maintain the actinide concentration in the electrorefiner salt. Salt adhering to the cobalt and noble metals in the anode baskets is removed by vaporization and returned to the electrorefiner. The noble metal-cobalt alloy remaining after salt removal is a waste.

A portion of the salt in the contactor is removed and mixed with zeolite-A. Contact with zeolite can remove essentially all of the di- and trivalent chlorides, and a large fraction of Rb and Cs chlorides. The remaining salt is returned to the salt/fuel contactor. Salt-occluded zeolite, the reaction product between zeolite and chloride salts, is blended with additional zeolite and glass frit, and then sintered at a high temperature to convert the zeolite to sodalite and make a waste form that consists of a glass matrix with dispersed sodalite particles. Sodalite

⁹ In this process, it is likely that Sm and Eu form divalent chlorides and behave similar to alkaline earths.

encapsulates the chloride ions along with some of the fission product cations. The balance of the fission product ions are dissolved in the glass as oxides.

Plutonium is added to replace that burned, cerium is added to replace that lost with the salt, and cobalt is added to replace that lost in the metal waste. A portion of the make-up plutonium is supplied in the makeup salt of the electrorefiner.

The proposed pyro-chemical process for treating discharged SLFFR fuel is based on the liquid metal-salt chemistry developed in the Chemical Technology Division at Argonne National Laboratory (ANL). It appears to be feasible although additional experimentation is needed. The equilibrium between the fuel alloy and salt in the Contactor is based on known thermodynamic free energies of the components. The metal and salt phases were assumed ideal solutions because activity coefficients are largely unknown. The Nuclear Engineering Division of ANL has an ongoing program to develop electrorefining. The required process equipment has, for the most part, been demonstrated and reported primarily by Argonne's Chemical Engineering Division and Oak Ridge's Molten Salt Reactor program, but the full process still needs to be demonstrated.

7. Conclusions

For effective burning of hazardous TRU elements of used nuclear fuel, a transformational advanced reactor concept SLFFR has been proposed based on stationary molten metallic fuel. The overall simplified concept is to use non-flowing liquid metallic alloy TRU fuel in a closed fuel container. The fuel enters the reactor vessel in a solid form and then it is heated to molten temperatures in a small melting heater. The fuel is contained within a closed, thick container with penetrating coolant channels, and thus it is not mixed with coolant nor flow through the primary heat transfer circuit. The makeup fuel is semi-continuously added to the system, and thus a very small excess reactivity is required. Gaseous fission products are also removed continuously, and a fraction of the fuel is periodically drawn off from the fuel container to a processing facility where non-gaseous mixed fission products and other impurities are removed and then the cleaned fuel is recycled into the fuel container.

A reference core design and a preliminary plant system design of a 1000 MWt TRU-burning SLFFR concept was developed using TRU-Ce-Co fuel, Ta-10W fuel container, and sodium coolant. Conservative design approaches were adopted to stay within the current material performance database. Detailed neutronics and thermal-fluidic analyses were performed to develop a reference core design. The analysis results indicate that the SLFFR of a zero TRU conversion ratio would be feasible while satisfying the conservatively imposed design constraints. The calculated reactivity feedback coefficients also showed that the prompt reactivity feedback due to liquid fuel thermal expansion is sufficiently negative. Compared to the solid fuel reactors with the same TRU conversion ratio, the core size and the reactivity control requirement are reduced significantly.

To access the passive safety features of the reference core design, a multi-channel safety analysis code (MUSA) tailored for a safety analysis of SLFFR was developed. The MUSA code consists of the following computational modules: a point kinetics module, a core thermal-fluidic module based on one-dimensional parallel channels, a primary loop thermal-fluidic module based on compressible volumes and liquid segments, and a reactivity-feedback calculation module. In order to investigate the safety characteristics of SLFFR, three beyond design basis accidents (BDBAs) were analyzed including the UTOP, the ULOHS, and the ULOF accidents. The transient analyses indicated that the thermal expansion of liquid fuel provides a sufficiently large negative feedback reactivity for passive shutdown of these hypothetical double-fault accidents. During the ULOF accident, the GEMs respond quickly to the primary pump head loss and introduce a large negative reactivity so that the peak outlet temperature of sodium coolant has a sufficient margin to the sodium boiling point.

A reference plant concept of 1000 MWt SLFFR was also developed. The primary system is configured in a loop-type arrangement with the reactor core, the direct reactor auxiliary cooling system (DRACS) heat exchangers contained in a reactor vessel, and the primary pumps and intermediate heat exchangers located in shielded cells outside the reactor vessel. The intermediate heat exchangers are established at the appropriate elevation to support natural circulation. Preliminary core operation strategies were developed as well. Applying the accumulated experiences for sodium cooled fast reactors, the operational procedures for fuel handling, and plant commissioning and startup were established. The reprocessing flowsheet was also developed for the liquid TRU fuel of SLFFR, composed of TRU, Ce, and Co. The

developed reprocessing flowsheet is capable of removing a sufficient fraction of fission products to maintain a low fuel melting point, and recover more than 99% of the actinides.

A readiness assessment of the SLFFR technology was performed using the technology readiness levels developed in the Global Nuclear Energy Partnership program. The SLFFR is a very innovative sodium-cooled fast reactor that shows promise for the future. In reviewing the technology readiness of the system and components that comprise the SLFFR, it is apparent that the fuel-structure system of the reactor core will be the greatest challenge with this reactor plant to understand whether this technology is feasible. It has the lowest technology readiness level of all the systems and components, and thus it should be the focus of future research and development efforts to continue the maturation of the SLFFR.

References

1. “Advanced Fuel Cycle Initiative: Objectives, Approach, and Technology Summary,” Report to Congress, U.S. Department of Energy (May 2005).
2. W. S. Yang, “Trends in Transmutation Performance and Safety Parameters Versus Conversion Ratio of Sodium-Cooled Recycle Reactors,” *Proc. of 10th Information Exchange Meeting on Actinide and Fission Product Partitioning and Transmutation*, Mito, Japan, October 6-10, 2008.
3. “Accelerator-driven Systems (ADS) and Fast Reactors (FR) in Advanced Nuclear Fuel Cycles: A Comparative Study,” NEA3109, OECD/NEA (2002).
4. W. S. Yang and C. Grandy, “Stationary Liquid Fuel Fast Reactor Concept for TRU Burning,” *Trans. Am. Nucl. Soc.*, **107**, 1045-1048 (2012).
5. C. H. Lee and W. S. Yang, “MC²-3: Multigroup Cross Section Generation Code for Fast System Analysis,” ANL/NE-11-41, Argonne National Laboratory (2011).
6. K. L. Derstine, “DIF3D: A Code to Solve One-, Two-, and Three-Dimensional Finite-Difference Diffusion Theory Problems,” ANL-82-64, Argonne National Laboratory (1984).
7. B. J. Toppel, “A User’s Guide to the REBUS-3 Fuel Cycle Analysis Capability,” ANL-83-2, Argonne National Laboratory (1983).
8. M. A. Smith, C. Adams, W. S. Yang, and E. E. Lewis, “VARI3D & PERSENT: Perturbation and Sensitivity Analysis,” ANL/NE-13/8, Argonne National Laboratory (2013).
9. ANSYS® Academic Research, Release 13.0.
10. J. C. Mankins, “Technology Readiness Levels: A White Paper” NASA, Office of Space Access and Technology, Advanced Concepts Office, April 6, 1995.
11. D. B. Hall, “Plutonium as a Fuel for the Los Alamos Molten Plutonium Reactor Experiment,” *Proc. of Plutonium as a Power Reactor Fuel*, Richland, Washington, September 13 and 14, 1962.
12. J. A. Lane, H. G. MacPherson, and F. Maslan eds., *Fluid Fuel Reactors*, Addison-Wesley Publishing Company, Inc. (1958).
13. J. D. McWhirter, “Temperature-Gradient Induced Circulation in Liquid Metal-Fueled Fast Reactor Systems,” *Proc. 7th Int. Conf. Nuclear Engineering*, Tokyo, Japan, April 19-23, 1999.
14. G. Palmiotti, and E. Feldman, “Fast Flux Fluid Fuel Reactor: A Concept for the Next Generation of Nuclear Power Production,” *Trans. Am. Nucl. Soc.*, **81**, 279 (1999).
15. R. M. Kiehn, “LAMPRE, A Molten Plutonium Fueled Reactor Concept,” LA-2112, Los Alamos Scientific Laboratory (1957).
16. E. O. Swickard, “Los Alamos Molten Plutonium Reactor Experiment (LAMPRE) Hazard Report,” LA-2327, Los Alamos Scientific Laboratory (1959).
17. “LAMPRE I Final Design Status Report,” LA-2833, Los Alamos Scientific Laboratory

- (1962).
18. J. W. Anderson, W. D. McNeese, and J. A. Leary, "Preparation and Fabrication of Plutonium Fuel Alloy for Los Alamos Molten Plutonium Reactor Experiment No. 1," LA-2439, Los Alamos Scientific Laboratory (1960).
 19. R. P. Hammond, R. E. L. Stanford, and J. R. Humphreys, Jr., "Mobile Fuel Plutonium Breeders," LA-2644, Los Alamos Scientific Laboratory (1961).
 20. R. P. Hammond and J. R. Humphreys, Jr., "Direct-Contact Core Systems," *Nucl. Sci. Eng.*, **18**, 421 (1964).
 21. W. H. Hannum and L. D. Kirkbride, "The Molten Plutonium Burnup Experiment," LA-3384-MA, Los Alamos Scientific Laboratory (1965).
 22. R. L. Andelin, L. D. Kirkbride, and R. H. Perkins, "High-Temperature Environmental Testing of Liquid Plutonium Fuels," LA-3631, Los Alamos Scientific Laboratory (1967).
 23. P. A. Tucker, D. E. Etter, and J. M. Gebhart, "Phase Equilibria in the Ternary System Plutonium-Cerium-Iron," *Proc. of Plutonium as a Power Reactor Fuel*, Richland, Washington, September 13 and 14, 1962.
 24. L. J. Wittenberg, D. E. Etter, J. E. Selle, and P. A. Tucker, "Phase Equilibria in the Plutonium-Cerium-Copper System," *Nucl. Sci. Eng.*, **23**, 1 (1965).
 25. V. I. Kutaitsev, N. T. Chebotarev, I. G. Lebedev, M. A. Addrianov, V. N. Konev, and T. S. Menshikova, "Phase Diagrams of Plutonium with the Metals of Groups IIA, IVA, VIIIA and IB," *Proc. of Plutonium as a Power Reactor Fuel*, Richland, Washington, September 13 and 14, 1962.
 26. A. S. Coffinberry, F. W. Schonfeld, E. M. Cramer, W. N. Miner, F. H. Ellinger, R. O. Elliott, and V. O. Struebing, "The Physical Metallurgy of Plutonium and its Alloys," *Proc. of 2nd Intl. Conf. on Peaceful Uses of Atomic Energy*, Geneva, Swiss (1958).
 27. L. D. Kirkbride, "Molten Plutonium Fuels," *High Temperature Nuclear Fuels, Metallurgical Society Conference*, Vol. 42, pp. 353, Gordon and Breach (1966).
 28. Cabot Supermetals, <http://www.cabot-corp.com>.
 29. D. Ofte and L. J. Wittenberg, "Viscosity-Composition Relationships in Molten Plutonium-Iron Alloys," *Transactions of the ASM*, **57**, 916 (1964).
 30. D. Ofte, W. G. Rohr, and L. J. Wittenberg, "Viscosity-Density-Composition Relationships for Liquid Plutonium-Cerium Alloys," *Proc. of the Third International Conference on Plutonium*, London, UK, 1965.
 31. L. J. Wittenberg, D. Ofte, and C. F. Curtiss, "Fluid Flow of Liquid Plutonium Alloys in an Oscillating-Cup Viscosimeter," *J. of Chem. Phys.*, **48**, 3253 (1968).
 32. L. J. Wittenberg, "Reactor Fuels and Materials Development - Plutonium Research, April - June 1963," Mound Lab., Miamisburg, Ohio (1963).
 33. H. Blank, G. Brossmann, and M. Kemmerich, "Zwei- Und Mehrstoffsysteme Mit Plutonium," KFK 105, Kernforschungszentrum Karlsruhe, Jun 1962.
 34. "Thermal Properties of Refractory Alloys," ASD-TDR-63-597, Air Force Materials

- Laboratory, June 1963.
35. Allegheny Ludlum Steel Corporation Research Center, "Tantalum Alloy Tubing Development Program," RTD Technical Report 8-109 (I), Air Force Materials Laboratory, October 1963.
 36. William S. de Rosset, "Explosive Bonding of Refractory Metal Liners," ARL-TR-3267, Army Research Laboratory, August 2004.
 37. C. K. Jun and H. Hoch, "Thermal Conductivity of Tantalum, Tungsten, Rhenium, Ta-10W, T111, T222, W-25Re in the Temperature Range 1500-2000," AFML-TR-66-367, November 1966.
 38. R. F. Mattas, "International Thermonuclear Experimental Reactor (ITER) Divertor Plate Performance and Lifetime Considerations," ANL/FPP/TM-246, March 1990.
 39. J. E. Fink, M. G. Chasanov, and L. Leibowitz, "Properties for Reactor Safety Analysis," ANL-CEN-RSD-82-2, May 1982.
 40. J. K. Fink and L. Leibowitz, "Thermodynamic and Transport Properties of Sodium Liquid and Vapor," ANL/RE-95/2, January 1995.
 41. X. P. Su, W. J. Zhang, and Z. M. Du, "A thermodynamic Modeling of the Co-Ce System." *Journal of Alloys and Compounds*, **267**, 121 (1998).
 42. T. B. Massalski and H. Okamoto, *Binary Alloy Phase Diagrams*, 2nd ed., American Society for Metals, Materials Park, Ohio (1990).
 43. F. H. Ellinger, C. C. Land, K. A. Johnson, and V. O. Struebing, "The Ternary System Plutonium-Cerium-Cobalt," *Transactions of the Metallurgical Society of AIME*, **236**, 1577 (1966).
 44. F. H. Ellinger, W. N. Miner, D. R. O'Boyle, F. W. Schonfeld, "Constitution of Plutonium Alloys," LA-3870, Los Alamos Scientific Laboratory (1968).
 45. H. Okamoto, "Am-Pu (americium-plutonium)," *Journal of Phase Equilibria*, **20**, 451 (1999).
 46. H. Okamoto, "Cm-Pu (curium-plutonium)," *Journal of Phase Equilibria*, **21**, 108 (2000).
 47. H. Okamoto, "Am-Pu (Americium-Plutonium)," *Journal of Phase Equilibria and Diffusion*, **32**, 575 (2011).
 48. V. D. Shushakov and N. T. Chebotarev, "Phase Diagram of the Pu-Cm System," *Radiochemistry*, **37**, 446 (1995).
 49. P. E. A. Turchi, A. I. Landa, and P. A. Soederlind, "Thermodynamic Assessment of the Am-Pu System with Input from ab initio," *Journal of Nuclear Materials*, **418**, 165 (2011).
 50. T. Ogawa, "Alloying Behavior among U, Np, Pu and Am Predicted with the Brewer Valence Bond Model," *Journal of Alloys and Compounds*, **194**, 1 (1993).
 51. D. M. Poole, M. G. Bale, P. G. Mardon, J. A. C. Marples, and J. L. Nichols, "Phase Diagrams Of Some Plutonium Alloy Systems," *Plutonium 1960, Proc. Int. Conf. Plutonium Metall.*, 2nd, 267 (1961).
 52. R. E. Alcouffe, F. W. Brinkley, D. R. Marr, and R. D. O'Dell, "User's Guide for

- TWODANT: A Code Package for Two-Dimensional, Diffusion-Accelerated, Neutral-Particle Transport,” LA-10049-M, Los Alamos National Laboratory (1990).
53. “Pool-Type LMFBR Plant 1000 MWe, Phase A Design’, General Electric Company (GE), EPRI NP-646, April 1978.
54. “Conceptual Design Report-1000 MWe Pool-Type LMFBR Plant”, Argonne National Laboratory, July 1982.
55. Charnock, H. O. and Holz, H. B., “Sodium Systems Components,” Sodium Technology, Session IV, Atomic International, North American Rockwell, 1970.
56. Nikulin, M. P., et al., “Experience Gained during BR-10 Reactor Operation,” TM-27172 and TM-26984, TWG-FR/123, Working Material, IAEA, pp211-217, 2005.
57. Dusan Lexa, “Occulsion and Ion Exchange in the Molten (Lithium Chloride + Potassium Chloride + Alkaline Earth Chloride) Salt + Zeolite 4A System with Alkaline-Earth Chlorides of Calcium and Strontium and in Molten (Lithium Chloride + Potassium Chloride + Actinide Chloride) Salt + Zeolite 4A System with the Actinide Chloride of Uranium,” *Metall. Trans. B*, 2003, Vol. 34B, pp. 201-208.
58. M. L. Gougar, “Fission Product Ion Exchange between Zeolite and a Molten Salt,” Ph. D. Dissertation, Pennsylvania State University, PA, 2004.
59. Chemical Engineering Division Semiannual Report, July-December 1964, ANL-6925, p 37.
60. F. Cafasso, H. Feder, I. Johnson, *J. Phys. Chem*, **68**, 1944 (1964).
61. “Handbook on Pb-Bi Eutectic Alloy and Lead Properties,” Chapter 3, Nuclear Energy Agency, 2007.
62. N. E. Todreas and M. S. Kazimi, *Nuclear Systems Vol. I: Thermal Hydraulic Fundamentals*, Chapter 4, 2nd Ed., CRC Press (2012).
63. W. S. Yang, S. Shi, C. Grandy, A. Borowski and L. Krajtl, “Stationary Liquid Fuel Fast Reactor – Preliminary Core Design and Overall Plant Concept,” PU/NE-13/06, Purdue University (2013).
64. L. R. CAMPBELL, et al, “Reactivity Worth of Gas Expansion Modules (GEMs) in the Fast Flux Test Facility,” *Trans. Am. Nucl. Soc.*, **53**, 457 (1986).
65. G. F. Flanagan, G.T. Mays, and I. K. Madni, “NRC Program on Knowledge Management for Liquid-Metal- Cooled Reactor,” NUREG/KM-0007 (2014).
66. “The SAS4A/SASYS-1 Safety Analysis Code System,” ANL/NE-12/4. Argonne National Laboratory (2012).
67. K. O. Ott and Robert J. Neuhold, *Introductory Nuclear Reactor Dynamics*, American Nuclear Society, La Grange Park, Illinois (1985).
68. “Decay Heat Power in Light Water Reactors,” ANSI/ANS-5.1-2005, American Nuclear Society, La Grange Park, Illinois (2005).
69. A. V. Vota, N. J. Curlee, Jr., and A. F. Henry, “WIGL3 - A Program for the Steady-State and Transient Solution of the One-Dimensional, Two-Group, Space Time Diffusion

- Equations Accounting for Temperature, Xenon, and Control Feedback,” WAPD-TM-788 (1969).
70. K. S. Smith, “An Analytic Nodal Method for Solving the Two-Group, Multidimensional, Static and Transient Neutron Diffusion Equations,” M.S. and N.E. Thesis, M.I.T. (1979).
 71. R. N. Lyon, “Liquid Metal Heat Transfer Coefficients,” *Chem. Eng. Prog.* Vol. 47, No. 2, pp.75-79 (1951).
 72. D. C. Wade, E. K. Fujita, “Trends Versus Reactor Size of Passive Reactivity Shutdown and Control Performance.” *Nuclear Science and Engineering*, **103**, 182-195 (1988).
 73. Government Accountability Office, “Best Practices, Better Management of Technology Development Can Improve Weapon System Outcomes” GAO/NSIAD-99-162 (1999).
 74. “RELAP5/MOD3.3 Code Manual,” Nuclear Safety Analysis Division, Information Systems Laboratories, Inc., Rockville, MD (2002)

Appendix A. Computational Models of Safety Analysis Code MUSA

To perform the transient analyses and assess the passive safety characteristics of the SLFFR, a MULTI-channel Safety Analysis code (MUSA) was developed, tailored to handle the unconventional geometry of the thermal-fluidic channel of the SLFFR core. MUSA solves the coupled, time-dependent coupled neutronics and thermal-fluidic problems. A point kinetics model with six delayed neutron groups is used to represent the power transients. The reactivity feedback is estimated by combining the temperature and density variations of liquid fuel, structural material and sodium coolant with the corresponding axial distributions of reactivity worth in each individual thermal-fluidic channel. The thermal-fluidic behavior of the core is described by representing the core with one-dimensional parallel channels. The primary heat transport system is modeled by connecting two compressible volumes (representing the upper and lower plenums) by two liquid segments: one represents the core and the other represents the hot leg, the intermediate heat exchanger and the cold leg.

A.1. Overall Solution Scheme

A transient calculation starts with determining the steady-state initial conditions for a given steady state power distribution. By solving the steady-state thermal-fluidic equations, the channel temperature distributions are determined first. The resulting axial distributions of the coolant, structure and fuel temperatures for each core channel are used as the base temperatures for the reactivity feedbacks. The temperatures and pressures in the inlet and outlet coolant plenums are also obtained from the core steady-state solution. The temperatures of all elements and compressible volumes in the hot side of the primary loop are set to the coolant temperature in the outlet plenum, and the temperatures of the components in the cold side of the primary loop are set to the inlet plenum temperature. After the primary loop temperatures are set, the pressure drops through all the components are calculated, and the pump head is calculated to achieve a pressure balance. In the current version of MUSA, the intermediate heat transport loops and steam generators are not modeled explicitly, and the heat removal rate or temperature of the intermediate heat exchanger (IHX) is specified as a boundary condition. The average temperature of the primary side of the IHX is obtained by averaging the inlet and outlet temperatures of the primary side of the IHX.

Four levels of time intervals are defined for transient analysis. The reactivity feedbacks are obtained in the main time step, which is specified by an input parameter. The primary-loop time step is a sub-step of the main step, which can either be provided as an input parameter or determined dynamically to satisfy the Courant-Friedrichs-Levy (CFL) stability condition for the coolant flow in the core channel. The heat transfer calculation from fuel to coolant shares the same time step with the primary loop. The point kinetic time step is a sub-step of the primary-loop time step given by an input value. The last level of the time step is the editing time step for the output of the results, which is also a fixed input parameter. In each main time step, the following sequence of computations is performed:

1. Calculate the new power level using the feedback reactivity from the last time step.
2. Determine the number of primary-loop time steps for core and primary loop thermal-fluidic calculations.

3. Perform the primary loop and core thermal-fluidic calculations with the updated power level over each primary-loop sub-interval and obtain the new core temperatures.
4. Calculate the reactivity feedbacks with updated core temperatures.

In each primary-loop time step, using the updated power level from the point kinetic calculation, the following sequence of computations is performed:

1. Determine the core pressure drop by performing the core thermal-fluidic calculation with the boundary conditions from the last time step.
2. Determine the outlet plenum pressure and the total coolant flow rate by solving the system of equations for the pressure drops and flow rates in the compressible volumes and liquid segments of the primary loop.
3. Solve the energy balance equation for the primary loop and obtain the inlet temperature.
4. Determine the flow splits among the core channels using the new total flow rate. The channel flow rates of the last time step are used as an initial guess.
5. Perform the thermal-fluidic and heat transfer calculations for individual core channels using the new channel flow rates, coolant inlet temperature and outlet plenum pressure.

In each point-kinetics time step, using the reactivity from the last main time step, the following sequence of calculations is performed:

1. Update the fission power level and delayed neutron concentrations using their values at the last point-kinetic time step and the reactivity of the last main time step.
2. Calculate the decay heat power with updated fission power level.
3. Calculate the total power level by adding the fission power and decay heat power.

A.2. Core Neutronics Model

In the point reactor model, it is assumed that the initial flux shape remains constant, and the local power production is determined by the product of the dimensionless, normalized power amplitude and the initial power distribution. The time-dependent power amplitude is expressed as the sum of the direct fission component, and the decay heat from fission and capture products. The direct fission power component is described by the point kinetics equations. Using the reduced precursor concentration [67], which represents the total number of delayed neutron precursors relative to the total fission neutrons, the point kinetics equation with six delayed neutron groups can be written as

$$\frac{dp(t)}{dt} = \frac{\rho(t) - \beta}{\Lambda} p(t) + \frac{1}{\Lambda} \sum_{i=1}^6 \lambda_i \zeta_i(t) \quad (\text{A.1})$$

$$\frac{d\zeta_i(t)}{dt} = \beta_i p(t) - \lambda_i \zeta_i(t), \quad (i = 1, \dots, 6) \quad (\text{A.2})$$

where $p(t)$ is the fission power amplitude relative to the initial power level, $\zeta_i(t)$ is the reduced delayed neutron precursor concentration of group i , $\rho(t)$ is the time dependent reactivity, Λ is the neutron generation time in the unit of second, and β_i and λ_i are the delayed

neutron fraction and the decay constant for the delayed neutron precursor in group i . For an initially critical reactor, $\rho(0) = 0$ and thus Eq. (A.1) and Eq. (A.2) at a steady state condition yield the initial conditions

$$p(0) = p_0 \quad (\text{A.3})$$

$$\zeta_i(0) = \frac{\beta_i}{\lambda_i} p_0, \quad (i = 1, \dots, 6) \quad (\text{A.4})$$

The decay heat is calculated using the ANS decay heat standards ANSI/ANS-5.1 [68], where the decay heat at time t after one fission pulse is represented as

$$k(t) = \sum_{i=1}^{23} \alpha_i e^{-\lambda_i t} \quad (\text{MeV/fission}) \quad (\text{A.5})$$

where α_i and λ_i are fitting parameters. The decay heat function is fissionable isotope dependent, and Ref. 68 provides the decay heat function for U-235, U-238 and Pu-239. In the current SLFFR study, the decay heat function for Pu-239 is used because the most abundant fissile isotope in TRU is Pu-239. For a known total power history $p_t(t)$, the decay heat power at time t can be calculated as follows:

$$p_d(t) = \frac{1}{Q} \sum_{i=1}^{23} \alpha_i \int_{-\infty}^t p_t(\tau) e^{-\lambda_i(t-\tau)} d\tau \quad (\text{A.6})$$

where Q is the average recoverable energy per fission. By evaluating the steady-state decay power level using Eq. (A.6), the initial fission power in Eq. (A.3) can be determined as

$$p(0) = p_t(0) - p_d(0) \quad (\text{A.7})$$

The point kinetics equations in Eq. (A.1) and Eq. (A.2) are discretized using the so-called theta-method [69,70], which is a variable time integration scheme. This method permits the resulting difference equations to range from fully explicit when $\theta = 0$ to fully implicit when $\theta = 1$. The Crank-Nicolson scheme is obtained when $\theta = 0.5$. Application of the theta method to Eq. (A.1) over a time step $t \in [t_{n-1}, t_n]$ yields

$$\left(\frac{1}{\Delta t_n} - \theta \frac{\rho^n - \beta}{\Lambda} \right) p^n - \theta \frac{1}{\Lambda} \sum_{i=1}^6 \lambda_i \zeta_i^n = \frac{p^{n-1}}{\Delta t_n} + (1 - \theta) \left[\frac{\rho^{n-1} - \beta}{\Lambda} p^{n-1} + \frac{1}{\Lambda} \sum_{i=1}^6 \lambda_i \zeta_i^{n-1} \right] \quad (\text{A.8})$$

The delayed neutron precursor equation in Eq. (A.8) can be integrated directly assuming that the power is a linear function of time within each time step. The resulting equation is

$$\zeta_i^n = e^{-\lambda_i \Delta t_n} \zeta_i^{n-1} + \frac{\beta_i}{\lambda_i} \left[\frac{1}{\lambda_i \Delta t_n} (1 - e^{-\lambda_i \Delta t_n}) - e^{-\lambda_i \Delta t_n} \right] p^{n-1} + \frac{\beta_i}{\lambda_i} \left[1 - \frac{1}{\lambda_i \Delta t_n} (1 - e^{-\lambda_i \Delta t_n}) \right] p^n \quad (\text{A.9})$$

Substitution of Eq. (A.9) into Eq. (A.8) yields

$$\left\{ \frac{\Lambda}{\Delta t_n} - \theta \left[\rho^n - \sum_{i=1}^6 \frac{\beta_i}{\lambda_i \Delta t_n} (1 - e^{-\lambda_i \Delta t_n}) \right] \right\} p^n = \sum_{i=1}^6 \lambda_i \zeta_i^{n-1} [1 - \theta(1 - e^{-\lambda_i \Delta t_n})] + \left\{ \frac{\Lambda}{\Delta t_n} + (1 - \theta)(\rho^{n-1} - \beta) + \theta \sum_{i=1}^6 \beta_i \left[\frac{1}{\lambda_i \Delta t_n} (1 - e^{-\lambda_i \Delta t_n}) - e^{-\lambda_i \Delta t_n} \right] \right\} p^{n-1} \quad (\text{A.10})$$

Using the temperatures and densities of fuel, coolant tube, and coolant at $t = t_n$ calculated with the previous time power amplitude, the reactivity ρ^n can be evaluated as discussed in the next section. For a known reactivity ρ^n , Eq. (A.10) can be easily solved for the new time power amplitude p^n .

A.3. Reactivity Feedback Model

In the point kinetics calculation for SLFFR, the reactivity is calculated as the sum of the following components, which are a function of time:

- User-defined reactivity to represent external reactivity, ρ_{ext}
- Fuel Doppler feedback reactivity, $\delta\rho_D$
- Reactivity feedback due to axial expansion of fuel and coolant tube, $\delta\rho_{ax}$
- Reactivity feedback due to radial expansion of fuel container, $\delta\rho_{re}$
- Coolant density or voiding feedback reactivity, $\delta\rho_{Na}$
- Reactivity induced by GEMs, $\delta\rho_{GEMs}$

Using these components, the reactivity in the point-kinetics equation in Eq. (A.10) can be expressed as

$$\rho(t) = \rho_{ext}(t) + \delta\rho_D(t) + \delta\rho_{ax}(t) + \delta\rho_{re}(t) + \delta\rho_{Na}(t) + \delta\rho_{GEMs}(t) \quad (\text{A.11})$$

The reactivity resulting from core dimension changes is the most important feedback mechanism of fast reactors, and in the SLFFR, the axial expansion of the fuel and the radial expansion of the fuel container are directly coupled. The radial expansion of the fuel container effectively reduces the height of liquid fuel. Consequently, the axial meshes of expanded fuel should be determined by simultaneously considering the axial fuel expansion and the radial expansion of the fuel container.

The fuel Doppler reactivity $\delta\rho_D^i$ at any axial location in a thermal-fluidic channel i is estimated assuming the usual $1/T$ dependence

$$\frac{d}{dT_f} \delta\rho_D^i = \frac{\alpha_D^i}{T_f^i} \quad (\text{A.12})$$

where T_f^i is the local, volumetric averaged fuel temperature, and α_D^i is the local fuel Doppler constant in the unit of $^\circ\text{C}^{-1}$. The axial distribution of the Doppler constant is specified for each thermal-fluidic channel by the user. Two sets of Doppler constant distribution need to be

specified: one is for the normal, coolant-in (flooded) condition and the other is for the coolant-out (voided), accident condition.

The local Doppler coefficient of fuel can be calculated as a function of axial and radial positions using a perturbation theory code such as VARI3D [8], and the axial distribution in each channel can be obtained by integrating the local coefficient distribution over a radial region corresponding to the channel. As an example, Figure A.1 shows the axial distributions of the fuel Doppler constants of a three-channel model of SLFFR. Channel 1, channel 2 and channel 3 represent the core central, middle and periphery channels, respectively. Using the specified Doppler constants, the Doppler reactivity feedback due to the temperature change of fuel at axial position z at time t is obtained by integrating Eq. (A.12) from the steady-state temperature to the temperature at time t

$$\delta\rho_D^i(z,t) = \alpha_D^i(z) \ln \frac{T_f^i(z,t)}{T_f^i(z,0)} \quad (\text{A.13})$$

Using the Doppler feedback distribution in Eq. (A.13), the total fuel Doppler feedback reactivity is calculated as

$$\delta\rho_D(t) = \sum_i \int_0^H \delta\rho_D^i(z,t) dz \quad (\text{A.14})$$

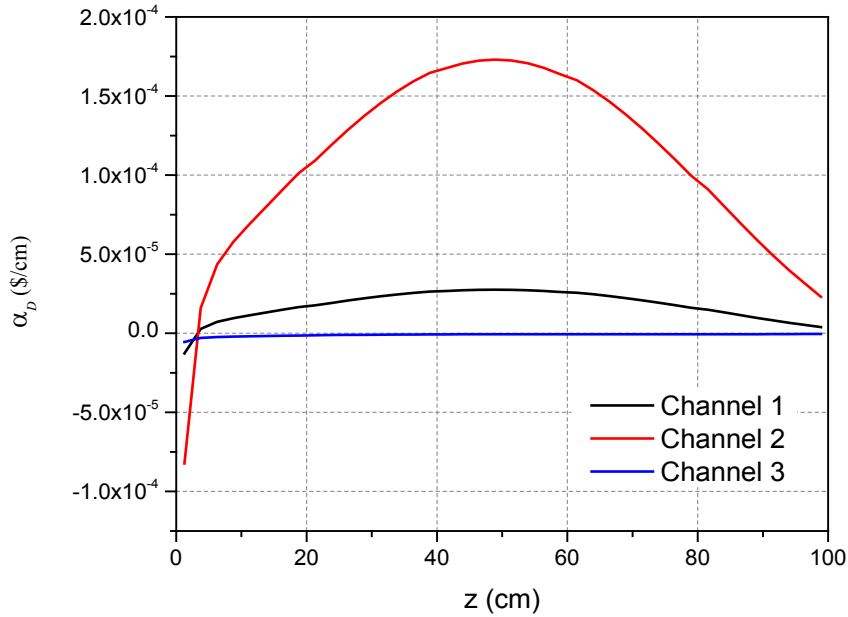


Figure A.1. Three Channel Example of Axial Distributions of Doppler Constant

The axial expansion effect of fuel on reactivity is estimated using its local density change and the local reactivity worth due to thermal expansion. The local reactivity worth per unit fuel mass can be calculated using a perturbation theory code (i.e., VARI3D), and the axial distribution for fuel worth in channel i can be calculated for a radially uniform perturbation as

$$\rho_{w,f}^i(z) = \frac{1}{\delta m_f^i(z) R^2} \int_{R_{i-1}}^{R_i} \frac{\partial \rho}{\partial m_f^i}(r,z) \delta m_f^i(z) r dr \quad (\text{A.15})$$

where m_f^i is the axial distribution of fuel mass in channel i , and R_i and R_{i-1} are the equivalent inner and outer radii of the radial region corresponding to the channel i . Figure A.2 shows a three-channel example of the axial distribution of fuel reactivity worth.

For each axial node k in a channel i , the axial expansions of fuel are calculated first as illustrated in Figure A.3. Using the original mesh size $\Delta z_{i,k}^0 = z_{i,k} - z_{i,k-1}$, the corresponding mesh size for expanded fuel at $t = t_n$ is determined as

$$\Delta z_{ax,i,k}^n = \Delta z_{i,k}^0 [1 + \alpha_{l,f} \Delta T_{f,i,k}^n] \quad (\text{A.16})$$

where $\alpha_{l,f}$ is the linear thermal expansion coefficient of fuel, and $\Delta T_{f,i,k}^n$ is the increase in the average fuel temperature of the axial mesh k of channel i at time $t = t_n$ from that at $t = 0$, calculated from the thermal-fluidic module. The linear expansion coefficient of liquid fuel is determined by evaluating the volumetric expansion coefficient derived from the density correlation.

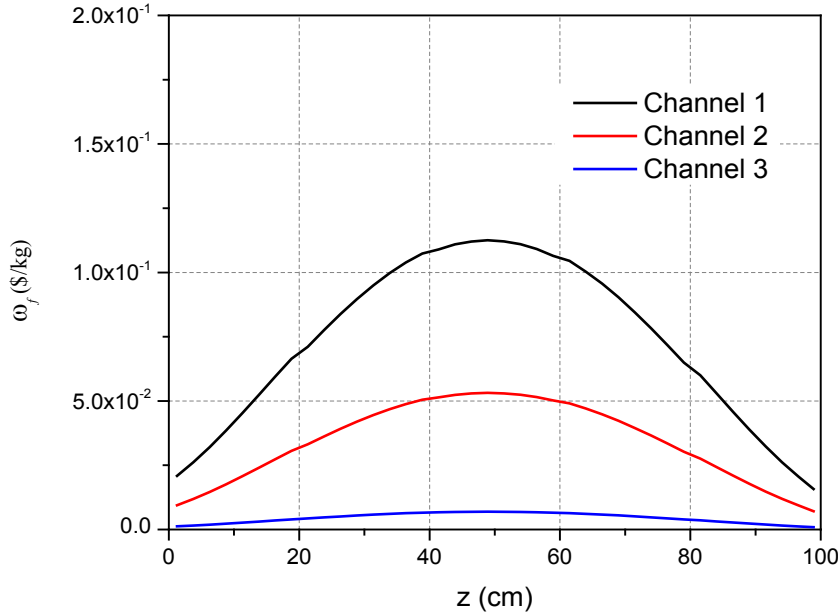


Figure A.2. Three Channel Example of Axial Distributions of Fuel Worth

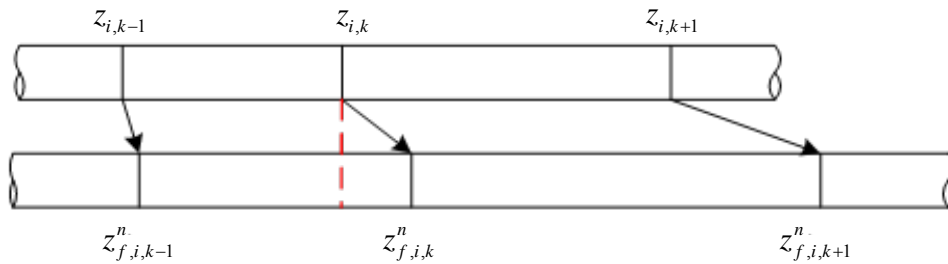


Figure A.3. Axial Meshes of Original and Expanded Fuel

As aforementioned, the axial fuel expansion is coupled with the radial expansion of the fuel container since the latter reduces the height of liquid fuel to preserve the fuel volume. The increased radius of the fuel container at axial mesh k at $t = t_n$ is simply estimated as

$$R_{w,k}^n = R_{w,k} (1 + \alpha_{l,w} \Delta T_{w,k}^n) \quad (\text{A.17})$$

where $\alpha_{l,w}$ is the linear thermal expansion coefficient of fuel container and $\Delta T_{w,k}^n$ is the increase in the average fuel container temperature of the axial mesh k at time $t = t_n$ from that at $t = 0$, calculated from the thermal-fluidic module. Since the liquid fuel volume is preserved for the container expansion, the fuel mesh interval is reduced by

$$\delta \Delta z_{rd,i,k}^n = \Delta z_{i,k}^0 [(1 + \alpha_{l,w} \Delta T_{w,k}^n)^{-2} - 1] \quad (\text{A.18})$$

By combining the axial and radial expansions in Eq. (A.16) and Eq. (A.18), the resulting axial mesh size of fuel can be obtained as

$$\begin{aligned} \Delta z_{f,i,k}^n &= \Delta z_{ax,i,k}^n + \Delta z_{rd,i,k}^n = \Delta z_{i,k}^0 [\alpha_{l,f} \Delta T_{f,i,k}^n + (1 + \alpha_{l,w} \Delta T_{w,k}^n)^{-2}] \\ &\approx \Delta z_{i,k}^0 [1 + \alpha_{l,f} \Delta T_{f,i,k}^n - 2\alpha_{l,w} \Delta T_{w,k}^n] \end{aligned} \quad (\text{A.19})$$

Using these mesh sizes, the upper boundary of mesh k can be determined as

$$z_{f,i,k}^n = \sum_{j=1}^k \Delta z_{f,i,j}^n = \sum_{j=1}^k \Delta z_{i,j}^0 [\alpha_{l,f} \Delta T_{f,i,j}^n + (1 + \alpha_{l,w} \Delta T_{w,j}^n)^{-2}] \quad (\text{A.20})$$

Denoting the reactivity worth per unit mass of fuel in the axial mesh k of channel i by $\rho_{w,f}^{i,k}$, the reactivity change due to the mesh boundary changes of axial mesh k of channel i from the axial fuel expansion and the radial expansion of the fuel container can be estimated as

$$\delta \rho_{f,i,k}^n = m_{f,i,k} \left[\rho_{w,f}^{i,k} \frac{z_{i,k}^n - z_{f,i,k-1}^n}{z_{f,i,k}^n - z_{f,i,k-1}^n} + \rho_{w,f}^{i,k+1} \frac{z_{f,i,k}^n - z_{i,k}^n}{z_{f,i,k}^n - z_{f,i,k-1}^n} - \rho_{w,f}^{i,k} \right] \quad (\text{A.21})$$

where $m_{f,i,k}$ is the fuel mass in the axial mesh k of channel i . The material worth in the region beyond the nominal fuel height is determined by linear extrapolation of the calculated worth. The total reactivity change due to fuel axial expansion can be determined by summing up the mesh-wise contributions in Eq. (A.21) as

$$\delta \rho_f^n = \sum_i \sum_{k=1}^K \delta \rho_{f,i,k}^n \quad (\text{A.22})$$

The reactivity feedback caused by axial expansion of coolant tubes is calculated using a similar expression to Eq. (A.21). That is, using the perturbed mesh boundaries $z_{w,i,k}^n$ and the reactivity worth per unit mass of coolant tube $\rho_{w,w}^{i,k}$, the reactivity change due to the mesh boundary changes of axial mesh k of channel i from the axial expansion of coolant tubes is determined as

$$\delta\rho_{w,w}^n = m_{w,w} \left[\rho_{w,w}^k \frac{z_k - z_{w,k-1}^n}{z_{w,k}^n - z_{w,k-1}^n} + \rho_{w,w}^{k+1} \frac{z_{w,k}^n - z_k}{z_{w,k}^n - z_{w,k-1}^n} - \rho_{w,w}^k \right] \quad (\text{A.23})$$

Figure A.4 shows a three-channel example of the axial distribution of coolant tube worth. The mesh size changes of coolant tubes are computed using Eq. (A.16) with the linear thermal expansion coefficient of coolant tube and the average temperature increase in the coolant tube. The total reactivity due to axial expansion of coolant tubes is obtained by summing up the individual mesh contributions in Eq. (A.23).

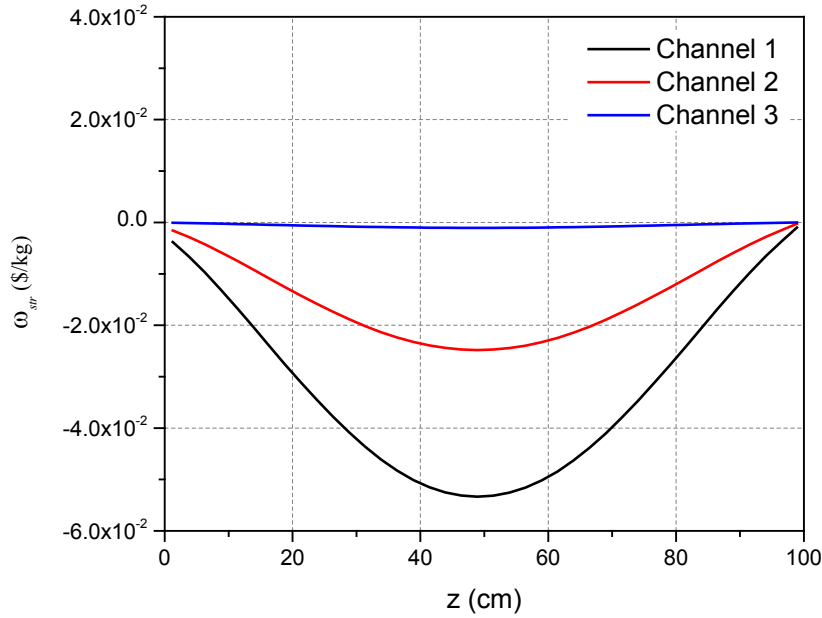


Figure A.4. Three Channel Example of Axial Distributions of Structure Material Worth

Reactivity feedback effects from either single-phase coolant density changes or two-phase coolant boiling are calculated using the local coolant density changes. Sodium void worth distributions are also the reactivity change per unit mass, but are in terms of the amount of mass reduced (voided) rather than the amount of mass present. The sodium density coefficient and sodium void coefficient can be calculated using a perturbation theory code such as the VARI3D code. Figure A.5 shows a three-channel example of the axial distribution of sodium coolant worth. The reactivity feedback from coolant density and voiding changes is calculated from

$$\delta\rho_{Na}^n = \sum_{k=1}^K \rho_{w,Na}^k \delta v_{Na,k}^n = \sum_{k=1}^K \rho_{w,Na}^k (-\delta m_{Na,k}^n) \quad (\text{A.24})$$

where $\rho_{w,Na}^{i,k}$ is the coolant void worth in axial mesh k of channel i in \$/g, and $\delta v_{Na,i,k}^n$ is the amount of coolant voided in axial mesh k of channel i at $t = t_n$, that is, $\delta v_{Na,k}^n = -\delta m_{Na,k}^n$ with $\delta m_{Na,k}^n$ being the coolant mass change.

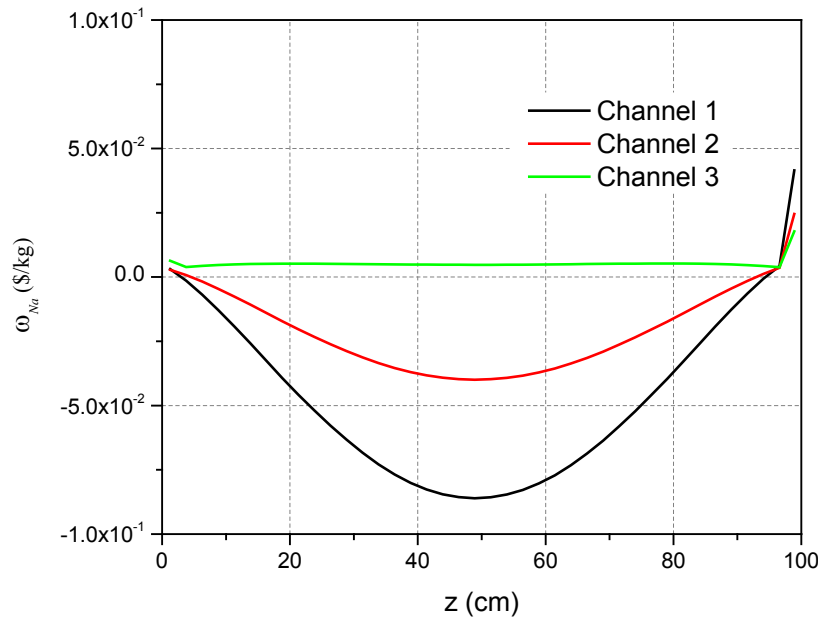


Figure A.5. Three Channel Example of Axial Distributions of Sodium Worth

A.4. Multi-Channel Thermal-Fluidic Model

The thermal-fluidic behavior of the core is described with one-dimensional parallel channels connected at the inlet and the outlet, as illustrated in Figure A.6. The inlet coolant flow is distributed among these channels to satisfy the equal pressure drop boundary conditions. Once the flow rates to individual channels are determined, the axial temperature distributions of coolant, coolant tube, and fuel are determined by solving the single-channel thermal-fluidic equations for an axial power distribution as well as inlet coolant flowrate and temperature.

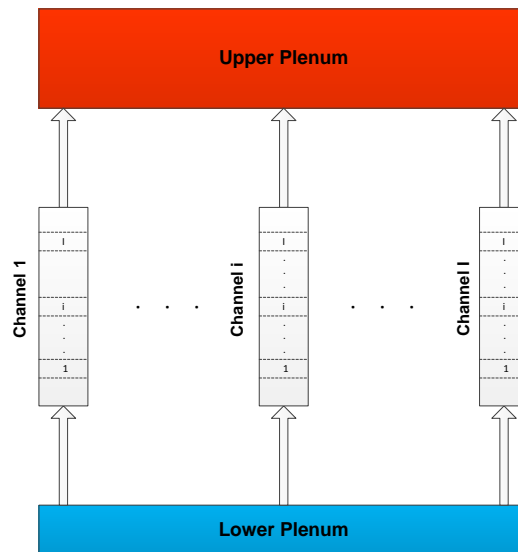


Figure A.6. Multiple Parallel Channel Model of SLFFR Core

A.4.1. Single-Channel Thermal-Fluidic Model

Figure A.7 shows a schematic planar view of the single channel thermal-fluidic model of SLFFR, which represents an average coolant channel with surrounding fuel. The sodium coolant flowing vertically in the center region of the model is separated by a Ta-10W coolant tube from TRU-Ce-Co liquid fuel. The fuel thickness is determined to conserve the fuel mass per coolant channel.

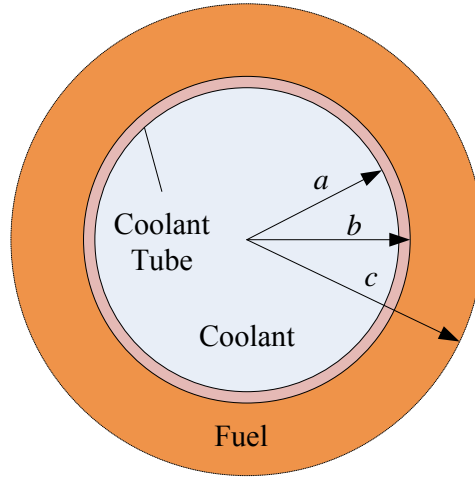


Figure A.7. Schematic Planar View of Single Channel Thermal-Fluidic Model

Neglecting the heat conduction and the shear forces due to velocity gradients in the fluid at open portions of the surface area, the mass, momentum, and energy balance equations for one-dimensional flow in a vertical coolant tube can be written as [62]

$$\frac{\partial}{\partial t} \rho(t, z) + \frac{\partial}{\partial z} [\rho(t, z)v(t, z)] = 0 \quad (\text{A.25})$$

$$\begin{aligned} \frac{\partial}{\partial t} [\rho(t, z)v(t, z)] + \frac{\partial}{\partial z} [\rho(t, z)v^2(t, z)] = & -\frac{\partial}{\partial z} P(t, z) - \rho(t, z)g \\ & - \frac{f \rho(t, z) |v(t, z)| v(t, z)}{2D_h} \end{aligned} \quad (\text{A.26})$$

$$\rho(t, z)c_p \left[\frac{\partial}{\partial t} T_c(t, z) + v(t, z) \frac{\partial}{\partial z} T_c(t, z) \right] = \frac{P_h}{A} q''(t, z) \quad (\text{A.27})$$

where ρ , v , T_c and P are the density, velocity, temperature, and pressure of coolant, respectively, c_p is the specific heat, and q'' is the heat flux at the coolant tube inner surface (i.e., coolant side). The parameters D_h , P_h , and A represent the hydraulic diameter, the wetted perimeter and the flow area of the coolant channel, respectively, and g is the gravitational acceleration. The parameter c_p is the specific heat of sodium coolant and f is the turbulent friction factor. For a smooth tube, the friction factor can be obtained from the relations [62]

$$f = \begin{cases} 0.316 \text{Re}^{-0.25}, & \text{Re} < 30,000 \text{ (Blasius relation)} \\ 0.184 \text{Re}^{-0.2}, & 30,000 < \text{Re} < 10^6 \text{ (McAdams relation)} \end{cases} \quad (\text{A.28})$$

where Re is the Reynolds number defined by

$$\text{Re} = \frac{\rho v D_h}{\mu} \quad (\text{A.29})$$

with fluid viscosity μ . The set of three first order differential equations from Eq. (A.25) to Eq. (A.27) can be solved using three boundary conditions (e.g., inlet flow rate, inlet temperature and outlet pressure) and three initial conditions.

Neglecting the axial conduction (which is much smaller than the radial conduction in SLFFR), the heat conduction in the annular fuel ring and the coolant tube can be represented by the following heat conduction equations:

$$\rho_f c_{p,f} \frac{\partial}{\partial t} T_f(r, z, t) = q'''(r, z, t) + \frac{1}{r} \frac{\partial}{\partial r} \left[r k_f \frac{\partial T_f(r, z, t)}{\partial r} \right] \quad (\text{A.30})$$

$$\rho_w c_{p,w} \frac{\partial}{\partial t} T_w(r, z, t) = \frac{1}{r} \frac{\partial}{\partial r} \left[r k_w \frac{\partial T_w(r, z, t)}{\partial r} \right] \quad (\text{A.31})$$

where T_f and T_w are the fuel and coolant tube temperatures, respectively, and q''' is the volumetric heat source in the fuel. The density, specific heat, and heat conductivity of fuel and coolant tube are denoted by ρ , c_p , and k , respectively, with a subscript f for fuel and w for coolant tube. The heat conduction equations of fuel and coolant tube are coupled through the interface conditions at the coolant tube outer wall:

$$\begin{cases} T_f(b, z, t) = T_w(b, z, t) \\ k_f \frac{\partial T_f(r, z, t)}{\partial r} \Big|_{r=b} = k_w \frac{\partial T_w(r, z, t)}{\partial r} \Big|_{r=b} \end{cases} \quad (\text{A.32})$$

The other boundary condition for the heat conduction in the fuel is given by the symmetry condition at the outer boundary of the fuel ring

$$\frac{\partial T_f(r, z, t)}{\partial r} \Big|_{r=c} = 0 \quad (\text{A.33})$$

The heat conduction equation for the coolant tube in Eq. (A.31) is coupled with the coolant energy equation in Eq. (A.27), through the Newton's law for heat convection at the coolant tube inner wall:

$$k_w \frac{\partial T_w(r, z, t)}{\partial r} \Big|_{r=c} = h_w [T_w(a, z, t) - T_c(z, t)] \quad (\text{A.34})$$

where h_w is the coefficient of convective heat transfer from the coolant tube inner wall to the coolant, which can be written in terms of the thermal conductivity of the coolant k , the hydraulic diameter of the coolant channel D_h , and the Nusselt number Nu as:

$$h_w = \frac{kNu}{D_h} \quad (A.35)$$

The Nusselt number characterizes the physical properties of the coolant and the dynamical characteristics of its flow. It is normally provided by empirical correlations. For this work, the Lyon-Martinelli correlation [71] is used

$$Nu = 7.0 + 0.025Pe^{0.8} \quad (A.36)$$

where the Peclet number Pe is the product of the Reynolds number Re and the Prandtl number Pr

$$Pe = Re Pr = \frac{\rho v D_h c_p}{k} \quad (A.37)$$

At the bottom and the top of the fuel, the power is negligible and thus the fuel and coolant tube temperatures would be equal to the coolant temperatures at the inlet and outlet, respectively. This yields the following boundary conditions

$$\begin{cases} T_f(r, 0, t) = T_w(r, 0, t) = T_{in}(t) \\ T_f(r, H, t) = T_w(r, H, t) = T_{out}(t) \end{cases} \quad (A.38)$$

where T_{in} is the coolant temperature at the core inlet and T_{out} is the coolant temperature at the core outlet.

The heat conduction equations in fuel and coolant tube are spatially discretized with the mesh-centered finite-difference scheme. A semi-implicit scheme is used for the temporal discretization of flow equations, but a fully implicit scheme is used for discretizing the heat conduction equations. The detailed numerical solutions methods for flow and heat conduction equations are explained in below.

A.4.1.1. Numerical Methods for Flow Equations

In the control volume approach of RELAP-5 [74] adopted in this study, the problem domain is divided into computational cells as illustrated in Figure A.8, where the regions bounded by horizontal lines denote the main computational cells. Each grid point is placed at the geometric center of each cell. Field variables such as density, pressure, and enthalpy are defined at these grid points, and the flow variables such as velocity component and mass flux are defined on cell faces (or junctions). The main control volumes for mass and energy balances are defined by these cells. The momentum control volume is displaced from the main control volume in the velocity direction, extending from grid points to grid points and encompassing the cell face upon which the velocity component is defined. The finite difference equations are derived by integrating the mass, momentum, and energy equations over the control volumes under the assumption that the values at the center of each control volume prevail over the control volume.

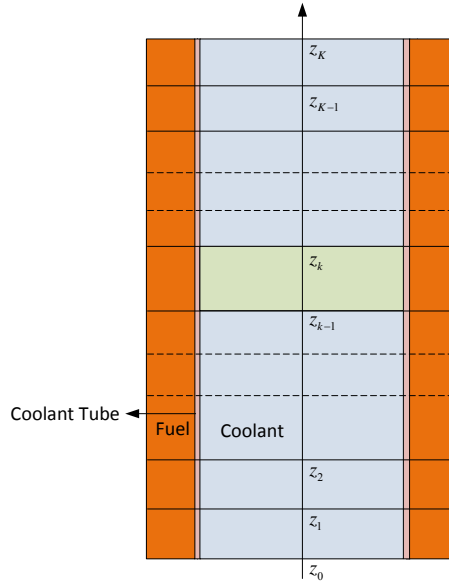


Figure A.8. Axial Discretization and Main Volume of Thermal-Fluidic Channel

By integrating the balance equation over the main control volume k ($z_{k-1} \leq z \leq z_k$) and by representing the coolant densities and temperatures at cell faces with the cell-center values using the donor cell (i.e., up-stream) difference scheme, the spatially discretized forms of the mass and energy conservation equations in Eq. (A.25) and Eq. (A.27) can be obtained as

$$\frac{\partial \bar{\rho}_k}{\partial t} + \frac{\bar{\rho}_k v_k - \bar{\rho}_{k-1} v_{k-1}}{\Delta z_k} = 0 \quad (\text{A.39})$$

$$\bar{\rho}_k \frac{\partial \bar{T}_k}{\partial t} + \bar{\rho}_{k-1} v_{k-1} \frac{\bar{T}_k - \bar{T}_{k-1}}{\Delta z_k} = \frac{P_h}{\bar{c}_{p,k} A} \bar{q}_k'' \quad (\text{A.40})$$

where $\bar{\rho}_k$ and \bar{T}_k are the coolant density and temperature at the cell center, \bar{q}_k'' is the cell-averaged heat flux, v_{k-1} and v_k are the velocities at the bottom and top faces of cell k , respectively, and $\Delta z_k = z_k - z_{k-1}$. The momentum balance equation for cell k is obtained by integrating Eq. (A.26) over the momentum control volume k ($z_{k-1} + \Delta z_k / 2 \leq z \leq z_k + \Delta z_{k+1} / 2$) and using the donor cell difference scheme as

$$\begin{aligned} \frac{d}{dt}(\bar{\rho}_k v_k) = & \frac{2}{\Delta z_k + \Delta z_{k+1}} \left(\frac{\bar{\rho}_{k-1}^2}{\bar{\rho}_k} v_{k-1}^2 - \frac{\bar{\rho}_k^2}{\bar{\rho}_{k+1}} v_k^2 \right) + \frac{2}{\Delta z_k + \Delta z_{k+1}} (\bar{P}_k - \bar{P}_{k+1}) \\ & - \frac{(\bar{\rho}_k \Delta z_k + \bar{\rho}_{k+1} \Delta z_{k+1})}{\Delta z_k + \Delta z_{k+1}} g - \frac{f_k \bar{\rho}_k v_k^2}{2D_h} \end{aligned} \quad (\text{A.41})$$

By combining Eq. (A.39) and Eq. (A.41), the momentum balance equation can be rewritten as

$$\begin{aligned} \frac{dv_k}{dt} = & \frac{\bar{\rho}_{k-1}v_{k-1}}{\bar{\rho}_k} \left(\frac{2}{\Delta z_k + \Delta z_{k+1}} \frac{\bar{\rho}_{k-1}}{\bar{\rho}_k} v_{k-1} - \frac{v_k}{\Delta z_k} \right) - v_k^2 \left(\frac{2}{\Delta z_k + \Delta z_{k+1}} \frac{\bar{\rho}_k}{\bar{\rho}_{k+1}} - \frac{1}{\Delta z_k} \right) \\ & + \frac{2}{\bar{\rho}_k(\Delta z_k + \Delta z_{k+1})} (\bar{P}_k - \bar{P}_{k+1}) - \frac{(\bar{\rho}_k \Delta z_k + \bar{\rho}_{k+1} \Delta z_{k+1})}{\bar{\rho}_k(\Delta z_k + \Delta z_{k+1})} g - \frac{f_k v_k^2}{2D_h} \end{aligned} \quad (\text{A.42})$$

where \bar{P}_k and \bar{P}_{k+1} are the pressure at the center of cell k and $k+1$, respectively. For the cell at the top of the coolant channel, Eq. (A.42) is reduced to

$$\frac{dv_K}{dt} = \frac{\bar{\rho}_{K-1}v_{K-1}}{\Delta z_K} \left(2 \frac{\bar{\rho}_{K-1}}{\bar{\rho}_K} v_{K-1} - v_K \right) - \frac{v_K^2}{\Delta z_K} + \frac{2}{\bar{\rho}_K \Delta z_K} (\bar{P}_K - P_{out}) - g - \frac{f_K v_K^2}{2D_h} \quad (\text{A.43})$$

where P_{out} is the outlet pressure.

The spatially discretized equations in Eq. (A.39), Eq. (A.40) and Eq. (A.42) provide a system of nonlinear ordinary differential equations for the cell-averaged temperatures, cell-center pressures, and cell-face velocities. By applying a fully explicit temporal difference scheme, these equations can be converted into a system of linear equations. However, for an incompressible flow, the fully explicit scheme does not yield an equation to update the coolant pressure. On the other hand, the fully implicit scheme yields a system of nonlinear equations, which requires a more complicated solution scheme. As a compromise, a semi-implicit scheme of the RELAP-5 code [74] has been adopted. This semi-implicit numerical solution scheme is based on replacing the system of differential equations with a system of finite difference equations partially implicit in time. The implicit terms are formulated to be linear in the dependent variables at new time. This results in a linear time-advancement matrix that is solved by direct inversion using a sparse matrix routine. Implicitness is selected such that the field equations can be reduced to a single difference equation per coolant control volume or mesh cell in terms of the hydrodynamic pressure.

Using the semi-implicit method of RELAP-5, the finite difference equations for the mass, energy, and momentum equations in Eq. (A.39), Eq. (A.40) and Eq. (A.42) can be obtained as

$$\bar{\rho}_k^n = \bar{\rho}_k^{n-1} - \frac{\Delta t_n}{\Delta z_k} (\bar{\rho}_k^{n-1} v_k^n - \bar{\rho}_{k-1}^{n-1} v_{k-1}^n) \quad (\text{A.44})$$

$$\bar{T}_k^n = \bar{T}_k^{n-1} + \frac{\bar{\rho}_{k-1}^{n-1} \Delta t_n}{\bar{\rho}_k^{n-1} \Delta z_k} v_{k-1}^n (\bar{T}_{k-1}^{n-1} - \bar{T}_k^{n-1}) + \frac{P_h}{A} \frac{\Delta t_n}{\bar{\rho}_k^{n-1} c_{p,k}} \bar{q}_k^{n-1} \quad (\text{A.45})$$

$$\begin{aligned} v_k^n = & v_k^{n-1} + \left[\frac{\bar{\rho}_{k-1}^{n-1} v_{k-1}^{n-1}}{\bar{\rho}_k^{n-1}} \left(\frac{2}{\Delta z_k + \Delta z_{k+1}} \frac{\bar{\rho}_{k-1}^{n-1}}{\bar{\rho}_k^{n-1}} v_{k-1}^{n-1} - \frac{v_k^{n-1}}{\Delta z_k} \right) - (v_k^{n-1})^2 \left(\frac{2}{\Delta z_k + \Delta z_{k+1}} \frac{\bar{\rho}_k^{n-1}}{\bar{\rho}_{k+1}^{n-1}} - \frac{1}{\Delta z_k} \right) \right. \\ & \left. + \frac{2}{\bar{\rho}_k^{n-1}(\Delta z_k + \Delta z_{k+1})} (\bar{P}_k^n - \bar{P}_{k+1}^n) - \frac{(1 + \bar{\rho}_{k+1}^{n-1} / \bar{\rho}_k^{n-1})}{1 + \Delta z_{k+1} / \Delta z_k} g - \frac{f_k (v_k^{n-1})^2}{2D_h} \right] \Delta t_n \end{aligned} \quad (\text{A.46})$$

For the node at the top of the coolant channel, Eq. (A.46) becomes

$$v_k^n = v_k^{n-1} + \left[\frac{\bar{\rho}_{k-1}^{n-1} v_{k-1}^{n-1}}{\Delta z_k} \left(2 \frac{\bar{\rho}_{k-1}^{n-1}}{\bar{\rho}_k^{n-1}} v_{k-1}^{n-1} - v_k^{n-1} \right) - \frac{(v_k^{n-1})^2}{\Delta z_k} + \right] \Delta t_n$$

$$+ \left[\frac{2}{\bar{\rho}_k^{n-1} \Delta z_k} (\bar{P}_k^n - P_{out}^n) - g - \frac{f_k (v_k^{n-1})^2}{2D_h} \right] \Delta t_n \quad (\text{A.47})$$

The system of equations in Eq. (A.44), Eq. (A.45), and Eq. (A.46) is closed with an equation of state that represents the coolant density as a function of temperature. By linearizing the density state relation about the old time value of the temperature, the provisional advanced time density can be obtained as

$$\bar{\rho}_k^n = \bar{\rho}_k^{n-1} + \left. \frac{d\rho}{dT} \right|_k^{n-1} (\bar{T}_k^n - \bar{T}_k^{n-1}) \quad (\text{A.48})$$

Inserting Eq. (A.48) into the mass balance equation given in Eq. (A.44) yields

$$\left. \frac{d\rho}{dT} \right|_k^{n-1} (\bar{T}_k^n - \bar{T}_k^{n-1}) = - \frac{\Delta t_n}{\Delta z_k} (\bar{\rho}_k^{n-1} v_k^n - \bar{\rho}_{k-1}^{n-1} v_{k-1}^n) \quad (\text{A.49})$$

By eliminating the new time temperature using Eq. (A.49) and Eq. (A.45), the cell-face velocities at new time can be obtained as

$$v_k^n = \omega_k^{n-1} v_{k-1}^n - \chi_k^{n-1} \quad (\text{A.50})$$

where

$$\omega_k^{n-1} = \frac{\bar{\rho}_{k-1}^{n-1}}{\bar{\rho}_k^{n-1}} \left[1 - \frac{1}{\bar{\rho}_k^{n-1}} \left. \frac{d\rho}{dT} \right|_k^{n-1} (\bar{T}_{k-1}^{n-1} - \bar{T}_k^{n-1}) \right] \quad (\text{A.51})$$

$$\chi_k^{n-1} = \frac{1}{\bar{\rho}_k^{n-1}} \left. \frac{d\rho}{dT} \right|_k^{n-1} \frac{P_h \Delta z_k}{A} \frac{\bar{q}_k^{n-1}}{\bar{\rho}_k^{n-1} c_{p,k}^{n-1}} \quad (\text{A.52})$$

By inserting the new time velocities v_k^n and v_{k-1}^n in Eq. (A.46) into Eq. (A.50), a system of linear equations for K cell-center pressures at new time can be obtained. For this, Eq. (A.46) can be rewritten as

$$v_k^n = \alpha_k^{n-1} + \beta_k^{n-1} (\bar{P}_k^n - \bar{P}_{k+1}^n) \quad (\text{A.53})$$

where

$$\alpha_k^{n-1} = v_k^{n-1} + \left[\frac{\bar{\rho}_{k-1}^{n-1} v_{k-1}^{n-1}}{\bar{\rho}_k^{n-1}} \left(\frac{2}{\Delta z_k + \Delta z_{k+1}} \frac{\bar{\rho}_{k-1}^{n-1}}{\bar{\rho}_k^{n-1}} v_{k-1}^{n-1} - \frac{v_k^{n-1}}{\Delta z_k} \right) \right.$$

$$- (v_k^{n-1})^2 \left(\frac{2}{\Delta z_k + \Delta z_{k+1}} \frac{\bar{\rho}_k^n}{\bar{\rho}_{k+1}^n} - \frac{1}{\Delta z_k} \right)$$

$$\left. - \frac{(1 + \bar{\rho}_{k+1}^{n-1} / \bar{\rho}_k^{n-1})}{1 + \Delta z_{k+1} / \Delta z_k} g - \frac{f_k (v_k^{n-1})^2}{2D_h} \right] \Delta t_n, \quad k = 1, 2, \dots, K-1 \quad (\text{A.54a})$$

$$\alpha_K^{n-1} = v_K^{n-1} + \left[\frac{\bar{\rho}_{K-1}^{n-1} v_{K-1}^{n-1}}{\Delta z_K} \left(2 \frac{\bar{\rho}_{K-1}^{n-1}}{\bar{\rho}_K^{n-1}} v_{K-1}^{n-1} - v_K^{n-1} \right) - \frac{(v_K^{n-1})^2}{\Delta z_K} - g - \frac{f_K (v_K^{n-1})^2}{2D_h} \right] \Delta t_n \quad (\text{A.54b})$$

$$\beta_k^{n-1} = \frac{2\Delta t_n}{\bar{\rho}_k^{n-1} (\Delta z_k + \Delta z_{k+1})}, \quad k = 1, 2, \dots, K-1 \quad (\text{A.55a})$$

$$\beta_K^{n-1} = \frac{2\Delta t_n}{\bar{\rho}_K \Delta z_K} \quad (\text{A.55b})$$

By substituting the new time velocities v_k^n and v_{k-1}^n for $k = 2, 3, \dots, K$ in Eq. (A.53) into Eq. (A.50), the following $K-1$ equations for K unknowns are obtained:

$$-\omega_k^{n-1} \beta_{k-1}^{n-1} P_{k-1}^n + (\omega_k^{n-1} \beta_{k-1}^{n-1} + \beta_k^{n-1}) P_k^n - \beta_k^{n-1} P_{k+1}^n = \omega_k^{n-1} \alpha_{k-1}^{n-1} - \alpha_k^{n-1} - \chi_k^{n-1}, \quad k = 2, 3, \dots, K \quad (\text{A.56})$$

One additional equation is obtained from the boundary condition. For the outlet pressure boundary condition, $P_{K+1}^n = P_{out}^n$, the pressure equation for $k = K$ can be obtained as

$$-\omega_K^{n-1} \beta_{K-1}^{n-1} P_{K-1}^n + (\omega_K^{n-1} \beta_{K-1}^{n-1} + \beta_K^{n-1}) P_K^n = \omega_K^{n-1} \alpha_{K-1}^{n-1} - \alpha_K^{n-1} - \chi_K^{n-1} + \beta_K^{n-1} P_{out}^n \quad (\text{A.57})$$

For the boundary conditions for the inlet flow rate and temperature, the inlet velocity can be determined since the density is a function of temperature only. Therefore, using a known inlet velocity, the pressure equation for $k = 1$ can be derived by inserting v_1^n in Eq. (A.53) into Eq. (A.50) as

$$\beta_1^{n-1} P_1^n - \beta_1^{n-1} P_2^n = \omega_1^{n-1} v_{in}^n - \chi_1^{n-1} - \alpha_1^{n-1} \quad (\text{A.58})$$

The coefficients and the source terms of Eq. (A.56), Eq. (A.57) and Eq. (A.58) for the time advanced pressures can be evaluated using the previous time step solutions, and thus they form a system of linear equations. Since the coefficient matrix is a tri-diagonal matrix, this system of linear equations can easily be solved by the forward elimination and backward substitution algorithm. Substitution of the new time pressures into Eq. (A.46) yields the new time velocities. Using the new time velocities, the new time densities and temperatures can be obtained from Eq. (A.44) and Eq. (A.45), respectively.

A.4.1.2. Numerical Methods for Heat Conduction Equations

The fuel and coolant tube are divided into computational cells as illustrated in Figure A.9, where the regions bounded by dashed lines denote the computational meshes. Each grid point is placed at the geometric center of each cell. The temperatures are defined at these grid points and denoted by a bar. The finite difference equations are derived by integrating the heat conduction equation over the cell volumes under the assumption that the values at the center of each cell prevail over the cell volume. Since the heat conduction equations for the fuel and the coolant tube in Eq. (A.30) and Eq. (A.31) are identical except for the heat conductivity and the heat generation rate, both equations can be solved simultaneously using the same numerical scheme.

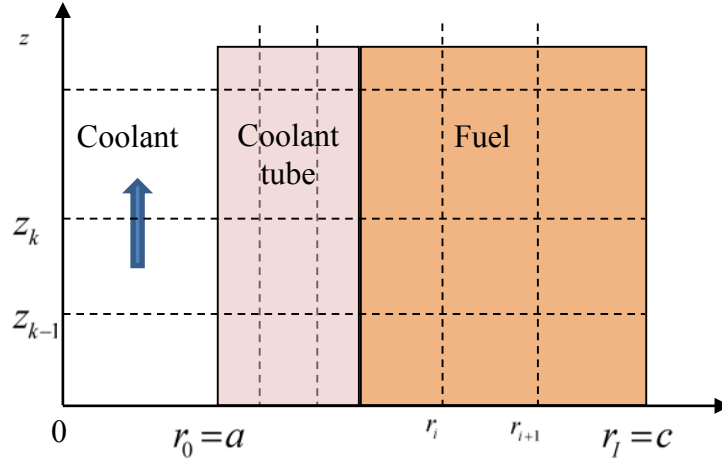


Figure A.9. Mesh Structure for Heat Conduction Calculations in Fuel and Coolant Tube

By integrating Eq. (A.30) over a mesh (i, k) bounded by $r_{i-1} \leq r \leq r_i$ and $z_{k-1} \leq z \leq z_k$, we obtain an first-order ordinary differential equation

$$\frac{d}{dt}(\rho_{ik} c_{p,ik} \bar{T}_{ik}) V_{ik} = - \left[2\pi r_i \bar{q}_{r,i}'' \Big|_{r=r_i} - 2\pi r_{i-1} \bar{q}_{r,i}'' \Big|_{r=r_{i-1}} \right] \Delta z_k + \bar{q}_{ik}''' V_{ik} \quad (\text{A.59})$$

where $V_{ik} = \pi(r_i^2 - r_{i-1}^2) \Delta z_k$, $A_i = \pi(r_i^2 - r_{i-1}^2)$ and the cell-averaged temperature and heat fluxes at the cell faces are given by

$$\bar{T}_{ik}(t) = \frac{2\pi}{V_{ik}} \int_{z_{k-1}}^{z_k} \int_{r_{i-1}}^{r_i} T_f(r, z, t) r dr dz \quad (\text{A.60})$$

$$\bar{q}_{r,i}''(r, t) = -k_{ik} \frac{\partial}{\partial r} \left[\frac{1}{\Delta z_k} \int_{z_{k-1}}^{z_k} T_f(r, z, t) dz \right] = -k_{ik} \frac{\partial}{\partial r} \bar{T}_{ik}^r(r, t) \quad (\text{A.61})$$

By assuming that the temperature varies linearly from the center of the mesh cell to the midpoints of its surfaces and by using the continuity condition at the cell interface, the surface average temperature of the interface of the cells (i, k) and $(i+1, k)$ can be obtained as

$$\bar{T}_{i+1/2,k} = \frac{(k_{ik} / \Delta r_i) \bar{T}_{ik} + (k_{i+1,k} / \Delta r_{i+1}) \bar{T}_{i+1,k}}{k_{ik} / \Delta r_i + k_{i+1,k} / \Delta r_{i+1}} \quad (\text{A.62})$$

Substituting Eq. (A.62) into Eq. (A.61) yields the heat flux at the interface

$$\bar{q}_{r,i}'' \Big|_{r=r_i} = a_{i,i+1}^k (\bar{T}_{ik} - \bar{T}_{i+1,k}) = -a_{i+1,i}^k (\bar{T}_{i+1,k} - \bar{T}_{ik}) \quad (\text{A.63})$$

where

$$a_{lm}^k = \frac{1}{\Delta r_l / (2k_{lk}) + \Delta r_m / (2k_{mk})} \quad (\text{A.64})$$

When a cell surface corresponds to an external boundary, the external boundary condition in Eq. (A.33) or Eq. (A.34) provides the relation needed for determining the boundary coupling coefficients. Under the assumption that the temperature varies linearly from the center of the

mesh cell to the midpoints of its surfaces, the heat flux at the radial boundaries can be obtained as

$$\bar{q}_{r,i}'' \Big|_{r=r_b} = -k_{ik} \frac{\partial T}{\partial r} \Big|_{r=r_b} = \begin{cases} -a_{1b}^k (\bar{T}_{1k} - \bar{T}_k) & \text{at inner surface of coolant tube} \\ 0 & \text{at outer surface of fuel} \end{cases} \quad (\text{A.65})$$

where \bar{T}_k is the bulk coolant temperature in the axial cell k of the coolant channel and

$$a_{1b}^k = \frac{h_{wk}}{1 + h_{wk} \Delta r_1 / (2k_{1k})} \quad (\text{A.66})$$

In Eq. (A.66), h_{wk} is the coefficient of convective heat transfer from the coolant tube inner wall to the coolant in the axial cell k .

By inserting the surface heat fluxes in Eq. (A.63) and Eq. (A.65) into Eq. (A.59), the mesh-centered finite difference equations are obtained as

$$\frac{d}{dt}(\rho_{ik} c_{p,ik} \bar{T}_{ik}) = c_{i,i+1}^k \bar{T}_{i+1,k} + c_{i,i-1}^k \bar{T}_{i-1,k} - d_{ik} \bar{T}_{ik} + \bar{q}_{ik}''' \quad (2 \leq i \leq I-1, 1 \leq k \leq K) \quad (\text{A.67})$$

$$\frac{d}{dt}(\rho_{ik} c_{p,ik} \bar{T}_{ik}) = c_{i,i+1}^k \bar{T}_{i+1,k} - d_{ik} \bar{T}_{ik} + c_b^k \bar{T}_k + \bar{q}_{ik}''' \quad (i=1) \quad (\text{A.68})$$

$$\frac{d}{dt}(\rho_{ik} c_{p,ik} \bar{T}_{ik}) = c_{i,i-1}^k \bar{T}_{i-1,k} - d_{ik} \bar{T}_{ik} + \bar{q}_{ik}''' \quad (i=I) \quad (\text{A.69})$$

where

$$c_{i,i+1}^k = \frac{2\pi r_i \Delta z_k}{V_{ik}} a_{i,i+1}^k = \frac{2r_i}{r_i^2 - r_{i-1}^2} a_{i,i+1}^k, \quad 1 \leq i \leq I-1 \quad (\text{A.70})$$

$$c_{i,i-1}^k = \frac{2\pi r_{i-1} \Delta z_k}{V_{ik}} a_{i,i-1}^k = \frac{2r_{i-1}}{r_i^2 - r_{i-1}^2} a_{i,i-1}^k, \quad 2 \leq i \leq I \quad (\text{A.71})$$

$$c_b^k = \frac{2\pi r_0 \Delta z_k}{V_{ik}} a_{1b}^k = \frac{2r_0}{r_1^2 - r_0^2} \frac{h_{wk}}{1 + h_{wk} \Delta r_1 / (2k_{1k})} \quad (\text{A.72})$$

$$d_{ij} = \begin{cases} c_{i,i+1}^k + c_{i,i-1}^k, & 2 \leq i \leq I-1 \\ c_{i,i+1}^k + c_{ib}^k, & i=1 \\ c_{i,i-1}^k, & i=I \end{cases} \quad (\text{A.73})$$

Using the fully implicit temporal difference scheme for temperatures and the previous time heat source, the final finite difference equations for the heat conduction equations in Eq. (A.67), Eq. (A.68), and Eq. (A.69) can be obtained as

$$-\frac{c_{i,i-1}^{k,n} \Delta t_n}{\rho_{ik}^n c_{p,ik}^n} \bar{T}_{i-1,k}^n + \left(1 + \frac{d_{ik}^n \Delta t_n}{\rho_{ik}^n c_{p,ik}^n} \right) \bar{T}_{ik}^n - \frac{c_{i,i+1}^{k,n} \Delta t_n}{\rho_{ik}^n c_{p,ik}^n} \bar{T}_{i+1,k}^n = \bar{T}_{ik}^{n-1} + \frac{\Delta t_n}{\rho_{ik}^n c_{p,ik}^n} \bar{q}_{ik}^{m,n-1}, \quad 2 \leq i \leq I-1 \quad (\text{A.74})$$

$$\left(1 + \frac{d_{ik}^n \Delta t_n}{\rho_{ik}^n c_{p,ik}^n}\right) \bar{T}_{ik}^n - \frac{c_{i,i+1}^{k,n} \Delta t_n}{\rho_{ik}^n c_{ik}^n} \bar{T}_{i+1,k}^n = \bar{T}_{ik}^{n-1} + \frac{\Delta t_n}{\rho_{ik}^n c_{p,ik}^n} (\bar{q}_{ik}^{m,n-1} + c_b^{k,n} T_k^n), \quad i=1 \quad (\text{A.75})$$

$$-\frac{c_{i,i-1}^{k,n} \Delta t_n}{\rho_{ik}^n c_{ij}^n} \bar{T}_{i-1,k}^n + \left(1 + \frac{d_{ik}^n \Delta t_n}{\rho_{ik}^n c_{p,ik}^n}\right) \bar{T}_{ik}^n = \bar{T}_{ik}^{n-1} + \frac{\Delta t_n}{\rho_{ik}^n c_{p,ik}^n} \bar{q}_{ik}^{m,n-1}, \quad i=I \quad (\text{A.76})$$

The finite difference equations given in Eq. (A.74), Eq. (A.75), and Eq. (A.76) form a system of equations for the advanced time temperatures of fuel and coolant tube. The coolant temperature on the right hand side of Eq. (A.74), Eq. (A.75), and Eq. (A.76) are determined by solving the coolant flow equations, and the volumetric heat sources are calculated using the initial power distribution and the power amplitude determined by solving the point kinetics equations. With known source terms, these equations form a system of nonlinear equations since the coefficients depend on the unknown temperatures through the temperature dependent material properties. This system of nonlinear equations can be solved iteratively. Initially the coefficients are estimated using the previous time temperatures. For known coefficients, the system of equations becomes a system of linear equations. This is a tri-diagonal system, and hence it can easily be solved by the forward elimination and backward substitution algorithm used for solving the system of coolant pressure equations. Using the updated temperatures, the temperature-dependent coefficients are updated. This iteration between temperatures and material properties continues until the successive temperatures converge within a specified limit.

A.4.2. Flow Split Calculation

The total coolant flow is distributed among multiple parallel channels that have common inlet and outlet plena, and thus it splits into the channels to yield the equal pressure drop across each channel. For a given mass flux G_i of channel i , the pressure drop ΔP_i across the channel i can be determined by solving the single-channel thermal-hydraulics problem, as discussed in Section A.4.1. Therefore, denoting the pressure drop as a function of the mass flux as $\Delta P_i(G_i)$, the system of governing equations for unknown mass fluxes for I parallel channels can be written as the following system of nonlinear equations:

$$\Delta P_1(G_1) = \Delta P_2(G_2) = \dots = \Delta P_I(G_I) = \bar{\Delta P} \quad (\text{A.77})$$

$$\sum_{i=1}^I N_i A_i G_i = W_T \quad (\text{A.78})$$

where N_i and A_i are the number of coolant tubes and flow area of channel i , and W_T is the total flow rate.

The system of nonlinear equations give in Eq. (A.77) and Eq. (A.78) can be solved iteratively using the Newton-Rapson method. The derivatives required in the Newton-Rapson method can be estimated by the finite difference approximation based on the single channel solutions for given mass fluxes. Using the pressure drop $\Delta P_i^{(n)}$ calculated with the n -th iterative solution $G_i^{(n)}$, the pressure drop for the $(n+1)$ -st solution can be approximated as

$$\Delta P_i^{(n+1)} = \Delta P_i^{(n)} + a_i^{(n)} (G_i^{(n+1)} - G_i^{(n)}), \quad i=1, 2, \dots, I \quad (\text{A.79})$$

where

$$a_i^{(n)} = \left. \frac{d(\Delta P_i)}{dG_i} \right|_{G_i=G_i^{(n)}} \cong \frac{\Delta P_i^{(n)} - \Delta P_i^{(n-1)}}{G_i^{(n)} - G_i^{(n-1)}} \quad (\text{A.80})$$

$$\Delta P_i^{(n)} = \Delta P_i(G_i^{(n)}) \quad (\text{A.81})$$

Requiring $\Delta P_i^{(n+1)}$ to be equal to the average pressure drop $\overline{\Delta P}^{(n+1)}$, Eq. (A.79) can be rewritten as

$$a_i^{(n)} G_i^{(n+1)} - \overline{\Delta P}^{(n+1)} = a_i^{(n)} G_i^{(n)} - \Delta P_i^{(n)}, \quad i = 1, 2, \dots, I \quad (\text{A.82})$$

Dividing Eq. (A.82) by $a_i^{(n)}$, multiplying by $N_i A_i$, and summing up the resulting equations, we have

$$\sum_{i=1}^I N_i A_i G_i^{(n+1)} - \sum_{i=1}^I \frac{N_i A_i}{a_i^{(n)}} \overline{\Delta P}^{(n+1)} = \sum_{i=1}^I N_i A_i G_i^{(n)} - \sum_{i=1}^I \frac{N_i A_i \Delta P_i^{(n)}}{a_i^{(n)}} \quad (\text{A.83})$$

Requiring the mass fluxes $G_i^{(n)}$ and $G_i^{(n+1)}$ to satisfy the flow conservation equation in Eq. (A.78), the average core pressure drop of the next iteration can be determined as

$$\overline{\Delta P}^{(n+1)} = \frac{\sum_{i=1}^I \frac{N_i A_i \Delta P_i^{(n)}}{a_i^{(n)}}}{\sum_{i=1}^I \frac{N_i A_i}{a_i^{(n)}}} \quad (\text{A.84})$$

Using this average pressure drop, the mass fluxes of the next iteration are obtained as

$$G_i^{(n+1)} = G_i^{(n)} + \frac{1}{a_i^{(n)}} [\overline{\Delta P}^{(n+1)} - \Delta P_i^{(n)}], \quad i = 1, 2, \dots, I \quad (\text{A.85})$$

This iteration procedure continues until the mass fluxes of two subsequent iterations converge within a specified limit. Specifically, channel flow rates are determined to satisfy the constant pressure drop boundary condition in the following steps:

- (1) Initial guesses are made for each channel mass flux and the core-average pressure drop using the values at the previous time step. For the initial steady state, a uniform initial mass flux $G_i^{(0)} = W_T / \sum_{i=1}^I N_i A_i$ and a zero core average pressure drop ($\overline{\Delta P}^{(0)} = 0$) is used. Using the assumed mass flux $G_i^{(0)}$, the channel pressure drop $\Delta P_i^{(0)}$ is computed for each channel.
- (2) For a perturbed mass flux $G_i^{(1)} = (1 + \varepsilon_G) G_i^{(0)}$, the perturbed channel pressure drop $\Delta P_i^{(1)}$ is computed. Here ε_G is the user-specified parameter for the flow rate perturbation used to evaluate the pressure derivatives initially. Using these perturbed pressure drops, the pressure derivatives with respect to the mass flux and the core-average pressure drop are computed as

$$a_i^{(1)} \cong a_i^{(2)} \cong \frac{\Delta P_i^{(2)} - \Delta P_i^{(1)}}{\varepsilon_G G_i^{(1)}} \quad (\text{A.86})$$

$$\overline{\Delta P}^{(2)} = \frac{\sum_i A_i \Delta P_i^{(1)} / a_i^{(1)}}{\sum_i A_i / a_i^{(1)}} \quad (\text{A.87})$$

- (3) The $(n+1)$ -st iteration of each channel mass flux $G_i^{(n+1)}$ is determined to satisfy the constant pressure drop boundary conditions approximately as

$$G_i^{(n+1)} = G_i^{(n)} + \frac{\overline{\Delta P}_i^{(n)} - \Delta P_i^{(n)}}{a_i^{(n)}} \quad (\text{A.88})$$

- (4) If the summation of individual channel flow rates is equal to the core flow rate, that is $\left| \sum_{i=1}^I N_i A_i G_i^{(n+1)} - W_T \right| / W_T < \varepsilon_w$, then the constant pressure drop boundary condition is satisfied. The iteration for channel mass fluxes is stopped, and the single channel analysis is performed for each channel.
- (5) Otherwise, the updated channel pressure drops $\Delta P_i^{(n+1)}$ are calculated with the channel flow rates $G_i^{(n+1)}$ and the pressure derivatives with respect to mass flux are updated as

$$a_i^{(n+1)} = \frac{\Delta P_i^{(n+1)} - \Delta P_i^{(n)}}{G_i^{(n+1)} - G_i^{(n)}} \quad (\text{A.87})$$

and go back to the step (3).

It was observed that using the flow rates at the last time step are used as the initial guess for the channel flow rates, the flow rates converged in 1 to 2 iterations in general.

A.5. Primary Loop Thermal-Fluidic Model

The primary heat transport system is configured in a loop-type arrangement. The reactor core and the direct reactor auxiliary cooling system (DRACS) heat exchangers contained in the reactor vessel, and the primary pumps and intermediate heat exchangers located in shielded cells outside the reactor vessel. The intermediate heat exchangers are established at the appropriate elevation to support natural circulation. Removal of decay heat from the reactor core is a fundamental safety function. In the loop SLFFR design, normal decay heat removal is through the normal power conversion systems, but a direct reactor auxiliary cooling system (DRACS) is provided, having both forced flow and natural convection capability. This system removes decay heat from the pool to the atmosphere using heat exchangers located in the cold part of the sodium pool and in the atmosphere above grade. If electrical power is available, forced flow can be used; in an emergency such as during the loss of all site power, natural convection flow removes the decay heat. The lower and upper plenum provide a large thermal inertia which delays the coolant temperature change significantly during the accident scenarios, especially for the ULOHS accident. For simplicity, it was assumed that the DRACS removes 1% of full power. The illustration of the primary loop is shown in Figure A.10.

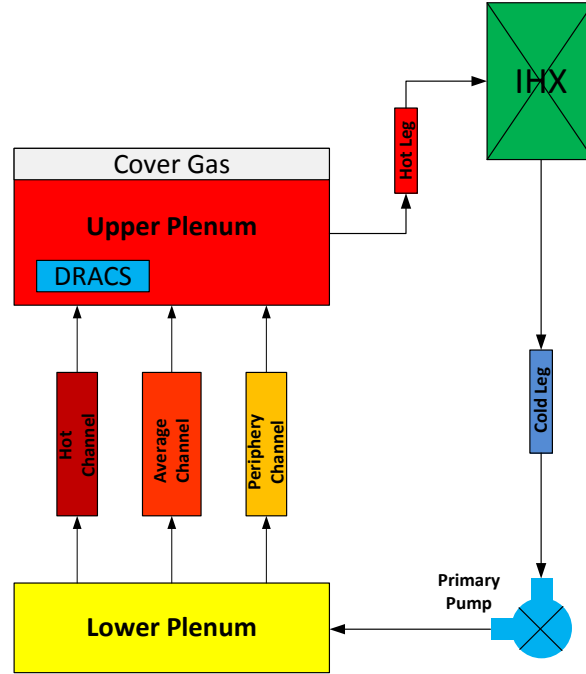


Figure A.10. Schematics of Primary Heat Transport System

A.5.1. Energy Balance Equations

For the primary loop thermal-fluidic analysis, the mass, momentum, and energy balance equations are solved simultaneously. For simplicity, the energy equations for individual components are solved first using lumped parameter models, and then the solutions are coupled with the mass and momentum equations through updated mass flow rates of core channels and IHX.

In the lumped parameter model, each component is represented by a single node with an average coolant temperature. Assuming that the structural materials are in thermal equilibrium with the sodium coolant in each component, the energy balance equations for the upper plenum, intermediate heat exchanger, and lower plenum can be written as

$$C_{up} \frac{d\bar{T}_{up}}{dt} = \dot{m}_{core} c_p \bar{T}_{out} - \dot{m}_{HX} c_p T_{in}^{HX} - \dot{Q}_{DHR} \quad (A.88)$$

$$C_{HX} \frac{d\bar{T}_{HX}}{dt} = \dot{m}_{HX} c_p T_{in}^{HX} - \dot{m}_{HX} c_p T_{out}^{HX} - \dot{Q}_{HX} \quad (A.89)$$

$$C_{lp} \frac{d\bar{T}_{lp}}{dt} = \dot{m}_{HX} c_p T_{out}^{HX} - \dot{m}_{core} c_p T_{in} \quad (A.90)$$

where C_{up} , C_{HX} and C_{lp} are the heat capacities of upper plenum, intermediate heat exchanger, and lower plenum, respectively, and \bar{T}_{up} , \bar{T}_{HX} , and \bar{T}_{lp} are the corresponding average temperatures. T_{in} and \bar{T}_{out} are the coolant inlet and outlet temperatures of the core, respectively; T_{in}^{HX} and T_{out}^{HX} are the inlet and outlet temperatures, respectively, of the primary sodium coolant

in the intermediate heat exchanger. \dot{m}_{core} and \dot{m}_{HX} are the coolant mass flow rates of core channels and IHX, respectively, and c_p is the specific heat of sodium at the corresponding temperature. \dot{Q}_{DHR} is the heat removal rate by DRACS, and \dot{Q}_{HX} is the heat removal rate by the secondary sodium in the intermediate heat exchanger, which can be written as

$$\dot{Q}_{HX} = hA(\bar{T}_{HX} - \bar{T}_{SNa}) \quad (A.91)$$

where \bar{T}_{SNa} is the average temperature of the secondary sodium, h is the average, overall heat transfer coefficient from the primary sodium coolant to the secondary sodium coolant and A is total heat transfer area in the intermediate heat exchanger.

Using the upwind scheme for spatial differencing, i.e., $T_{in}^{HX} = \bar{T}_{up}$, $T_{out}^{HX} = \bar{T}_{HX}$, and $T_{in} = \bar{T}_{lp}$, and using the explicit scheme for time differencing, a set of finite difference equation can be derived as

$$\bar{T}_{up}^n = \bar{T}_{up}^{n-1} + \frac{\dot{m}_{core}^{n-1} c_p^{n-1} \Delta t_n}{C_{up}} \bar{T}_{out}^{n-1} - \frac{\dot{m}_{HX}^{n-1} c_p^{n-1} \Delta t_n}{C_{up}} \bar{T}_{up}^{n-1} - \frac{\dot{Q}_{DHR}^{n-1} \Delta t_n}{C_{up}} \quad (A.92)$$

$$\bar{T}_{HX}^n = \bar{T}_{HX}^{n-1} + \frac{\dot{m}_{HX}^{n-1} c_p^{n-1} \Delta t_n}{C_{HX}} \bar{T}_{up}^{n-1} - \frac{\dot{m}_{HX}^{n-1} c_p^{n-1} \Delta t_n}{C_{HX}} \bar{T}_{HX}^{n-1} - \frac{\dot{Q}_{HX}^{n-1} \Delta t_n}{C_{HX}} \quad (A.93)$$

$$\bar{T}_{lp}^n = \bar{T}_{lp}^{n-1} + \frac{\dot{m}_{HX}^{n-1} c_p^{n-1} \Delta t_n}{C_{lp}} \bar{T}_{HX}^{n-1} - \frac{\dot{m}_{core}^{n-1} c_p^{n-1} \Delta t_n}{C_{lp}} \bar{T}_{lp}^{n-1} \quad (A.94)$$

where n denotes the time node and $\Delta t_n = t_n - t_{n-1}$. The initial conditions can be obtained from the steady state results as

$$\bar{T}_{up}^0 = \bar{T}_{out}^0 - \frac{\dot{Q}_{DHR}^0}{\dot{m}_{core}^0 c_p^0} \quad (A.95)$$

$$\bar{T}_{HX}^0 = \bar{T}_{up}^0 - \frac{\dot{Q}_{HX}^0}{\dot{m}_{HX}^0 c_p^0} \quad (A.96)$$

$$\bar{T}_{lp}^0 = \bar{T}_{HX}^0 \quad (A.97)$$

A.5.2. Compressible Equation for Liquid Segments

The compressible volume and liquid segment models of the SASSYS code were adopted for the primary loop thermal-fluidic calculations. [66] In this approach, the primary heat transport system (PHTS) is modeled by connecting compressible volumes by liquid segments. Compressible volumes are used to represent the inlet plenum, outlet plenum with cover gas, pool, etc. and characterized by pressure, volume, mass, and temperature. They can accumulate liquid or gas by compressing the cover gas or the liquid, and it is the pressure in the compressible volume that drives the flow through the liquid and gas segments. Liquid segments are one-dimensional flow paths between two control volumes, and each liquid segment can contain one or more elements such as core assembly channels, shell and tube sides of an

intermediate heat exchanger, shell and tube sides of a heat exchanger of the direct reactor auxiliary cooling system (DRACS), pipes, etc.

The primary loop is modeled with two compressible volumes connected with two liquid elements as illustrated in Figure A.10. The inlet plenum is represented as a compressible volume without cover gas, and the outlet plenum is represented as a compressible volume with cover gas. The liquid segment from the inlet plenum to the outlet plenum represents the core side of the primary loop, and the liquid segment from the outlet plenum to the inlet plenum includes the intermediate heat exchanger and the primary pump.

The coolant fluid equations for the primary heat transport loops are solved by a fully implicit time differencing scheme in which the pressures and flows for all connected compressible volumes and segments are solved simultaneously. By linearizing the equations for each time step, a fully implicit scheme solution can be obtained without resorting to iteration techniques for solving a system of nonlinear equations. Three equations are used in calculating the pressures in the compressible volumes and the flow rates in the connecting liquid segments. They are the momentum equation for incompressible single-phase flow in a segment, an expression for the average flow rate in a segment during a time step, and an expression for the change in pressure in a compressible volumes resulting from in-flow and out-flow during a time step.

A.5.3. Momentum Equation for Liquid Segments

The momentum equation for a single-phase, incompressible one-dimensional flow can be written as

$$\frac{1}{A} \frac{\partial w}{\partial t} + \frac{1}{A^2} \frac{\partial}{\partial z} \left(\frac{w^2}{\rho} \right) = -\frac{\partial P}{\partial z} - \left(\frac{\partial P}{\partial z} \right)_{loss} \quad (\text{A.98})$$

where w is the mass flow rate. By integrating Eq. (A.98) over a segment containing several elements, the basic equation for the flow in segment i can be obtained as

$$\sum_{k \in i} \frac{L_k}{A_k} \frac{\partial w_i}{\partial t} = P_{i,in}(t) - P_{i,out}(t) - \Delta P_{i,fr}[w_i(t)] - \Delta P_{i,form}[w_i(t)] - \Delta P_{i,gr}(t) + \Delta P_{i,p} \quad (\text{A.99})$$

where A_k and L_k are the flow area and length of element k , respectively. The term $P_{i,in}$ is the pressure at the inlet to segment i , which is equal to the pressure P_{ji} in the compressible volume ji at the inlet to segment i , and the term $P_{i,out}$ is the pressure at the outlet of segment i , which is equal to the pressure P_{jo} in the compressible volume jo at the outlet of segment i . The pressure drop $\Delta P_{i,fr}$ is the sum of the frictional pressure losses for all the elements in segment i , the pressure drop $\Delta P_{i,form}$ is the total form pressure loss due to the valves, fittings, orifices, bends, etc. in segment i . The term $\Delta P_{i,gr}$ is the gravity-head pressure drop, and the term $\Delta P_{i,p}$ is the pump-head pressure increase from all of the pumps in segment i . The pump head and torque of a centrifugal pump are functions of pump speed and flow rate, but in this study, a simple model was used by specifying the pump head as a function of time as

$$\Delta P_p = \Delta P_{p0} h(t) \quad (\text{A.100})$$

where ΔP_{p0} is the reference pump head with $h(0) = 1$.

The skin friction and form pressure losses are proportional to the square of the mass flow rate, and hence Eq. (A.100) can be written as

$$\sum_{k \in i} \frac{L_k}{A_k} \frac{\partial w_i}{\partial t} = f(w_i, t) \quad (\text{A.101})$$

By applying a fully implicit differencing scheme, Eq. (A.101) can be written in finite difference form as

$$\sum_{k \in i} \frac{L_k}{A_k} \frac{\Delta w_i(t)}{\Delta t} = f[w_i(t + \Delta t), t + \Delta t] \quad (\text{A.102})$$

where $\Delta w_i(t) = w_i(t + \Delta t) - w_i(t)$. The right hand side of Eq. (A.102) can be linearized around $w_i(t)$ as

$$f[w_i(t + \Delta t), t + \Delta t] = f[w_i(t), t] + \frac{\partial f}{\partial w_i} \Delta w_i(t) + \frac{\partial f}{\partial t} \Delta t \quad (\text{A.103})$$

By inserting Eq. (A.103) into Eq. (A.102) and using the right hand side of Eq. (A.99) for $f(w_i, t)$, the flow rate change Δw_i can be obtained as

$$\Delta w_i(t) = \frac{a_{i1} + a_{i2} + \Delta t(\Delta P_{ji} - \Delta P_{jo})}{a_{i0} - a_{i3}} \quad (\text{A.104})$$

where

$$\Delta P_{ji} = \frac{\partial P_{ji}}{\partial t} \Delta t \quad (\text{A.105})$$

$$\Delta P_{jo} = \frac{\partial P_{jo}}{\partial t} \Delta t \quad (\text{A.106})$$

$$a_{i0} = \sum_{k \in i} \frac{L_k}{A_k} \quad (\text{A.107})$$

$$\begin{aligned} a_{i1} &= f(w_i, t) \Delta t = \Delta t [P_{i,in}(t) - P_{i,out}(t) + \Delta P_{i,p} - \Delta P_{i,fr}(w_i) - \Delta P_{i,form}(w_i) - \Delta P_{i,gr}(t)] \\ &= \Delta t [P_{i,in}(t) - P_{i,out}(t)] + \Delta t \sum_k [\Delta P_{k,p} - \Delta P_{k,fr}(w_i) - \Delta P_{k,form}(w_i) - \Delta P_{k,gr}(t)] \end{aligned} \quad (\text{A.108})$$

$$\begin{aligned} a_{i2} &= \frac{\partial f}{\partial t} (\Delta t)^2 = (\Delta t)^2 \frac{\partial}{\partial t} [\Delta P_{i,p}(t) - \Delta P_{i,fr}(w_i) - \Delta P_{i,form}(w_i) - \Delta P_{i,gr}(t)] \\ &= (\Delta t)^2 \sum_k \frac{\partial}{\partial t} [\Delta P_{k,p}(t) - \Delta P_{k,gr}(t)] \end{aligned} \quad (\text{A.109})$$

$$\begin{aligned}
 a_{i3} &= \frac{\partial f}{\partial w_i} \Delta t = -\Delta t \frac{\partial}{\partial w_i} [\Delta P_{i,p}(t) - \Delta P_{i,fr}(w_i) - \Delta P_{i,form}(w_i) - \Delta P_{i,gr}(t)] \\
 &= -\Delta t \sum_k \frac{\partial}{\partial w_i} [\Delta P_{k,fr}(w_i) + \Delta P_{k,form}(w_i)]
 \end{aligned} \tag{A.110}$$

By taking a simple average of the flow rate at the beginning of the time step and that of the end of time step, the average mass flow rate in a liquid segment during a time step can be written in terms of the flow rate change as

$$\bar{w}_i = \frac{1}{2} [w_i(t) + w_i(t + \Delta t)] = w_i(t) + \Delta w_i(t) \tag{A.111}$$

where the rightmost side is obtained by linearizing the flow rate over the time step. Inserting Eq. (A.104) into Eq. (A.111), the average mass flow rate in a segment during a time step can be obtained as

$$\bar{w}_i = w_i(t) + \frac{a_{i1} + a_{i2} + \Delta t(\Delta P_{ji} - \Delta P_{jo})}{2(a_{i0} - a_{i3})} \tag{A.112}$$

Pipes and Intermediate Heat Exchangers

In considering the flow through a pipe or an intermediate heat exchanger, the contribution of element k to a_{i0} in Eq. (A.107) is given by

$$\Delta a_{k0} = \frac{L_k}{A_k} \tag{A.113}$$

The pressure drop contribution of the element to a_{i1} in Eq. (A.108) is composed of a number of terms. The frictional pressure drop is written as

$$\Delta P_{k,fr} = f \frac{L_k}{D_{hk}} \frac{\rho_k v_k |v_k|}{2} = f \frac{L_k}{D_{hk}} \frac{w_k |w_k|}{2\rho_k A_k^2} \tag{A.114}$$

where D_{hk} is the equivalent hydraulic diameter of element k and the Moody friction factor f for turbulent flow in pipes is taken as

$$f = C_1 \left[1 + \left(C_2 \frac{\varepsilon}{D_h} + \frac{C_3}{\text{Re}} \right)^{C_4} \right] \tag{A.115}$$

with $C_1 = 0.0055$, $C_2 = 20,000$, $C_3 = 1 \times 10^6$, and $C_4 = 1/3$. In Eq. (A.115), $\text{Re} = D_h |w| / A\mu$ is the Reynolds number and ε is the roughness of the element. For a laminar flow, the friction factor is taken as

$$f = \frac{64}{\text{Re}} \tag{A.116}$$

The form pressure loss due to the fittings, orifices, bends, etc. is represented with the user-supplied loss coefficient K_k as

$$\Delta P_{k,form} = K_k \frac{w_k |w_k|}{2\rho_k A_k^2} \quad (\text{A.117})$$

The gravity head term for the element is taken as

$$\Delta P_{k,gr} = g(z_{k,out} - z_{k,in})\bar{\rho}_k \quad (\text{A.118})$$

where $z_{k,out}$ and $z_{k,in}$ are the heights of the element outlet and inlet, respectively, and $\bar{\rho}_k$ is the average of the inlet and outlet fluid densities.

Using Eq. (A.114), Eq. (A.117) and Eq. (A.118), the contribution from the element to a_{i1} is obtained as

$$\Delta a_{k1} = -\Delta t \left[f \frac{L_k}{D_{hk}} \frac{w_k |w_k|}{2\rho_k A_k^2} + K_k \frac{w_k |w_k|}{2\rho_k A_k^2} + g(z_{k,out} - z_{k,in})\bar{\rho}_k \right] \quad (\text{A.119})$$

Since the friction factors and geometry are assumed not to change independently with time, the contribution to a_{i2} , which is the derivative of the pressure drops with respect to time, is zero

$$\Delta a_{k2} = 0 \quad (\text{A.120})$$

The contribution to a_{i3} , which is the derivative of the pressure drops with respect to the mass flow rate, is obtained as

$$\Delta a_{k3} = -\Delta t \left[\frac{L_k}{D_{hk}} \frac{1}{2\rho_k A_k^2} \left\{ 2f |w_k| + w_k |w_k| \frac{\partial f}{\partial w} \right\} + K_k \frac{|w_k|}{\rho_k A_k^2} \right] \quad (\text{A.121})$$

where

$$\frac{\partial f}{\partial w} = \begin{cases} -\frac{C_1 C_3 C_4}{\text{Re} |w|} \left(C_2 \frac{\varepsilon}{D_h} + \frac{C_3}{\text{Re}} \right)^{C_4-1} & \text{for turbulent flow} \\ -f / w & \text{for laminar flow} \end{cases} \quad (\text{A.122})$$

A.5.4. Compressible Volume Pressure Changes

By assuming that the pressure in a compressible volume varies linearly with changes in the mass or temperature of the liquid, the change ΔP_j in pressure in the compressible volume j during a time step can be obtained as

$$\Delta P_j = b_{j0} + b_{j1} \left[\sum_i \bar{w}_{i,in} - \sum_i \bar{w}_{i,out} \right] + b_{j2} \left[\sum_i \bar{w}_{i,in} T_{j,in}^i - \sum_i \bar{w}_{i,out} T_{j,out} \right] \quad (\text{A.123})$$

where $\bar{w}_{i,in}$ is the average mass flow rate of segment i which flows into compressible volume j and $\bar{w}_{i,out}$ is the average mass flow rate of segment i which flows out from compressible volume j . The temperature $T_{j,in}^i$ is the temperature of the flow incoming to compressible volume j through segment i , which is equal to the outlet temperature $T_{i,out}$ of segment i , and $T_{j,out}$ is the outlet temperature of compressible volume j , which is equal to the inlet

temperature of segment i . The coefficients b_{j1} and b_{j2} include the time-step size and are computed for each type of compressible volume. The remaining term b_{j0} also contains the time step size, and it can be used to account for the effects of heat transfer to the compressible liquid from the compressible volume wall or from other components.

A.5.4.1. Compressible Volume with No Cover Gas

A compressible volume with no cover gas is treated as a compressible liquid in an expandable container. The volume V is assumed vary linearly with pressure P and temperature T

$$V = V_r[1 + \alpha_p(P - P_r) + \alpha_T(T - T_r)] \quad (\text{A.124})$$

where V_r is the volume at a reference pressure P_r and reference temperature T_r . Also the sodium density ρ is assumed to vary linearly with P and T

$$\rho = \rho_r[1 + \beta_p(P - P_r) + \beta_T(T - T_r)] \quad (\text{A.125})$$

Since the mass of the liquid in the compressible volume is $m = \rho V$, the mass can be written to first order as

$$m = m_r[1 + (\alpha_p + \beta_p)(P - P_r) + (\alpha_T + \beta_T)(T - T_r)] \quad (\text{A.126})$$

Eq. (A.126) can be rewritten as

$$\delta P = \frac{\delta m / m_r - (\alpha_T + \beta_T)\delta T}{\alpha_p + \beta_p} \quad (\text{A.127})$$

Using the conservation of mass, the change in the liquid mass Δm during the time step Δt can be written as

$$\Delta m = \Delta t \left[\sum_i \bar{w}_{i,in} - \sum_i \bar{w}_{i,out} \right] \quad (\text{A.128})$$

In addition, the conservation of energy for the compressible volume gives

$$(m + \Delta m)(T + \Delta T) = mT + \Delta t \left[\sum_i \bar{w}_{i,in} T_{j,in}^i - \sum_i \bar{w}_{i,out} T_{j,out} \right] + Q\Delta t / c_l \quad (\text{A.129})$$

where Q is the heat flow rate from the compressible walls and from other components in contact with the compressible volume liquid, and c_l is the heat capacity of the liquid in the compressible volume. Solving Eq. (A.129) for the change in the liquid temperature during the time step, the temperature change can be obtained to first order as

$$\Delta T = \frac{-T\Delta m + \Delta t \left[\sum_i \bar{w}_{i,in} T_{j,in}^i - \sum_i \bar{w}_{i,out} T_{j,out} \right] + Q\Delta t / c_l}{m + \Delta m} \quad (\text{A.130})$$

To first order, the denominator is approximated as m . Inserting Eq. (A.128) and (A.130) into Eq. (A.127) yields

$$\Delta P = \frac{\Delta t \left[\sum_i \bar{w}_{i,in} - \sum_i \bar{w}_{i,out} \right]}{\alpha_p + \beta_p} \left[\frac{1}{m_r} + \frac{(\alpha_T + \beta_T)T}{m} \right] - \frac{(\alpha_T + \beta_T)\Delta t}{(\alpha_p + \beta_p)m} \left[\sum_i \bar{w}_{i,in} T_{j,in}^i - \sum_i \bar{w}_{i,out} T_{j,out} + Q / c_l \right] \quad (\text{A.131})$$

Comparison of Eq. (A.123) and Eq. (A.131) yields that for the compressible volume with no cover gas

$$b_{j0} = -\frac{(\alpha_T + \beta_T)\Delta t Q}{(\alpha_p + \beta_p)mc_l} \quad (\text{A.132})$$

$$b_{j1} = \frac{\Delta t}{\alpha_p + \beta_p} \left[\frac{1}{m_r} + \frac{(\alpha_T + \beta_T)T}{m} \right] \quad (\text{A.133})$$

$$b_{j2} = -\frac{(\alpha_T + \beta_T)\Delta t}{(\alpha_p + \beta_p)m} \quad (\text{A.134})$$

A.5.4.2. Compressible Volume with Cover Gas

A compressible volume with cover gas is treated in a fashion similar to that without cover gas except that the compression of the liquid is neglected compared with the compression of gas, so that all of the expansion or compression is attributed entirely to the gas. The cover gas is assumed to expand or compress adiabatically, and an increase in the gas volume is equal to the decrease in the liquid volume. At an elevation z_r in the compressible volume, the liquid pressure is given by

$$P_l = P_g + \rho_l g(z_i - z_r) \quad (\text{A.135})$$

where z_i is the height of liquid and gas interface. Thus, the change in the liquid pressure in the compressible volume can be obtained by taking differentials of Eq. (A.135) as

$$\Delta P_l = \Delta P_g + g(z_i - z_r)\Delta \rho_l + \rho_l g \Delta z_i \quad (\text{A.136})$$

Adiabatic compression of the cover gas can be taken as

$$P_g V_g^\gamma = \text{const} \quad (\text{A.137})$$

where V_g is the volume of cover gas and γ is the ratio of the specific heat at constant pressure to that at constant volume for the cover gas. In differential form, Eq. (A.137) becomes

$$\frac{\Delta P_g}{P_g} + \gamma \frac{\Delta V_g}{V_g} = 0 \quad (\text{A.138})$$

The conservation of liquid mass and the conservation of energy for a compressible volume yields

$$\Delta m_l = \Delta t \left[\sum_i \bar{w}_{i,in} - \sum_i \bar{w}_{i,out} \right] \quad (\text{A.139})$$

$$(m_l + \Delta m_l)(T_l + \Delta T_l) = m_l T_l + \Delta t \left[\sum_i \bar{w}_{i,in} T_{j,in}^i - \sum_i \bar{w}_{i,out} T_{j,out} \right] \quad (\text{A.140})$$

Neglecting Δm_l in compression with m_l , the temperature change can be obtained as

$$\Delta T = \frac{\Delta t}{m_l} \left[\sum_i \bar{w}_{i,in} T_{j,in}^i - \sum_i \bar{w}_{i,out} T_{j,out} \right] - \frac{Q \Delta t}{c_p m_l} \quad (\text{A.141})$$

In addition, we have the following relations

$$\Delta V_g = -\Delta V_l \quad (\text{A.142})$$

$$V_l = m_l / \rho_l \quad (\text{A.143})$$

$$\Delta z_l = \Delta V_l / A \quad (\text{A.144})$$

Differentiating Eq. (A.143), we have

$$\Delta V_l = \frac{\Delta m_l}{\rho_l} - \frac{m_l}{\rho_l^2} \Delta \rho_l \quad (\text{A.145})$$

For an incompressible fluid, the density change can be written as

$$\Delta \rho_l = \frac{\partial \rho}{\partial T} \Delta T_l \quad (\text{A.146})$$

Using Eq. (A.138) to Eq. (A.146), the changes in the gas pressure and liquid elevation can be written in terms of the changes in the liquid mass and temperature as

$$\frac{\Delta P_g}{P_g} = \gamma \frac{\Delta V_l}{V_g} = \frac{\gamma}{V_g} \left(\frac{\Delta m_l}{\rho_l} - \frac{m_l}{\rho_l^2} \frac{\partial \rho}{\partial T} \Delta T_l \right) \quad (\text{A.147})$$

$$\Delta z_l = \frac{1}{A} \left(\frac{\Delta m_l}{\rho_l} - \frac{m_l}{\rho_l^2} \frac{\partial \rho}{\partial T} \Delta T_l \right) \quad (\text{A.148})$$

Inserting Eq. (A.146), Eq. (A.147) and Eq. (A.148) into Eq. (A.136), we have

$$\Delta P_l = \left(\frac{\gamma P_g}{V_g} + \frac{\rho_l g}{A} \right) \left(\frac{\Delta m_l}{\rho_l} - \frac{m_l}{\rho_l^2} \frac{\partial \rho}{\partial T} \Delta T_l \right) + g(z - z_r) \frac{\partial \rho}{\partial T} \Delta T_l \quad (\text{A.149})$$

Inserting Eq. (A.139) and Eq. (A.141) into Eq. (A.149) yields

$$\begin{aligned} \Delta P_l = & \left(\frac{\gamma P_g}{V_g \rho_l} + \frac{g}{A} \right) \Delta t \left[\sum_i \bar{w}_{i,in} - \sum_i \bar{w}_{i,out} \right] \\ & + \left[\frac{g(z_i - z_r)}{m_l} - \frac{1}{\rho_l} \left(\frac{\gamma P_g}{V_g \rho_l} + \frac{g}{A} \right) \right] \frac{\partial \rho}{\partial T} \Delta t \left[\sum_i \bar{w}_{i,in} T_{j,in}^i - \sum_i \bar{w}_{i,out} T_{j,out} - \frac{Q}{c_p} \right] \end{aligned} \quad (\text{A.150})$$

Comparison of Eq. (A.123) and Eq. (A.150) yields that for the compressible volume with cover gas

$$b_{j0} = \left[\frac{g(z_i - z_r)}{m_l} - \frac{1}{\rho_l} \left(\frac{\gamma P_g}{V_g \rho_l} + \frac{g}{A} \right) \right] \frac{\partial \rho}{\partial T} \frac{Q}{c_p} \Delta t \quad (\text{A.151})$$

$$b_{j1} = \left(\frac{\gamma P_g}{V_g \rho_l} + \frac{g}{A} \right) \Delta t \quad (\text{A.152})$$

$$b_{j2} = \left[\frac{g(z_i - z_r)}{m_l} - \frac{1}{\rho_l} \left(\frac{\gamma P_g}{V_g \rho_l} + \frac{g}{A} \right) \right] \frac{\partial \rho}{\partial T} \Delta t \quad (\text{A.153})$$

A.5.5. Primary Loop Solution Strategy

Equations (A.112) and (A.123) constitute a set of simultaneous equations for the average mass flow rates \bar{w}_i of the liquid segments and the pressure changes ΔP_j in the compressible volumes during a time step. Eliminating the average mass flow rates \bar{w}_i , these equations can be written as a single matrix equation for the pressure changes as

$$\sum_n c_{mn} \Delta P_n = d_m, \quad m = 1, 2, \dots \quad (\text{A.154})$$

The coefficient c_{mn} is the sum of contributions $c_{m \leftarrow n}^i$ from each segment i from control volume n to control volume m or the sum of contributions $c_{m \rightarrow n}^i$ from each segment i from control volume m to control volume n

$$c_{mn} = \sum_i c_{m \leftarrow n}^i \quad \text{or} \quad \sum_i c_{m \rightarrow n}^i \quad (\text{A.155})$$

and the diagonal element c_{mm} is given by

$$c_{mm} = 1 + \sum_i c_{m \leftarrow n}^i + \sum_i c_{m \rightarrow n}^i \quad (\text{A.156})$$

The driving force term d_m is the sum of contributions $d_{m \leftarrow}^i$ of each segment i flowing into compressible volume m and $d_{m \rightarrow}^i$ flowing out from into compressible volume m

$$d_m = b_{0m} + \sum_i d_{m \leftarrow}^i + \sum_i d_{m \rightarrow}^i \quad (\text{A.157})$$

By inserting Eq. (A.112) into Eq. (A.123), the coefficient $c_{m \leftarrow n}^i$ and d_m^i can be obtained as

$$c_{m \leftarrow n}^i = - \frac{(b_{m1} + b_{m2} T_{i,out}) \Delta t}{2(a_{i0} - a_{i3})} \quad (\text{A.158})$$

$$c_{m \rightarrow n}^i = - \frac{(b_{n1} + b_{n2} T_{i,in}) \Delta t}{2(a_{i0} - a_{i3})} \quad (\text{A.159})$$

$$d_{m \leftarrow}^i = \left[w_i + \frac{a_{i1} + a_{i2}}{2(a_{i0} - a_{i3})} \right] (b_{m1} + b_{m2} T_{i,out}) \quad (\text{A.160})$$

$$d_{m \rightarrow}^i = - \left[w_i + \frac{a_{i1} + a_{i2}}{2(a_{i0} - a_{i3})} \right] (b_{m1} + b_{m2} T_{i,in}) \quad (\text{A.161})$$

Equation (A.154) can be solved for the changes in the pressures in control volumes, and subsequently the average mass flow rates in liquid segments can be determined using Eq. (A.112).

Appendix B. User's Guide of Safety Analysis Code MUSA

B.1. Input Data Description

The input parameters of MUSA are grouped into 17 blocks as listed in Table B.1. Each parameter is specified by its name and the corresponding value separated by an equal sign. The input parameters may appear in any order. The given parameter values are used to override the default values, so some parameters may be omitted if they are not needed for a particular run.

Table B.1. MUSA Input Blocks and Specifications

Input blocks	Specifications
&problem_control	Problem type and fuel, coolant and structure materials
&core_TH	Total power, total flow rate, coolant inlet temperature, outlet plenum pressure and number of channel
&channel	Channel power and geometrical parameters
&flow_split	Initial guess channel flow rates, flow rate perturbations and channel form factors
&power	Axial distribution of channel power
&primary_loop	Primary loop control parameters
&cold_pool	Geometrical parameters and physical properties of the lower plenum
&hot_pool	Geometrical parameters and physical properties of the upper plenum
&IHX	Geometrical parameters and physical properties of the IHX
&pipe	Geometrical parameters and physical properties of the primary loop pipes.
&pump	Pumping head and decay constant
&DHR	Power of decay heat removal system
&transient	Transient scenarios and time control parameters
&Point_kinetics	Solution scheme, initial condition and kinetic parameters
&decay_heat	Parameters for decay heat power calculation
&feedback	Axial distribution of the feedback reactivity coefficient
&GEMs	Polynomial coefficients for GEMs worth as a function of gas and sodium interface height

B.2. Sample Input File

```

&problem_control
  name='SLFFR'           ! optional input
  ptype='transient'      ! (SS, transient)
  GEOM='SINK-IN'         ! (SINK-IN, SOURCE-IN)
  COOLANT='SODIUM'       ! (SODIUM, ...)
  FUEL='TRU-CE-CO'       ! (TRU-CE-CO, ...)
  STRU='TA-10W'          ! (TA-10W, ...)
/

&core_TH
  power_total=1000000    ! total reactor power (kWt)
  temperature_in=723.15  ! coolant inlet temperature (K)
  pressure_out=0.154     ! outlet plenum pressure (MPa)
  flow_in=6715           ! total coolant mass flow rate (kg/s)
  tube_num=18181         ! total number of coolant channels
  z_nodes=20             ! number of nodes on axial direction
  ep=0.01                ! absolute temperature convergence criteria (°C)
  imax=5                 ! maximum number of temperature iteration
/

&channel
  channel_num=3           ! number of thermal hydraulic channels
  channel_power=86.7, 56.5, 29.3 ! weighted channel power (kW)
  channel_diam1=1.28, 1.28, 1.28 ! outer diameter of the TH channel (cm)
  channel_diam2=1.0, 1.0, 1.0    ! outer diameter of the coolant tube (cm)
  channel_diam3=0.6, 0.6, 0.6    ! inner diameter of the coolant tube (cm)
  nmesh_fuel=10             ! number of meshes in fuel region
  nmesh_clad=5              ! number of meshes in tube region
  channel_len=100.0         ! length of the TH channel (cm)
  channel_form=1.23, 3.47, 9.13 ! form friction factor of the TH channel
/

&flow_split
  channel_flowrate=0.369, 0.369, 0.369 !initial guess of channel flow rates (kg/s)
  channel_tubenum=955, 15120, 2106      !number of coolant tubes included in the
                                         !orifacing zones
  pt=1.0005,0.9998,0.9998              !initial guess perturbation of flow rates
/

&power
  PID='EXTERNAL'          ! type of power shape (UNIFORM, SKEWED, COSINE or EXTERNAL)
  ! (provide nomorlized channel power distribution if PID='EXTERNAL')
  power_node=40           ! number of axial nodes for the input power distribution

!
!      z(i)(cm)  p1(i)(kw)  p2(i)(kw)  p3(i)(kw)
power_shape(1:4,1:40)=1.25   1.28E-02  1.28E-02  1.28E-02
                      3.76   1.46E-02  1.46E-02  1.46E-02
                      6.27   1.64E-02  1.64E-02  1.64E-02
                      8.78   1.82E-02  1.82E-02  1.82E-02
                      11.29  1.99E-02  1.99E-02  1.99E-02
                      13.80  2.16E-02  2.16E-02  2.16E-02
                      16.30  2.31E-02  2.31E-02  2.31E-02
                      18.81  2.46E-02  2.46E-02  2.46E-02
                      21.32  2.54E-02  2.54E-02  2.54E-02
                      23.83  2.66E-02  2.66E-02  2.66E-02
                      26.34  2.77E-02  2.77E-02  2.77E-02
                      28.85  2.87E-02  2.87E-02  2.87E-02
                      31.36  2.96E-02  2.96E-02  2.96E-02
                      33.86  3.04E-02  3.04E-02  3.04E-02
                      36.37  3.10E-02  3.10E-02  3.10E-02

```

```

38.88      3.16E-02  3.16E-02  3.16E-02
41.39      3.18E-02  3.18E-02  3.18E-02
43.90      3.21E-02  3.21E-02  3.21E-02
46.41      3.23E-02  3.23E-02  3.23E-02
48.91      3.23E-02  3.23E-02  3.23E-02
51.42      3.23E-02  3.23E-02  3.23E-02
53.93      3.21E-02  3.21E-02  3.21E-02
56.44      3.18E-02  3.18E-02  3.18E-02
58.95      3.14E-02  3.14E-02  3.14E-02
61.46      3.11E-02  3.11E-02  3.11E-02
63.97      3.05E-02  3.05E-02  3.05E-02
66.47      2.97E-02  2.97E-02  2.97E-02
68.98      2.88E-02  2.88E-02  2.88E-02
71.49      2.78E-02  2.78E-02  2.78E-02
74.00      2.67E-02  2.67E-02  2.67E-02
76.51      2.55E-02  2.55E-02  2.55E-02
79.02      2.42E-02  2.42E-02  2.42E-02
81.52      2.33E-02  2.33E-02  2.33E-02
84.03      2.17E-02  2.17E-02  2.17E-02
86.54      2.01E-02  2.01E-02  2.01E-02
89.05      1.83E-02  1.83E-02  1.83E-02
91.56      1.65E-02  1.65E-02  1.65E-02
94.07      1.45E-02  1.45E-02  1.45E-02
96.58      1.25E-02  1.25E-02  1.25E-02
98.91      1.05E-02  1.05E-02  1.05E-02

/

&primary_loop
  lp_num=4      ! number of loop
  theta_pr=0.5  ! implicit of the primary loop pressure equation solution scheme
/

&cold_pool
  alph_p=0.000001      ! pressure expansion coefficient
  alph_t=1.787E-005    ! temperature expansion coefficient
  CP_height=1.0         ! Sodium height in the cold pool (m)
  CP_mass=13729.48      ! Sodium mass in the cold pool (kg)
  gamma=1.67           ! adiabatic gas constant (Cp/Cv)
/

&hot_pool
  gas_height=1.0        ! height of the gas region in the upper plenum (m)
  gas_vol=31.67         ! volume of the gas region in the upper plenum (m3)
  HP_area=31.67         ! upper plenum cross-sectional area (m2)
  HP_mass=131430.6      ! total sodium mass in the upper plenum (kg)
/

&IHX
  IHX_pressure_drop=119000 ! coolant pressure drop in the IHX (Pa)
  sink_p=1              ! if provided, IHX power is fixd (ratio to nominal
                        ! power)
  IHX_power=1000000      ! nominal IHX power (kW)
  ! IHX_SINK_T=623.15    ! if provide, IHX sink temperature is fixed (K)
  IHX_mass=18313.0       ! mass of sodium in the IHX (kg)
/

&pipe
  len_pipe=20           ! total length of the primary loop pipes (m)
  area_pipe=0.34        ! cross-sectional area of the pipe (m2)
  diam_pipe=0.66        ! pipe diameter (m)
  f_pipe=0.008          ! friction factor of the pipes
  form_factor=0.115     ! form factor
  HL_height=6.0         ! height of the hot leg (m)

```

```

    CL_height=7.8                ! height of the cold leg (m)
/

&pump
    pump_head=83.1              ! pumping head (m)
    pump_decay_const=0.1155     ! pump coast-down decay constant (ln2/half_time)
/

&DHR
    DHR_power=10000             ! decay heat remover power (kW)
/

!(the following inputs are required when ptype='transient')

&transient
    scenario='UTOP'             ! NULL, UTOP, ULOHS, ULOF
    time_end=200                ! simulation time (s)
    del_t_print=0.1             ! editing time interval (s)
    del_t_MAIN=0.0001           ! feedback time interval (s)
    del_t_PR=1                  ! del_t_PR=1, search the TH time step to satisfy CFL condition
    ! del_t_PR=0.0001           ! user specified time interval for primary loop thermal
                                ! hydraulic calculation
    del_t_PKE=0.00001           ! point kinetics time interval
/

&Point_kinetics
    method='theta'              ! method for solving point kinetics equation
    theta=0.5                   ! implicit for theta method
    reactivity=0.5              ! external reactivity ($)
    source=0.0                  ! external source
    p_initial=1.0               ! initial power level
    gen_time=7.94255187E-08     ! neutron generation time (s)
    dgroup_num=6                ! number of delayed neutron groups
    !delay_coef=beta_effective(:) lambda(:)
    delay_coef= 5.7771E-05  1.3354E-02
                  4.9505E-04  3.0582E-02
                  3.0367E-04  1.1492E-01
                  6.8159E-04  2.9822E-01
                  3.4601E-04  8.5603E-01
                  1.1646E-04  2.8786E+00
/

&decay_heat_removal
    n_decay=23

!decay_coef   =      alpha(:)   lambda(:)
decay_coef    =      2.083E+01  1.002E+01
                  3.853E-01  6.433E-01
                  2.213E-01  2.186E-01
                  9.460E-02  1.004E-01
                  3.531E-02  3.728E-02
                  2.292E-02  1.435E-02
                  3.946E-03  4.549E-03
                  1.317E-03  1.328E-03
                  7.052E-04  5.356E-04
                  1.432E-04  1.730E-04
                  1.765E-05  4.881E-05
                  7.347E-06  2.006E-05
                  1.747E-06  8.319E-06
                  5.481E-07  2.358E-06
                  1.671E-07  6.450E-07

```

```

2.112E-08 1.278E-07
2.996E-09 2.466E-08
5.107E-11 9.378E-09
5.730E-11 7.450E-10
4.138E-14 2.426E-10
1.088E-15 2.210E-13
2.454E-17 2.640E-14
7.557E-17 1.380E-14

/
&feedback
  fuel_mass=576.38, 7576.98, 1695.07      ! fuel mass for each orificing zone
  reactivity_node=40                      ! number of nodes for reactivity distribution
! reactivity_coef = z_coef(:) Doppler(:) NaDen(:) FueWorth(:) StrDen(:)
! repeat for all channels
  reactivity_coef(:,1) = 1.25   -1.27E-05   -2.32E-07   2.09E-02   8.06E-07
                        3.76    2.83E-06    1.05E-07   2.62E-02   1.40E-06
                        6.27    7.27E-06    5.11E-07   3.21E-02   2.06E-06
                        8.78    9.57E-06    9.57E-07   3.85E-02   2.77E-06
                        11.29   1.14E-05    1.43E-06   4.53E-02   3.52E-06
                        13.80   1.31E-05    1.93E-06   5.23E-02   4.30E-06
                        16.30   1.49E-05    2.43E-06   5.94E-02   5.08E-06
                        18.81   1.66E-05    2.94E-06   6.64E-02   5.86E-06
                        21.32   1.76E-05    3.42E-06   7.11E-02   6.60E-06
                        23.83   1.92E-05    3.88E-06   7.76E-02   7.32E-06
                        26.34   2.07E-05    4.32E-06   8.38E-02   8.01E-06
                        28.85   2.21E-05    4.73E-06   8.96E-02   8.66E-06
                        31.36   2.34E-05    5.10E-06   9.50E-02   9.25E-06
                        33.86   2.45E-05    5.44E-06   9.98E-02   9.78E-06
                        36.37   2.55E-05    5.74E-06   1.04E-01   1.02E-05
                        38.88   2.63E-05    5.98E-06   1.07E-01   1.06E-05
                        41.39   2.67E-05    6.17E-06   1.09E-01   1.09E-05
                        43.90   2.72E-05    6.31E-06   1.11E-01   1.11E-05
                        46.41   2.74E-05    6.40E-06   1.12E-01   1.13E-05
                        48.91   2.75E-05    6.43E-06   1.13E-01   1.13E-05
                        51.42   2.75E-05    6.40E-06   1.12E-01   1.13E-05
                        53.93   2.72E-05    6.32E-06   1.11E-01   1.11E-05
                        56.44   2.67E-05    6.18E-06   1.09E-01   1.09E-05
                        58.95   2.61E-05    6.00E-06   1.06E-01   1.06E-05
                        61.46   2.56E-05    5.76E-06   1.04E-01   1.03E-05
                        63.96   2.47E-05    5.47E-06   1.00E-01   9.82E-06
                        66.47   2.35E-05    5.13E-06   9.56E-02   9.29E-06
                        68.98   2.22E-05    4.75E-06   9.03E-02   8.70E-06
                        71.49   2.08E-05    4.34E-06   8.44E-02   8.06E-06
                        74.00   1.93E-05    3.90E-06   7.83E-02   7.36E-06
                        76.51   1.77E-05    3.44E-06   7.16E-02   6.64E-06
                        79.02   1.61E-05    2.96E-06   6.49E-02   5.89E-06
                        81.52   1.49E-05    2.46E-06   6.00E-02   5.12E-06
                        84.03   1.32E-05    1.95E-06   5.29E-02   4.34E-06
                        86.54   1.15E-05    1.44E-06   4.58E-02   3.55E-06
                        89.05   9.76E-06    9.46E-07   3.89E-02   2.79E-06
                        91.56   8.12E-06    4.79E-07   3.23E-02   2.06E-06
                        94.07   6.58E-06    4.74E-08   2.62E-02   1.38E-06
                        96.58   5.16E-06    -3.19E-07   2.06E-02   7.61E-07
                        98.91   3.93E-06    -3.10E-06   1.57E-02   2.10E-07

  reactivity_coef(:,2) = 1.25 -8.23E-05   -2.76E-06   9.46E-03   4.37E-06
                        3.76  1.60E-05    -7.35E-07   1.19E-02   7.88E-06
                        6.27  4.35E-05    1.72E-06   1.46E-02   1.18E-05
                        8.78  5.79E-05    4.47E-06   1.76E-02   1.62E-05
                        11.29  6.92E-05    7.43E-06   2.07E-02   2.07E-05
                        13.80  8.00E-05    1.05E-05   2.40E-02   2.55E-05
                        16.30  9.07E-05    1.37E-05   2.73E-02   3.03E-05
                        18.81  1.01E-04    1.69E-05   3.06E-02   3.51E-05

```


21.32	1.09E-04	1.99E-05	3.32E-02	3.97E-05
23.83	1.19E-04	2.29E-05	3.62E-02	4.42E-05
26.34	1.29E-04	2.57E-05	3.92E-02	4.85E-05
28.85	1.37E-04	2.83E-05	4.20E-02	5.25E-05
31.36	1.46E-04	3.07E-05	4.45E-02	5.62E-05
33.86	1.53E-04	3.29E-05	4.68E-02	5.95E-05
36.37	1.59E-04	3.48E-05	4.88E-02	6.24E-05
38.88	1.65E-04	3.63E-05	5.05E-02	6.48E-05
41.39	1.68E-04	3.76E-05	5.14E-02	6.67E-05
43.90	1.71E-04	3.85E-05	5.24E-02	6.80E-05
46.41	1.72E-04	3.90E-05	5.29E-02	6.89E-05
48.91	1.73E-04	3.92E-05	5.32E-02	6.92E-05
51.42	1.72E-04	3.90E-05	5.30E-02	6.89E-05
53.93	1.71E-04	3.85E-05	5.24E-02	6.81E-05
56.44	1.68E-04	3.76E-05	5.15E-02	6.68E-05
58.95	1.64E-04	3.64E-05	5.02E-02	6.49E-05
61.46	1.60E-04	3.49E-05	4.91E-02	6.26E-05
63.97	1.54E-04	3.30E-05	4.71E-02	5.98E-05
66.47	1.46E-04	3.09E-05	4.48E-02	5.65E-05
68.98	1.38E-04	2.85E-05	4.23E-02	5.28E-05
71.49	1.29E-04	2.58E-05	3.95E-02	4.88E-05
74.00	1.20E-04	2.30E-05	3.66E-02	4.45E-05
76.51	1.10E-04	2.01E-05	3.34E-02	4.00E-05
79.02	9.95E-05	1.70E-05	3.02E-02	3.53E-05
81.52	9.12E-05	1.39E-05	2.76E-02	3.06E-05
84.03	8.04E-05	1.06E-05	2.43E-02	2.57E-05
86.54	6.97E-05	7.47E-06	2.10E-02	2.10E-05
89.05	5.92E-05	4.39E-06	1.78E-02	1.63E-05
91.56	4.91E-05	1.49E-06	1.47E-02	1.19E-05
94.07	3.97E-05	-1.18E-06	1.19E-02	7.75E-06
96.58	3.10E-05	-3.54E-06	9.36E-03	4.02E-06
99.08	2.30E-05	-2.41E-05	7.13E-03	7.46E-07
reactivity_coef(:,3) =				
1.25	-5.48E-06	-1.40E-06	1.22E-03	4.13E-08
3.76	-2.92E-06	-8.52E-07	1.54E-03	7.66E-08
6.27	-2.38E-06	-9.55E-07	1.89E-03	1.14E-07
8.78	-2.11E-06	-1.03E-06	2.27E-03	1.53E-07
11.29	-1.91E-06	-1.08E-06	2.68E-03	1.94E-07
13.80	-1.73E-06	-1.12E-06	3.10E-03	2.37E-07
16.30	-1.57E-06	-1.14E-06	3.52E-03	2.81E-07
18.81	-1.41E-06	-1.14E-06	3.94E-03	3.26E-07
21.32	-1.24E-06	-1.14E-06	4.30E-03	3.70E-07
23.83	-1.12E-06	-1.14E-06	4.71E-03	4.13E-07
26.34	-1.02E-06	-1.13E-06	5.09E-03	4.54E-07
28.85	-9.44E-07	-1.12E-06	5.45E-03	4.93E-07
31.36	-8.78E-07	-1.11E-06	5.78E-03	5.29E-07
33.86	-8.22E-07	-1.10E-06	6.08E-03	5.62E-07
36.37	-7.75E-07	-1.08E-06	6.34E-03	5.90E-07
38.88	-7.29E-07	-1.07E-06	6.56E-03	6.14E-07
41.39	-6.87E-07	-1.06E-06	6.70E-03	6.34E-07
43.90	-6.53E-07	-1.05E-06	6.83E-03	6.48E-07
46.41	-6.31E-07	-1.05E-06	6.90E-03	6.56E-07
48.91	-6.14E-07	-1.05E-06	6.93E-03	6.59E-07
51.42	-6.01E-07	-1.05E-06	6.90E-03	6.57E-07
53.93	-5.91E-07	-1.05E-06	6.83E-03	6.49E-07
56.44	-5.86E-07	-1.06E-06	6.72E-03	6.35E-07
58.95	-5.89E-07	-1.07E-06	6.54E-03	6.16E-07
61.46	-5.98E-07	-1.08E-06	6.37E-03	5.92E-07
63.97	-6.04E-07	-1.10E-06	6.11E-03	5.64E-07
66.47	-6.03E-07	-1.11E-06	5.82E-03	5.32E-07
68.98	-6.02E-07	-1.13E-06	5.49E-03	4.96E-07
71.49	-6.00E-07	-1.14E-06	5.13E-03	4.56E-07
74.00	-6.00E-07	-1.15E-06	4.75E-03	4.15E-07

	76.51	-6.01E-07	-1.15E-06	4.34E-03	3.72E-07
	79.02	-6.13E-07	-1.16E-06	3.93E-03	3.28E-07
	81.52	-6.32E-07	-1.15E-06	3.56E-03	2.83E-07
	84.03	-6.32E-07	-1.14E-06	3.14E-03	2.38E-07
	86.54	-6.14E-07	-1.12E-06	2.71E-03	1.95E-07
	89.05	-5.88E-07	-1.08E-06	2.30E-03	1.53E-07
	91.56	-5.51E-07	-1.02E-06	1.91E-03	1.13E-07
	94.07	-5.02E-07	-9.44E-07	1.55E-03	7.68E-08
	96.58	-4.29E-07	-8.44E-07	1.22E-03	4.30E-08
	99.08	-3.90E-07	-3.90E-06	9.25E-04	1.11E-08
/					
&GEMs					
	Lgas0=1.2	! initial length of the inert gas			
	!coefficients of the polynomial to represent the reactivity insertion as function				
	!of sodium height in the GEMs				
	!r(h)=poly(5)*h ⁴ + poly(4)*h ³ + poly(3)*h ² + poly(2)*h+poly(1)				
	poly(1)= -2.2778				
	poly(2)= -0.3266				
	poly(3)= 2.264				
	poly(4)= 5.3606				
	poly(5)= -5.0215				
/					



School of Nuclear Engineering

Purdue University

400 Central Drive

West Lafayette, IN 47907

www.purdue.edu